

**Springer Theses**  
Recognizing Outstanding Ph.D. Research

Mohammad Farshadnia

# Advanced Theory of Fractional-Slot Concentrated- Wound Permanent Magnet Synchronous Machines



Springer

# **Springer Theses**

Recognizing Outstanding Ph.D. Research

## **Aims and Scope**

The series “Springer Theses” brings together a selection of the very best Ph.D. theses from around the world and across the physical sciences. Nominated and endorsed by two recognized specialists, each published volume has been selected for its scientific excellence and the high impact of its contents for the pertinent field of research. For greater accessibility to non-specialists, the published versions include an extended introduction, as well as a foreword by the student’s supervisor explaining the special relevance of the work for the field. As a whole, the series will provide a valuable resource both for newcomers to the research fields described, and for other scientists seeking detailed background information on special questions. Finally, it provides an accredited documentation of the valuable contributions made by today’s younger generation of scientists.

## **Theses are accepted into the series by invited nomination only and must fulfill all of the following criteria**

- They must be written in good English.
- The topic should fall within the confines of Chemistry, Physics, Earth Sciences, Engineering and related interdisciplinary fields such as Materials, Nanoscience, Chemical Engineering, Complex Systems and Biophysics.
- The work reported in the thesis must represent a significant scientific advance.
- If the thesis includes previously published material, permission to reproduce this must be gained from the respective copyright holder.
- They must have been examined and passed during the 12 months prior to nomination.
- Each thesis should include a foreword by the supervisor outlining the significance of its content.
- The theses should have a clearly defined structure including an introduction accessible to scientists not expert in that particular field.

More information about this series at <http://www.springer.com/series/8790>

Mohammad Farshadnia

# Advanced Theory of Fractional-Slot Concentrated-Wound Permanent Magnet Synchronous Machines

Doctoral Thesis accepted by  
the University of New South Wales, Sydney, Australia



Springer

*Author*  
Dr. Mohammad Farshadnia  
School of Electrical Engineering and  
Telecommunications  
The University of New South Wales  
Sydney, NSW  
Australia

*Supervisor*  
Prof. John E. Fletcher  
School of Electrical Engineering and  
Telecommunications  
The University of New South Wales  
Sydney, NSW  
Australia

ISSN 2190-5053

Springer Theses

ISBN 978-981-10-8707-3

<https://doi.org/10.1007/978-981-10-8708-0>

ISSN 2190-5061 (electronic)

ISBN 978-981-10-8708-0 (eBook)

Library of Congress Control Number: 2018934888

© Springer Nature Singapore Pte Ltd. 2018

This work is subject to copyright. All rights are reserved by the Publisher, whether the whole or part of the material is concerned, specifically the rights of translation, reprinting, reuse of illustrations, recitation, broadcasting, reproduction on microfilms or in any other physical way, and transmission or information storage and retrieval, electronic adaptation, computer software, or by similar or dissimilar methodology now known or hereafter developed.

The use of general descriptive names, registered names, trademarks, service marks, etc. in this publication does not imply, even in the absence of a specific statement, that such names are exempt from the relevant protective laws and regulations and therefore free for general use.

The publisher, the authors and the editors are safe to assume that the advice and information in this book are believed to be true and accurate at the date of publication. Neither the publisher nor the authors or the editors give a warranty, express or implied, with respect to the material contained herein or for any errors or omissions that may have been made. The publisher remains neutral with regard to jurisdictional claims in published maps and institutional affiliations.

Printed on acid-free paper

This Springer imprint is published by the registered company Springer Nature Singapore Pte Ltd.  
part of Springer Nature

The registered company address is: 152 Beach Road, #21-01/04 Gateway East, Singapore 189721,  
Singapore

*To My Parents, Sister, and My Loving Wife  
For Blessing My Life with Their  
Unconditional Love and Support*

# **Supervisor's Foreword**

Recent advances in multiphase fractional-slot concentrated-wound (FSCW) interior permanent magnet (IPM) machines have made them prime candidates for high-performance applications such as advanced electric drives in automobiles, aircraft, and marine vessels. The knowledge and understanding of the design and analysis of such revolutionary machines is limited, impeding further advances in research and development, both in the academia and the industry. This thesis addresses the knowledge gap by comprehensively analyzing, using first principles, the operation of such machines in a systematic manner.

In this book, which is the outcome of around 4 years of research, basic electromagnetic and machine theories are synthesized to develop the complex magnetic fields in generalized FSCW IPM machines. Two models are proposed and assessed for such machines: A detailed electromagnetic model for conceptual understanding and insight of the working principles; and a less complex electrical model for facilitating precise control of the machine. Furthermore, based on the rigorous analysis framework, for the first time, a general design methodology is proposed for multiphase machines using FSCW windings.

The original ideas presented in this book support the evolution of electric drive industries and can shape the further development of advanced electrical machines for the energy sector.

Sydney, NSW, Australia  
January 2018

Prof. John E. Fletcher  
UNSW Sydney

# Abstract

This thesis focuses on the analytical modeling of fractional-slot concentrated-wound (FSCW) interior permanent magnet (IPM) machines and establishes a basis for their magnetic and electrical analysis. In the state-of-the-art methods for analyzing such machines, the nonhomogeneous magnetic saturation and the nonlinear  $B$ - $H$  curve of the rotor iron are not considered. Moreover, the effect of the FSCW stator on the machine magnetic characteristics is overlooked.

Aiming at precise modelling of FSCW IPM machines' magnetic and electrical characteristics, a comprehensive mathematical treatment of the stator magneto-motive force (MMF), the IPM rotor nonhomogeneous magnetic saturation, and its airgap flux density are presented. The FSCW stator spatial MMF harmonics are analytically formulated, based on which, a novel heuristic algorithm is proposed for the design of optimal winding layouts for multiphase FSCW stators with different slot/pole combinations.

The nonhomogeneous magnetic saturation of the rotor iron due to its  $B$ - $H$  curve and the residual flux of the embedded magnets is modeled and a saturation map is proposed for the rotor iron. Accordingly, a novel airgap function is proposed for FSCW IPM machines taking into account the effect of the FSCW stator and the nonhomogeneously saturated rotor. A precise mathematical model is then proposed for calculation of the airgap PM flux density.

The proposed mathematical models for the FSCW stator and the IPM rotor are combined to derive detailed mathematical expressions for its operational inductances, electromagnetic torque, torque ripple, and their respective subcomponents, as a function of the machine geometry and design parameters. Both normal operation of the machine and open-phase fault condition are considered in the aforementioned formulations. A "maximum torque per ampere" algorithm is then proposed for the machine under an open-phase fault condition in which customized currents are injected such that maximum average torque with a low torque ripple is

guaranteed. Lastly, the derived geometry-based models for the machine characteristics are used to propose an extended  $dq$  model for FSCW IPM machines which takes into account its non-sinusoidal parameters.

The proposed theories and analytical models are validated using finite element analysis and experimental tests on a prototype FSCW IPM machine.

**Parts of this thesis have been published in the following articles:**

### **Journal Publications**

- [1] **M. Farshadnia**, M. A. Masood Cheema, A. Pouramin, R. Dutta and J. Edward Fletcher, “Design of Optimal Winding Configurations for Symmetrical Multiphase Concentrated-Wound Surface-Mount PMSMs to Achieve Maximum Torque Density Under Current Harmonic Injection,” in IEEE Transactions on Industrial Electronics, vol. 65, no. 2, pp. 1751–1761, Feb. 2018.
- [2] **M. Farshadnia**, M. A. M. Cheema, R. Dutta, J. E. Fletcher and M. F. Rahman, “Detailed Analytical Modeling of Fractional-Slot Concentrated-Wound Interior Permanent Magnet Machines for Prediction of Torque Ripple,” in IEEE Transactions on Industry Applications, vol. 53, no. 6, pp. 5272–5283, Nov.–Dec. 2017.
- [3] **M. Farshadnia**, M. A. M. Cheema, R. Dutta and J. E. Fletcher, “Analytical Modeling of Armature Reaction Air-Gap Flux Density Considering the Non-Homogeneously Saturated Rotor in a Fractional-Slot Concentrated-Wound IPM Machine,” in IEEE Transactions on Magnetics, vol. 53, no. 2, pp. 1–12, Feb. 2017.

### **Conference Publications**

- [4] **M. Farshadnia**, A. Pouramin, R. Dutta and J. E. Fletcher, “Airgap magnetic field estimation for IPM rotors considering their non-uniform local saturation,” 2017 20th International Conference on Electrical Machines and Systems (ICEMS), Sydney, NSW, 2017, pp. 1–6.
- [5] **M. Farshadnia**, M. A. M. Cheema, R. Dutta, J. E. Fletcher and M. F. Rahman, “Detailed analytical modelling of fractional-slot concentrated-wound interior permanent magnet machines for prediction of torque ripple,” 2016 IEEE Energy Conversion Congress and Exposition (ECCE), Milwaukee, WI, 2016, pp. 1–8.
- [6] **M. Farshadnia**, M. A. M. Cheema, R. Dutta, J. E. Fletcher, H. C. Lovatt and M. F. Rahman, “An extended dq model for concentrated-wound interior permanent magnet machines considering non-ideal machine parameters,” 8th IET International Conference on Power Electronics, Machines and Drives (PEMD 2016), Glasgow, 2016, pp. 1–6.
- [7] **M. Farshadnia**, M. A. M. Cheema, R. Dutta and J. E. Fletcher, “Analytical modeling of pulsating torque in concentrated-wound interior permanent magnet machines to achieve maximum average torque under an open-phase fault condition,” 2016 IEEE 8th International Power Electronics and Motion Control Conference (IPEMC-ECCE Asia), Hefei, 2016, pp. 2813–2819.
- [8] **M. Farshadnia**, M. A. M. Cheema, R. Dutta, J. E. Fletcher and M. F. Rahman, “Anomalies in experimental measurement of operational inductances of a concentrated-wound IPM machine under field-weakening region,” IECON 2015—41st Annual Conference of the IEEE Industrial Electronics Society, Yokohama, 2015, pp. 004880–004885.

- [9] **M. Farshadnia**, R. Dutta, J. E. Fletcher, K. Ahsanullah, M. F. Rahman and H. C. Lovatt, “Analysis of MMF and back-EMF waveforms for fractional-slot concentrated-wound permanent magnet machines,” 2014 International Conference on Electrical Machines (ICEM), Berlin, 2014, pp. 1976–1982.

# Acknowledgements

First and foremost, I would like to express my deepest gratitude to my supervisors, Prof. John Fletcher and Dr. Rukmi Dutta for their valuable guidance, support, and trust throughout the course of the research presented in this thesis.

I have been very fortunate to spend my doctoral period at the Energy Systems Research Group, School of Electrical Engineering and Telecommunications, UNSW Sydney, Australia. I am grateful to Prof. Faz Rahman for his support and input, and also the High Voltage laboratory and Power Electronics and Drives laboratory staff members, Mr. Liu Zhenyu and Dr. Dan Xiao, for their steady support and assistance. I would also like to extend my gratitude to my colleagues in the Energy System Research Group for their insightful discussions and suggestions: Dr. Kazi Ahsanullah, Mr. Alireza Pouramin, Dr. Dai Nguyen, etc.

I particularly acknowledge the help and input from Dr. Muhammad Ali Masood Cheema during the time of my research, with whom I enjoyed collaborating.

I am immensely grateful to my parents and sister for their constant support, love, and encouragement. They are an irreplaceable tower of strength and inspiration in my life.

Last but not least, I would like to express my gratitude to my wife, Atina. Meeting her in the final year of my doctoral period was a true blessing. Her cheerfulness and positive thinking have always been a source of inspiration and happiness throughout my career and life.

# Contents

<b>1</b>	<b>Introduction and Literature Review . . . . .</b>	<b>1</b>
1.1	Problem Statement and Research Motivations . . . . .	1
1.2	Research Objectives and Contributions . . . . .	4
1.3	Literature Review . . . . .	6
1.3.1	Types of PMSMs . . . . .	6
1.3.2	Machine Magnetic Characteristics . . . . .	9
1.3.3	Detailed Electrical Models and Equivalent Circuits for the Machine . . . . .	14
1.4	Thesis Outline . . . . .	15
1.5	Conclusion . . . . .	17
	References . . . . .	18
<b>2</b>	<b>Analytical Modelling of Stator Magnetic Characteristics in Fractional-Slot Concentrated-Wound Permanent Magnet Machines . . . . .</b>	<b>23</b>
2.1	Introduction . . . . .	23
2.2	Properties of an Optimal FSCW Stator Winding Layout . . . . .	24
2.2.1	Unbalanced Magnetic Pull . . . . .	25
2.3	Derivation of MMF Expression in FSCW Stators . . . . .	26
2.3.1	Basic Principles of MMF in FSCW Stators . . . . .	27
2.3.2	Analysis and Formulation of the MMF Produced by FSCW Stators . . . . .	30
2.3.3	MMF Expressions for the Most Common Three-Phase FSCW PMSMs . . . . .	36
2.4	Fault-Tolerant Capability in FSCW Machines . . . . .	46
2.5	Formulation of the Harmonic Winding Factors . . . . .	47
2.5.1	MMF Expression as a Function of the Harmonic Winding Factor . . . . .	53
2.6	Formulation of the Back-EMF . . . . .	53

2.7 Case-Study: The Effect of the Slot and Pole Combination on the Back-EMF . . . . .	56
2.8 Conclusion . . . . .	58
References . . . . .	59
<b>3 Design of Optimal Winding Layouts for Multiphase Fractional-Slot Concentrated-Wound Permanent Magnet Machines . . . . .</b>	<b>61</b>
3.1 Introduction . . . . .	61
3.2 Characteristics of an Optimal Winding Layout in Multiphase FSCW PMSM . . . . .	62
3.3 Determination of the Optimal Winding Layout for Multiphase FSCW Stators . . . . .	63
3.3.1 Definition of the Winding Performance Index . . . . .	64
3.3.2 A Heuristic Algorithm for Design of Optimal Winding Layout . . . . .	65
3.4 Case-Studies . . . . .	68
3.4.1 Three-Phase FSCW PMSM with 14 Poles and 18 Slots . . . . .	68
3.4.2 Five-Phase FSCW PMSM with 48 Poles and 50 Slots . . . . .	68
3.4.3 Five-Phase FSCW PMSM with 18 Poles and 20 Slots . . . . .	76
3.4.4 Five-Phase FSCW PMSM with 28 Poles and 30 Slots . . . . .	79
3.5 Validation of the Results Using FEA and Experiment . . . . .	82
3.5.1 Five-Phase FSCW PMSM with 48 Poles and 50 Slots . . . . .	82
3.5.2 Five-Phase FSCW PMSM with 18 Poles and 20 Slots . . . . .	86
3.5.3 Three-Phase FSCW PMSM with 14 Poles and 18 Slots . . . . .	89
3.6 Conclusion . . . . .	93
References . . . . .	93
<b>4 Analytical Modelling of Rotor Magnetic Characteristics in an Interior Permanent Magnet Rotor . . . . .</b>	<b>95</b>
4.1 Introduction . . . . .	95
4.2 Principles of Magnetic Circuits in an IPM Machine . . . . .	95
4.2.1 Properties of the Magnetic Core Material . . . . .	98
4.3 Geometrical Relationships in a V-shaped IPM Rotor . . . . .	101
4.4 Geometric Analysis of the PM Flux Paths and Non-uniform Distribution of Saturation in a V-shaped IPM Rotor . . . . .	104
4.5 Calculation of the PM Flux Density Distribution in the Air-Gap . . . . .	111
4.5.1 State of the Art Rectangular Model for PM Flux Density . . . . .	112
4.5.2 Proposed Trapezoidal Model for PM Flux Density . . . . .	114
4.6 Case-Study: Validation of the Proposed Models . . . . .	116
4.6.1 Calculation of the Non-uniform Saturation Model and the PM Flux Density . . . . .	116

4.6.2	Estimation of the Back-EMF Based on the Calculated PM Flux Densities . . . . .	123
4.7	Conclusion . . . . .	124
	References . . . . .	125
<b>5</b>	<b>Calculation of Airgap Function and Inductance in Fractional-Slot Concentrated-Wound Interior</b>	
	<b>Permanent Magnet Machines . . . . .</b>	127
5.1	Introduction . . . . .	127
5.2	Inductances in FSCW PMSMs . . . . .	127
5.2.1	Magnetizing Inductance and Airgap Leakage Inductance . . . . .	128
5.2.2	Slot Leakage Inductance . . . . .	131
5.2.3	Tooth-Tip Leakage Inductance . . . . .	133
5.2.4	End-Winding Leakage Inductance . . . . .	133
5.3	Modelling of the Equivalent Airgap Function . . . . .	134
5.3.1	State of the Art Equivalent Airgap Function . . . . .	134
5.3.2	Proposed Equivalent Airgap Function Taking into Account the Non-uniformly Saturated Stator . . . . .	136
5.4	Case-Study: Validation of the Proposed Airgap Function . . . . .	146
5.5	Conclusion . . . . .	153
	References . . . . .	154
<b>6</b>	<b>Detailed Analytical Modelling of Inductances and Electromagnetic Torque in Fractional-Slot Concentrated-Wound Interior Permanent Magnet Machines Under Healthy and Open-Phase Fault Conditions . . . . .</b>	155
6.1	Introduction . . . . .	155
6.2	Detailed Modelling of FSCW IPM Machine Operational Inductances . . . . .	156
6.2.1	Analytical Model of the Self-inductance . . . . .	156
6.2.2	Analytical Model of the Mutual Inductance . . . . .	160
6.3	Detailed Modelling of FSCW IPM Machine Electromagnetic Torque Under Normal Operating Condition . . . . .	162
6.3.1	Formulation of Alignment Torque . . . . .	164
6.3.2	Formulation of Reluctance Torque Equation . . . . .	168
6.3.3	Complete Torque Equation . . . . .	172
6.3.4	Validation Through Finite Element Analysis . . . . .	173
6.4	Detailed Modelling of FSCW IPM Machine Electromagnetic Torque Under an Open-Phase Fault Condition . . . . .	175
6.4.1	Stator MMF Under an Open-Phase Fault Condition . . . . .	177
6.4.2	Alignment Torque in a FSCW IPM Machine Operating Under an Open-Phase Fault Condition . . . . .	179
6.4.3	Reluctance Torque in a FSCW IPM Machine Operating Under an Open-Phase Fault Condition . . . . .	181

6.4.4	Complete Torque Equation Under an Open-Phase Fault . . . . .	183
6.4.5	Validation Through Finite Element Analysis . . . . .	184
6.5	Comparison of the FSCW IPM Machine Performance Under Normal and Open-Phase Fault Conditions . . . . .	190
6.6	Conclusion . . . . .	191
	References . . . . .	192
<b>7</b>	<b>An Extended <math>dq</math> Model for Fractional-Slot Concentrated-Wound Interior Permanent Magnet Machines Considering Non-ideal Machine Parameters</b> . . . . .	195
7.1	Introduction . . . . .	195
7.2	Standard $dq$ Model of PMSMs . . . . .	196
7.2.1	Machine Model in the $abc$ -System . . . . .	196
7.2.2	Transformation of the Machine Model to the $qd0$ -Reference Frame . . . . .	198
7.2.3	Electromagnetic Torque in the $qd0$ -Reference Frame . . . . .	201
7.3	Proposed Extended $dq$ Model for FSCW PMSMs . . . . .	202
7.3.1	Detailed Machine Model in the $abc$ -System . . . . .	203
7.3.2	Transformation of the Detailed Machine Model to the $qd0$ -Reference Frame . . . . .	204
7.3.3	Formulation of the Electromagnetic Torque Using the Proposed Extended $dq$ Model . . . . .	209
7.3.4	Experimental Tests for Determination of the Parameters in the Proposed Extended $dq$ Model . . . . .	210
7.4	Experimental Results and Discussion . . . . .	212
7.4.1	Measurement of the Extended $dq$ Model Parameters . . . . .	212
7.4.2	Estimation of the Average Torque and Torque Ripple for the Prototype FSCW IPM Machine . . . . .	214
7.5	Conclusion . . . . .	217
	References . . . . .	218
<b>8</b>	<b>Conclusions and Future Works</b> . . . . .	219
8.1	Conclusions . . . . .	219
8.1.1	Stator Magnetic Characteristics . . . . .	219
8.1.2	Rotor Magnetic Characteristics . . . . .	220
8.1.3	Overall Performance Characteristics for the Machine . . . . .	220
8.2	Suggestions for Future Work . . . . .	221
<b>Appendix A: Analytical Calculation of Magnetic Reluctance and Magnetic Permeance in Objects of Different Geometrical Shapes</b> . . . . .		223
<b>Appendix B: Developed Code in Matlab for Computing the Proposed Equivalent Airgap Function</b> . . . . .		229

Contents	xix
<b>Appendix C: Experimental Measurement of the FSCW IPM Machine Inductances .....</b>	<b>239</b>
<b>About the Author .....</b>	<b>251</b>

# Abbreviations

2D	Two-dimensional
3D	Three-dimensional
HCI	Harmonic current injection
DRM	Dynamic reluctance mesh
DW	Distributed-wound
EMF	Electromotive force
FEA	Finite element analysis
FFT	Fast Fourier transform
FSCW	Fractional-slot concentrated-wound
GCD	Greatest common divisor
IPM	Interior permanent magnet
LCM	Least common multiple
MCL	Magnetic circuit length
MEC	Magnetic equivalent circuit
MMF	Magnetomotive force
MTPA	Maximum torque per ampere
PM	Permanent magnet
PMSM	Permanent magnet synchronous machine
SPM	Surface permanent magnet
THD	Total harmonic distortion
VSI	Voltage-source inverter
WFT	Winding function theory
WPI	Winding performance index

# Chapter 1

## Introduction and Literature Review



### 1.1 Problem Statement and Research Motivations

Fractional-slot concentrated-wound (FSCW) permanent magnet synchronous machines (PMSMs) are an attractive candidate for many industrial and household applications. This is because of their simpler manufacturing process and attractive characteristics such as higher power-to-weight ratio, and wider constant power speed range, compared with their distributed-wound (DW) counterparts. Among the several types FSCW PMSMs, those that use an interior permanent magnet (IPM) rotor are becoming more popular. This is because of their better mechanical robustness and superior performance.

With an aim to improve the understanding of FSCW IPM machines and their utilization, the main motivations behind the research reported in this thesis, are:

1. *The lack of accurate analytical models in the literature for FSCW PMSM characteristics, such as the stator and rotor magnetic fields, flux linkages, back-EMFs, inductances, and the developed average torque and torque ripple under healthy and open-phase fault conditions.*

It is essential during the design and analysis of FSCW IPM machines to have a thorough understanding of the magnetic field interactions in the machine. In particular, precise analytical formulae are required for calculation of machine characteristics, such as stator and rotor magnetic fields, flux linkages, back-EMFs, inductances, and the developed average torque and torque ripple. This assists in determining the effect of different geometrical parameters on the machine performance characteristics.

Two sources of magnetic fields are present in a FSCW PMSM:

- The field generated by the FSCW stator, and
- the field developed by the IPM rotor.

Electromagnetic torque in a PMSM is developed by the interaction of the stator and rotor magnetic fields in the airgap. This makes accurate analytical models of the magnetic fields essential to correct prediction of the torque.

The magnetic field intensity of a FSCW stator in the airgap of the machine is generated by the stator magneto-motive force (MMF) across the airgap and has the following relationship:

$$H_s(t, \theta_s) = \frac{1}{g(t, \theta_s)} MMF(t, \theta_s) \quad (1.1)$$

where  $\theta_s$  is the angle subtended along the stator inner circumference, and  $g$  is the equivalent airgap length and is a function of time,  $t$ , and  $\theta_s$ . The MMF of a FSCW stator is rich in spatial harmonics with their amplitudes determined by the slot and pole combination of the machine. According to (1.1), this yields harmonics in the stator magnetic field.

The stator MMF is also used for calculation of the machine inductances. The self- and mutual inductances between phases  $x$  and  $y$  of a FSCW PMSM can be analytically calculated from their respective winding functions as follows:

$$L_{xy} = \mu_0 r l_{st} \int_0^{2\pi} \frac{w_x(\theta_s) w_y(\theta_s)}{g(t, \theta_s)} d\theta_s \quad (1.2)$$

where  $w_x$  and  $w_y$  are the winding functions of phases  $x$  and  $y$ . Equation (1.2) gives self-inductance of phase  $x$  by setting  $x = y$ . The winding function of phase  $x$  is found from the MMF by setting the current of their respective phases equal to unity:

$$w_x(\theta_s) = MMF(t, \theta_s)|_{i_x=1} \quad (1.3)$$

From (1.1) to (1.3) it is observed that knowledge of the MMF and the equivalent airgap function are essential to calculating the stator magnetic field and inductances. Thus, analytical modelling of the MMF and equivalent airgap function are the first steps to formulating the machine characteristics. Nevertheless, these topics have not received enough attention in the literature. There is only sparse research reporting analytical modelling of the MMF produced by FSCW stators with different slot and pole combinations. Moreover, the existing equivalent airgap function that is being used in the literature for IPM machines is adopted from the inset-permanent magnet (PM) machine theory and returns inaccurate results for IPM machines. Therefore, for a FSCW IPM machine, analytical modelling of the stator MMF and machine equivalent airgap function are essential to correct calculation of the stator magnetic field and inductances, and subsequently torque and torque ripple.

The magnetic field produced by an IPM rotor originates from the residual flux of the embedded magnets in the rotor. The magnetic field intensity in the airgap generated by the rotor PMs can be calculated from the PM flux density,  $B_{PM}$ , as a function of  $t$  and  $\theta_s$  and as follows:

$$H_r(t, \theta_s) = \frac{1}{\mu_0} B_{PM}(t, \theta_s) \quad (1.4)$$

An accurate estimation of the PM flux density is essential for the calculation of the rotor field intensity. The residual flux of the embedded PMs in the rotor causes a non-uniform distribution of magnetic saturation in the rotor iron and should be taken into consideration in the calculation of the PM flux density. The current methods in the literature for analytical calculation of the PM flux density in IPM rotors are proven to yield inaccurate results, which is mainly due to neglecting the non-homogenously saturated rotor iron and the assumption of a rectangular PM flux density in the airgap. This makes correct analytical modeling of the magnetic saturation of the rotor iron and the PM flux density essential to accurate calculation of the rotor magnetic field. The non-homogeneous saturation of the rotor iron also affects the equivalent airgap function of the machine. However, this has not been taken into account in the existing literature.

Once accurate analytical models for the non-homogenously saturated rotor iron, rotor magnetic field, machine equivalent airgap function, and the stator MMF under healthy and open-phase fault conditions are obtained, in addition to the inductances and developed torque, analytical calculation of the back-EMF and PM flux linkages also becomes feasible.

2. *The lack of a comprehensive algorithm for designing multiphase FSCW stators that would yield maximum torque density considering all the torque production field harmonics.*

A thorough understanding of the stator and rotor magnetic fields through their analytical models enables systematic design of the stator winding configuration in a multi-phase FSCW PMSM. In an  $m$ -phase PMSM, injection of current harmonics with an odd order smaller than  $m$  increases the developed average torque. The existing methods in the literature for designing the winding configuration of multi-phase FSCW stators are based on the spatial field harmonics that are associated with the fundamental harmonic of the injected current, and no account is taken of the spatial field harmonics associated with the higher order current harmonics. In order to have a global design procedure for multiphase FSCW stators that would yield maximum torque density, all the field harmonics that can contribute to the average torque must be considered.

3. *The lack of an accurate dq model for FSCW PMSMs that considers all the machine non-ideal parameters.*

The standard  $dq$  model used for PMSMs is based on the assumption of a sinusoidal MMF which yields sinusoidal machine parameters. However, for a FSCW PMSM, the generated MMF by the stator is not sinusoidal and contains a wide range of spatial harmonics. This affects other parameters of the machine such as electromagnetic torque, back-EMFs, PM flux linkages, and inductances. Currently, the standard  $dq$  model of a PMSM is mainly used in the literature for

FSCW IPM machines. This requires formulating a general  $dq$  model for FSCW IPM machines that takes into account all the machine non-idealities.

## 1.2 Research Objectives and Contributions

As a first step in accurate calculation of the FSCW IPM machine characteristics, the accurate equivalent airgap function for the machine should be calculated. From Sect. 1.1, the main shortcomings in the literature regarding analytical calculation of the equivalent airgap function for FSCW IPM machines are ignoring the complicated flux path, magnetic characteristics of the machine magnetic material, and the non-homogeneous saturation of the rotor iron.

These shortcomings are addressed in this thesis and an equivalent airgap function is proposed based on the magnetic circuit length of the stator flux paths inside the IPM rotor iron. To this end, the non-homogeneous saturation of the rotor iron in a V-shaped FSCW IPM machine is modelled by deriving mathematical formulae for the saturation intensity and relative permeability at different regions of the magnetically saturated rotor. This model is governed by the  $B$ - $H$  curve of the rotor magnetic material and the machine geometry. The proposed saturation model is used to obtain the magnetic circuit lengths of the stator flux paths in an IPM rotor, which is later used for computing the equivalent airgap function in an FSCW IPM machine.

In contrast with the existing methods where the equivalent airgap function is just dependent on the angle subtended along the rotor circumference, the research conducted in this thesis reveals that equivalent airgap length is a function of the rotor angular position as well as the angle subtended along the rotor circumference.

The proposed equivalent airgap function in this thesis is compatible for use in the standard formulae and techniques for analytical derivation of machine performance characteristics. Accordingly, PM flux linkages, armature reaction airgap flux density, and the machine inductance will be analytically formulated in this thesis.

Apart from the equivalent airgap function, correct analytical formulae for the stator MMF are also essential to field calculations in a FSCW IPM machine. With an aim to fill the knowledge gap in this regards, a thorough analysis of the MMF of FSCW stators with different slot and pole combinations are conducted, leading to proposition of lumped analytical formulae for the MMF. These analytical expressions are used to derive formulae for the harmonic winding factors of the machine which will be later used in formulating the PM flux linkages, back-EMFs, torque, and torque ripple.

The other essential component in the analytical calculations of the IPM machine characteristics is the PM flux density. As explained in Sect. 1.1, the current analytical models for the PM flux density are incapable of correctly predicting this quantity for IPM rotors. In order to address this shortcoming, a trapezoidal model is proposed in this thesis for the PM flux density that helps in a more accurate

calculation of the machine output characteristics. The parameters of the proposed PM flux density model are based on the proposed equivalent airgap function.

The other contribution of the research reported in this thesis is proposing detailed formulae for the electromagnetic torque and torque ripple for an FSCW IPM machine under both healthy and open-phase fault conditions. These models provide a tool for customizing the input currents to the machine such that the output torque under an open-phase fault condition gives maximum achievable average torque with less torque ripple compared with the state of the art methods.

The obtained detailed expressions for the FSCW IPM machine in this thesis are further used to propose an extended  $dq$  model that takes into account all the machine non-ideal parameters. An equivalent circuit is also proposed for the extended  $dq$  model which is later used in formulating a detailed expression for the developed torque of the machine in terms of the proposed extended  $dq$  model parameters.

The final contribution of this thesis is a heuristic algorithm for designing the winding configuration of multiphase FSCW stators with an objective of maximizing the torque density. As explained in Sect. 1.1, in the existing methods, only the fundamental torque producing harmonic of the magnetic field is considered. Contrary to the state of the art, in the proposed algorithm, all the torque producing harmonics in the magnetic field are taken into account in designing the winding configuration. A “*winding performance index*” is proposed for evaluating the torque density of different winding configurations. The proposed heuristic algorithm is based on the rigorous analysis performed on the MMF and harmonic winding factors in this thesis.

According to the above discussion, the main contributions of the research reported in this thesis are:

- Analytical modelling of the MMF produced by FSCW stators with different slot and pole combinations, leading to lumped formulae for the MMF and harmonics winding factors of the machine
- Formulation of a general heuristic algorithm for designing the optimal winding layout in multiphase FSCW PMSMs
- Analytical modelling of the non-homogeneous magnetic saturation in the rotor iron due to the residual flux of the embedded magnets
- Analytical modelling of the airgap function in a FSCW PMSM taking into account the effect of the non-homogeneously saturated rotor iron and the FSCW stator
- Analytical modelling of the airgap PM flux density
- Analytical modelling of the torque and torque ripple for FSCW PMSMs operating under healthy and open-phase fault conditions
- Proposing customized input currents for the FSCW IPM machine such that maximum average torque under an open-phase fault condition is generated
- Formulation of an extended  $dq$  model for FSCW PMSMs that takes into account all the machine non-idealities.

## 1.3 Literature Review

Several types of PMSMs have been investigated in the literature, for which, a brief review is first presented in this section. An overview on the choice of slot and pole combination in a FSCW PMSM which determines its electric and magnetic characteristics follows. The literature concerning analytical modelling of the electric and magnetic characteristics of FSCW PMSMs are then reviewed which fall into the following categories:

- Analytical modeling of the machine magnetic characteristics such as stator and rotor spatial field distributions, the equivalent airgap function, stator MMF, and rotor PM flux density. These magnetic characteristics can be used in formulating detailed expressions for the machine output characteristics such as inductances, flux linkages, back-EMFs, and electromagnetic torque.
- Detailed electrical models and equivalent circuits for the machine.

### 1.3.1 Types of PMSMs

Radial flux PMSMs are commonly categorized with respect to their rotor and stator types. The stator utilized in a PMSM is usually either from the FSCW or DW stator families as shown in Fig. 1.1, each of them with their own distinct features; while the rotor can be chosen from a vast range of structures including, surface PM rotors, inset PM rotors, and IPM rotors as shown in Fig. 1.2.

DW stator topologies are the major stator type used in PMSMs. This is due to their near sinusoidal MMF which yields a high main harmonic winding factor and low torque ripple. It was not until very recently that it was shown that the right choice of slot and pole combination for a FSCW stator could yield a high main harmonic winding factor which is essential to having a high average torque [1, 2]. As shown in Fig. 1.1, contrary to DW stators, the windings in a FSCW stator are non-overlapping which yields to a shorter end-winding resulting in a less copper usage, less copper losses, and a more compact design. Other advantages of FSCW stators over their DW counterparts are the easier manufacturing process, higher slot fill-factor, wider field-weakening region caused by their higher self-inductance, reduced cogging torque, and a better fault tolerant capability [2–6].

The important factors in designing a FSCW PMSM that affect the machine output characteristics are the number of slots and poles, and the number of winding layers in the slots. The most common FSCW stators are either single-layer or double-layer as shown in Fig. 1.1a and b, respectively. Each of these designs has its own benefits and characteristics. Compared with single-layer FSCW stators, double-layer stators feature lower spatial MMF harmonic content which lead to lower magnet eddy current losses, lower airgap leakage inductance, lower torque ripple at the cost of a reduction in the average torque, higher torque density leading

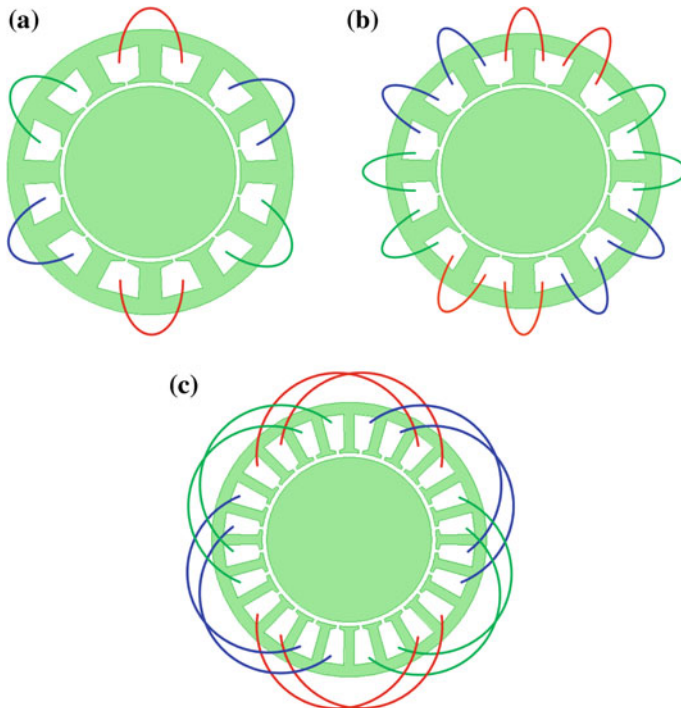


**Fig. 1.1** Common stator types: **a** Single-layer FSCW stator. **b** Double-layer FSCW stator. **c** DW stator

to a more compact design, and higher efficiency [2, 7, 8]. The key advantage of single-layer FSCW stators over double-layer stators is their improved fault tolerance capability due to their phase windings being magnetically decoupled which yields a lower mutual inductance [3].

Not all combinations of slots and poles for an FSCW stator yield acceptable performance. Commonly, for a three-phase machine, the slot and pole combination should be chosen such that a sinusoidal back-EMF, a high main harmonic winding factor resulting in a high average torque, and reduced torque ripple and cogging torque, are achieved [9–11]. Various slot and pole combinations for a FSCW machines and design considerations for obtaining an optimal design are investigated in [3, 12–16].

It is the choice of the design engineer to choose the most suitable type of winding and slot and pole combination for designing application-oriented FSCW PMSMs.

Another design choice for PMSMs is the rotor topology for which the most common types was shown in Fig. 1.2. In Surface PM (SPM) rotors and some inset-PM rotors the magnets are glued to the rotor surface, directly accessing the airgap, as shown in Fig. 1.2a and b, respectively. However, in IPM machines, the

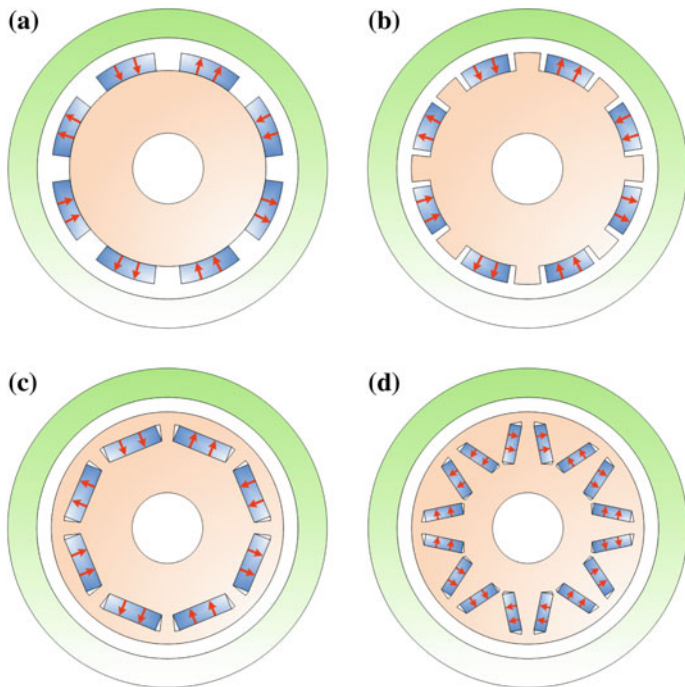


**Fig. 1.2** Common PM rotor types: **a** Surface PM rotor. **b** Inset PM rotor. **c** Flat-shaped IPM rotor. **d** V-shaped IPM rotor

magnets are buried inside the rotor iron, which makes IPM machines superior over SPM and inset PM machines in several aspects, including [5, 17–20]:

- Higher power rating.
- Smaller eddy current losses in the PMs and smaller possibility of their demagnetization since they are not directly exposed to the airgap.
- Lower iron losses under open-circuit conditions.
- Higher overall efficiency.
- Smaller airgap, making the machine more suitable for flux-weakening operation. In SPM machines, since the permeability of the magnets is close to that of air, the effective airgap becomes relatively large.
- Increased mechanical robustness of the rotor because the magnets are buried inside the rotor iron. This makes the rotor capable of withstanding higher speeds.
- Presence of a reluctance torque component compared with SPM machines due to the saliency of IPM machines. This leads to production of more torque and can be used to extend and enhance the flux-weakening operation.
- Easier sensorless control of the machine because of the saliency effect.

### 1.3.2 Machine Magnetic Characteristics

Electromagnetic torque generation in a PMSM originate from the interaction between the rotor and stator magnetic fields in the airgap. Several methods have been explored in the literature for obtaining the magnetic characteristics of electric machines, among which, numerical techniques such as dynamic reluctance mesh (DRM) modelling [21–23] and finite element analysis (FEA) [24–27] are the most accurate ones that consider magnetic saturation in the rotor and stator iron. This has led to their extensive use in the past two decades for analysis and enhanced design of electric machines. Nevertheless, these techniques suffer from the common drawback of being time consuming. Besides, they cannot provide an insight into the effect of different geometry parameters on the machine performance characteristics.

In order to overcome the shortcomings of numerical techniques, analytical methods have been used in the literature for computing the magnetic fields in electric machines. Among analytical techniques, direct analytical methods that are based on the solution of Laplacian or quasi-Poissonian field equations are most accurate [28–31]. These equations are solved by applying boundary conditions on the interface between the stator slots, magnets, and the airgap. The main assumption in these techniques is a negligible reluctance for the stator and rotor yoke which means neglecting the saturation.

Direct analytical methods are commonly used for inset-PM and SPM rotors [28–30, 32]. However, for an IPM rotor, the embedded magnets in the rotor saturate the iron bridges, complicating the boundary conditions which in turn make analytical solution of Laplacian or quasi-Poissonian equations unfeasible. This has led to introduction of analytical methods that are based on magnetic equivalent circuit (MEC) model and winding function theory (WFT) [33–36] of the IPM machine [37–39]. In these techniques, flux sources are used to model the saturated rotor iron bridges. These flux sources produce a constant flux density of  $B_{sat}$  which is the saturated flux density of the rotor iron and obtained from its  $B$ - $H$  curve. In MEC- and WFT-based methods, similar to direct analytical methods, the rotor and stator yoke reluctances are often neglected, thus saturation due to the stator currents is not considered. Such assumptions could lead to negligible errors in the airgap magnetic field calculation [23, 37–41].

#### 1.3.2.1 Equivalent Airgap Function

Magnetic reluctance and the MMF across the reluctance are the crucial elements in MEC- and WFT-based techniques. In these methods, a constant MMF equal to that of the stator is assumed across a position variant equivalent reluctance. This equivalent reluctance is realized by an equivalent airgap length that is a function of the angle subtended along the rotor circumference. Magnetic potential distribution in SPM and inset-PM machines is uniform on the rotor surface. Thus, because of

the similar permeability of the permanent magnets and air, the equivalent airgap length is obtained by summing the physical airgap length and the permanent magnet height [38, 42] as shown in Fig. 1.3. The effect of the slot openings on the equivalent airgap function can also be accounted for by multiplying the equivalent airgap function by the Carter coefficient [43]. The same approach has been adopted for IPM machines in the literature [27, 38]. Nevertheless, such adoption produces inaccurate results for IPM machines as the flux of the buried magnets inside the rotor causes non-homogeneous saturation of the rotor iron, resulting in unequal magnetic potential regions on its surface which is different than inset-PM and SPM machines. This contradiction can be partially accounted for by including a rotor MMF in the field calculations [33]. Even though this improves the magnetic field calculation accuracy, it adds to its complexity. Furthermore, the complete effect of the non-homogeneous saturation of the rotor iron on the flux paths is not taken into account.

Magnetic reluctance of the flux path is inversely proportional with the cross-sectional area perpendicular to the flux direction [44]. In a FSCW PM machine, the stator flux radiates out of the stator teeth and crosses the airgap into the PM rotor. In this process, the flux passes through various cross-sectional areas. Reluctance of the flux path is represented by the equivalent airgap function which should account for the aforementioned phenomena. This unique property of FSCW stators is overlooked in the existing literature [27].

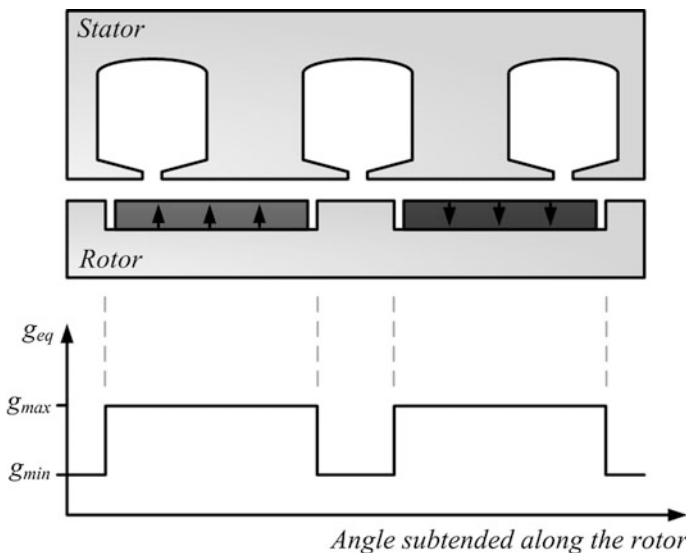


**Fig. 1.3** State of the art equivalent airgap function for one pole pitch of an inset-PM machine

### 1.3.2.2 Stator MMF

The total MMF produced by a 20-pole 24-slot FSCW stator and the associated winding function is shown in Fig. 1.4. Evidently, unlike DW stators, the MMF of a FSCW stator is rich in harmonics. This causes the machine's advantageous high self-inductance [45]; on the other hand, this high harmonic content leads to torque ripple, unbalanced saturation, distorted back-EMF waveforms, and iron losses, unless a proper slot and pole combinations is selected [46–48]. Each slot and pole combination features unique characteristics that should be investigated prior to its adoption for a FSCW stator. Harmonic winding factors are often used as the indicator for the characteristics of a slot and pole combination [49–51]. A general method for calculating the harmonic winding factors is to use lumped expressions that describe the stator winding function [52]. From (1.3) and Fig. 1.4, the winding function is found from the single-phase MMF of the machine. Therefore, knowledge of lumped expressions of the FSCW stator spatial MMF distribution becomes essential for formulating the winding function [53]. Although a few research reports have analyzed the MMF produced by FSCW stators [54, 55]; there is still a deep gap in the knowledge in this regards.

### 1.3.2.3 Rotor PM Flux Density

The rotor PM flux density in an IPM machine is due to the residual flux of the embedded magnets in the rotor iron. As mentioned earlier, the most accurate analytical solution for calculating the PM flux density in the airgap of SPM and inset-PM machines are to solve the Laplacian or quasi-Poissonian field equations

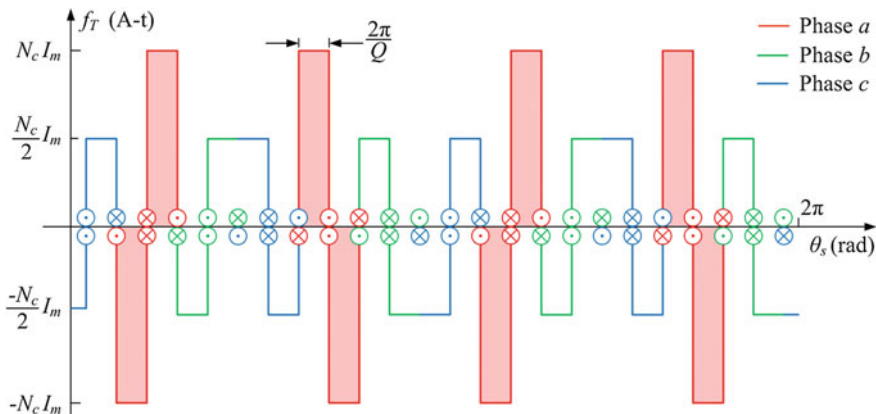


**Fig. 1.4** Total MMF produced by a 20-pole 24-slot FSCW machine supplied with a three-phase balanced current:  $i_a = I_m$ ,  $i_b = -I_m$ , and  $i_c = -I_m$ . The shaded area represents the winding function provided that  $I_m = 1\text{A}$

[29–32, 56–58]. In order to obtain the boundary conditions for solving the aforementioned equations, the assumption of an unsaturated iron core is essential. This assumption causes negligible error in SPM and inset-PM machine's magnetic field calculations; however, it is not applicable to IPM machines in which the rotor iron is non-homogenously saturated as shown in Fig. 1.5. Therefore, as the boundary conditions in an IPM machine are too complicated, solving the Laplacian or quasi-Poissonian field equations become impractical.

The literature dealing with calculation of the PM flux density in IPM motors are based on the MEC of the machine [37, 39, 59–61]. The methods employed in these papers are straightforward and simple. However, the saturated iron bridges, as shown in Fig. 1.5, are assumed to be fully saturated with a constant flux density equal to the saturation flux density of the iron core  $B$ - $H$  curve. Moreover, the distribution of the PM flux density in the airgap is assumed to be rectangular, which is in contrast to the semi-trapezoidal shape of the spatial PM flux density distribution in the airgap. These assumptions cause significant errors in calculation of the airgap PM flux density which in turn lead to errors in calculation of the machine output characteristics such as flux linkages, back-EMFs, and electromagnetic torque.

In order to account for the above shortcomings, methods based on lumped nonlinear permeance networks were proposed which use an iterative process to determine the permeance and flux density of different points on the iron core [62–67]. In some of these methods, the rotation of the rotor and the saturation of the stator iron were also included to have more accurate results for different operating condition of the machine. These methods are proven to provide high accuracy, however they are quite complicated to implement and are time consuming.

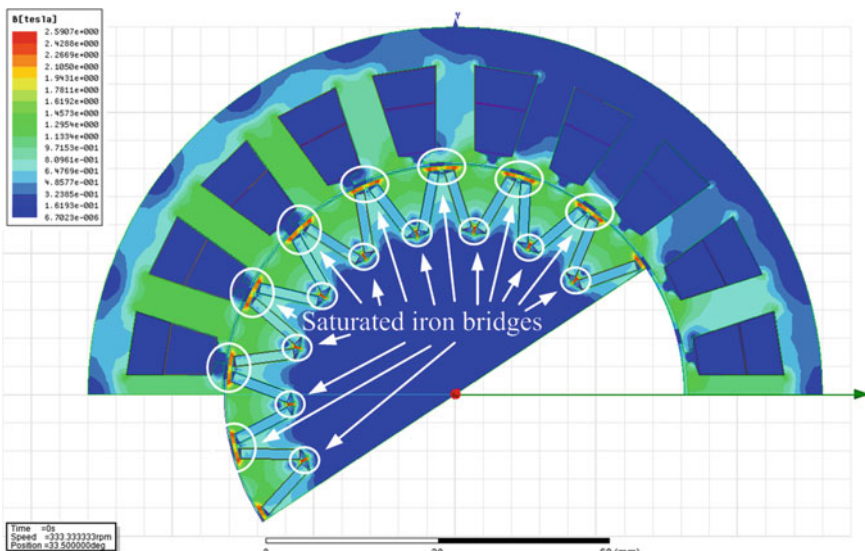


**Fig. 1.5** Non-homogeneously saturated rotor iron due to the residual flux of the embedded permanent magnets. Illustration obtained from FEA in Maxwell 2D

### 1.3.2.4 Machine Inductances

Several methods have been proposed in the literature for calculating the machine inductances. Over the past two decades, numerical techniques such as FEA have been extensively used for the design and analysis of electric machines [26, 27, 68–72]. Many inductance calculation techniques are based on machine variables that are directly obtained by FEA. Inductance calculation methods based on the stored energy/co-energy in the magnetic field [69, 70], three-phase flux linkages [26, 71], or the machine voltage and current in the ac standstill test [27] are examples of this kind. These methods require many FEA problems to be solved. To decrease the number of FEA solutions and to consider the magnetic saturation, the concept of *frozen permeability* was used in some methods [72]. FEA was also used in combination with the machine electrical equations to find the inductances [73, 74]. The FEA-based methods are relatively straightforward and consider the iron magnetic saturation; however their common drawback is being time-consuming, especially if used in an iterative design optimization process. Hence, analytical inductance calculation techniques are receiving attention as an alternative scheme allowing rapid evaluation over the search space.

Analytical inductance calculation techniques are mainly based on the theory of MEC. As explained earlier, the key elements in MEC-based techniques are the magnetic reluctance of the flux path and the MMF across it, which are represented by the equivalent airgap function and winding function, respectively. According to (1.2), the machine inductances can be calculated using the winding function and the equivalent airgap function. As explained in Sect. 1.3.1, in contrast to the SPM and inset-PM machines, in an IPM machine due to the complicated flux paths inside the rotor iron resulting from the non-homogeneous iron saturation caused by the embedded magnets, the airgap function cannot be straightforwardly calculated. This necessitates special considerations in analyzing the IPM machines inductances.

One way to analytically calculate the inductance in an IPM machine is to find the MMF drop across the physical airgap [33, 34]. In this approach, the PMs are not magnetized and the resultant non-homogeneous saturation is neglected. Consequently, the actual flux paths in the rotor that indicate the MMF drop are not considered. As an alternative solution, the equivalent airgap function of the inset PM machine has been applied to the IPM machine and used in combination with the winding function for inductance calculations [27, 38]. Despite the simplicity of this method, as explained in Sect. 1.3.1 this adoption is flawed and yields inaccurate results for FSCW IPM machines.

Another MEC-based method for calculating the inductances is to construct and solve the permeance network of the IPM machine to obtain the flux linkages [62–67]. The inductances can then be obtained by dividing the flux linkages by the supplied current [62]. The permeance network-based methods need an iterative process to be solved, and are relatively complicated and time consuming. Moreover, they do not provide information about the effect of different machine geometrical parameters on the inductances.

The machine inductances can be either calculated in the *abc*-system or the *dq* reference frame. In the analytical calculations of the inductances in the *abc*-system, they are commonly treated as sinusoidal functions of the rotor position with respect to a stator reference, and the *dq* inductances are calculated accordingly [53]. This is not the case in FSCW IPM machines and inductances may contain spatial harmonics of higher order. Despite having methods for obtaining the inductance values, there is a gap in the literature for their detailed equations based on the machine geometrical and magnetic parameters. Moreover, detailed formulae for their calculation in the *dq* reference frame as a function of their harmonics in the *abc*-system are yet to be proposed.

### ***1.3.3 Detailed Electrical Models and Equivalent Circuits for the Machine***

A PMSM is a first order system with each of its phase windings modelled by a series resistive-inductive (R-L) branch. Conventionally, the parameters of a PMSM are assumed sinusoidal leading to the standard *dq* model of the machine with constant parameters. This assumption can be used for PMsMs with a DW stator which have a near sinusoidal MMF. However, in PMsMs which utilize a FSCW stator, due to the high spatial harmonic content of the MMF, the machine parameters become non-sinusoidal, invalidating the standard *dq* model [75]. The spatial MMF harmonics of an FSCW stator are dependent on the slot and pole combination of the machine. In FSCW PMsMs, the inductances and flux linkages are non-sinusoidal due to the interaction of the airgap function spatial harmonics and the PM flux density spatial harmonics with the stator spatial MMF harmonics. This introduces pulsations into the developed electromagnetic torque. Therefore, it is necessary to account for the effect of the non-sinusoidal machine parameters in the electric model of FSCW PMsMs.

Literature that have addressed DW PMsMs with non-ideal parameters conclude that harmonics in the self- and mutual inductances as well as the back-EMF harmonics lead to torque pulsations [76–80]. However, the cause of the non-sinusoidal machine parameters has not been addressed in the literature. Furthermore, a detailed *dq* model for PMsMs that considers all the machine non-sinusoidal parameters has not yet been proposed. The latter is of significant importance in efficient and accurate control of the machine. From the study performed in [81], spatial MMF harmonics in an electric machine could lead to discrepancy in its measure *dq* inductances if they are obtained based on the ideal machine model.

Not much work has been done in the literature for analytical study of FSCW PMsMs. In [82] the FSCW PMSM parameters are found using FEA and the electromagnetic torque equation is modified to account for losses. A study based on calculating the FSCW PMSM *dq* inductances using FEA is performed in [24]; accordingly, the effect of the 6th harmonic of the *dq* inductances is included in the

machine voltage equations. Nevertheless, this model does not consider the non-sinusoidal PM flux linkages, and does not detail a mathematical model for the inductances and the developed torque. The effect of the back-EMF harmonics on the developed torque by a FSCW PMSM is computed in [83] in the *abc*-system. This analysis is incomplete as the effect of the machine saliency on the output torque pulsation is ignored. In order to include the effect of the non-sinusoidal parameters in the machine model, [84] proposes an improved *dq* model based on FEA results. The performed study lacks a mathematical approach toward the modelling of the non-sinusoidal machine parameters. An extended Park transformation is used in [85] to obtain a general *dq* model for PMSMs, however, the non-sinusoidal machine parameters are not taken into consideration.

Although many papers have tried to address the non-ideal parameters of a FSCW PMSM and include them in the *dq* model of the machine, there is still a gap in the knowledge in this regards. In particular, a mathematically sound *dq* model which is based on rigorous mathematical modelling of the machine is yet to be proposed in the literature.

## 1.4 Thesis Outline

This thesis comprises eight chapters with structures as follows:

### **Chapter 1: Introduction**

The problem statement and research motivations are first described in this chapter. Accordingly, the main research objectives and contributions of this thesis are explained. A brief overview on the various types PMSMs is then presented, after which, a thorough literature review on the modelling of the magnetic characteristics of the machine and the electrical models of PMSMs are provided.

### **Chapter 2: Analytical modelling of stator magnetic characteristics in fractional-slot concentrated-wound permanent magnet machines**

This chapter lays the basis for the rest of this thesis. A thorough analysis is first performed on the MMF produced by different FSCW configurations, based on which, FSCW stators are classified into “*classes*” and “*categories*”, each of them with their own distinct features. Lumped equations are then proposed for different stator categories. The harmonic winding factors of the different FSCW stator categories are then formulated based on which the flux linkages and back-EMFs are calculated. A case-study is then investigated to evaluate the application of the proposed equations in the selection process for the most appropriate slot and pole combination for application-oriented FSCW stators.

### **Chapter 3: Design of optimal winding layouts for multiphase fractional-slot concentrated-wound permanent magnet machines**

This chapter proposes a heuristic algorithm for the design of optimal winding layouts for multiphase FSCW stators to achieve maximum torque density. The

proposed heuristics algorithm is based on the analysis performed in Chap. 2 of this thesis for determining the harmonic winding factors for FSCW stators. A new indicator referred to as the “*winding performance index*” is proposed that evaluates the torque production ability of different winding layouts for FSCW stators. Multiple case-studies are investigated to evaluate the application of the proposed heuristic algorithm. The obtained results are validated through FEA and tests on a prototype FSCW machine.

#### **Chapter 4: Analytical modelling of rotor magnetic characteristics in an interior permanent magnet rotor**

This chapter proposes a technique for analytical modelling of the non-homogenous magnetic saturation in the rotor iron, based on which an analytical model for calculation of the PM flux density is proposed. The principles of the magnetic equivalent circuit in electric machines are first explained. The flux paths in a V-shaped IPM rotor due to the magnet residual flux are then classified into five groups. Accordingly, geometrical relationships in the IPM rotor are derived and used in analytical modelling of the non-homogenous magnetic saturation in the rotor iron. The  $B$ - $H$  curve of the rotor core material is taken into account in the proposed approach. The proposed model provides information regarding the flux density and relative permeability of the iron in different regions of the rotor. In the next step, the state of the art analytical model for the PM flux density is briefed, for which, a novel model is proposed that is based on the novel magnetic saturation map that was derived earlier in this chapter. A case-study was then investigated to evaluate the proposed techniques using FEA and experimental results from the prototype machine.

#### **Chapter 5: Calculation of airgap function and inductance in fractional-slot concentrated-wound interior permanent magnet machines**

This chapter deals with analytical modeling of the equivalent airgap function in a FSCW IPM machine which is later used for calculation of the inductances and the stator flux density in the airgap. The conventional equivalent airgap function is first introduced. A novel equivalent airgap function is then proposed that is based on the specific characteristics of an FSCW stator and the analytical model of the non-homogeneous magnetic saturation of the rotor iron that was previously proposed in Chap. 4. The inductances of the machine and the stator flux density in the airgap are then analytically calculated using the proposed equivalent airgap function and the MMF obtained in Chap. 2. The results are validated through a case-study using FEA and experimental measurements of the prototype FSCW IPM machine.

#### **Chapter 6: Detailed analytical modelling of inductances and electromagnetic torque in fractional-slot concentrated-wound interior permanent magnet machines under healthy and open-phase fault conditions**

This chapter proposes detailed novel analytical models for the machine self- and mutual inductances, field-alignment torque, reluctance torque and torque ripple in FSCW IPM machines operating under healthy and open-phase fault conditions. The proposed analytical models are a function of the machine geometrical parameters which are then substituted by the machine electrical parameters to obtain equations that can be readily used for real-time implementation on the machine.

At first healthy operation of the machine is considered and the proposed models for the electromagnetic torque is used to obtain the optimum current angle that results in maximum average torque at different operating conditions. The obtained results are validated through FEA simulation of a FSCW IPM machine.

In the next step, under an open-phase condition a four-leg inverter is considered and injection of custom currents with adjustable phase angles is assumed. An analytical model is first proposed for the stator MMF generated by such currents. This model is then used to derive the average field-alignment torque, reluctance torque, and their torque ripple under the open-phase fault condition. The derived analytical models are used to propose a maximum torque per ampere (MTPA) algorithm under an open-phase fault condition. The obtained analytical formulae and MTPA approach are validated through FEA model of a FSCW IPM machine.

#### **Chapter 7: An extended $dq$ model for fractional-slot concentrated-wound interior permanent magnet machines considering non-ideal machine parameters**

In this chapter an extended  $dq$  model is proposed for FSCW IPM machines. This is obtained by transforming the detailed analytical formulae of the machine parameters from the  $abc$ -system to the  $dq$  reference frame. The detailed analytical formulae in the  $abc$ -system that were obtained in Chaps. 2 and 6 are used for this purpose. The proposed extended  $dq$  model contains new parameters; accordingly, experimental tests are discussed for their measurement. The average electromagnetic torque and torque ripple are then formulated based on the proposed extended  $dq$  model. The proposed extended  $dq$  model is evaluated through experimental results from a prototype FSCW IPM machine along with FEA simulation.

#### **Chapter 8: Conclusions and future works**

This chapter discusses the significance of this research and concludes the contributions of this work. Suggestions are also provided for future expansion of this work.

## **1.5 Conclusion**

The motivations behind the research reported in this thesis were discussed, based on which, the research objectives and contributions of this work were introduced. The literatures pertinent to the objectives of this research were reviewed, discussed and the existing shortcomings highlighted. The thesis outline was also provided at the end.

## References

1. J. Cros, P. Viarouge, Synthesis of high performance PM motors with concentrated windings. *IEEE Trans. Energy Convers.* **17**, 248–253 (2002)
2. F. Magnussen, C. Sadarangani, Winding factors and Joule losses of permanent magnet machines with concentrated windings, in *IEEE International Electric Machines and Drives Conference, 2003, IEMDC'03*, vol. 1 (2003), pp. 333–339
3. N. Bianchi, S. Bolognani, M.D. Pre, G. Grezzani, Design considerations for fractional-slot winding configurations of synchronous machines. *IEEE Trans. Ind. Appl.* **42**, 997–1006 (2006)
4. I. Morita, T. Kanayama, T. Ueta, Load characteristics comparisons of interior permanent magnet synchronous motors by pole-slot combinations, in *International Conference on Electrical Machines and Systems, 2009, ICEMS 2009* (2009), pp. 1–6
5. L. Chong, *Design of an interior permanent magnet machine with concentrated windings for field weakening applications*. Ph.D., Electrical Engineering, The University of New South Wales, 2011
6. J.W. Bennett, G.J. Atkinson, B.C. Mecrow, D.J. Atkinson, Fault-tolerant design considerations and control strategies for aerospace drives. *IEEE Trans. Ind. Electron.* **59**, 2049–2058 (2012)
7. A.M. El-Refaie, Z.Q. Zhu, T.M. Jahns, D. Howe, Winding inductances of fractional slot surface-mounted permanent magnet brushless machines, in *Industry Applications Society Annual Meeting, 2008, IAS '08* (IEEE, 2008), pp. 1–8
8. D. Ishak, Z.Q. Zhu, D. Howe, Comparison of PM brushless motors, having either all teeth or alternate teeth wound. *IEEE Trans. Energy Convers.* **21**, 95–103 (2006)
9. K. Ahsanullah, R. Dutta, M.F. Rahman, Design of a 4 KW interior permanent magnet machine suitable for low speed application, in *2013 International Conference on Electrical Machines and Systems (ICEMS)* (2013), pp. 986–991
10. W. Daohan, W. Xiuhe, J. Sang-Yong, Cogging torque minimization and torque ripple suppression in surface-mounted permanent magnet synchronous machines using different magnet widths. *IEEE Trans. Magn.* **49**, 2295–2298 (2013)
11. H. Seok-Hee, T.M. Jahns, W.L. Soong, M.K. Guven, M.S. Illindala, Torque ripple reduction in interior permanent magnet synchronous machines using stators with odd number of slots per pole pair. *IEEE Trans. Energy Convers.* **25**, 118–127 (2010)
12. U.-J. Seo, Y.-D. Chun, J.-H. Choi, S.-U. Chung, P.-W. Han, D.-H. Koo, General characteristic of fractional slot double layer concentrated winding synchronous machine. *J. Electr. Eng. Technol.* **8**, 282–287 (2013)
13. D. Wu, Z.Q. Zhu, Influence of slot and pole number combinations on voltage distortion in surface-mounted permanent magnet machines with local magnetic saturation. *IEEE Trans. Energy Convers.* **30**, 1460–1471 (2015)
14. Z.Q. Zhu, L.J. Wu, M.L.M. Jamil, Influence of pole and slot number combinations on cogging torque in permanent-magnet machines with static and rotating eccentricities. *IEEE Trans. Ind. Appl.* **50**, 3265–3277 (2014)
15. Z.Q. Zhu, M.L.M. Jamil, L.J. Wu, Influence of slot and pole number combinations on unbalanced magnetic force in PM machines with diametrically asymmetric windings. *IEEE Trans. Ind. Appl.* **49**, 19–30 (2013)
16. P. Ponomarev, P. Lindh, J. Pyrhönen, Effect of slot-and-pole combination on the leakage inductance and the performance of tooth-coil permanent-magnet synchronous machines. *IEEE Trans. Ind. Electron.* **60**, 4310–4317 (2013)
17. K. Yamazaki, M. Shina, Y. Kanou, M. Miwa, J. Hagiwara, Effect of eddy current loss reduction by segmentation of magnets in synchronous motors: difference between interior and surface types. *IEEE Trans. Magn.* **45**, 4756–4759 (2009)

18. Z.Q. Zhu, Y.S. Chen, D. Howe, Iron loss in permanent-magnet brushless AC machines under maximum torque per ampere and flux weakening control. *IEEE Trans. Magn.* **38**, 3285–3287 (2002)
19. P.B. Reddy, A.M. El-Refaie, H. Kum-Kang, J.K. Tangudu, T.M. Jahns, Comparison of interior and surface PM machines equipped with fractional-slot concentrated windings for hybrid traction applications. *IEEE Trans. Energy Convers.* **27**, 593–602 (2012)
20. S. Morimoto, Y. Takeda, T. Hirasa, Current phase control methods for permanent magnet synchronous motors. *IEEE Trans. Power Electron.* **5**, 133–139 (1990)
21. Y. Li, K. J. Bradley, P. Sewell, D. Gerada, Cascaded doubly fed induction machine system modelling based on Dynamic Reluctance Mesh modelling method, in *Proceedings of the ICEM* (2008), pp. 1–5
22. J.K. Tangudu, T.M. Jahns, A. El-Refaie, Z.Q. Zhu, Lumped parameter magnetic circuit model for fractional-slot concentrated-winding interior permanent magnet machines, in *Proceedings of the ECCE* (2009), pp. 2423–2430
23. E.C. Lovelace, T.M. Jahns, J.H. Lang, A saturating lumped-parameter model for an interior PM synchronous machine. *IEEE Trans. Ind. Appl.* **38**, 645–650 (2002)
24. P. Ponomarev, I. Petrov, J. Pyrhonen, Influence of travelling current linkage harmonics on inductance variation, torque ripple and sensorless capability of tooth-coil permanent-magnet synchronous machines. *IEEE Trans. Magn.* **50**, 1–8 (2014)
25. G. Dajaku, X. Wei, D. Gerling, Reduction of low space harmonics for the fractional slot concentrated windings using a novel stator design. *IEEE Trans. Magn.* **50**, 1–12 (2014)
26. J. Nerg, M. Rilla, V. Ruuskanen, J. Pyrhonen, S. Ruotsalainen, Direct-driven interior magnet permanent-magnet synchronous motors for a full electric sports car. *IEEE Trans. Ind. Electron.* **61**, 4286–4294 (2014)
27. R. Dutta, M.F. Rahman, L. Chong, Winding inductances of an interior permanent magnet (IPM) machine with fractional slot concentrated winding. *IEEE Trans. Magn.* **48**, 4842–4849 (2012)
28. A.B. Proca, A. Keyhani, A. El-Antably, L. Wenzhe, D. Min, Analytical model for permanent magnet motors with surface mounted magnets. *IEEE Trans. Energy Convers.* **18**, 386–391 (2003)
29. A. Rahideh, M. Mardaneh, T. Korakianitis, Analytical 2-D calculations of torque, inductance, and back-EMF for brushless slot less machines with surface inset magnets. *IEEE Trans. Magn.* **49**, 4873–4884 (2013)
30. A. Rahideh, T. Korakianitis, Analytical magnetic field calculation of slotted brushless permanent-magnet machines with surface inset magnets. *IEEE Trans. Magn.* **48**, 2633–2649 (2012)
31. B. Gaussens, E. Hoang, O.D.I. Barriere, J. Saint-Michel, P. Manfe, M. Lecrivain, et al., Analytical armature reaction field prediction in field-excited flux-switching machines using an exact relative permeance function. *IEEE Trans. Magn.* **49**, 628–641 (2013)
32. D. Zarko, D. Ban, T.A. Lipo, Analytical calculation of magnetic field distribution in the slotted air gap of a surface permanent-magnet motor using complex relative air-gap permeance. *IEEE Trans. Magn.* **42**, 1828–1837 (2006)
33. L. Qi, F. Tao, W. Xuhui, Armature-reaction magnetic field analysis for interior permanent magnet motor based on winding function theory. *IEEE Trans. Magn.* **49**, 1193–1201 (2013)
34. C. Hong, L. Dawei, Q. Ronghai, Z. Zhe, L. Jian, An improved analytical model for inductance calculation of interior permanent magnet machines. *IEEE Trans. Magn.* **50**, 1–8 (2014)
35. J.C. Moreira, T.A. Lipo, Modeling of saturated AC machines including air gap flux harmonic components. *IEEE Trans. Ind. Appl.* **28**, 343–349 (1992)
36. J. Faiz, I. Tabatabaei, Extension of winding function theory for nonuniform air gap in electric machinery. *IEEE Trans. Magn.* **38**, 3654–3657 (2002)
37. M. Chunting, M. Filippa, L. Weiguo, M. Ruiqing, Analytical method for predicting the air-gap flux of interior-type permanent-magnet machines. *IEEE Trans. Magn.* **40**, 50–58 (2004)

38. G. Dajaku, D. Gerling, Stator slotting effect on the magnetic field distribution of salient pole synchronous permanent-magnet machines. *IEEE Trans. Magn.* **46**, 3676–3683 (2010)
39. Z. Li, S.Z. Jiang, Z.Q. Zhu, C.C. Chan, Analytical modeling of open-circuit air-gap field distributions in multisegment and multilayer interior permanent-magnet machines. *IEEE Trans. Magn.* **45**, 3121–3130 (2009)
40. T. Wen-Bin, C. Ting-Yu, Analysis of flux leakage in a brushless permanent-magnet motor with embedded magnets. *IEEE Trans. Magn.* **35**, 543–547 (1999)
41. H. Chang-Chou, Y.H. Cho, Effects of leakage flux on magnetic fields of interior permanent magnet synchronous motors. *IEEE Trans. Magn.* **37**, 3021–3024 (2001)
42. B.N. Cassimere, S.D. Sudhoff, D.H. Sudhoff, Analytical design model for surface-mounted permanent-magnet synchronous machines. *IEEE Trans. Energy Convers.* **24**, 347–357 (2009)
43. X. Hung Vu, D. Lahaye, H. Polinder, J.A. Ferreira, Influence of stator slotting on the performance of permanent-magnet machines with concentrated windings. *IEEE Trans. Magn.* **49**, 929–938 (2013)
44. W.B. Hird, The reluctance of the teeth in a slotted armature. *J. Inst. Electr. Eng.* **29**, 933–941 (1900)
45. P. Ponomarev, P. Lindh, J. Pyrhonen, Effect of slot-and-pole combination on the leakage inductance and the performance of tooth-coil permanent-magnet synchronous machines. *IEEE Trans. Ind. Electron.* **60**, 4310–4317 (2013)
46. N. Bianchi, E. Fornasiero, Impact of MMF space harmonic on rotor losses in fractional-slot permanent-magnet machines. *IEEE Trans. Energy Convers.* **24**, 323–328 (2009)
47. A.M. El-Refaie, Fractional-slot concentrated-windings synchronous permanent magnet machines: opportunities and challenges. *IEEE Trans. Ind. Electron.* **57**, 107–121 (2010)
48. L. Jian, C. Da-Woon, S. Dong-Hyeok, C. Yun-Hyun, Effects of MMF harmonics on rotor eddy-current losses for inner-rotor fractional slot axial flux permanent magnet synchronous machines. *IEEE Trans. Magn.* **48**, 839–842 (2012)
49. T.J.E. Miller, R. Rabinovici, Back-EMF waveforms and core losses in brushless DC motors. *IEE Proc. Electr. Power Appl.* **141**, 144–154 (1994)
50. Z.Q. Zhu, D. Howe, Instantaneous magnetic field distribution in permanent magnet brushless DC motors. IV. Magnetic field on load. *IEEE Trans. Magn.* **29**, 152–158 (1993)
51. A.O. Di Tommaso, F. Genduso, R. Miceli, A software for the evaluation of winding factor harmonic distribution in high efficiency electrical motors and generators, in *Proceedings of the EVER* (2013), pp. 1–6
52. R.F. Burbidge, A rapid method of analysing the m.m.f. wave of a single or polyphase winding. *IEE Proc. Part C: Monogr.* **105**, 307–311 (1958)
53. P.C. Krause, O. Wasynczuk, S.D. Sudhoff, S. Pekarek, *Analysis of Electric Machinery and Drive Systems*, vol. 75 (Wiley, 2013)
54. C.-C. Lai, T.-S. Liu, M.-T. Peng, Design and analysis of permanent magnet motor with movable stators. *Prog. Electromagn. Res. B* **58**, 219–232 (2014)
55. X. Chen, J. Wang, V.I. Patel, A generic approach to reduction of magnetomotive force harmonics in permanent-magnet machines with concentrated multiple three-phase windings. *IEEE Trans. Magn.* **50**, 1–4 (2014)
56. A. Bellara, Y. Amara, G. Barakat, B. Dakyo, Two-dimensional exact analytical solution of armature reaction field in slotted surface mounted PM radial flux synchronous machines. *IEEE Trans. Magn.* **45**, 4534–4538 (2009)
57. T. Lubin, S. Mezani, A. Rezzoug, 2-D exact analytical model for surface-mounted permanent-magnet motors with semi-closed slots. *IEEE Trans. Magn.* **47**, 479–492 (2011)
58. T. Lubin, S. Mezani, A. Rezzoug, Two-dimensional analytical calculation of magnetic field and electromagnetic torque for surface-inset permanent-magnet motors. *IEEE Trans. Magn.* **48**, 2080–2091 (2012)
59. M. Rahman, T. Little, G. Slemon, Analytical models for interior-type permanent magnet synchronous motors. *IEEE Trans. Magn.* **21**, 1741–1743 (1985)
60. H. Chang-Chou, Y.H. Cho, Effects of leakage flux on magnetic fields of interior permanent magnet synchronous motors. *IEEE Trans. Magn.* **37**, 3021–3024 (2001)

61. T. Wen-Bin, C. Ting-Yu, Analysis of flux leakage in a brushless permanent-magnet motor with embedded magnets. *IEEE Trans. Magn.* **35**, 543–547 (1999)
62. E.C. Lovelace, T.M. Jahns, J.H. Lang, A saturating lumped-parameter model for an interior PM synchronous machine. *IEEE Trans. Ind. Appl.* **38**, 645–650 (2002)
63. S.H. Han, T.M. Jahns, W.L. Soong, A magnetic circuit model for an IPM synchronous machine incorporating moving airgap and cross-coupled saturation effects, in *2007 IEEE International Electric Machines & Drives Conference* (2007), pp. 21–26
64. Y. Kano, T. Kosaka, N. Matsui, Simple nonlinear magnetic analysis for permanent-magnet motors. *IEEE Trans. Ind. Appl.* **41**, 1205–1214 (2005)
65. M. Moallem, G.E. Dawson, An improved magnetic equivalent circuit method for predicting the characteristics of highly saturated electromagnetic devices. *IEEE Trans. Magn.* **34**, 3632–3635 (1998)
66. C. Ming, K.T. Chau, C.C. Chan, E. Zhou, X. Huang, Nonlinear varying-network magnetic circuit analysis for doubly salient permanent-magnet motors. *IEEE Trans. Magn.* **36**, 339–348 (2000)
67. J. Farooq, S. Srarri, A. Djerdir, A. Miraoui, Use of permeance network method in the demagnetization phenomenon modeling in a permanent magnet motor. *IEEE Trans. Magn.* **42**, 1295–1298 (2006)
68. C. Shi-Uk, K. Ji-Won, C. Yon-Do, W. Byung-Chul, H. Do-Kwan, Fractional slot concentrated winding PMSM with consequent pole rotor for a low-speed direct drive: reduction of rare earth permanent magnet. *IEEE Trans. Energy Convers.* **30**, 103–109 (2015)
69. D. Pavlik, V.K. Garg, J.R. Repp, J. Weiss, A finite element technique for calculating the magnet sizes and inductances of permanent magnet machines. *IEEE Trans. Energy Convers.* **3**, 116–122 (1988)
70. T.W. Nehl, F.A. Fouad, N.A. Demerdash, Determination of saturated values of rotating machinery incremental and apparent inductances by an energy perturbation method. *IEEE Power Eng. Rev.* **PER-2**, 28–29 (1982)
71. R. Escarela-Perez, E. Campero-Littlewood, M.A. Arjona-Lopez, A. Laureano-Cruces, Comparison of two techniques for two-dimensional finite-element inductance computation of electrical machines. *IEE Proc. Electr. Power Appl.* **152**, 855–861 (2005)
72. N. Bianchi, S. Bolognani, Magnetic models of saturated interior permanent magnet motors based on finite element analysis, in *Conference Record on 33rd IAS Annual Meeting* (1998), pp. 27–34
73. S. Kallio, J. Karttunen, P. Peltoniemi, P. Silventoinen, O. Pyrhonen et al., Determination of the inductance parameters for the decoupled d-q model of double-star permanent magnet synchronous machines. *IET Electr. Power Appl.* **8**, 39–49 (2014)
74. K.J. Meessen, P. Thelin, J. Soulard, E.A. Lomonova, Inductance calculations of permanent-magnet synchronous machines including flux change and self- and cross-saturations. *IEEE Trans. Magn.* **44**, 2324–2331 (2008)
75. M. Farshadnia, R. Dutta, J.E. Fletcher, K. Ahsanullah, M.F. Rahman, H.C. Lovatt, Analysis of MMF and back-EMF waveforms for fractional-slot concentrated-wound permanent magnet machines, in *IEEE Proceedings of the ICEM* (2014), pp. 1976–1982
76. B.H. Ng, M.F. Rahman, T.S. Low, K.W. Lim, An investigation into the effects of machine parameters on torque pulsations in a brushless DC drive, in *Proceedings of the IECON* (1988), pp. 749–754
77. T.S. Low, K.J. Tseng, T.H. Lee, K.W. Lim, K.S. Lock, Strategy for the instantaneous torque control of permanent-magnet brushless DC drives. *Proc. IEE Elect. Power Appl.* **137**, 355–363 (1990)
78. H.R. Bolton, R.A. Ashen, Influence of motor design and feed-current waveform on torque ripple in brushless DC drives. *Proc. Elect. Power Appl.* **131**, 82–90 (1984)
79. K.Y. Cho, J.D. Bae, S.K. Chung, M.J. Youn, Torque harmonics minimization in PM synchronous motor with back EMF estimation, in *Proceedings of the TENCON*, vol. 5 (1993), pp. 589–593

80. A. Gebregergis, M.H. Chowdhury, M.S. Islam, T. Sebastian, Modeling of permanent-magnet synchronous machine including torque ripple effects. *IEEE Trans. Ind. Appl.* **51**, 232–239 (2015)
81. A. Chiba, F. Nakamura, T. Fukao, M. Azizur Rahman, Inductances of cageless reluctance-synchronous machines having nonsinusoidal space distributions. *IEEE Trans. Ind. Appl.* **27**, 44–51 (1991)
82. F. Meier, J. Soulard, dq theory applied to a permanent magnet synchronous machine with concentrated windings, in *Proceedings of the PEMD* (2008), pp. 194–198
83. F. Magnussen, H. Lendenmann, Parasitic effects in PM machines with concentrated windings. *IEEE Trans. Ind. Appl.* **43**, 1223–1232 (2007)
84. M. Fasil, C. Antaloae, N. Mijatovic, B.B. Jensen, J. Holboll, Improved dq-axes model of PMSM considering airgap flux harmonics and saturation. *IEEE Trans. Appl. Supercond.* **26**, 1–5 (2016)
85. J. Liu, W. Chen, Generalized DQ model of the permanent magnet synchronous motor based on extended park transformation, in *2013 1st International Future Energy Electronics Conference (IFEEC)* (2013), pp. 885–890

## Chapter 2

# Analytical Modelling of Stator Magnetic Characteristics in Fractional-Slot Concentrated-Wound Permanent Magnet Machines



## 2.1 Introduction

Precise modeling of the spatial MMF distribution in an electric machine is essential to analytical formulation of the machine characteristics such as back-EMF, flux linkage, and electromagnetic torque. The spatial MMF distribution in a FSCW stator is characterized by high harmonic content that could result in increased rotor losses, unbalanced saturation of the iron core, distorted back-EMF waveforms, and ripple in the electromagnetic torque.

Commonly, numerical approaches based on FEA are used in the literature for analysis of the FSCW PMSM characteristics. Rigorous mathematical analysis and modeling of the electromagnetic interactions in a FSCW PMSM with respect to their slot and pole combinations has not received much research attention.

In order to address the above gap in the knowledge, an analytical investigation into the spatial MMF distribution of FSCW PMSMs is reported in this chapter. Design considerations for an optimal FSCW stator are first discussed. FSCW stator “classes” and “categories” are then introduced and general expressions are proposed for the development of the spatial MMF distribution in the airgap. Based on the performed analysis, remarks are made regarding the fault-tolerant capability of different FSCW stator categories. Subsequently, harmonic winding factors are formulated as an essential factor in evaluation of the machine performance and output characteristics. The PM flux linkages and back-EMFs of an FSCW stator are then formulated based on the harmonic winding factors of the machine.

The performed mathematical analysis and obtained expressions in this chapter will be used in Chaps. 3–7 of this thesis as a basis for machine design, modeling and analysis. Case studies are presented at the end of this chapter to demonstrate the application and value of the proposed expressions. Validation is performed in Chap. 3 using FEA and experimental tests on a prototype FSCW PMSM in the laboratory.

## 2.2 Properties of an Optimal FSCW Stator Winding Layout

FSCW stator topologies are characterized by their slots per pole per phase ratio, denoted  $S_{pp}$ . This value, which should be in its simplest fractional form, is positive, smaller than unity, and determines the winding layout of the stator. Slot and pole combinations that yield the same value of  $S_{pp}$ , are referred to as a FSCW stator “class” in this thesis. In a symmetrical winding layout, it is impossible to generate MMF harmonics with an order that is a multiple of the phase number. Therefore, stator classes with a pole number that is a multiple of the phase number are invalid. This is discussed in Sect. 2.3.

Each FSCW stator class (slot and pole combination) has its own distinct features, and should be chosen for use in a FSCW stator based on the following criteria:

- A high torque density (a requirement of an optimal design).
- A low cogging torque.

The torque density of a stator class can be evaluated through its harmonic winding factors. These factors indicate the utilization of the stator windings. For three-phase FSCW stators, a high main harmonic winding factor leads to a high torque density. This is thoroughly explained in Sect. 2.5.

Cogging torque in a PMSM contributes to the torque ripple of the machine. In a PMSM, cogging torque arises from the magnetic interaction between the rotor magnets and the stator teeth, creating a torque that aligns the rotor such that permeance of the flux path is maximized [1]. Cogging torque in a FSCW stator is evaluated based on the least common multiple (LCM) of the number of slots and poles. When comparing FSCW stators, a higher value of LCM usually leads to a lower peak value for the developed cogging torque. However, other factors also affect the cogging torque such as skewing of the stator or magnets, slot opening width and the width of the magnets [2]. The LCM of a stator class is not constant and strictly depends on the number of slots and poles.

A valid winding layout for double-layer FSCW stators need to meet the following conditions:

- The number of poles need to be an even number, and cannot be a multiple of the phase number.
- The number of stator slots in the winding layout need to be an integer multiple of the phase number. This is to ensure allocation of the same number of slots to each phase winding which allows a symmetrical distribution of all the phase windings in the stator.
- A zero net magnetic pull should be achieved to avoid excessive vibration and noise. This can be realized by setting the periodicity of the base winding configuration greater than or equal to 2, as explained in Sect. 2.2.1.

Winding periodicity,  $\wp$ , in a machine with  $Q$  slots and  $P$  poles is defined by:

$$\wp = \text{GCD}\{Q, P\} \quad (2.1)$$

where GCD stands for the greatest common divisor of  $Q$  and  $P$ . A periodicity of  $\wp$  indicates that the stator can be divided into  $\wp$  equal sections in which the slots allocated to the phase windings are the same, regardless of the coil polarities. In other words,  $\wp$  is the number of symmetries in the winding layout.

For each stator class, “*base winding layout*” is identified as the winding layout associated with the minimum possible number of slots,  $Q_{base}$ , and poles,  $P_{base}$ . From the stated conditions for a valid winding layout, periodicity of the base winding layout is equal to 2; consequently, the number of slots for the base winding layout in an  $m$ -phase machine that meets the validity conditions should be an integer multiple of  $2m$ . For such winding, the  $S_{pp}$  value is found as follows:

$$S_{pp} = \frac{Q_{base}}{m \times P_{base}} = \frac{2mk}{m \times P_{base}} \quad (2.2)$$

Hence,

$$S_{pp} = \frac{k}{P_{base}/2} \quad (2.3)$$

where  $k$  is an integer number. Since  $S_{pp}$  is the simplest form of a fraction, it is concluded from the definition of the base winding layout that (2.3) is indivisible. Therefore, the number of poles in the base winding layout,  $P_{base}$ , associated to a  $S_{pp}$  is twice the denominator in  $S_{pp}$ . The number of slots in the base winding layout,  $Q_{base}$ , can be found accordingly. The denominator in  $S_{pp}$  is denoted by  $c$  in the rest of this thesis:

$$c = P_{base}/2 \quad (2.4)$$

For the base winding layout, by having the number of slots and poles, the optimal coil arrangement can be determined using a novel approach that will be proposed in Chap. 3. For FSCW stators that have the same  $S_{pp}$  but a higher number of slots and poles, the winding layout is determined by repeating the base winding layout  $P/P_{base}$  ( $=P/2c$ ) times, where  $P$  is the number of poles in the FSCW stator. Therefore, it is possible to derive a general expression for the spatial MMF distribution of FSCW stator topologies that belong to the same stator class (feature the same  $S_{pp}$ ), as will be discussed in Sect. 2.3.

### 2.2.1 Unbalanced Magnetic Pull

Distribution of the radial magnetic forces in a machine is dependent on the choice of slots and poles,  $S_{pp}$ . A zero sum of these forces is desirable in a stator; otherwise

unidirectional pulling forces are generated that peripherally rotate in the stator with respect to time. Such forces are the main source of noise and vibration and may excite the resonant frequencies of the machine [3]. Therefore, careful consideration should be given to elimination of these radial forces when selecting a combination of slots and poles.

The radial magnetic force vector is given by Maxwell's tensor law as a function of time,  $t$ , and the angle subtended along the stator circumference,  $\theta_s$ , as follows [4]:

$$\vec{F}_r(t, \theta_s) = \int_s \frac{1}{2\mu_0} (B_r^2 - B_t^2) ds \vec{n} \quad (2.5)$$

where  $\mu_0 = 4\pi \times 10^{-7}$  H/m is the permeability of free space,  $B_r$  and  $B_t$  are the radial and tangential components of the airgap flux density, respectively,  $s$  is the surface of integration, and  $\vec{n}$  is the radial unit vector perpendicular to the surface of integration,  $s$ .

From (2.5), the radial magnetic force is proportional to the square of the radial and tangential components of the flux density. This indicates that the radial magnetic force is independent of the coil polarities. Therefore, symmetry in the winding layout, regardless of the coil polarities, yields zero unbalanced magnetic pull.

In  $P$ -pole  $Q$ -slot FSCW stators that are obtained by repeating the optimal base winding layout  $P/2c$  times, the periodicity (number of symmetries in the winding layout) equals  $P/c$ . Therefore, a zero net magnetic pull is guaranteed.

### 2.3 Derivation of MMF Expression in FSCW Stators

This section sets a basis for a general analytical approach for the analysis of the MMF and the formulation of its detailed expression in a double-layer FSCW stator. A set of standard assumptions are made throughout this section as follows [5, 6]:

- The stator and rotor steel have an infinite permeability; therefore a non-zero magnetic field only exists in the airgap.
- Magnetic saturation in the steel is neglected.
- The effect of slots on the MMF is neglected.
- The airgap length is small relative to the inside stator diameter; therefore, the magnetic field inside the airgap is radial.
- The PMs in the rotor are not magnetized; therefore they do not contribute to the magnetic field in the airgap.

### 2.3.1 Basic Principles of MMF in FSCW Stators

In a FSCW stator, each coil is wound around a single tooth, resulting in a winding span of  $2\pi/Q$ . The magnetic field intensity,  $H$ , and the flux density,  $B$ , inside a material with permeability  $\mu$  have the following relationship:

$$B(\theta_s) = \mu H(\theta_s) \quad (2.6)$$

where  $\mu = \mu_0 \mu_r$  and  $\mu_r$  is the relative permeability.

A single-coil FSCW stator is shown in Fig. 2.1, where the sign  $\otimes$  indicates a flow of the current into the paper, and  $\odot$  indicates a current direction out of the paper. The direction of the current in the coil of Fig. 2.1 is such that the field is being projected out of the stator tooth into the air-gap. The air-gap MMF due to the single coil of Fig. 2.1 can be found from Ampere's law. From Ampere's law, the line integral of the magnetic field intensity along a closed path called "Ampere's path" is equal to the net current,  $i$ , enclosed within the path:

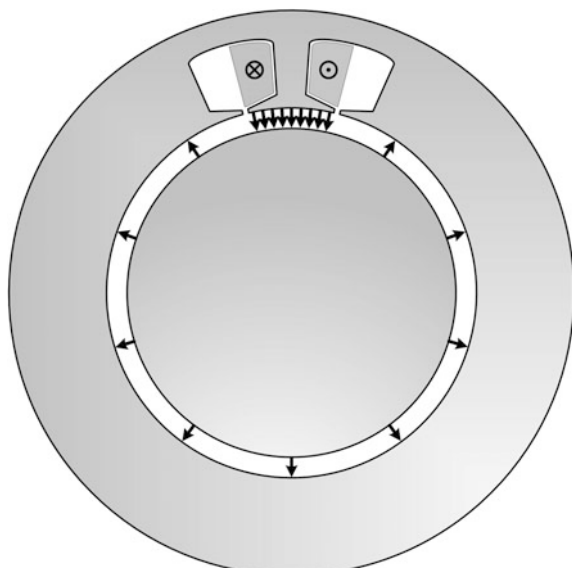
$$\oint_{\Gamma} \vec{H} \cdot d\vec{L} = \sum i \quad (2.7)$$

where  $\Gamma$  is the Ampere's path.

Two Ampere's paths for the single-coil stator of Fig. 2.1 are shown in Fig. 2.2a, b. In Fig. 2.2a the Ampere's path does not enclose any current-carrying conductors. Therefore, (2.7) simplifies to:

$$\int_{\Gamma_{steel}} \vec{H} \cdot d\vec{L} + \int_{\Gamma_{airgap}} \vec{H} \cdot d\vec{L} = 0 \quad (2.8)$$

**Fig. 2.1** Magnetic field distribution in a single-coil stator. The arrows indicate the magnetic field intensity and its direction



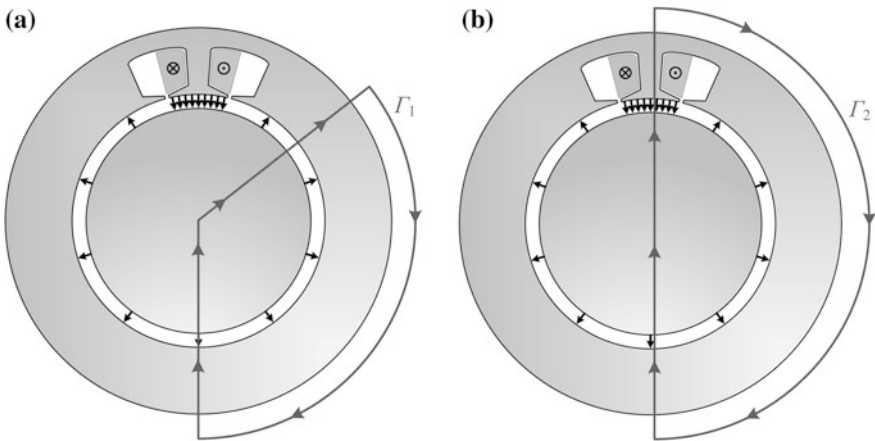


**Fig. 2.2** Ampere's path in a single-coil stator. The black arrows indicate the magnetic field intensity and its direction. The red closed loops,  $\Gamma_1$  and  $\Gamma_2$ , are the Ampere's paths where the red arrows indicate the direction of the length elements. **a** Ampere's path does not enclose any current-carrying conductors. **b** Ampere's path encloses current-carrying conductors

where,  $\Gamma_{\text{steel}}$  and  $\Gamma_{\text{airgap}}$  indicate the path of integration inside the steel and airgap, respectively. The field intensity is zero inside the steel due to its high permeability. Therefore, the first term on the left-hand side of (2.8) is equal to zero; thus:

$$\int_{\Gamma_{\text{airgap}}} \vec{H} \cdot d\vec{L} = 0 \quad (2.9)$$

$$\therefore \delta H = 0$$

where  $\delta$  is the airgap length.

MMF is defined as the line integral of the field intensity, therefore the left-hand side of (2.9) indicates the MMF. From (2.9) it is concluded that the MMF obtained by Ampere's law is zero in the airgap if no current-carrying conductor is enclosed by the Ampere's path. That is everywhere in the airgap other than beneath the stator tooth.

The Ampere's path in Fig. 2.2b encloses current-carrying conductors. If the coil has  $N_c$  turns, by assuming a negative sign for the current flowing out of the paper, (2.7) simplifies to:

$$\int_{\Gamma_{\text{steel}}} \vec{H} \cdot d\vec{L} + \int_{\Gamma_{\text{airgap}}} \vec{H} \cdot d\vec{L} = -N_c i \quad (2.10)$$

The first term on the left-hand side of (2.10) is equal to zero. The field intensity is not identical in the airgap on the Ampere's path  $\Gamma_2$ . In solving the integral in (2.10), from the conclusion of (2.9) the field intensity in regions other than underneath the stator tooth is provisionally assumed zero. Therefore, for the region underneath the tooth, (2.10) yields:

$$\begin{aligned}\delta H \cos(180^\circ) &= -N_c i \\ \therefore \delta H &= N_c i\end{aligned}\quad (2.11)$$

Therefore,

$$\text{MMF} = N_c i \quad (2.12)$$

The airgap spatial MMF distribution can now be plotted as shown in Fig. 2.3a. However, the assumption made in obtaining Fig. 2.3a should be further investigated.

Gauss's law states:

$$\oint_S \vec{B} \cdot d\vec{S} = 0 \quad (2.13)$$

where  $S$  is an imaginary cylindrical surface surrounding the rotor in the airgap. Equation (2.13) implies that the net flux passing the airgap is always zero. This is not in harmony with the assumption made earlier in solving Ampere's law, since the obtained MMF in Fig. 2.3a is unidirectional, resulting in the flux to flow in one direction across the airgap. Gauss's law can be satisfied by shifting the average

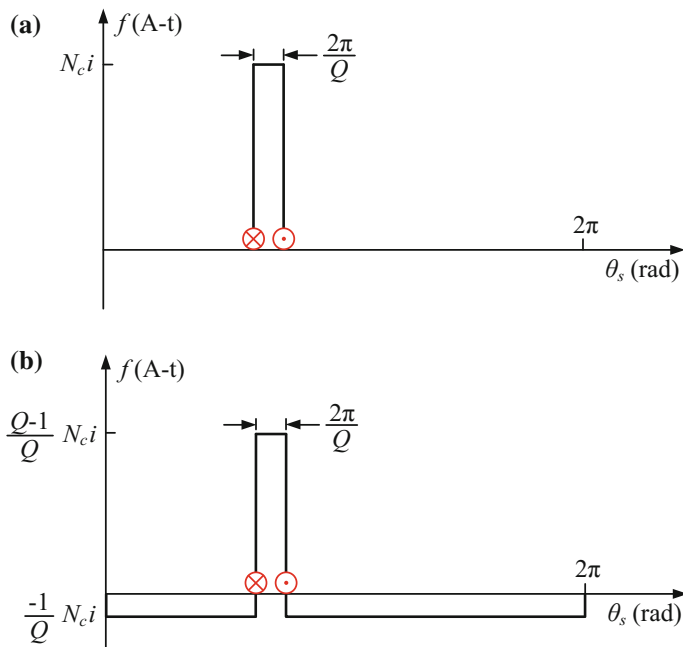


**Fig. 2.3** Airgap spatial MMF distribution for the single-coil stator **a** The MMF in regions other than underneath the stator tooth is assumed zero. **b** The modified MMF spatial distribution that satisfies Gauss's law

MMF of Fig. 2.3a such that a zero average value is obtained. Therefore, the airgap spatial MMF distribution is modified as shown in Fig. 2.3b.

From the above discussion, in a  $Q$ -slot FSCW stator each coil is wound around a single tooth, for which the spatial MMF distribution is a square pulse with its width equal to  $2\pi/Q$  mechanical radians, as shown in Fig. 2.3b. Thus, the spatial MMF distribution of a single coil is a function of time and space and can be expressed by:

$$f(t, \theta_s) = \begin{cases} \left(1 - \frac{1}{Q}\right)N_c i_j & \text{under the tooth} \\ -\frac{1}{Q}N_c i_j & \text{elsewhere} \end{cases} \quad (2.14)$$

where  $f$  is the MMF in Ampere-turns,  $\theta_s$  is the stator peripheral angle in mechanical radians,  $N_c$  is the number of turns in the coil, and  $i_j$  is the instantaneous current in Amperes that flows through phase  $j$  winding in which the coil exists.

### 2.3.2 Analysis and Formulation of the MMF Produced by FSCW Stators

The spatial MMF distribution of a phase winding is found by superimposing the MMFs of all its coils. Due to winding periodicity, the MMF of each phase winding comprises of periodic square pulses and can be expressed by a Fourier series of harmonics.

A “coil pair” in the base winding layout is defined as a pair of coils displaced by  $\theta_b/2$  mechanical radians in the stator, where  $\theta_b$  is the angular span for the base winding layout. Polarities of the coils in a coil pair determine its MMF. Assuming the coils have the same polarity, the spatial MMF distribution of a coil pair is as shown in Fig. 2.4a, whereas if polarities of the coils are in the opposite direction, the MMF produced by a coil pair is as shown in Fig. 2.4b. The Fourier series describing the spatial MMF distributions of Fig. 2.4 is:

$$\begin{aligned} f(t, \theta_s) &= \sum_k a_k \cdot \cos(k\theta_s - k\alpha) \\ a_k &= \frac{4N_c i_j}{k\pi} \sin\left(\frac{k\pi}{Q}\right) \end{aligned} \quad (2.15)$$

where

$k = 2, 4, 6, \dots$  when coils have the same polarity (Fig. 2.4a)

$k = 1, 3, 5, \dots$  when coils are of opposite polarity (Fig. 2.4b)

and  $\alpha$  is the spatial displacement of the first coil from the origin as shown in Fig. 2.4, and  $a_k$  is the amplitude of the  $k$ th harmonic component. If the coils in a coil pair are of the same polarity, as shown in Fig. 2.4a,  $k$  is even. If the coils are oriented to be of opposite polarity, as shown in Fig. 2.4b,  $k$  is odd. Therefore, for the coils with the same polarity, only even MMF harmonics exist and for the coils with an opposite polarity, only odd MMF harmonics are produced.

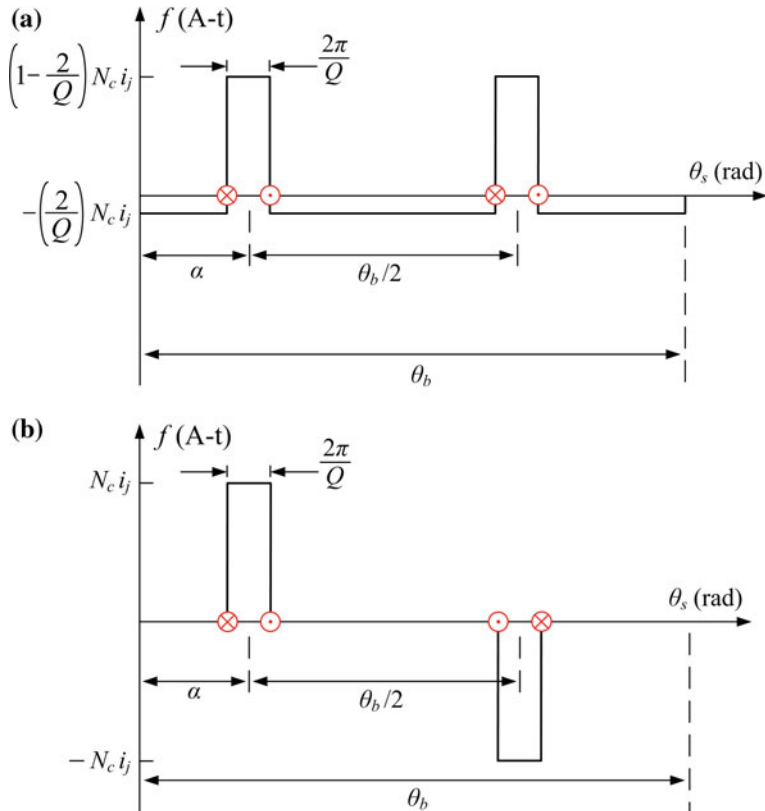


**Fig. 2.4** MMF generated by a coil pair of the base winding layout. **a** Coils in the coil pair are of the same polarity, applicable to FSCW PMSMs with their base winding layout having an even number of pole pairs. **b** Coils in the coil pair are of opposite polarity, applicable to FSCW PMSMs with their base winding layout having an odd number of pole pairs

In a  $P$ -slot  $Q$ -pole FSCW stator, the base winding layout should be repeated  $P/2c$  times to result in the complete winding layout for the machine. In such a case, the Fourier series of a coil pair that is repeated  $P/2c$  times in the stator is described by:

$$f(\theta_s) = \sum a_n \cdot \cos(n\theta_s - n\alpha) \quad (2.16)$$

$$a_n = \frac{P}{2c} \frac{4N_c i_j}{n\pi} \sin\left(\frac{n\pi}{Q}\right), \quad n = \frac{kP}{2c}$$

and

$$k = 1, 3, 5, \dots \quad \text{when } c \text{ is an odd number}$$

$$k = 2, 4, 6, \dots \quad \text{when } c \text{ is an even number}$$

For a phase winding, the MMF produced by the coil pairs as described by (2.16), add to give the total MMF of that phase:

$$f_j(t, \theta_s) = \sum_n F_{j,n} \cos(n\theta_s - n\theta_j), \quad n = \frac{kP}{2c} \quad (2.17)$$

where  $k$  is as defined in (2.16), the subscript  $j$  indicates the phase,  $\theta_j$  is the phase angle in mechanical radians associated to phase  $j$  winding and is equal to 0,  $2\pi/3$  and  $-2\pi/3$  for phase  $a$ ,  $b$ , and  $c$ , respectively, and  $F_{j,n}$  is the amplitude of the  $n$ th spatial MMF harmonic of phase  $j$  which should be calculated based on the winding configuration of the machine as will be discussed in the next section. All the single-phase MMFs should be summed to give the total MMF distribution in the air-gap which comprises clockwise- and counterclockwise-rotating harmonics [7].

The spatial MMF harmonic that participates in torque generation is referred to as the “*main spatial harmonic*” and is of order  $v = P/2$  [8]. To this end, for a base winding layout that has an even number of pole pairs, only even spatial MMF harmonics are present; thus, from (2.16) the coils in each coil pair should be of the same polarity. On the other hand, when an odd number of pole pairs is assumed, only odd spatial MMF harmonics should be generated; hence, according to (2.16) the orientations of the coils in each coil pair would be in the opposite direction. The denominator in  $S_{pp}$  denoted by  $c$  can be used as an indicator of this—an even value of  $c$  indicates an even number of pole pairs in the base winding layout, while when  $c$  is an odd number, the base winding layout will have an odd number of pole pairs.

Two three-phase stator topologies with  $S_{pp} = 1/4$  and  $S_{pp} = 1/5$  are used as examples. The base winding layout for these two topologies has 6 slots/8 poles and 6 slots/10 poles, respectively. This results in two teeth being allocated to each phase winding. The main spatial harmonic of the 8-pole machine is of 4th order while for the 10-pole machine it is of 5th order. Hence, in the machine with  $S_{pp} = 1/4$ , the coils should have the same polarity to produce even spatial MMF harmonics, while for the machine with  $S_{pp} = 1/5$  the coil spatial orientations should be in the opposite polarity to produce odd spatial MMF harmonics. The resulting base winding layout and the single-phase MMF waveforms for these two topologies are shown in Fig. 2.5 and Fig. 2.6, respectively.

For a  $P$ -pole  $Q$ -slot FSCW stator with  $S_{pp} = 1/4$  or  $S_{pp} = 1/5$ , a general equation for the harmonic amplitudes  $F_{j,n}$  in (2.17) for the single-phase MMF distributions shown in Fig. 2.6 is obtained based on (2.16) as follows:

$$F_{j,n} = \frac{P}{2c} \frac{4N_c i_j}{n\pi} \sin\left(\frac{n\pi}{Q}\right), \quad n = \frac{kP}{2c} \quad (2.18)$$

where  $k$  is as defined in (2.16).

The total spatial MMF distribution in the airgap is found by summing all the single-phase MMFs. Before proceeding with the calculation of the total MMF, the

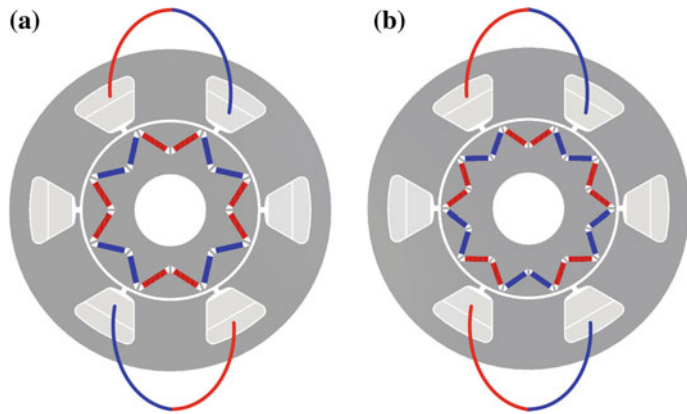


**Fig. 2.5** Base winding layout for a single phase of three-phase FSCW PMSMs. **a**  $S_{pp} = 1/4$ , 6-slot 8-pole machine. **b**  $S_{pp} = 1/5$ , 6-slot 10-pole machine

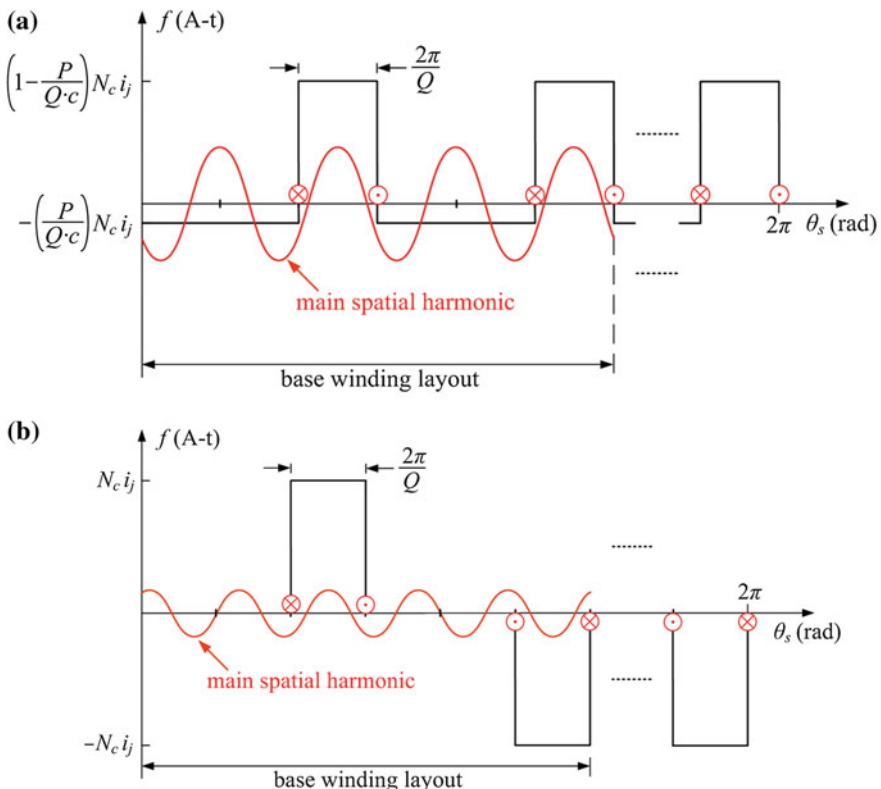


**Fig. 2.6** MMF generated by a phase winding by different three-phase FSCW stators. **a**  $S_{pp} = 1/4$ , base winding layout is of 6 slots/8 poles. **b**  $S_{pp} = 1/5$ , base winding layout is of 6 slots/10 poles

concept of the winding function should be introduced. The winding function describes the number of times that a winding links the flux density at different positions in the stator. Therefore, winding function of phase  $j$  can be obtained from its MMF if the phase winding is supplied by unity  $dc$  current:

$$w_j(\theta_s) = \sum_n W_n \cos(n\theta_s - n\theta_j), \quad n = \frac{kP}{2c} \quad (2.19)$$

$$W_n = F_{j,n}, \quad i_j = 1 \quad (2.20)$$

In (2.19),  $k$  is as defined in (2.16),  $w_j$  is the winding function of phase  $j$ , and  $W_n$  is the amplitude of the  $n$ th winding function harmonic. From (2.16), it can be concluded that:

$$F_{j,n} = W_n i_j \quad (2.21)$$

Assume a three-phase FSCW stator that is fed with a balanced current set:

$$\begin{aligned} i_a(t) &= I_m \cos(\omega_e t) \\ i_b(t) &= I_m \cos(\omega_e t - \frac{2\pi}{3}) \\ i_c(t) &= I_m \cos(\omega_e t + \frac{2\pi}{3}) \end{aligned} \quad (2.22)$$

where  $I_m$  is the amplitude of the supplied current, and  $\omega_e$  is the angular electrical frequency, found from the electrical frequency,  $f_e$ , and equals to:

$$\omega_e = 2\pi f_e \quad (2.23)$$

The total MMF produced by an FSCW stator can be obtained as:

$$f_T(t, \theta_s) = f_a(t, \theta_s) + f_b(t, \theta_s) + f_c(t, \theta_s) \quad (2.24)$$

Substituting the single-phase MMFs from (2.17) yields:

$$f_T(t, \theta_s) = F_{a,n} \cos(n\theta_s) + F_{b,n} \cos(n\theta_s - n\frac{2\pi}{3}) + F_{c,n} \cos(n\theta_s + n\frac{2\pi}{3}) \quad (2.25)$$

Replacing  $F_{a,n}$ ,  $F_{b,n}$ , and  $F_{c,n}$  from (2.21) gives:

$$f_T(t, \theta_s) = \sum_n W_n \left( i_a \cos(n\theta_s) + i_b \cos(n\theta_s - n\frac{2\pi}{3}) + i_c \cos(n\theta_s + n\frac{2\pi}{3}) \right) \quad (2.26)$$

Substituting the currents from (2.22) results in:

$$\begin{aligned} f_T(t, \theta_s) = & \sum_n W_n I_m \left( \cos(\omega_e t) \cos(n\theta_s) + \cos(\omega_e t - \frac{2\pi}{3}) \cos(n\theta_s - n\frac{2\pi}{3}) \right. \\ & \left. + \cos(\omega_e t + \frac{2\pi}{3}) \cos(n\theta_s + n\frac{2\pi}{3}) \right) \end{aligned} \quad (2.27)$$

Further mathematical steps, reduces the above expression to:

$$\begin{aligned} f_T(t, \theta_s) = & \sum_{n=\frac{P}{2c}(6k+b)} f_{ccw,n}(t, \theta_s) \\ & + \sum_{n=\frac{P}{2c}(6k-b)} f_{cw,n}(t, \theta_s), \quad k = 0, 1, 2, 3, \dots \end{aligned} \quad (2.28)$$

where

$$f_{ccw,n}(t, \theta_s) = F_n \cos(\omega_e t - n\theta_s) \quad (2.29)$$

$$f_{cw,n}(t, \theta_s) = F_n \cos(\omega_e t + n\theta_s) \quad (2.30)$$

In the above equations the subscripts *cw* and *ccw* indicate the clockwise and counter clockwise rotations, respectively, and  $F_n$  is the amplitude of the  $n$ th spatial harmonic of the total MMF.  $F_n$  is equal to the single-phase spatial MMF harmonic amplitude when the instantaneous current  $i_j$  is replaced by its amplitude,  $I_m$ , as follows:

$$F_n = \frac{3}{2} F_{j,n}, \quad i_j = I_m \quad (2.31)$$

The constant  $b$  in (2.28) is determined based on the stator topology. For FSCW machines that have an odd number of pole pairs in their base winding layout,  $b$  is equal to 1; whereas when an even number of pole pairs is present in the base winding layout,  $b$  is equal to 2. Therefore (2.28) only comprises spatial MMF harmonic orders in accordance to the pole pair number. Although the single-phase spatial MMF harmonic spectrum contains triplen harmonics, they are cancelled when all the winding MMFs are summed to the total MMF of the FSCW stator. Therefore, no spatial harmonics with an order that is a multiple of the number of phases will exist in the total MMF distribution in the airgap.

Equation (2.28) indicates that depending on the number of pole pairs in the base winding layout, the total MMF harmonic spectrum comprises either odd spatial harmonics or even spatial harmonics. Furthermore, the only spatial harmonics that exist in the total MMF harmonic spectrum are of order  $n = (P/2c) \times (6k \pm b)$ . Each of these spatial harmonics has a distinct magnitude and phase angle that are

time-independent, and may rotate either in the same or the opposite direction to the rotor. The angular speed of the  $n$ th harmonic in mechanical radians per second is:

$$\omega_n = \begin{cases} -\frac{\omega_e}{n} & \text{for clockwise-rotating harmonics} \\ \frac{\omega_e}{n} & \text{for counterclockwise-rotating harmonics} \end{cases} \quad (2.32)$$

According to (2.28), harmonics of order  $n = (P/2c) \times (6k - b)$  rotate in the clockwise direction, while those of order  $n = (P/2c) \times (6k + b)$  are counterclockwise.

A rotating spatial MMF harmonic creates a number of virtual pole-pairs in the airgap equal to its harmonic order. In a  $P$ -pole PMSM, the rotor is locked onto the main MMF harmonic of order  $v = P/2$  and rotates with it synchronously. Therefore, all other spatial MMF harmonics rotate asynchronously with the rotor. As will be seen in the next chapters, spatial MMF harmonics other than the main spatial harmonic have no contribution to the average electromagnetic torque. These harmonics lead to iron saturation and increased core losses; moreover, their interaction with the rotor PM flux density and inductances lead to undesirable torque ripple [9].

### 2.3.3 MMF Expressions for the Most Common Three-Phase FSCW PMSMs

A general equation for the single-phase spatial MMF distribution is given by (2.17), as follows:

$$f_j(t, \theta_s) = \sum_n F_{j,n} \cos(n\theta_s + n\theta_j), \quad n = \frac{kP}{2c} \quad (2.33)$$

$k = 1, 3, 5, \dots$  when  $c$  is an odd number

$k = 2, 4, 6, \dots$  when  $c$  is an even number

The single-phase spatial MMF harmonic amplitude,  $F_{j,n}$ , is constant for all the stator phases. The three-phase MMF can be directly found from the single-phase MMF using (2.28)–(2.31). Lumped expressions for  $F_{j,n}$  are derived for the most common FSCW stator classes in the following. As mentioned earlier, a stator class is referred to  $Q$ -slot  $P$ -pole stators that have the same  $S_{pp}$ . Some stator classes have the same number of slots with the same winding layout, but a different number of poles. Such stator topologies produce the same spatial MMF distribution in the airgap. These stator classes fall under the same stator “category”, as follows:

- **Category “A”:**  $Q$ -slot  $P$ -pole FSCW stators with  $S_{pp} = 1/(3k \pm 1)$  and  $k = 1, 3, 5, \dots$
- **Category “B”:**  $Q$ -slot  $P$ -pole FSCW stators with  $S_{pp} = 1/(3k \pm 1)$  and  $k = 2, 4, 6, \dots$

- **Category “C”:**  $Q$ -slot  $P$ -pole FSCW stators with  $S_{pp} = 2/(6k \pm 1)$  and  $k = 1, 3, 5, \dots$
- **Category “D”:**  $Q$ -slot  $P$ -pole FSCW stators with  $S_{pp} = 3/(9k \pm 2)$  and  $k = 1, 3, 5, \dots$
- **Category “E”:**  $Q$ -slot  $P$ -pole FSCW stators with  $S_{pp} = 3/(9k \pm 1)$  and  $k = 1, 3, 5, \dots$

General expressions are found in the following for the spatial MMF distribution of these stator categories.

*Category “A” FSCW Stators:*  $S_{pp} = 1/(3k \pm 1)$  and  $k = 1, 3, 5, \dots$

Some example stator classes that fall under this category are:

$Q$ -slot  $P$ -pole FSCW stators with  $S_{pp} = 1/2, 1/4, 1/8, 1/10, 1/14, 1/16, \dots$

The base winding layout for this stator category has 6 slots with its winding arrangement and spatial MMF distribution as shown in Fig. 2.7a and b, respectively. Due to the presence of an even number of pole-pairs in the base winding layout of this stator class, the polarities of the coils in the coil pair are in the same

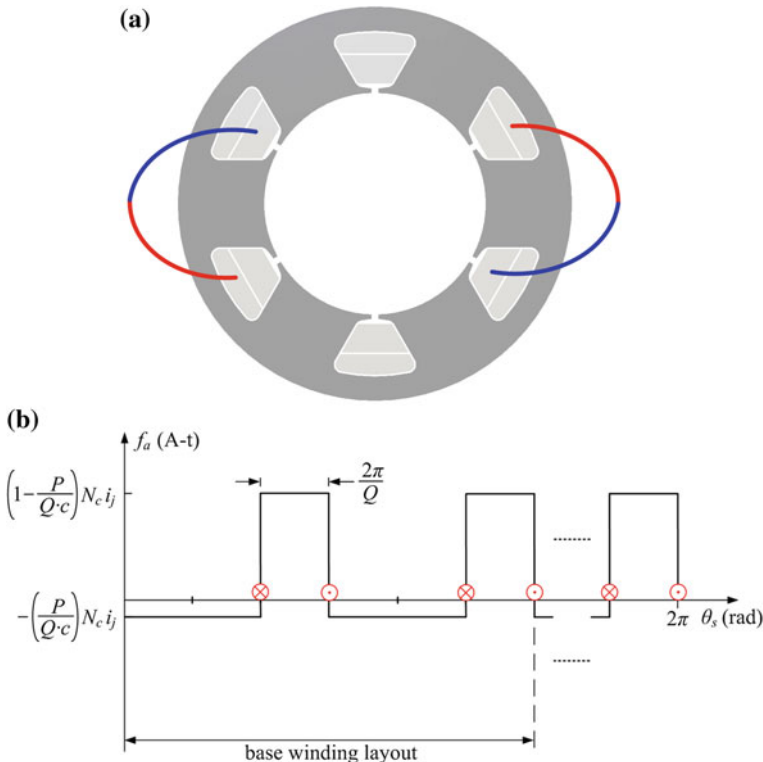


**Fig. 2.7** Category “A” FSCW stator. **a** Base winding layout. **b** Single-phase Spatial MMF distribution

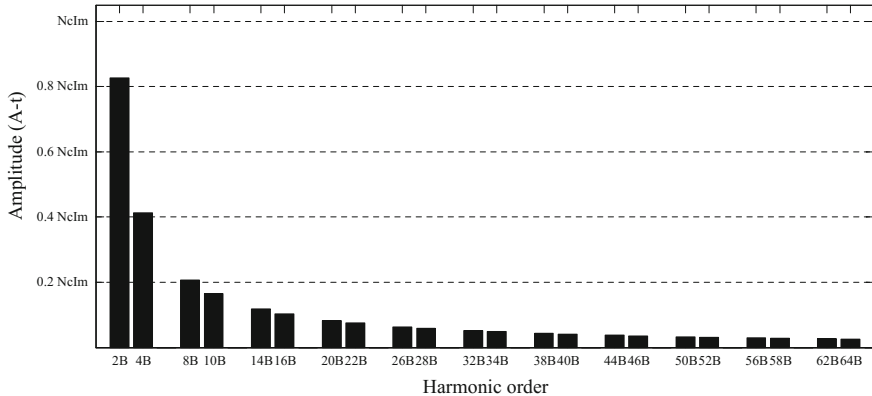


**Fig. 2.8** Harmonic spectrum of the total MMF produced by FSCW stators of category “A”. The multiplier B equals to  $P/2c$

direction to produce even spatial MMF harmonics in the airgap. A general expression for the single-phase spatial MMF harmonic amplitude for category “A” FSCW stators can be found from (2.16) as follows:

$$F_{j,n} = \frac{P}{2c} \frac{4N_c i_j}{n\pi} \sin\left(\frac{n\pi}{Q}\right), \quad n = \frac{2P}{2c}, \frac{4P}{2c}, \frac{6P}{2c}, \dots \quad (2.34)$$

The spatial harmonic amplitudes of the total MMF obtained from (2.31) and (2.34) for a  $Q$ -slot  $P$ -pole FSCW stator of category “A” is shown in Fig. 2.8. Evidently, only even spatial MMF harmonics that are a multiple of  $P/2c$  are present in the harmonic spectrum of the base-winding layout of category “A” FSCW stators. Moreover, triplen harmonics of the single phase MMFs are cancelled in the total MMF of the stator.

*Category “B” FSCW Stators:*  $S_{pp} = 1/(3k \pm 1)$  and  $k = 2, 4, 6, \dots$

Some example stator classes that fall under this category are:

$Q$ -slot  $P$ -pole FSCW stators with  $S_{pp} = 1/5, 1/7, 1/11, 1/13, 1/17, 1/19, \dots$

The base winding layout for this stator category represents 6 slots. The base winding layout and spatial MMF distribution for this category of FSCW stators are illustrated in Fig. 2.9a and b, respectively. The base winding layout of this category of stators has an odd number of pole-pairs, thus the coil polarities of the coil pair are in the opposite direction. A general expression describing the single-phase spatial MMF harmonic amplitudes for category “B” FSCW stators can be obtained based on (2.16) as follows:

$$F_{j,n} = \frac{P}{2c} \frac{4N_c i_j}{n\pi} \sin\left(\frac{n\pi}{Q}\right), \quad n = \frac{P}{2c}, \frac{3P}{2c}, \frac{5P}{2c}, \dots \quad (2.35)$$

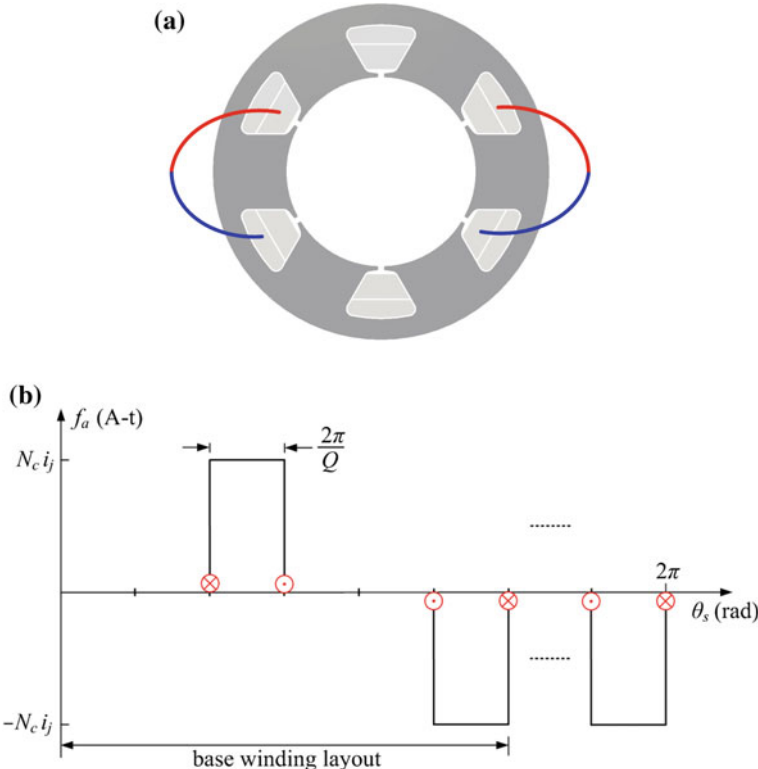


**Fig. 2.9** Category “B” FSCW stator. **a** Base winding layout. **b** Single-phase Spatial MMF distribution

Harmonic spectrum of the total spatial MMF distribution of category “B” FSCW stators obtained from (2.31) and (2.35) for a  $P$ -pole  $Q$ -slot stator is illustrated in Fig. 2.10. It is observed that only spatial MMF harmonics with orders that are odd multiples of  $P/2c$  are present in the base winding layout of category “B” FSCW stators. In Fig. 2.10 triplen harmonics of the single phase MMFs are cancelled in the total MMF of the stator.

*Category “C” FSCW Stators:*  $S_{pp} = 2/(6k \pm 1)$  and  $k = 1, 3, 5, \dots$

Some example FSCW stator classes for this category are:

$Q$ -slot  $P$ -pole FSCW stators with  $S_{pp} = 2/5, 2/7, 2/17, 2/19, 2/29, 2/31, \dots$

The base winding layout for this stator category has 12 slots. This category of FSCW stators has an odd number of pole-pairs in its base winding layout; hence coil polarities in its coil pairs should be of opposite direction, as shown in the base winding layout of Fig. 2.11a. The spatial MMF distribution of such layout is shown in Fig. 2.11b. A general expression describing the spatial MMF distribution of a  $Q$ -slot  $P$ -pole FSCW stator, as shown in Fig. 2.11b, is derived in the following.

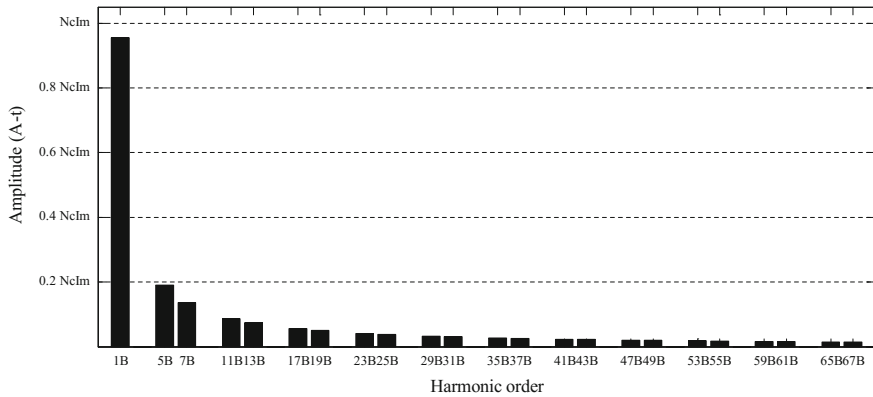


**Fig. 2.10** Harmonic spectrum of the total MMF produced by FSCW stators of category “B”. The multiplier B equals to  $P/2c$

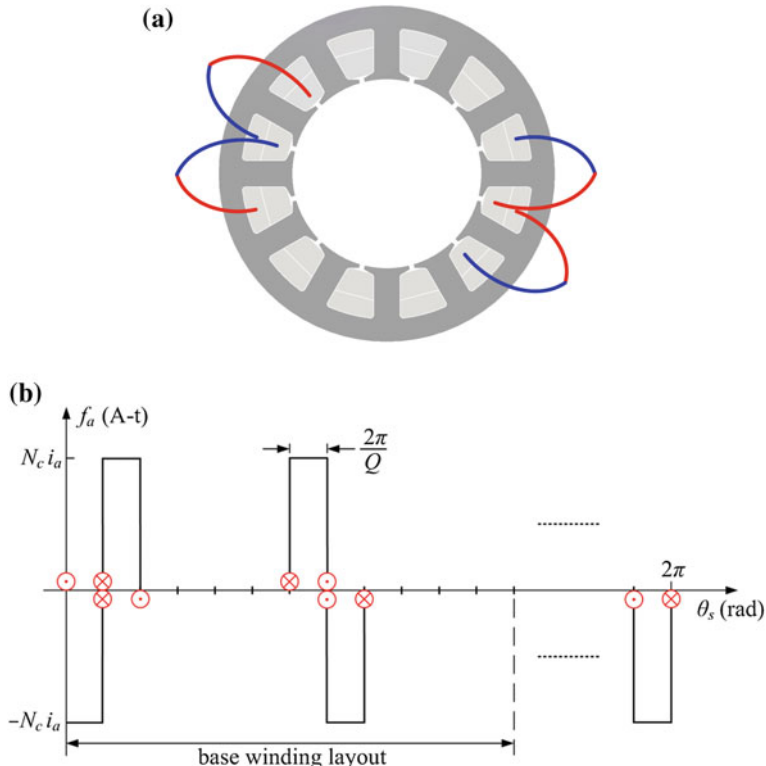


**Fig. 2.11** Category “C” FSCW stator. **a** Base winding layout. **b** Single-phase Spatial MMF distribution

The spatial displacement between the adjacent coils in a FSCW stator equals to  $2\pi/Q$ . The single-phase spatial MMF distribution is obtained by adding the MMF of all the coil-pairs shown in Fig. 2.11, as described by (2.16) as follows:

$$f_j = -\frac{P}{2c} \sum_n \frac{4N_c i_j}{n\pi} \sin\left(\frac{n\pi}{Q}\right) \left( \cos(n\theta_s - n\frac{\pi}{Q}) + \cos(n\theta_s - n\frac{15\pi}{Q}) \right), \quad (2.36)$$

$$n = \frac{P}{2c}, \frac{3P}{2c}, \frac{5P}{2c}, \dots$$

Simplification of (2.36) yields:

$$f_j = -\frac{P}{2c} \sum_n \frac{4N_c i_j}{n\pi} \sin\left(\frac{n\pi}{Q}\right) \left( 2 \cos\left(\frac{7\pi}{Q}n\right) \right) \cos(n\theta_s - n\frac{8\pi}{Q}), \quad (2.37)$$

$$n = \frac{P}{2c}, \frac{3P}{2c}, \frac{5P}{2c}, \dots$$

A comparison between (2.37) and (2.33) yields the following general equation for the spatial MMF harmonic amplitudes of category “C” FSCW stators:

$$F_{j,n} = \frac{P}{2c} \frac{4N_c i_j}{n\pi} \sin\left(\frac{n\pi}{Q}\right) \left( 2 \cos\left(\frac{7\pi}{Q}n\right) \right), \quad (2.38)$$

$$n = \frac{P}{2c}, \frac{3P}{2c}, \frac{5P}{2c}, \dots$$

The harmonic spectrum of the total MMF of a  $P$ -pole  $Q$ -slot FSCW stator of category “C” can be obtained from (2.31) and (2.38) as shown in Fig. 2.12. In this figure, only harmonics where their order is an odd multiple of  $P/2c$  are present. It is

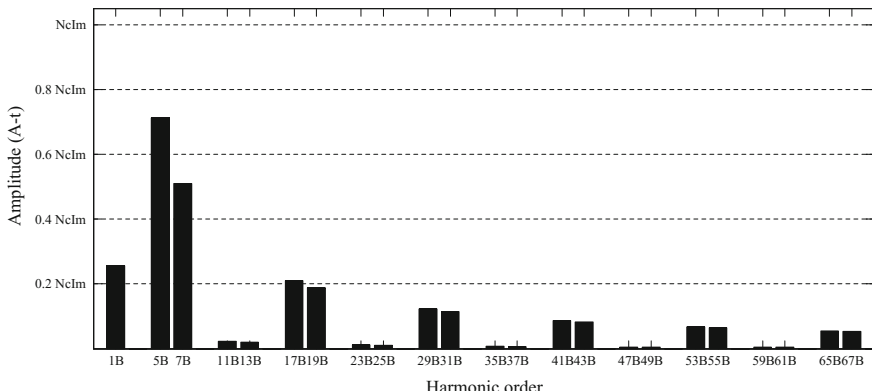


**Fig. 2.12** Harmonic spectrum of the total MMF produced by FSCW stators of category “C”. The multiplier B equals to  $P/2c$

observed in Fig. 2.12 that the triplen harmonics of the single-phase MMFs are cancelled in the total MMF of the machine.

*Category “D” FSCW Stators:*  $S_{pp} = 3/(9k \pm 2)$  and  $k = 1, 3, 5, \dots$

Some example FSCW stator classes for this category are:

$Q$ -slot  $P$ -pole FSCW stators with  $S_{pp} = 3/7, 3/11, 3/25, 3/29, 3/43, 3/47, \dots$

The base winding layout and spatial MMF distribution for this FSCW stator category is shown in Fig. 2.13a and b, respectively. The number of slots in the base winding layout of this FSCW stator category is 18. This FSCW stator category features an odd number of pole-pairs in its base winding layout. Therefore, only odd spatial MMF harmonics are expected in the base winding layout resulting in coil polarities in a coil pair to be in opposite direction, as shown in Fig. 2.13a.

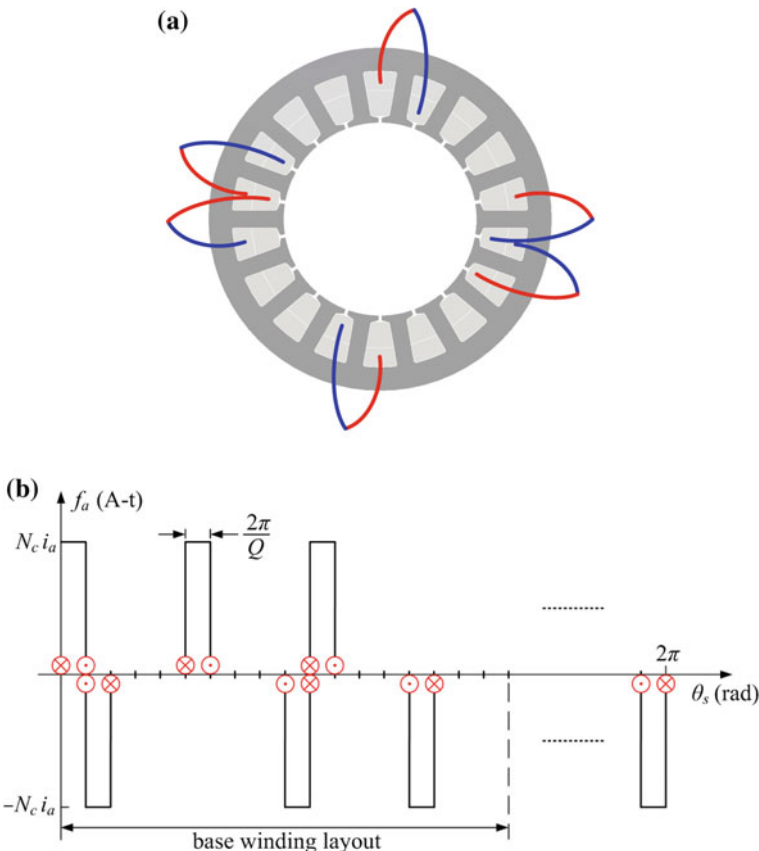


**Fig. 2.13** Category “D” FSCW stator. **a** Base winding layout. **b** Single-phase Spatial MMF distribution

The single-phase spatial MMF distribution is obtained by adding the MMF of all the coil-pairs shown in Fig. 2.13:

$$f_j = \frac{P}{2c} \sum_n \frac{4N_c i_j}{n\pi} \sin\left(\frac{n\pi}{Q}\right) \left( \cos(n\theta_s - n\frac{\pi}{Q}) + \cos(n\theta_s - n\frac{11\pi}{Q}) + \cos(n\theta_s - n\frac{21\pi}{Q}) \right), \quad n = \frac{P}{2c}, \frac{3P}{2c}, \frac{5P}{2c}, \dots \quad (2.39)$$

Simplifying (2.39) gives:

$$f_j = \frac{P}{2c} \sum_n \frac{4N_c i_j}{n\pi} \sin\left(\frac{n\pi}{Q}\right) \left( 1 + 2 \cos\left(\frac{10\pi}{Q}n\right) \right) \cos(n\theta_s - n\frac{11\pi}{Q}) \quad (2.40)$$

$$n = \frac{P}{2c}, \frac{3P}{2c}, \frac{5P}{2c}, \dots$$

A comparison between (2.40) and (2.33) yields the following expression for the spatial MMF harmonic amplitudes of category “D” FSCW stators:

$$F_{j,n} = \frac{P}{2c} \frac{4N_c i_j}{n\pi} \sin\left(\frac{n\pi}{Q}\right) \left( 1 + 2 \cos\left(\frac{10\pi}{Q}n\right) \right), \quad n = \frac{P}{2c}, \frac{3P}{2c}, \frac{5P}{2c}, \dots \quad (2.41)$$

Harmonic spectrum of the three-phase spatial MMF distribution for a  $P$ -slot  $Q$ -pole category “D” FSCW stator is obtained from (2.31) and (2.41) as shown in Fig. 2.14. It can be observed that the triplen harmonics are eliminated in the total MMF of the machine. Moreover, only harmonics that are an odd multiple of  $P/2c$  are present in the total MMF of category “D” FSCW stators.

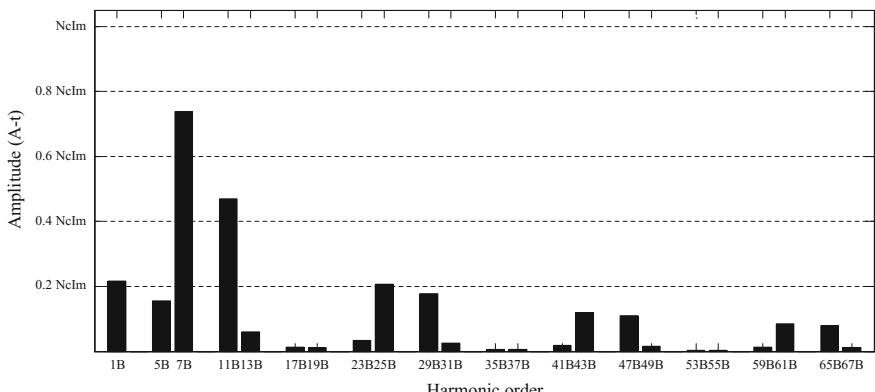


**Fig. 2.14** Harmonic spectrum of the total MMF produced by FSCW stators of category “D”. The multiplier B equals to  $P/2c$

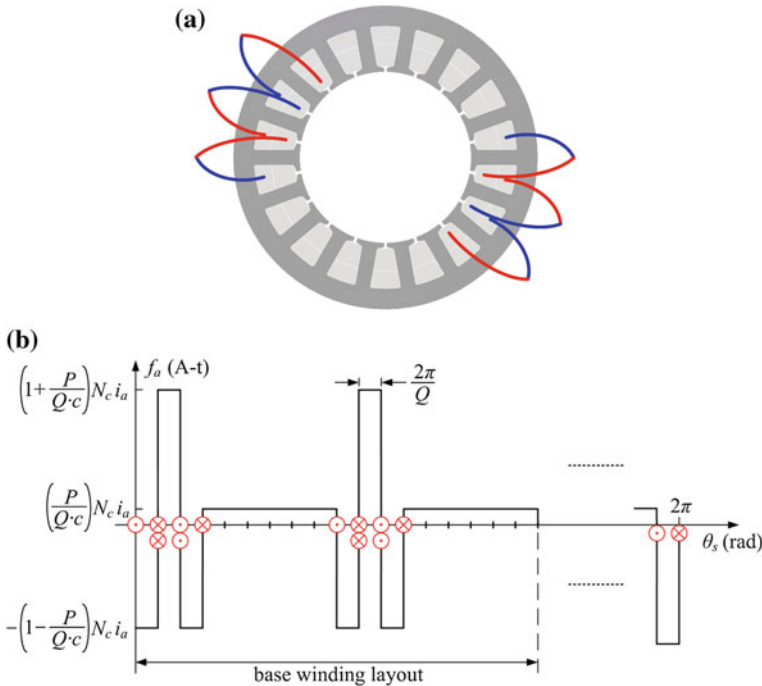


**Fig. 2.15** Category “E” FSCW stator. **a** Base winding layout. **b** Single-phase Spatial MMF distribution

*Category “E” FSCW Stators:*  $S_{pp} = 3/(9k \pm 1)$  and  $k = 1, 3, 5, \dots$

Some example FSCW stator classes for this category are:

$Q$ -slot  $P$ -pole FSCW stators with  $S_{pp} = 3/8, 3/10, 3/26, 3/28, 3/44, 3/46, \dots$

The base winding layout for this stator category has 18 slots as shown in Fig. 2.15a. The spatial MMF distribution for a  $Q$ -slot  $P$ -pole FSCW stator of category “E” is shown in Fig. 2.15b. There is an even number of pole-pairs in the base winding layout; thus, only even spatial harmonics are expected. This explains the same polarity of the coils in the coil pairs of the base winding layout of Fig. 2.15.

The spatial displacement between the adjacent coils is  $2\pi/Q$  mechanical radians. The single-phase spatial MMF distribution is obtained by adding the MMF of all the coil-pairs shown in Fig. 2.15, as described by (2.16) as follows:

$$f_j = -\frac{P}{2c} \sum_n \frac{4N_c i_j}{n\pi} \sin\left(\frac{n\pi}{Q}\right) \left( \cos(n\theta_s - n\frac{\pi}{Q}) - \cos(n\theta_s - n\frac{3\pi}{Q}) + \cos(n\theta_s - n\frac{5\pi}{Q}) \right), \quad n = \frac{2P}{2c}, \frac{4P}{2c}, \frac{6P}{2c}, \dots \quad (2.42)$$

Simplifying the above equation gives:

$$f_j = \frac{P}{2c} \sum_n \frac{4N_c i_j}{n\pi} \sin\left(\frac{n\pi}{Q}\right) \left( 1 - 2 \cos\left(\frac{2\pi}{Q}n\right) \right) \cos(n\theta_s - n\frac{3\pi}{Q}) \quad (2.43)$$

$$n = \frac{2P}{2c}, \frac{4P}{2c}, \frac{6P}{2c}, \dots$$

A comparison between (2.43) and (2.33) yields the following expression for the spatial MMF harmonic amplitudes of category “E” FSCW stators:

$$F_{j,n} = \frac{P}{2c} \frac{4N_c i_j}{n\pi} \sin\left(\frac{n\pi}{Q}\right) \left( 1 - 2 \cos\left(\frac{2\pi}{Q}n\right) \right), \quad n = \frac{2P}{2c}, \frac{4P}{2c}, \frac{6P}{2c}, \dots \quad (2.44)$$

The harmonic spectrum of the three-phase spatial MMF distribution for a  $P$ -slot  $Q$ -pole category “E” FSCW stator is obtained from (2.31) and (2.44) as shown in Fig. 2.16. It can be observed that the triplen harmonics are eliminated in the total MMF of the machine. Moreover, only harmonics that are an even multiple of  $P/2c$  are present in the total MMF of category “E” FSCW stators.

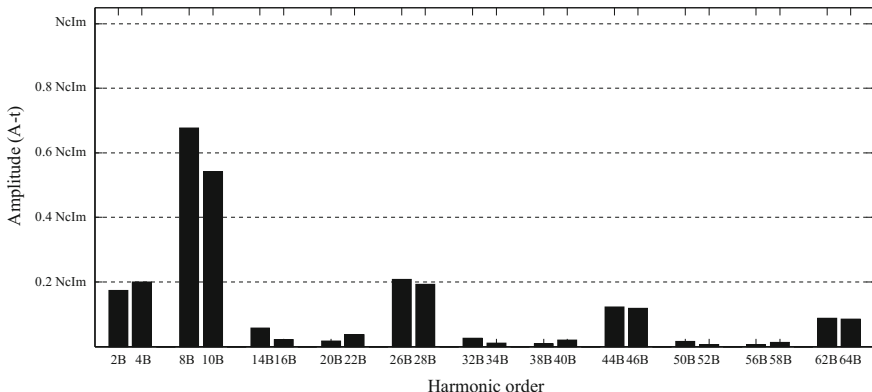


**Fig. 2.16** Harmonic spectrum of the total MMF produced by FSCW stators of category “E”. The multiplier B equals to  $P/2c$

## 2.4 Fault-Tolerant Capability in FSCW Machines

The FSCW stator topology [10] has the following fault-tolerance features:

- Physical separation (no overlapping) of the phase windings
- A high self-inductance to limit short circuit currents
- A low mutual inductance to magnetically decouple the phases

Physical separation of the phase windings prevents from phase-to-phase short-circuit faults. This can be ultimately achieved in single-layer FSCW stators since each slot is filled with the conductors of the same winding. In comparison to single-layer FSCW stators, double-layer FSCW stators are less immune to such faults; however they still represent superior fault-tolerance capability compared with DW stators, since their end-windings do not overlap and their slot number is much smaller.

A high self-inductance helps to limit short-circuit currents in the machine. The slot-leakage inductance and air-gap leakage inductance are quite high in FSCW machines. This high inductance increases the winding reactance. Therefore, in case of occurrence of a short-circuit fault, this high reactance may prevent damaging currents in the machine windings. The self-inductance can be increased with proper selection of the FSCW stator class.

A low mutual-inductance is necessary to magnetically decouple the machine phases. This avoids healthy phases from becoming affected by faulty phases. A low mutual inductance can be obtained with the right choice of slots and poles in FSCW stators. Mutual inductance between phase  $x$  and phase  $y$  windings is expressed as [6]:

$$M_{xy}(\theta_r) = \mu_0 r_g l_{eff} \int_0^{2\pi} \frac{w_x(\theta_s) w_y(\theta_s)}{g(\theta_r)} d\theta_s \quad (2.45)$$

where  $r_g$  is the average air-gap radius,  $l_{eff}$  is the active axial length of the machine, and  $g$  is the air-gap function.

If the two phases are magnetically decoupled, (2.45) returns a non-zero value. As discussed in the previous sections, in FSCW machines with an even number of pole-pairs in their base winding layout, the MMF produced by a phase winding is non-zero in all angles around the stator circumference. This makes a magnetic connection between the individual phases as their spatial MMF distributions overlap, resulting in a non-zero value for (2.45). However, with an odd number of pole pairs in the base winding layout, the MMF associated to a phase winding is non-zero only in areas underneath the phase winding's teeth. Therefore, the spatial MMF distributions of the phase windings do not overlap resulting in the integral in (2.45) to become zero. In such cases, the mutual inductance reduces to small

leakage terms. Therefore, to the aim of increasing the fault-tolerance capability by decreasing the mutual inductance, FSCW stator classes with an odd number of pole pairs are preferable. These stator classes are those that have an odd value of  $c$  in the denominator of  $S_{pp}$ .

Among the five common FSCW stator categories discussed in Sect. 2.3.3, only FSCW stators that belong to Categories B, C, and D are suitable candidates for fault-tolerant applications as their single-phase spatial MMF distributions do not overlap.

## 2.5 Formulation of the Harmonic Winding Factors

The rotating rotor PM flux in a PMSM does not intersect all the coils in a phase winding simultaneously. This results in a phase displacement in the induced voltages in the different coils. The sum of all the coil voltage phasors results in the total induced voltage phasor of the phase winding with an amplitude lower than when all the coil voltage phasors are in-phase. In a FSCW machine, in addition to the first harmonic, higher order harmonics are also induced in the back-EMF. The weight of each back-EMF harmonic is accounted for by the harmonic winding factors in the back-EMF equation. Harmonic winding factors have a positive value smaller than unity, strictly depend on  $S_{pp}$  and determine the efficiency of the coil arrangement in terms of torque production capability in a phase winding. The main harmonic winding factor which corresponds to the main spatial MMF harmonic can be considered as the effective number of turns affecting the machine performance characteristics. A high value for the main harmonic winding factor is always desired.

Several approaches have been proposed for calculation of the harmonic winding factors:

- Calculation of the main harmonic winding factor using the “*star of slot*” of EMF phasors as described in [11].
- Calculation of the harmonic winding factors using closed form expressions as a product of the distribution factor and pitch factor as detailed in [12].
- Calculation of the harmonic winding factors based on the winding function theory [13].

The latter method combined with the results of Sect. 2.3.3 enables the formulation of a systematic approach for derivation of a single lumped expression for calculation of the harmonic winding factors for each of the stator categories introduced in Sect. 2.3.3.

In an  $m$ -phase machine the weight of each spatial winding function harmonic in the back-EMF is obtained by dividing their amplitude by a scaling factor, resulting in the associated harmonic winding factor [13]:

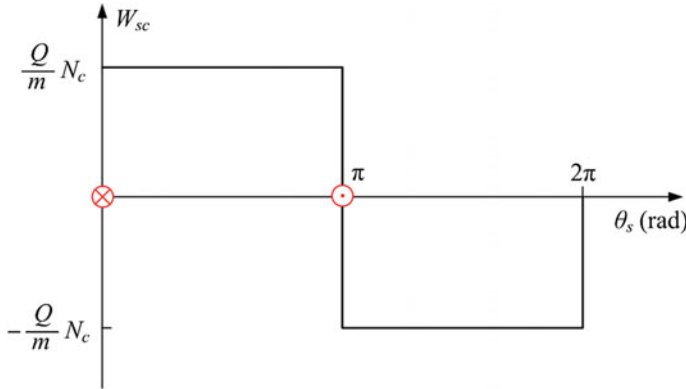


**Fig. 2.17** Winding function for a hypothetical stator winding that has a single coil with  $N_c Q/m$  turns which spans  $\pi$  radians around the stator circumference

$$k_{w,n} = \frac{W_n}{W_{sc,n}}, \quad n = \frac{kP}{2c} \quad (2.46)$$

In the above equation,  $k$  is determined from the number of pole-pairs in the base winding layout of a stator class, as defined in (2.16), and  $W_{sc,n}$  is the scaling factor for the  $n$ th spatial winding function harmonic.  $W_{sc,n}$  is considered as the amplitude of the  $n$ th spatial harmonic of the winding function for a hypothetical stator winding that has a single coil with  $N_c Q/m$  turns which spans  $\pi$  radians around the stator circumference, as shown in Fig. 2.17.  $W_{sc,n}$  can be found from the Fourier decomposition of the square wave of Fig. 2.17, as follows:

$$W_{sc,n} = \frac{2QN_c}{mn\pi} \quad (2.47)$$

Three-phase stator topologies for use in PMSMs are assessed based on their main harmonic winding factor that is associated with the main spatial harmonic of their winding function.

Harmonic winding factors for the different FSCW stator categories introduced in Sect. 2.3.3 are found from (2.46) as follows:

*Category “A” FSCW Stators:*  $S_{pp} = 1/(3k \pm 1)$  and  $k = 1, 3, 5, \dots$

$$k_{w,n} = \frac{P}{2c} \frac{6}{Q} \sin\left(\frac{n\pi}{Q}\right), \quad n = \frac{2P}{2c}, \frac{4P}{2c}, \frac{6P}{2c}, \dots \quad (2.48)$$

*Category “B” FSCW Stators:*  $S_{pp} = 1/(3k \pm 1)$  and  $k = 2, 4, 6, \dots$

$$k_{w,n} = \frac{P}{2c} \frac{6}{Q} \sin\left(\frac{n\pi}{Q}\right), \quad n = \frac{P}{2c}, \frac{3P}{2c}, \frac{5P}{2c}, \dots \quad (2.49)$$

*Category “C” FSCW Stators:*  $S_{pp} = 2/(6k \pm 1)$  and  $k = 1, 3, 5, \dots$

$$\begin{aligned} k_{w,n} &= \frac{P}{2c} \frac{6}{Q} \sin\left(\frac{n\pi}{Q}\right) \left( 2 \cos\left(\frac{7\pi}{Q}n\right) \right), \\ n &= \frac{P}{2c}, \frac{3P}{2c}, \frac{5P}{2c}, \dots \end{aligned} \quad (2.50)$$

*Category “D” FSCW Stators:*  $S_{pp} = 3/(9k \pm 2)$  and  $k = 1, 3, 5, \dots$

$$k_{w,n} = \frac{P}{2c} \frac{6}{Q} \sin\left(\frac{n\pi}{Q}\right) \left( 1 + 2 \cos\left(\frac{10\pi}{Q}n\right) \right), \quad n = \frac{P}{2c}, \frac{3P}{2c}, \frac{5P}{2c}, \dots \quad (2.51)$$

*Category “E” FSCW Stators:*  $S_{pp} = 3/(9k \pm 1)$  and  $k = 1, 3, 5, \dots$

$$k_{w,n} = \frac{P}{2c} \frac{6}{Q} \sin\left(\frac{n\pi}{Q}\right) \left( 1 - 2 \cos\left(\frac{2\pi}{Q}n\right) \right), \quad n = \frac{2P}{2c}, \frac{4P}{2c}, \frac{6P}{2c}, \dots \quad (2.52)$$

The harmonic winding factors of category “A” to category “E” FSCW stators are calculated using (2.48)–(2.52) as illustrated in Figs. 2.18, 2.19, 2.20, 2.21 and 2.22. The main harmonic winding factor in these figures are of order  $v = P/2$ . A high value of the main harmonic winding factor close to unity indicates better utilization of the windings, a higher flux linkage, a higher back-EMF and a higher torque density.

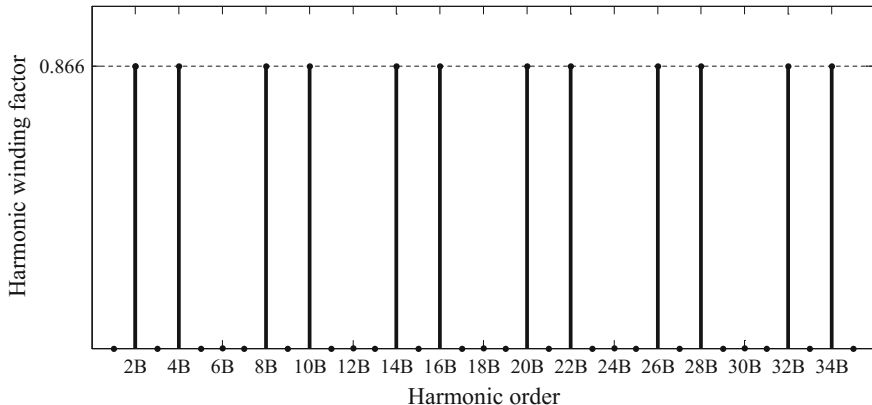


**Fig. 2.18** Harmonic winding factors of FSCW stators of category “A”. The multiplier B equals to  $P/2c$ . The main harmonic winding factor is of order  $v = P/2$ , i.e. 2B, 4B, 8B, 10B, ...

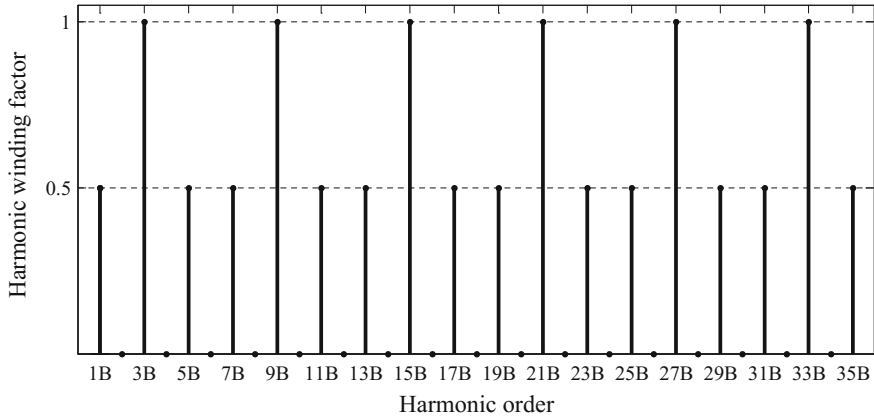


**Fig. 2.19** Harmonic winding factors of FSCW stators of category “B”. The multiplier B equals to  $P/2c$ . The main harmonic winding factor is of order  $v = P/2$ , i.e. 1B, 5B, 7B, 11B, ...

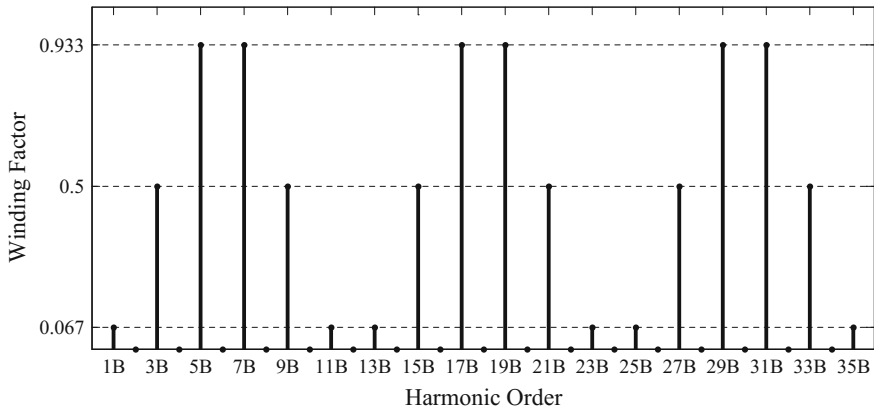


**Fig. 2.20** Harmonic winding factors of FSCW stators of category “C”. The multiplier B equals to  $P/2c$ . The main harmonic winding factor is of order  $v = P/2$ , i.e. 5B, 7B, 17B, 19B, ...

In Figs. 2.18, 2.19, 2.20, 2.21 and 2.22, for a given combination of slots and poles, harmonic winding factors that have the same value as the main harmonic winding factor are associated with the “*slot harmonics*” of the MMF and are of order [14]:

$$n = kQ \pm P/2, \quad k = 0, 1, 2, 3, \dots \quad (2.53)$$

Slot harmonics could either be sub-harmonics or higher order harmonics with respect to the main harmonic. For a given FSCW stator, slot harmonics indicate alternative rotors with a different number of pole pairs that can be utilized with the

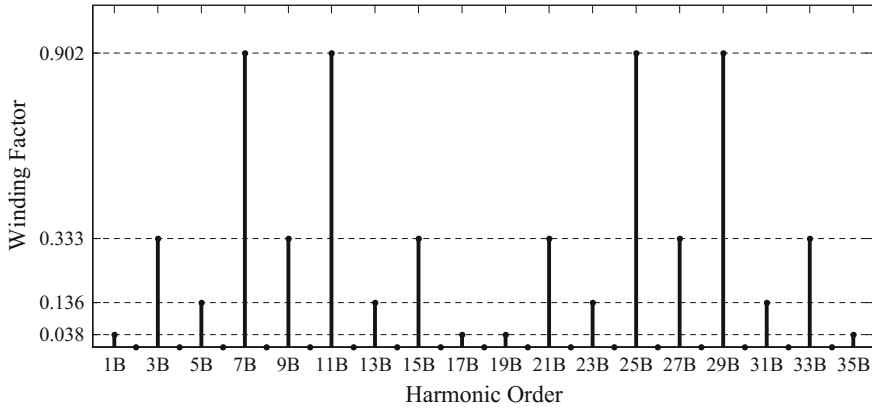


**Fig. 2.21** Harmonic winding factors of FSCW stators of category “D”. The multiplier B equals to  $P/2c$ . The main harmonic winding factor is of order  $v = P/2$ , i.e.  $7B, 11B, 25B, 29B, \dots$

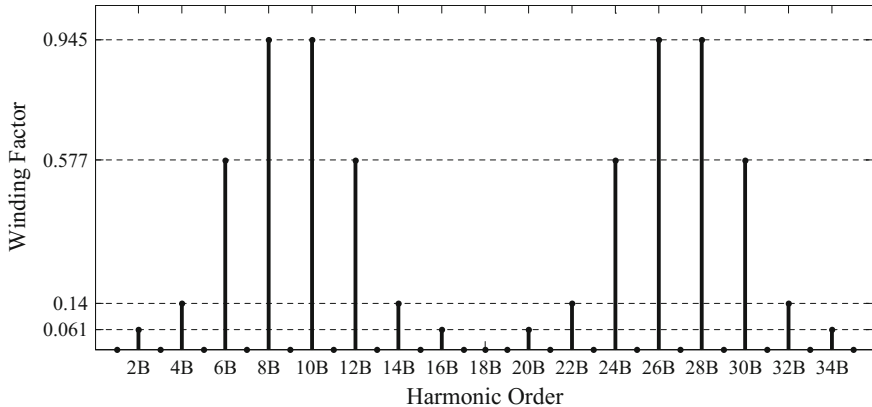


**Fig. 2.22** Harmonic winding factors of FSCW stators of category “E”. The multiplier B equals to  $P/2c$ . The main harmonic winding factor is of order  $v = P/2$ , i.e.  $8B, 10B, 26B, 28B, \dots$

same stator and would result in the same value for the main harmonic winding factor. These alternative stator classes belong to the same stator category. Table 2.1 summarizes the main harmonic winding factor for double-layer FSCW stators of different class and categories. The stator classes that have a high main harmonic winding factor are shown with a bold line in this table. Among the stator classes of Table 2.1, the 5/14 stator class has the highest main harmonic winding factor equal to 0.951. The 4/11 and 4/13 stator classes stand at the second place with the main harmonic winding factor of 0.949. FSCW stator classes that belong to category “E” with a main harmonic winding factor of 0.945 have the third highest main harmonic winding factor among other stator classes. All these stator classes represent a high

**Table 2.1** Main harmonic winding factor for different classes of double-layer FSCW PMSM

$P \setminus Q$		4	8	10	14	16	20	22	26	28
6	$S_{pp}$	1/2	1/4	1/5	1/7	1/8	1/10	1/11	1/13	1/14
	$k_{w,(P/2)}$	0.866	0.866	0.5	0.5	0.866	0.866	0.5	0.5	0.866
	LCM	12	24	30	42	48	60	66	78	84
12	$S_{pp}$		1/2	2/5	2/7	1/4	1/5	2/11	2/13	1/7
	$k_{w,(P/2)}$		0.866	0.933	0.933	0.866	0.5	0.25	0.25	0.5
	LCM		24	60	84	48	60	132	156	84
18	$S_{pp}$		3/4	3/5	3/7	3/8	3/10	3/11	3/13	3/14
	$k_{w,(P/2)}$		0.617	0.735	0.902	0.945	0.945	0.902	0.735	0.617
	LCM		72	90	126	144	180	198	234	252
24	$S_{pp}$			4/5	4/7	1/2	2/5	4/11	4/13	2/7
	$k_{w,(P/2)}$			0.583	0.760	0.866	0.933	0.949	0.949	0.933
	LCM			120	168	48	120	264	312	168
30	$S_{pp}$				5/7	5/8	1/2	5/11	5/13	5/14
	$k_{w,(P/2)}$				0.640	0.711	0.866	0.874	0.936	0.951
	LCM				210	240	60	330	390	420
36	$S_{pp}$				6/7	3/4	3/5	6/11	6/13	3/7
	$k_{w,(P/2)}$				0.548	0.617	0.735	0.783	0.867	0.902
	LCM				252	144	180	396	468	252
42	$S_{pp}$					7/8	7/10	7/11	7/13	1/2
	$k_{w,(P/2)}$					0.538	0.650	0.701	0.790	0.866
	LCM					336	420	462	546	84
48	$S_{pp}$						4/5	8/11	8/13	4/7
	$k_{w,(P/2)}$						0.583	0.630	0.718	0.760
	LCM						240	528	624	336
54	$S_{pp}$							9/10	9/13	9/14
	$k_{w,(P/2)}$							0.525	0.656	0.695
	LCM							540	702	756

	Category “A”
	Category “B”
	Category “D”
	Category “E”
	Category “C”
	Invalid

value for LCM which indicates the possibility of achieving a low cogging torque. The base winding layout for the 5/14 stator class has 28 poles, whereas the base winding layout of the 4/11 and 4/13 stator classes represent 22 poles and 26 poles, respectively. This indicates that these stator classes are suitable for low speed applications as they feature a high number of poles and a low cogging torque. The category “E” stator classes have an even number of pole pairs and therefore do not present a favorable fault-tolerance capability due to their relatively high mutual inductance. For FSCW stators with a high synchronous speed, only category “C” and “D” are suitable candidates as their base winding layouts have 14 poles and 10 poles, respectively and their mutual inductances are limited to leakage inductance

terms only. Table 2.1 indicates that as the number of poles increases, achieving a FSCW stator class with a higher main harmonic winding factor becomes possible. Moreover, such stator classes would represent a high value for LCM which represents the possibility of a lower cogging torque.

The spatial MMF harmonics in a FSCW stator result in core losses. The rotor loss density due to an MMF harmonic is proportional to the square of its peak electric loading which is in turn proportional to the associated harmonic winding factor. In electric machines, the main spatial MMF harmonic has the highest peak electric loading due to having the highest value for its associated winding factor. Similarly, the slot harmonics have the same peak electric loading as the main harmonic. Hence, the slot harmonics have a major contribution to the rotor losses [14, 15]. Reduction of the slot harmonic winding factors for a given FSCW stator class is not feasible.

### 2.5.1 MMF Expression as a Function of the Harmonic Winding Factor

It is common in machine analysis to express machine characteristics in terms of the harmonic winding factors. From (2.21) and (2.31), the amplitude of the total spatial MMF distribution for a three-phase machine can be expressed as:

$$F_n = \frac{3}{2} F_{j,n} = \frac{3}{2} W_n I_m, \quad n = \frac{P}{2c} (6k \pm b), \quad k = 0, 1, 2, 3, \dots \quad (2.54)$$

In a three-phase system, substituting (2.47) in (2.46) and solving it for  $W_n$  yields:

$$W_n = \frac{2}{3} \frac{QN_c}{n\pi} k_{w,n} \quad (2.55)$$

Substitution of (2.55) into (2.54) results in  $F_n$  as a function of the harmonic winding factors:

$$F_n = \frac{Q}{n\pi} N_c I_m k_{w,n}, \quad n = \frac{P}{2c} (6k \pm b), \quad k = 0, 1, 2, 3, \dots \quad (2.56)$$

## 2.6 Formulation of the Back-EMF

Back-EMF is generated due to the rotor PM flux linking the stator windings. For a counterclockwise rotating rotor, Fourier series is used to express the PM flux density as follows [8]:

$$B_{PM}(t, \theta_s) = \sum_{n=\frac{P}{2}k}^{\infty} B_{\max,n} \cos(n\omega_r t - n\theta_s), \quad k = 1, 3, 5, \dots \quad (2.57)$$

where  $\omega_r$  is the mechanical angular speed, and  $B_{\max,n}$  is the amplitude of the  $n$ th spatial harmonic component of the PM flux density and depends on the rotor structure. Equation (2.57) implies that all the spatial harmonics of the PM flux density are synchronous with the rotor movement. A study on the PM flux density and methods for its analytical calculation are presented in Chap. 4.

PM flux linkage for a phase winding is defined as the rotor flux that links all the coil turns of the winding and for phase  $j$  of an  $m$ -phase FSCW stator is given by:

$$\lambda_{PM,j} = r_g l_{eff} \int_0^{2\pi} w_j(\theta) B_{PM}(\theta, t) d\theta \quad (2.58)$$

Replacing (2.19) and (2.57) in (2.58) yields:

$$\begin{aligned} \lambda_{PM,j} &= r_g l_{eff} \int_0^{2\pi} \sum_{n=\frac{P}{2}k}^{\infty} W_n \cos(n\theta_s - n\theta_j) d\theta_s \\ &\quad \cdot \sum_{h=\frac{P}{2}k}^{\infty} B_{\max,h} \sin(h\omega_r t - h\theta_s) d\theta_s \end{aligned} \quad (2.59)$$

The above integral returns a non-zero value only when  $n = h$ :

$$\int_0^{2\pi} \cos(n\theta_s - n\theta_j) \sin(n\omega_r t - n\theta_s) d\theta_s = \pi \sin(n\omega_r t - n\theta_j) \quad (2.60)$$

Hence, (2.59) simplifies to:

$$\begin{aligned} \lambda_{PM,j} &= r_g l_{eff} \pi \sum_k^{\infty} W_{(P/2)k} B_{\max,(P/2)k} \sin\left(\frac{P}{2}k\omega_r t - \frac{P}{2}k\theta_j\right), \\ k &= 1, 3, 5, \dots \end{aligned} \quad (2.61)$$

Substituting (2.55) into (2.61) yields:

$$\begin{aligned} \lambda_{PM,j} &= r_g l_{eff} \frac{4}{3P} Q N_c \sum_k^{\infty} \frac{1}{k} k_{w,(P/2)k} B_{\max,(P/2)k} \sin\left(\frac{P}{2}k\omega_r t - \frac{P}{2}k\theta_j\right), \\ k &= 1, 3, 5, \dots \end{aligned} \quad (2.62)$$

The total number of turns in a phase winding in a three-phase system is equal to:

$$N_j = \frac{Q}{3} N_c \quad (2.63)$$

Therefore, (2.62) simplifies to:

$$\lambda_{PM,j} = \sum_k \lambda_{\max,k} \sin\left(\frac{P}{2}k\omega_r t - \frac{P}{2}k\theta_j\right), \quad k = 1, 3, 5, \dots \quad (2.64)$$

$$\lambda_{\max,k} = r_g l_{eff} \frac{4}{Pk} N_j k_{w,(P/2)k} B_{\max,(P/2)k} \quad (2.65)$$

where  $\lambda_{\max,k}$  is the amplitude of the  $k$ th PM flux linkage harmonic.

The induced back-EMF in phase  $j$  winding of the stator is obtained by using Faraday's Law:

$$e_j = -\frac{d\lambda_{PM,j}}{dt} \quad (2.66)$$

Substituting (2.65) in (2.66) yields:

$$e_j = \sum_k E_{\max,k} \cos\left(\frac{P}{2}k\omega_r t - \frac{P}{2}k\theta_j\right), \quad k = 1, 3, 5, \dots \quad (2.67)$$

$$E_{\max,k} = -2r_g l_{eff} \omega_r k_{w,(P/2)k} N_j B_{\max,(P/2)k} \quad (2.68)$$

where  $E_{\max,k}$  is the amplitude of the  $k$ th back-EMF harmonic. In a  $P$ -pole machine the rotational speed of the rotor is equal to:

$$\omega_r = \frac{\omega_e}{P/2} \quad (2.69)$$

where  $\omega_e$  is the frequency of the applied currents to the machine. Moreover,  $\theta_j$  which is in mechanical radians can be converted to electrical radians as follows:

$$\theta_{j,e} = \frac{P}{2}\theta_j \quad (2.70)$$

Substituting (2.69) and (2.70) into (2.67) yields:

$$e_j = \sum_k E_{\max,k} \cos(k\omega_e t - k\theta_{j,e}), \quad k = 1, 3, 5, \dots \quad (2.71)$$

where the phase angle  $\theta_{j,e}$  in three-phase systems is equal to 0,  $2\pi/3$  and  $-2\pi/3$  for phase  $a$ ,  $b$ , and  $c$ , respectively. From (2.68) it is observed that the air-gap PM flux density harmonics of order  $n = kP/2$  correspond to the  $k$ th order voltage harmonics in the generated back-EMF.

The above calculations showed that the only MMF spatial harmonics that participate in the generation of the back-EMF are those that have an equivalent component in the rotor PM flux density. These harmonics include the main spatial MMF harmonic of order  $v = P/2$ , and all other harmonics that their order is an odd multiple of the main harmonic order. In general, (2.68) indicates that the air-gap flux harmonic of order  $n = kP/2$  is responsible for generating the back-EMF harmonic of order  $k$ . The remaining spatial harmonics of the MMF participate in core losses and contribute to an increase in the machine inductance [16].

## 2.7 Case-Study: The Effect of the Slot and Pole Combination on the Back-EMF

The case-study presented in the following demonstrates the effect of slot and pole combination on the generated back-EMF of FSCW machines. Three FSCW machines that belong to category “B”, “C”, and “D” are studied. The studied machines are of the same size, dimensions, and synchronous speed. A 14-pole rotor with a single pole-pair PM flux density as shown in Fig. 2.23a is assumed. The normalized spatial harmonic spectrum of the rotor PM flux density is shown in Fig. 2.23b. The base speed for this rotor configuration is:

$$\omega_r = 44.9 \text{ rad/s} = 428.6 \text{ rpm} \quad (2.72)$$

Three stators are used with the 14-pole rotor:

- A 6-slot stator resulting in  $S_{pp} = 1/7$  (Category “B” FCSW stator)
- A 12-slot stator resulting in  $S_{pp} = 2/7$  (Category “C” FCSW stator)
- An 18-slot stator resulting in  $S_{pp} = 3/7$  (Category “D” FCSW stator)

The harmonic winding factors for these stator classes can be calculated using (2.49), (2.50), and (2.51), as shown in Fig. 2.19, Fig. 2.20, and Fig. 2.21, respectively. These stator classes have a main harmonic winding factor of 0.5, 0.933, and 0.902, respectively.

The generated line-to-neutral back-EMF harmonics by the above FSCW machines at the base speed of 428.6 rpm are calculated using (2.68) and compared as shown in Fig. 2.24. A comparison between the fundamental harmonics of the generated back-EMFs is shown in Fig. 2.24a, while other back-EMF harmonics are compared in Fig. 2.24b. It is observed that the machine that belongs to the 1/7

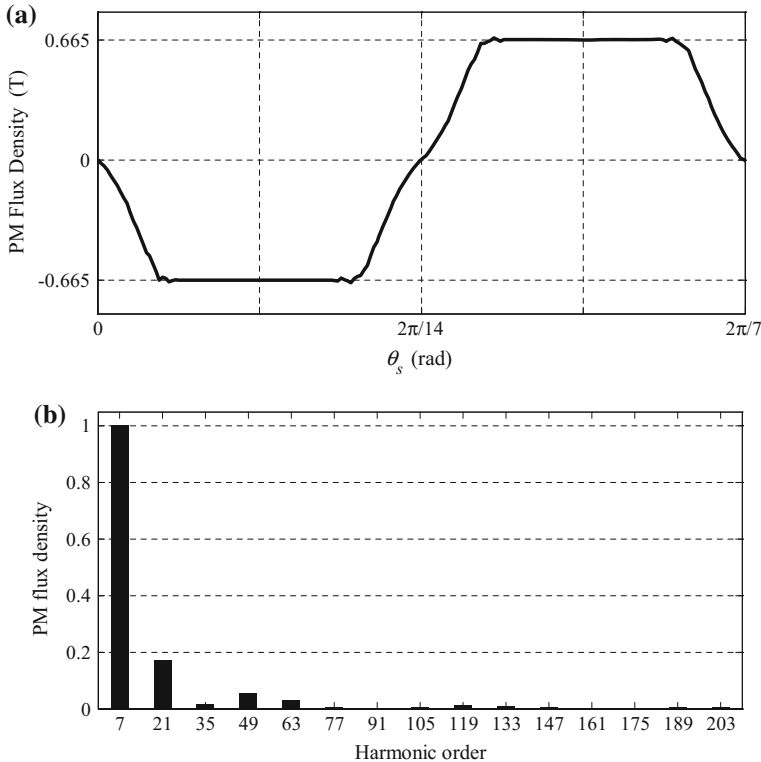


**Fig. 2.23** Rotor PM flux density. **a** Spatial distribution for a single pole-pair. **b** Normalized spatial harmonic spectrum

stator class is the least efficient due to its high harmonic content and smaller fundamental back-EMF harmonic which is caused by its low main harmonic winding factor. In the machines that belong to the 3/7 and 2/7 stator classes, the latter produces a back-EMF with a higher fundamental component due to its higher main harmonic winding factor. However, this comes at the price of a higher harmonic content in the back-EMF and consequently a higher total harmonic distortion (THD).

Knowledge of the harmonic component of the back-EMF is essential in the initial design stages since they directly contribute to the output torque. The design engineer must strike a compromise between the amplitude of the fundamental harmonic and the harmonic content of the back-emf, as they contribute to the average torque and torque ripple respectively, and select the most appropriate slot and pole combination for a given design specification.

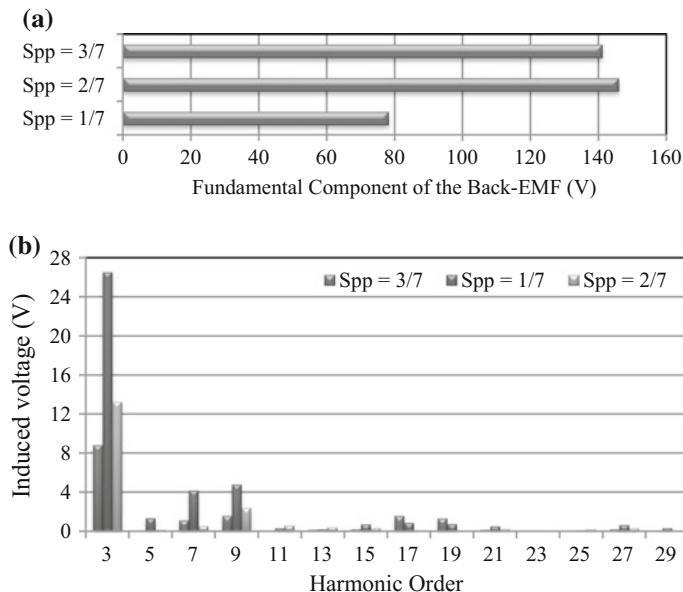


**Fig. 2.24** Line-to-neutral back-EMF harmonics of the 14-pole 6-slot, 14-pole 12-slot and 14-pole 18-slot FSCW machines. **a** Fundamental component. **b** Harmonic content

## 2.8 Conclusion

This chapter addressed the gap in the knowledge regarding the mathematical analysis and modelling of the generated MMF and back-EMF by FSCW PMSMs. First, design considerations for an optimal FSCW layout were discussed. A comprehensive mathematical analysis of the generated MMF by FSCW stators was then performed. FSCW stators were classified into different *classes* and *categories*. General formulas were proposed for the generated MMF and the harmonic winding factors of different FSCW stator categories. The generated back-EMF was then formulated as a function of the harmonic winding factors. Based on this analysis, fault tolerant capability of different stator categories was investigated.

The proposed general expressions for the MMF and harmonic winding factors of different FSCW categories are crucial for analytical calculations during the initial design stages of a FSCW PMSM. In particular they can be used for selecting the most appropriate slot and pole combination for a given application, and provide means of estimating the machine dimensions based on its speed and power ratings. Moreover, they are useful in predicting the harmonics of the machine's output characteristics such as electromagnetic torque.

A comparison between three FSCW PMSM topologies was also conducted to highlight the application of the proposed expressions in evaluation of the output characteristics of different FSCW stator classes.

## References

1. R. Islam, I. Husain, A. Fardoun, K. McLaughlin, Permanent-magnet synchronous motor magnet designs with skewing for torque ripple and cogging torque reduction. *IEEE Trans. Ind. Appl.* **45**, 152–160 (2009)
2. Z.Q. Zhu, D. Howe, Influence of design parameters on cogging torque in permanent magnet machines. *IEEE Trans. Energy Convers.* **15**, 407–412 (2000)
3. C. Sadarangani, *Electrical Machines-Design and Analysis of Introduction and Permanent Magnet Motors* (2006)
4. J.A. Guemes, A.M. Iraolagoitia, P. Fernández, M.P. Donsio, et al., Comparative study of PMSM with integer-slot and fractional-slot windings, in *2010 XIX International Conference on Electrical Machines (ICEM)* (2010), pp. 1–6
5. K.-H. Shin, J.-S. Yu, J.-Y. Choi, H.-W. Cho, Design and analysis of interior permanent magnet synchronous motor considering saturated rotor bridge using equivalent magnetic circuit. *J. Magn.* **19**, 404–410 (2014)
6. P.C. Krause, O. Wasynczuk, S.D. Sudhoff, S. Pekarek, *Analysis of Electric Machinery and Drive Systems*, vol. 75 (Wiley, 2013)
7. K. Huilin, Z. Libing, W. Jin, Harmonic winding factors and MMF analysis for five-phase fractional-slot concentrated winding PMSM, in *2013 International Conference on Electrical Machines and Systems (ICEMS)* (2013), pp. 1236–1241
8. M. Farshadnia, R. Dutta, J.E. Fletcher, K. Ahsanullah, M.F. Rahman, H.C. Lovatt, Analysis of MMF and back-EMF waveforms for fractional-slot concentrated-wound permanent magnet machines, in *Proceedings of the ICEM* (2014), pp. 1976–1982
9. L. Alberti, M. Barcaro, N. Bianchi, Design of a low-torque-ripple fractional-slot interior permanent-magnet motor. *IEEE Trans. Ind. Appl.* **50**, 1801–1808 (2014)
10. N. Bianchi, S. Bolognani, M.D. Pre, G. Grezzani, Design considerations for fractional-slot winding configurations of synchronous machines. *IEEE Trans. Ind. Appl.* **42**, 997–1006 (2006)
11. J. Pyrhonen, T. Jokinen, V. Hrabovcová, *Design of Rotating Electrical Machines* (Wiley, 2009)
12. A.O. Di Tommaso, F. Genduso, R. Miceli, A software for the evaluation of winding factor harmonic distribution in high efficiency electrical motors and generators, in *Proceedings of the EVER* (2013), pp. 1–6
13. R.F. Burbidge, A rapid method of analysing the m.m.f. wave of a single or polyphase winding. *Proc. IEE Part C: Monogr.* **105**, 307–311 (1958)
14. E. Fornasiero, N. Bianchi, S. Bolognani, Slot harmonic impact on rotor losses in fractional-slot permanent-magnet machines. *IEEE Trans. Ind. Electron.* **59**, 2557–2564 (2012)
15. N. Bianchi, E. Fornasiero, Index of rotor losses in three-phase fractional-slot permanent magnet machines. *Electr. Power Appl. IET* **3**, 381–388 (2009)
16. A.M. El-Refaie, Fractional-slot concentrated-windings synchronous permanent magnet machines: opportunities and challenges. *IEEE Trans. Ind. Electron.* **57**, 107–121 (2010)

# Chapter 3

## Design of Optimal Winding Layouts for Multiphase Fractional-Slot Concentrated-Wound Permanent Magnet Machines



### 3.1 Introduction

Performance characteristics of an electric machine strictly depend on its stator spatial MMF distribution that is determined by the stator winding layout. A FSCW stator could either be single-layer or double-layer; the double layer is preferred due to lower spatial MMF harmonics that result in less torque ripple and losses [1]. Multiphase machines could be realized with either a symmetrical or an asymmetrical winding layout, among which, the symmetrical winding layouts require a less complex control system and provide more reliable operation under faults associated with the drive system [2, 3]. Therefore, the scope of this chapter is limited to double-layer symmetrical windings for multiphase FSCW stators.

A heuristic algorithm for the systematic design of optimal winding layout for double-layer symmetrical multiphase FSCW PMSMs is proposed in this chapter that aims at maximizing the average torque by considering all the spatial MMF harmonics that contribute to average torque production. The proposed approach is based on the exhaustive mathematical modeling and analysis of the FSCW stator magnetic interactions detailed in Chap. 2.

With an increase in the number of phases, the number of valid winding configurations for a given combination of slots and poles significantly increases. A “winding performance index” is proposed for evaluation of the torque producing capability of each of the valid stator winding layouts.

Multiple case-studies are presented for the design of optimal multiphase concentrated-wound layouts. FEA and experimental results from a prototype FSCW PMSM are reported and used to validate the proposed analytical method.

### 3.2 Characteristics of an Optimal Winding Layout in Multiphase FSCW PMSM

Compared with three-phase FSCW PMSMs, multiphase FSCW PMSMs exhibit a relatively small torque ripple. Moreover, their fault-tolerance to open-phase faults is increased due to the extra degrees of freedom provided by more phase windings [4, 5].

Torque density can be enhanced in multiphase FSCW PMSMs using stator harmonic current injection (HCI) techniques [6, 7]. In general, for an  $m$ -phase machine, where  $m$  is an odd number, all odd harmonic currents with an order smaller than  $m$  interact with their respective MMF spatial harmonics and produce an additional average torque [6]. For this purpose, the multiphase winding layout should be optimally designed such that a high harmonic winding factor is obtained for the spatial MMF harmonics that are involved in the average torque production. Similar to three-phase machines, the harmonic winding factors that represent the MMF harmonics that contribute to average torque are termed “*main harmonic winding factors*”. In a multiphase FSCW PMSM with  $m$  phases, the order of the main harmonic winding factors are  $v = kP/2$  where  $k$  is all the odd numbers that are smaller than  $m$  [6]. A main harmonic winding factor with an order of  $kP/2$  is known as the  $k$ th main harmonic winding factor.

From the discussion in Sect. 3.2, an optimal multiphase winding layout should satisfy the following conditions:

- A high torque density.
- A low cogging torque.

To satisfy the first condition, a “*winding performance index*” is formulated in Sect. 3.3 to assess the torque producing capability of different winding layouts. Using the proposed winding performance index in the design of a stator topology assures selection of a winding layout that has the maximum torque density for a given combination of slots and poles.

As explained in Chap. 2, the interaction between the rotor magnets and the stator teeth generate cogging torque. This torque component is not dependent on the machine excitation or number of phases. Therefore, similar to the three-phase machines, cogging-torque for a combination of slots and poles can be evaluated based on the LCM of the number of slots and poles.

Similar to three-phase FSCW stators, multiphase FSCW stator classes are also recognized by their slot per pole per phase value. For each stator class a “*base winding layout*” exists that represents the winding arrangement of a FSCW stator with the lowest possible number of slots and poles in its associated class. For other slot and pole combinations that belong to the same stator class, the winding arrangement is obtained by  $P/2c$  times repeating the base winding layout.

From the analysis performed in Chap. 2, similar to three-phase FSCW machines, a valid base winding layout for an  $m$ -phase machine should meet the following conditions:

- The number of poles needs to be an even number, and cannot be a multiple of the number of phases.
- The number of stator slots needs to be an integer multiple of the phase number. This ensures allocation of the same number of slots to each phase winding and therefore realization of a symmetrical distribution for all the phase windings.
- A zero net magnetic pull is preferred. This is achievable if the periodicity of the base winding layout is equal to 2.

In brief, in a multiphase FSCW PMSM with  $m$  phases, the number of stator slots for the base winding layout of a stator class that satisfies the last two conditions should be an integer multiple of  $2m$ .

### 3.3 Determination of the Optimal Winding Layout for Multiphase FSCW Stators

Achieving a maximum average torque density is usually the main requirement in designing rotary machines. Two approaches are mainly used in the literature to determine the winding layout in FSCW machines:

- The approach based on the star of slots for single-layer windings [8] and double-layer windings [9]
- The approach based on  $S_{pp}$  for double-layer windings of three phases [10] or a higher number of phases up to six [11]

Both of the above approaches are restricted to the sole design objective of maximizing the synchronous winding factor (first main harmonic winding factor). Moreover, these techniques do not consider the higher order harmonic winding factors that are associated with the spatial MMF harmonics that can contribute to average torque production. Additionally, these approaches do not provide any information on the harmonic content of the MMF which could significantly affect the torque ripple as well as the losses.

The average torque generated in an electric machine is directly proportional to its main harmonic winding factors, as well as its rotor structure. With an increase in the number of machine phases, the number of valid winding layouts that produce a relatively high first harmonic winding factor increases. In selection of the optimal winding layout, a compromise should be made between the first main harmonic winding factor and the rest of the main harmonic winding factors, taking into account the rotor PM flux density, such that maximum average torque is achieved.

An index, referred to as the “*winding performance index*” is formulated here to quantify the torque producing ability of a winding layout with respect to its rotor characteristics. A heuristic algorithm is then proposed for determining the optimal winding layout for a double-layer symmetrical  $m$ -phase  $Q$ -slot and  $P$ -pole FSCW PMSM. In the proposed method all the valid winding layouts for a given slots and poles combination are generated and their winding performance indices

are computed. The winding layout with the highest winding performance index which indicates the highest average torque density is selected as the optimal solution.

### 3.3.1 Definition of the Winding Performance Index

Winding performance index is defined here to quantify the optimality of a winding layout with respect to its torque density. In a three-phase machine, the torque production can be maximized by selecting the winding layout with the highest main harmonic winding factor. However, this becomes complicated in a multiphase machine which uses the HCI technique for torque enhancement. The average alignment torque in an  $m$ -phase  $P$ -pole symmetrical machine running under HCI technique is calculated from [12, 13]:

$$T_{align} = \left(\frac{m}{2}\right) \left(\frac{P}{2}\right) \sum_k k i_{q,k} \lambda_{max,k}, \quad k = 1, 3, 5, \dots \quad \text{and } k < m \quad (3.1)$$

where  $i_{q,k}$  is the harmonic current of  $k$ th order in the  $q$ -axis. The magnitude ratio of the  $k$ th harmonic current to the fundamental is commonly chosen the same as that of their respective phase-to-neutral back-EMF harmonics [12].

From Chap. 2, the phase-to-neutral back-EMF harmonic amplitude and the PM flux linkage amplitude are calculated as follows:

$$E_{max,k} = -2r_g l_{eff} \omega_r k_{w,(P/2)k} N_j B_{max,(P/2)k} \quad (3.2)$$

$$\lambda_{max,k} = r_g l_{eff} \frac{4}{Pk} N_j k_{w,(P/2)k} B_{max,(P/2)k} \quad (3.3)$$

It has to be noted that although the above equations were calculated for a three-phase machine, they are valid for multiphase machines. This is due to both of the above quantities being the product of the interaction between the single-phase winding function and the rotor PM flux density without any dependency on the other phase windings or the phase number.

Equations (3.2) and (3.3) conclude that:

$$E_{max,k} \text{ is proportional to } k_{w,(P/2)k} B_{max,(P/2)k}$$

$$\lambda_{max,k} \text{ is proportional to } \frac{1}{k} k_{w,(P/2)k} B_{max,(P/2)k}$$

Since the injected current harmonic magnitude in the HCI technique is proportional to its respective back-EMF harmonic magnitude of the same order, the

winding performance index,  $WPI$ , can be defined based on (3.1) and the above proportions as:

$$WPI = \sum_k \left( k_{w,(P/2)k} B_{\max,(P/2)k,pu} \right)^2, \quad k = 1, 3, 5, \dots \quad \text{and} \quad k < m \quad (3.4)$$

$B_{\max,(P/2)k,pu}$  in the above equation is the per-unit value of  $B_{\max,(P/2)k}$  which can be obtained from the Fourier decomposition of the PM flux density. This quantity strictly depends on the rotor structure and is independent of the stator winding layout.

Among the vast possibility of winding layouts for a given number of slots and poles, the  $m$ -phase winding layout with the highest  $WPI$  will result in the highest torque density.

### 3.3.2 A Heuristic Algorithm for Design of Optimal Winding Layout

The analysis performed in Chap. 2 concludes that each phase winding of a FSCW stator comprises a number of coil pairs. A summary of the equations that were obtained in Chap. 2 is repeated in the following for use in the proposed algorithm.

In a  $P$  pole  $Q$  slot FSCW stator, the spatial winding function distribution of a coil pair displaced by  $\alpha$  mechanical radians from the origin was found based on the denominator of  $S_{pp}$  as follows:

$$\begin{aligned} w_{cp}(\theta_s) &= \sum_n W_{cp,n} \cos(n\theta_s - n\alpha) \\ W_{cp,n} &= \frac{P}{2c} \frac{4N_c}{n\pi} \sin\left(\frac{n\pi}{Q}\right), \quad n = \frac{kP}{2c} \end{aligned} \quad (3.5)$$

and

$$k = 1, 3, 5, \dots \quad \text{when } c \text{ is an odd number}$$

$$k = 2, 4, 6, \dots \quad \text{when } c \text{ is an even number}$$

It was shown that the complete winding function for phase  $j$  winding is obtained by the arithmetic sum of all its coil pairs:

$$w_j(\theta_s) = \sum_n W_n \cos(n\theta_s - n\theta_j), \quad n = \frac{kP}{2c} \quad (3.6)$$

The harmonic winding factors can be obtained from:

$$k_{w,n} = \frac{W_n}{W_{sc,n}}, \quad n = \frac{kP}{2c} \quad (3.7)$$

where

$$W_{sc,n} = \frac{2QN_c}{mn\pi} \quad (3.8)$$

Based on the above equations, a heuristic algorithm is proposed in the follows for determination of the optimal winding layout in multiphase FSCW stators. A flowchart detailing the procedure of the proposed heuristic algorithm is shown in Fig. 3.1. The inputs to the algorithm are the number of phases, slots and poles. The number of slots needs to be a multiple of  $2m$  to meet the conditions mentioned in Sect. 3.2. The flowchart shown in Fig. 3.1 can be divided into the below steps:

1. The number of slots,  $Q$ , poles,  $P$ , and phases,  $m$ , are the inputs to the algorithm.
2. Calculation of the  $S_{pp}$  value and the number of slots,  $Q_{base}$ , and poles,  $P_{base}$ , for the base winding layout.
3. Obtaining all the valid winding layouts in the base stator with  $Q_{base}$  slots. The periodicity for the base winding layout is chosen equal to 2. This indicates that in a stator with the base winding layout, each coil pair will have a coil in the first half of the stator. Thus,  $T_{1/2}$  which indicates half of the stator teeth count is calculated, among which  $T_{ph}$  teeth are solely assigned to a phase winding.
4. Finding all the possible distributions of  $T_{ph}$  coils among  $T_{1/2}$  teeth which creates a set  $\Pi_1$  of arrays of length  $T_{1/2}$ . Each array of this set represents one possible solution for distributing the coils in the stator for phase number 1. In the next step, array sets  $\Pi_k$ ,  $k = 2, 3, \dots, m$  are generated which correspond to all the possible teeth allocations to coils of phase  $k$ . As a symmetrical stator is considered, the array set  $\Pi_k$  is generated by circular shifting of  $\Pi_{k-1}$  by  $T_{ph}$ .
5. Each tooth of a double-layer FSCW stator is allocated to a single coil. Thus, in this step a comparison is made between the respective arrays of the set  $\Pi_1$  and  $\Pi_k$ ,  $k = 2, 3, \dots, m$ , out of which those that result in a single tooth allocated to more than a coil are eliminated. Furthermore, those arrays that produce similar winding layouts that are spatially shifted are eliminated.
6. In this step all possible unique coil polarities for array set  $\Pi_1$  are created, each representing half of a valid base winding layout for a single phase of the  $m$ -phase stator. The other half of the winding layout is generated by duplicating the arrays in  $\Pi_1$  such that the coil polarities are selected from the number of pole pairs in the base winding layout as explained in Chap. 2. In particular, for an even number of  $P_{base}/2$  (for an even number of  $c$ ) the coils in the second half of the base winding layout should have similar polarity to those in the first half, while if  $P_{base}/2$  is an odd number (for an odd number of  $c$ ) the coil polarities in the second half of the base winding layout will be opposite to those of the first half.

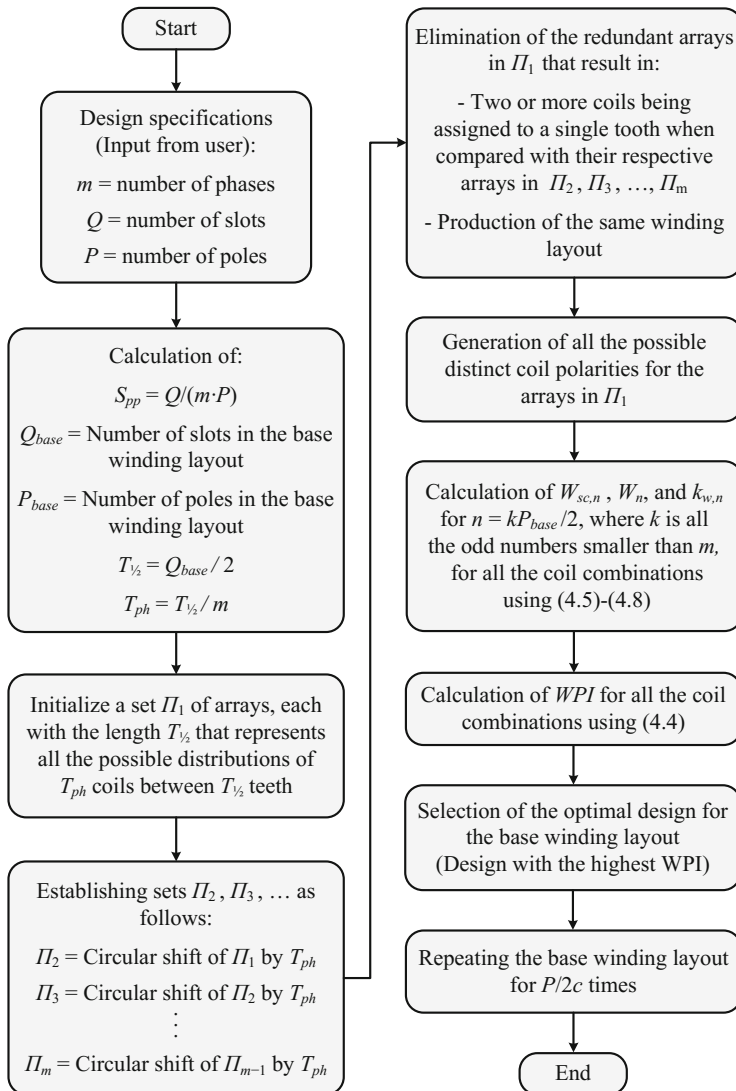


**Fig. 3.1** Flowchart of the proposed heuristic algorithm for obtaining the optimum winding layout for an  $m$ -phase  $Q$ -slot  $P$ -pole FSCW PMSM

7. Harmonic amplitudes of all main harmonics of the winding function which are of order  $k = 1, 3, 5, \dots, k < m$  are calculated for the arrays in  $\Pi_1$ , each of which represent a valid base winding layout. This is done by arithmetically summing the main harmonics of all coil pairs obtained from (3.5).
8. In this step the main harmonic winding factors that are of order  $k = 1, 3, 5, \dots, k < m$  are calculated for the arrays of  $\Pi_1$  using (3.6)–(3.8).

9. Now,  $WPI$  is calculated using (3.4) for all the base winding layouts of  $\Pi_1$ , among which the layout with the highest  $WPI$  is chosen as the optimal winding layout for a given  $S_{pp}$ .
10. Lastly, the optimal base winding layout is repeated for  $P/2c$  times to establish the complete single-phase winding layout for an  $m$ -phase FSCW PMSM with  $Q$  slots and  $P$  poles.

## 3.4 Case-Studies

Example case-studies are presented into following for determination of the optimal winding layout for FSCW PMSMs using the proposed heuristic algorithm.

### 3.4.1 Three-Phase FSCW PMSM with 14 Poles and 18 Slots

For a 14-pole 18-slot FSCW stator,  $S_{pp}$  is equal to 3/7. This stator represents the base winding layout for the three-phase 3/7 stator class.

The heuristic algorithm illustrated in Fig. 3.1 generates a total number of 12 distinct winding layouts that satisfy the conditions of a symmetrical stator winding with a zero magnetic pull. These winding layouts are shown in Fig. 3.2a. The main harmonic winding factors for the base winding layouts of Fig. 3.2a are obtained using the proposed algorithm as illustrated in Fig. 3.2b. Since only a single main harmonic winding factor exists in three-phase machines, according to (3.4) the base winding layout with the highest main harmonic winding factor is qualified as the optimal base winding layout. The winding layout with code number “7” in Fig. 3.2a has the highest main harmonic winding factor as shown in Fig. 3.2b and will result in the highest torque density; therefore, it is chosen as the optimal base winding layout. The single-phase coil arrangement for the 14-pole 18-slot FSCW PMSM according to the optimal winding layout and its spatial MMF distribution obtained from the proposed technique are shown in Fig. 3.3a and b, respectively. The obtained harmonic winding factors for the 3/7 FSCW stator class calculated using the proposed scheme are shown Fig. 3.4. As can be seen, the main harmonic winding factor in a  $P$ -pole 3/7 FSCW machine is of order  $P/2$  and has a value of 0.902.

### 3.4.2 Five-Phase FSCW PMSM with 48 Poles and 50 Slots

A 48-pole 50-slot five-phase stator represents the base winding layout for the five-phase 5/24 stator class. For this slot and pole combination, the proposed

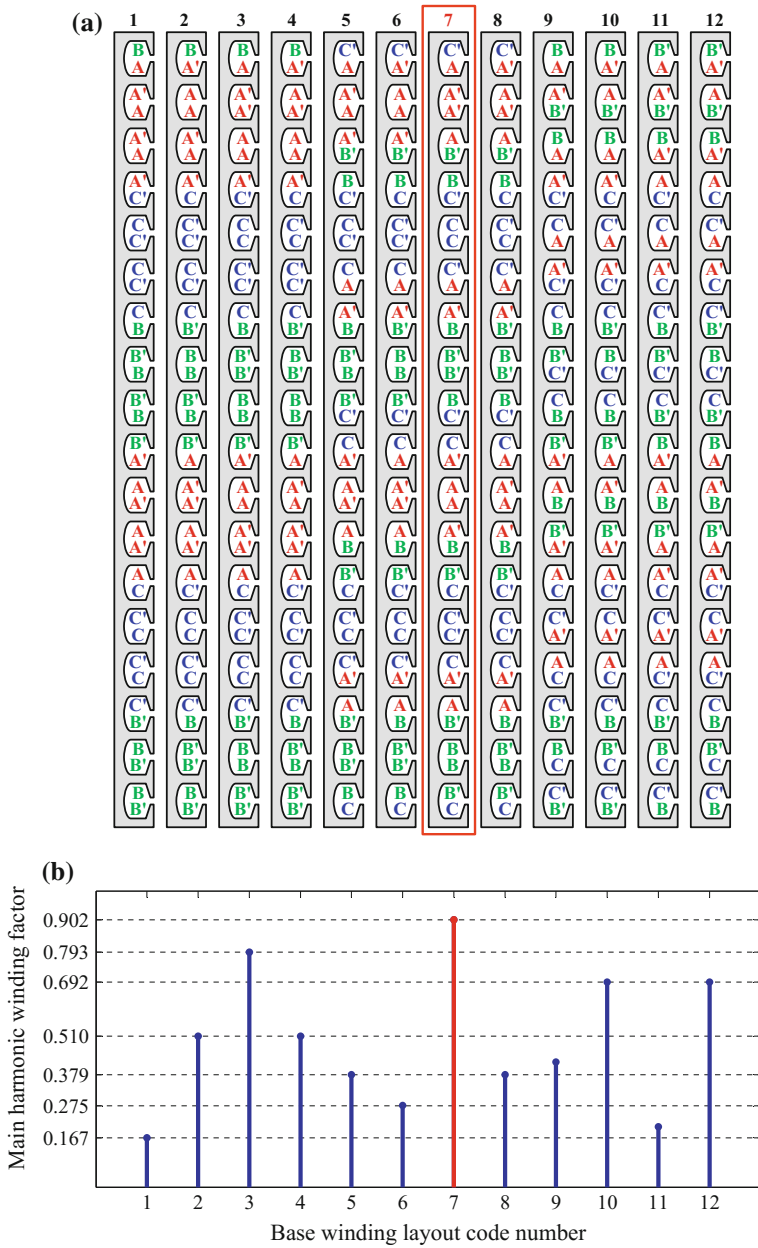


**Fig. 3.2** Valid base winding layouts for the three-phase 3/7 stator class, generated by the proposed heuristic algorithm. **a** Coil arrangements. **b** Associated main harmonic winding factors

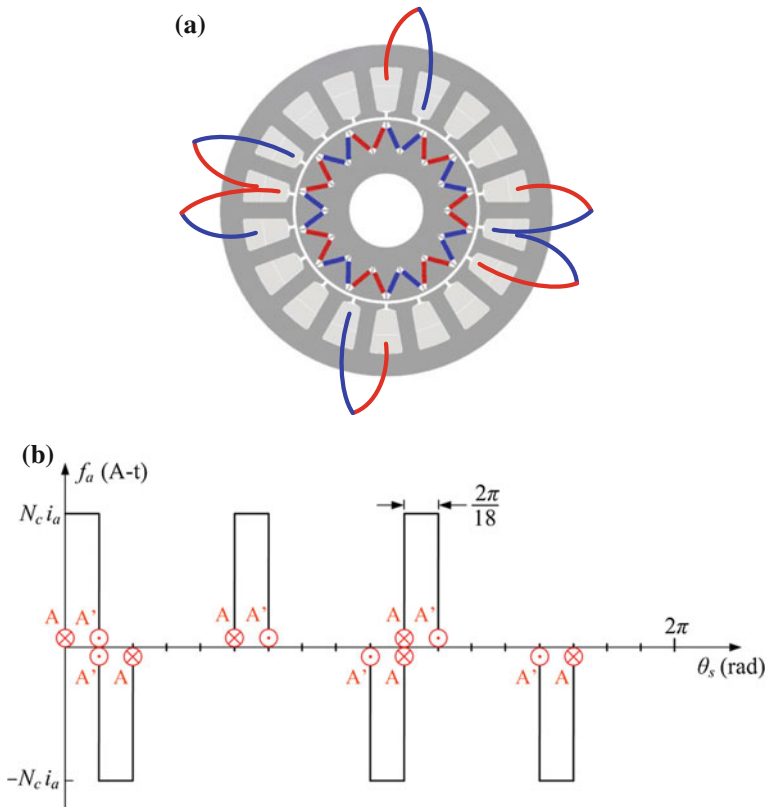


**Fig. 3.3** 14 poles 18 slots FSCW PMSM according to the optimal base winding layout shown in Fig. 3.2a, b with code number 7. **a** Single-phase winding layout. **b** Single-phase spatial MMF distribution

heuristic algorithm as shown in Fig. 3.1 narrows down the search for a base winding layout to a total number of 2000 valid layouts. These valid layouts are symmetrical and have a zero magnetic pull. The first and third main harmonic winding factors in a five-phase machine are of order  $P/2$  and  $3P/2$ , respectively. These harmonic winding factors are found from the heuristic algorithm for all the valid winding layouts as shown in Fig. 3.5a, b. The associated winding performance indices for all winding layouts are calculated using (3.4) as shown in Fig. 3.6. Evidently, among all the valid winding layouts, a small number of them feature a relatively high  $WPI$ , among which the layout with the first main harmonic winding factor of 0.982 and the third main harmonic winding factor of 0.848 represent the highest  $WPI$  equal to 0.986 and is considered as the optimal winding layout that yields the maximum torque density. This winding layout (referred to as

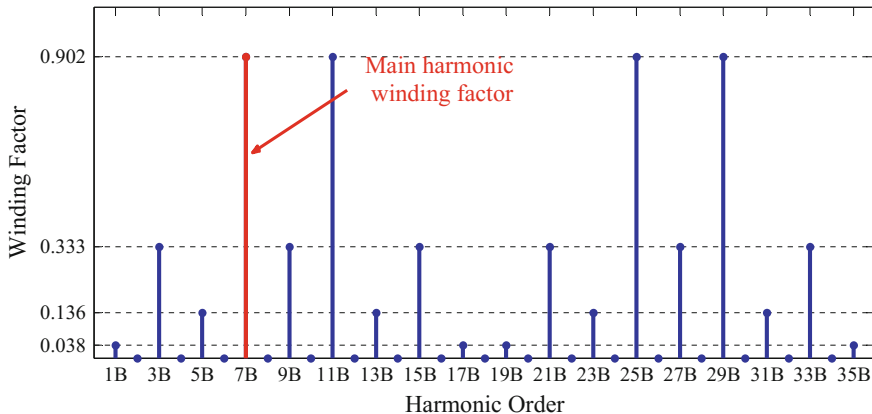


**Fig. 3.4** Harmonic winding factors of the optimal winding layout for the 3/7 FSCW stator class. In this figure  $B = P/2c$

*Design A*) for the 48-pole 50-slot five-phase FSCW stator is the standard winding layout used for 5/24 five-phase stator class [14].

From Figs. 3.5 and 3.6, the proposed heuristic algorithm provides an alternative solution for the five-phase 5/24 stator class that has a *WPI* equal to 0.95 with a first main harmonic winding factor of 0.967 and a third main harmonic winding factor of 0.729. This alternative winding configuration is referred to as *Design B* for the 48-pole 50-slot five-phase FSCW stator.

In calculation of the winding performance indices, knowledge of the PM flux density of the rotor used in the construction of the multiphase FSCW PMSM is essential. From (3.1), the average torque in a five-phase machine is proportional to the 24th and 72nd harmonics of the PM flux density. Accordingly, in calculation of the *WPI* using (3.4) as shown in Fig. 3.6, normalized amplitudes of the 24th and 72nd PM flux density harmonics should be known. Here, amplitude of the 72nd rotor PM flux density harmonic is assumed to be 17% of the fundamental component based on the PM flux density of Fig. 2.23.

The single-phase optimal winding layouts for *Design A* and *Design B* of the 48-pole 50-slot five-phase stator that indicate the base winding layouts for the 5/24 FSCW stator class, obtained using the proposed algorithm are illustrated in Fig. 3.7 and Fig. 3.8, respectively. Clearly, other stator phases have the same winding layout, but spatially displaced by  $2\pi/5$  radians with respect to each other. Accordingly, the single-phase MMF and the harmonic winding factors for a  $Q$ -slot  $P$ -pole five-phase 5/24 FSCW stator of *Design A* and *Design B* generated by the proposed technique are shown in Fig. 3.9 and Fig. 3.10, respectively.

A general expression describing the harmonic amplitudes of the single-phase spatial MMF distribution of Fig. 3.9a for a  $Q$ -slot  $P$ -pole five-phase 5/24 stator of *Design A* can be obtained using the proposed approach in Chap. 2 as follows:

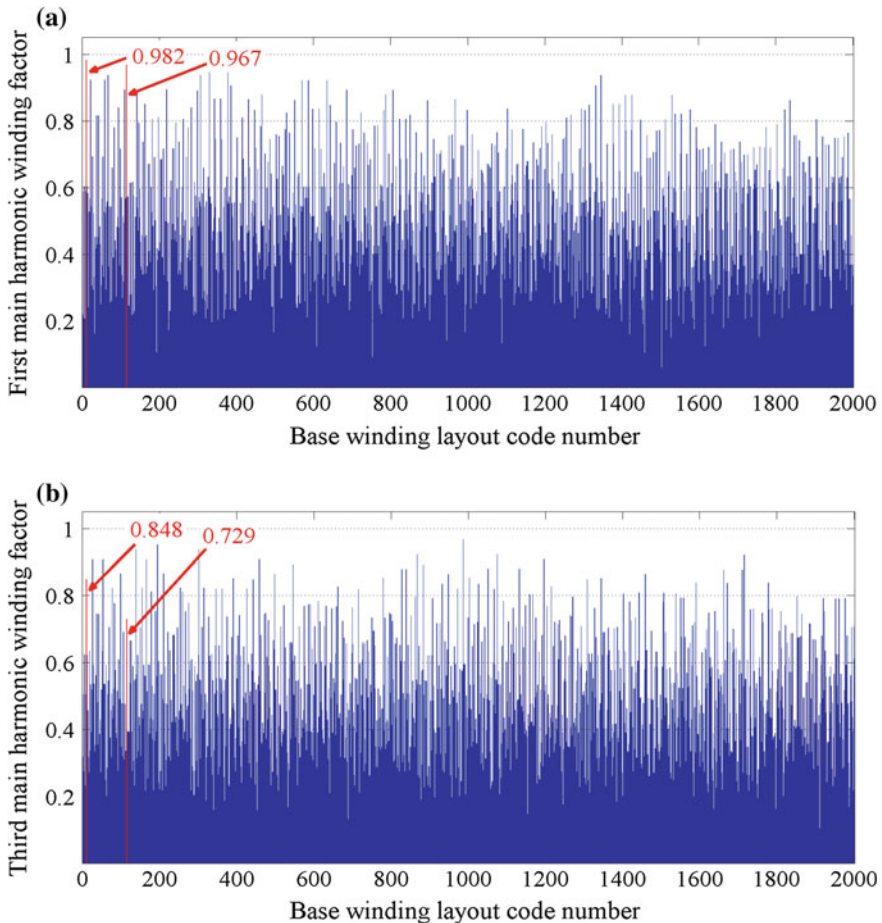
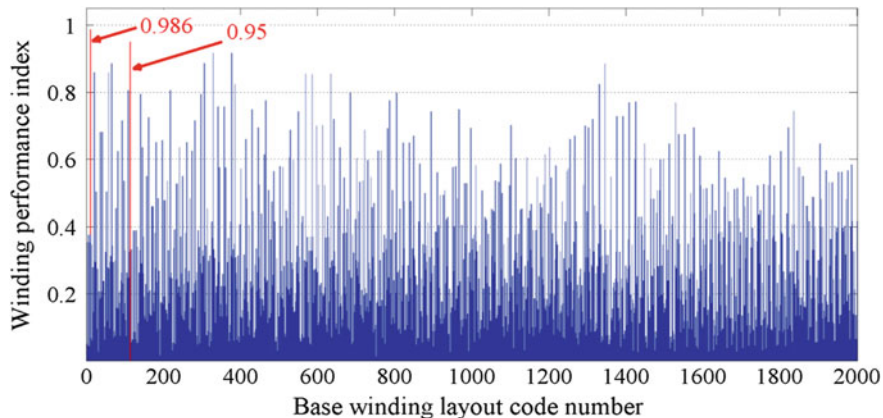


**Fig. 3.5** Valid base winding layouts for the five-phase 5/24 stator class. **a** First main harmonic winding factor. **b** Third main harmonic winding factor

$$F_{j,n} = \frac{P}{2c} \frac{4N_c i_j}{n\pi} \sin\left(\frac{n\pi}{Q}\right) \left( 1 - 2 \cos\left(\frac{2\pi}{Q}n\right) + 2 \cos\left(\frac{4\pi}{Q}n\right) \right), \quad (3.9)$$

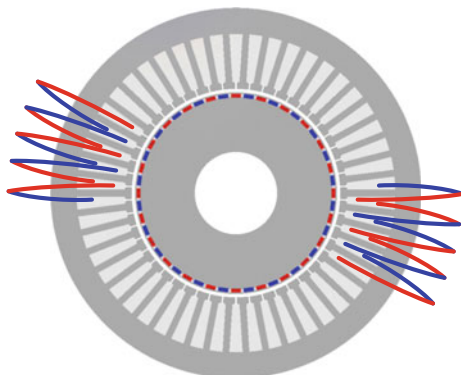
$$n = \frac{2P}{2c}, \frac{4P}{2c}, \frac{6P}{2c}, \dots$$

From (3.7), (3.8), and (3.9), a general equation for the harmonic winding factors of a  $Q$ -slot  $P$ -pole FSCW stator of the 5/24 class of *Design A* can be obtained as follows:

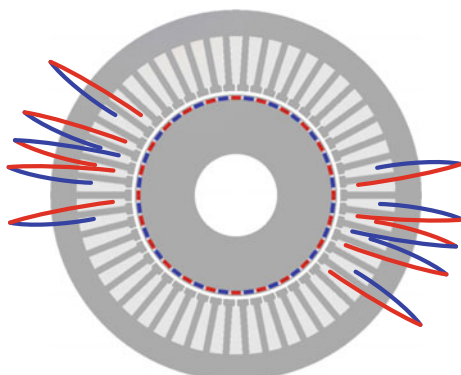


**Fig. 3.6** Winding performance indices (*WPI*) of the valid base winding layouts for the five-phase 5/24 stator class

**Fig. 3.7** Single-phase optimal winding layout for *Design A* of the 48-pole 50-slot five-phase FSCW stator obtained using the proposed algorithm. This winding layout represents the standard base winding layout for the five-phase 5/24 FSCW stator class



**Fig. 3.8** Single-phase optimal winding layout for *Design B* the 48-pole 50-slot five-phase FSCW stator obtained using the proposed algorithm. This winding layout represents an alternative base winding layout for the five-phase 5/24 FSCW stator class



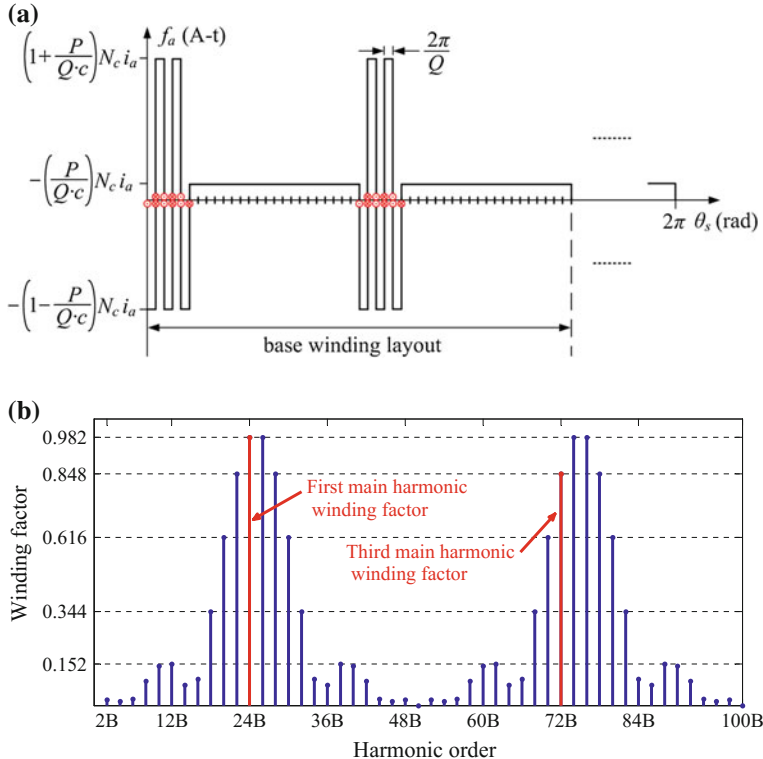


**Fig. 3.9** Design A for five-phase 5/24 stator with  $P$  poles and  $Q$  slots. **a** Single-phase MMF. **b** Harmonic winding factors, where  $B = P/2c$

$$k_{w,n} = \frac{P}{2c} \frac{10}{Q} \sin\left(\frac{n\pi}{Q}\right) \left( 1 - 2 \cos\left(\frac{2\pi}{Q}n\right) + 2 \cos\left(\frac{4\pi}{Q}n\right) \right), \quad (3.10)$$

$$n = \frac{2P}{2c}, \frac{4P}{2c}, \frac{6P}{2c}, \dots$$

A general expression for the harmonic amplitudes of the single-phase spatial MMF distribution of Fig. 3.10a for a  $Q$ -slot  $P$ -pole five-phase 5/24 stator of *Design B* obtained using the proposed approach in Chap. 2 is:

$$F_{j,n} = \frac{P}{2c} \frac{4N_c i_j}{n\pi} \sin\left(\frac{n\pi}{Q}\right) \left( 1 - 2 \cos\left(\frac{2\pi}{Q}n\right) \cos\left(\frac{4\pi}{Q}n\right) \right), \quad (3.11)$$

$$n = \frac{2P}{2c}, \frac{4P}{2c}, \frac{6P}{2c}, \dots$$

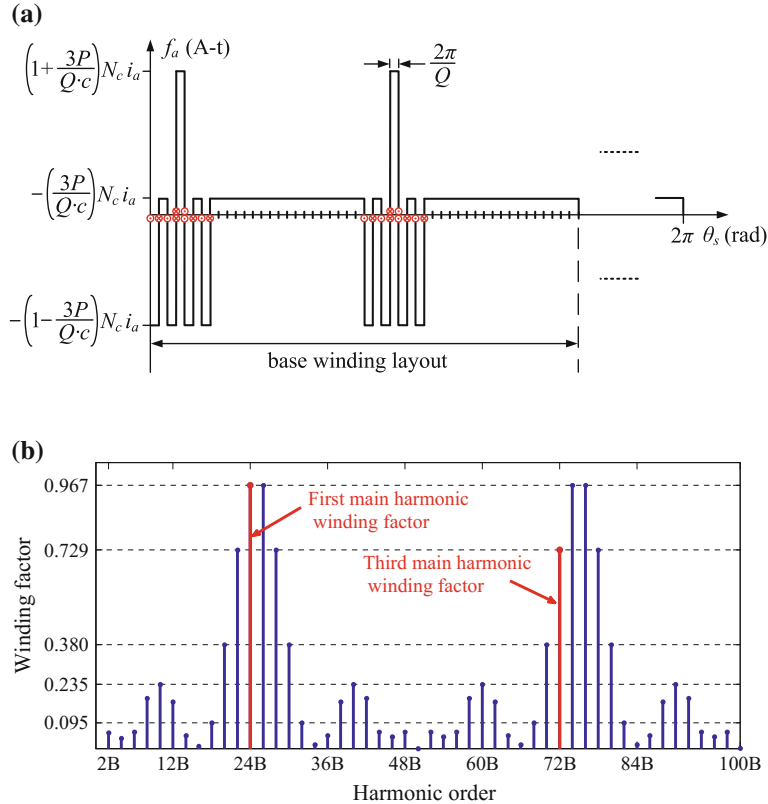


**Fig. 3.10** Design B for five-phase 5/24 stator with  $P$  poles and  $Q$  slots. **a** Single-phase MMF. **b** Harmonic winding factors, where  $B = P/2c$

From (3.7), (3.8), and (3.11), a general equation for the harmonic winding factors of a  $Q$ -slot  $P$ -pole FSCW stator of the 5/24 class of *Design B* can is:

$$k_{w,n} = \frac{P}{2c} \frac{10}{Q} \sin\left(\frac{n\pi}{Q}\right) \left(1 - 2 \cos\left(\frac{2\pi}{Q}n\right) \cos\left(\frac{4\pi}{Q}n\right)\right), \quad (3.12)$$

$$n = \frac{2P}{2c}, \frac{4P}{2c}, \frac{6P}{2c}, \dots$$

Performance characteristics of the obtained winding configurations for *Design A* and *Design B* for the five-phase 5/24 FSCW stator class will be evaluated in Sect. 3.5.

Some remarks should be made regarding the five-phase 5/24 stator class:

- The optimal base winding layout is found from Fig. 3.6 and is the layout with the highest *WPI*. As can be observed in Fig. 3.6, there are other possible winding layouts with *WPI* values similar to the highest *WPI* (i.e. 0.95 and 0.916). Such winding layouts could be used as alternative solutions for the

optimal base winding layout. These alternative designs have a different spatial MMF distribution than the optimal base winding layout that could lead to better performance in terms of torque ripple, core losses and overall efficiency. For a FSCW stator class, the alternative solutions found for the winding configuration, obtained using the proposed heuristic algorithm, should be investigated as they may lead to better performance. An analysis on the core losses caused by the spatial MMF harmonics is detailed in [15].

- The base winding layout of this stator class features an even number of pole-pairs. This indicates the same polarity of the coils in each coil pair of the winding. Therefore, the single-phase MMF is non-zero in all the areas in the airgap. This indicates overlapping of the spatial MMF distribution of the different phase windings. Therefore, the mutual inductance in such a stator comprises terms in addition to the leakage terms, making this stator class a poor candidate for fault-tolerant applications.
- As seen in (3.4),  $WPI$  is a function of the rotor PM flux density harmonics which is determined based on the rotor structure. Therefore, knowledge of rotor PM flux density is essential to designing the optimal winding layout.

### 3.4.3 Five-Phase FSCW PMSM with 18 Poles and 20 Slots

A 18-pole 20-slot five-phase stator represents the base winding layout for the five-phase 2/9 stator class. The proposed heuristic algorithm of Fig. 3.1 is used to find the optimal winding layout for this slot and pole combination. This yields a total number of 6 valid base winding layouts, among which the highest  $WPI$  is 0.97. The first and third main harmonic winding factors as well as the calculated winding performance indices for all the valid base winding layouts are shown in Fig. 3.11a, Fig. 3.11b and Fig. 3.12, respectively. Note that in obtaining the winding performance indices the 9th and 27th PM flux density harmonics are involved. Similar to the previous case-study for the five-phase 5/24 FSCW stator class, the 27th PM flux density harmonic amplitude is assumed to be 17% of that of the 9th harmonic.

The base winding layout for a single phase of the 20-slot 18-pole five-phase FSCW PMSM is shown in Fig. 3.13. Other phase windings have the same coil arrangement, but spatially displaced by  $2\pi/5$  radians with respect to each other. Accordingly, the single-phase MMF and the harmonic winding factors for a five-phase 2/9 FSCW stator with  $Q$  slots and  $P$  poles obtained from the proposed technique are shown in Fig. 3.14a and b, respectively.

A general expression describing the harmonic amplitudes of the single-phase spatial MMF distribution of Fig. 3.14a for a  $Q$ -slot  $P$ -pole five-phase 2/9 stator can be obtained using the proposed approach in Chap. 2 as follows:

$$F_{j,n} = \frac{P}{2c} \frac{4N_c i_j}{n\pi} \sin\left(\frac{n\pi}{Q}\right) \left( 2 \cos\left(\frac{11\pi}{Q}n\right) \right), \quad n = \frac{P}{2c}, \frac{3P}{2c}, \frac{5P}{2c}, \dots \quad (3.13)$$

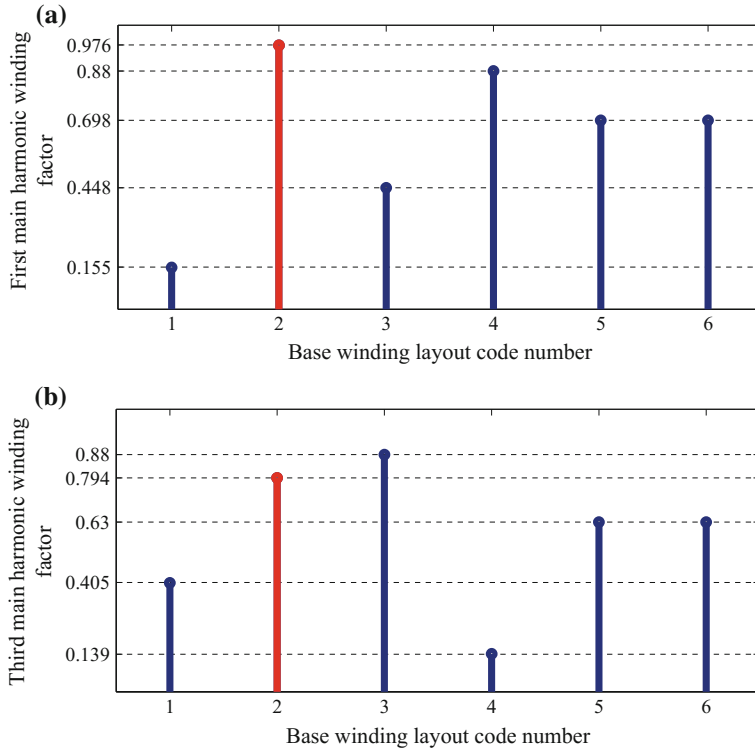


**Fig. 3.11** Valid base winding layouts for the five-phase 2/9 stator class. **a** First main harmonic winding factor. **b** Third main harmonic winding factor

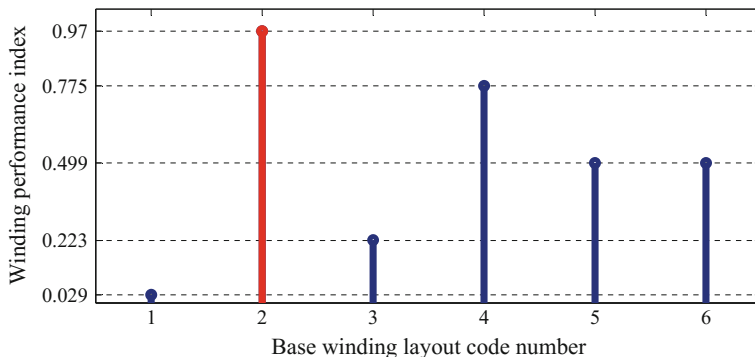


**Fig. 3.12** Winding performance indices (WPI) of the valid base winding layouts for the five-phase 2/9 stator class

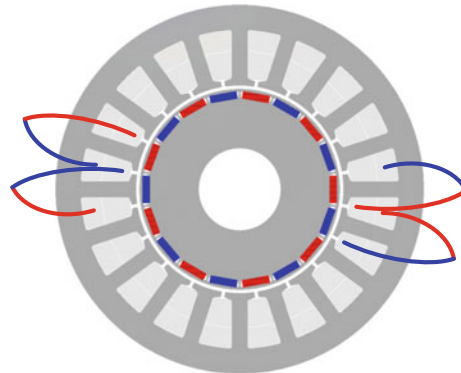


**Fig. 3.13** Single-phase winding layout for the 18-pole 20-slot five-phase FSCW stator obtained using the proposed algorithm. This winding layout represents the base winding layout for the five-phase 2/9 FSCW stator class

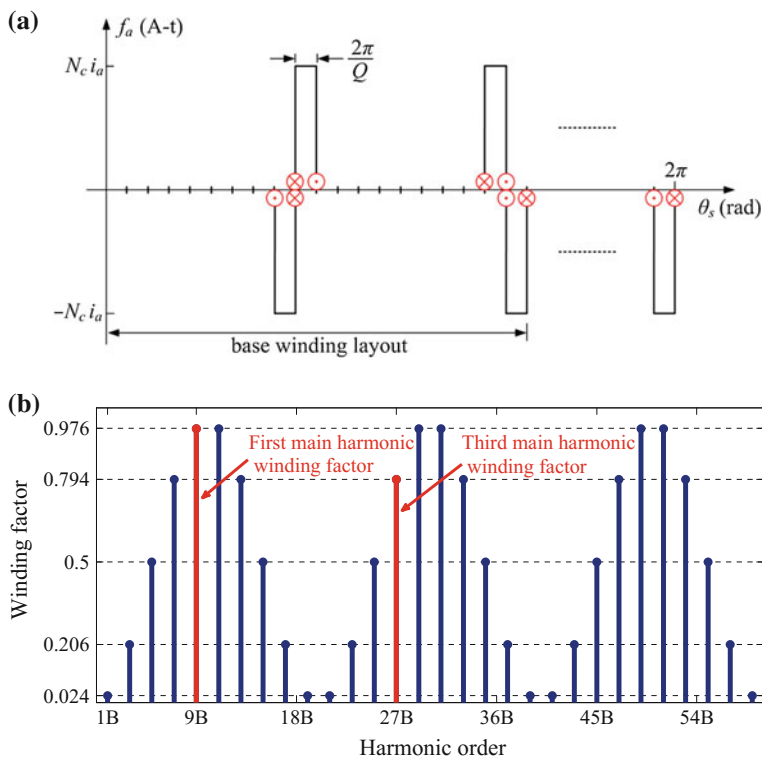


**Fig. 3.14** Five-phase 2/9 FSCW stator with  $P$  poles and  $Q$  slots. **a** Single-phase MMF. **b** Harmonic winding factors, where  $B = P/2c$

As can be observed from Fig. 3.14a, the spatial MMF distribution of each phase is zero in areas other than underneath their respective teeth. Therefore, the MMFs produced by different phase windings do not overlap, resulting in a mutual inductance to be limited to the leakage inductance only. As explained earlier, this feature is favorable for fault-tolerant applications.

A general equation for the harmonic winding factors of a  $Q$ -slot  $P$ -pole FSCW stator of the 2/9 class can be obtained from (3.7), (3.8), and (3.13) as follows:

$$k_{w,n} = \frac{P}{2c} \frac{10}{Q} \sin\left(\frac{n\pi}{Q}\right) \left( 2 \cos\left(\frac{11\pi}{Q}n\right) \right), \quad n = \frac{P}{2c}, \frac{3P}{2c}, \frac{5P}{2c}, \dots \quad (3.14)$$

### 3.4.4 Five-Phase FSCW PMSM with 28 Poles and 30 Slots

A 28-pole 30-slot five-phase stator represents the base winding layout for the five-phase 3/14 stator class. The proposed heuristic algorithm in Fig. 3.1 is used to find the optimal winding layout for this slot and pole combination. This results in 35 valid base winding layouts with their first and third main harmonic winding factors as shown in Fig. 3.15a and b, respectively. The calculated winding performance indices for these layouts are shown in Fig. 3.16. As can be observed, among all the valid base winding layouts, the layout with code number 3 has the highest value of *WPI* Equal to 0.98. This layout has first and third main harmonic winding factors of 0.98 and 0.83, respectively. In obtaining the winding performance indices the 14th and 42nd PM flux density harmonics are involved. Similar to the previous case-studies for five-phase FSCW stators, the 42nd PM flux density harmonic amplitude is assumed to be 17% of that of the 14th harmonic.

The single-phase base winding layout for the 3/14 stator class, realized using the proposed technique is shown in Fig. 3.17. The single-phase MMF and the harmonic winding factors for a  $Q$ -slot  $P$ -pole five-phase 3/14 FSCW stator realized by using the proposed technique are shown in Fig. 3.18a and b, respectively.

A general expression describing the harmonic amplitudes of the single-phase spatial MMF distribution of Fig. 3.18a for a  $Q$ -slot  $P$ -pole five-phase 3/14 stator can be obtained using the proposed approach in Chap. 2 as follows:

$$F_{j,n} = \frac{P}{2c} \frac{4N_c i_j}{\pi} \sin\left(\frac{n\pi}{Q}\right) \left( 1 - 2 \cos\left(\frac{2\pi}{Q}n\right) \right), \quad n = \frac{2P}{2c}, \frac{4P}{2c}, \frac{6P}{2c}, \dots \quad (3.15)$$

As can be observed from Fig. 3.18a, the spatial MMF distribution of each phase winding is non-zero at all the points in the airgap along the stator peripheral angle. Therefore, the MMF produced by different phase windings overlap, resulting in the mutual inductance to comprise extra terms other than the leakage terms. As explained earlier, this is a drawback when it comes to fault-tolerant operation of the multiphase FSCW PMSM.

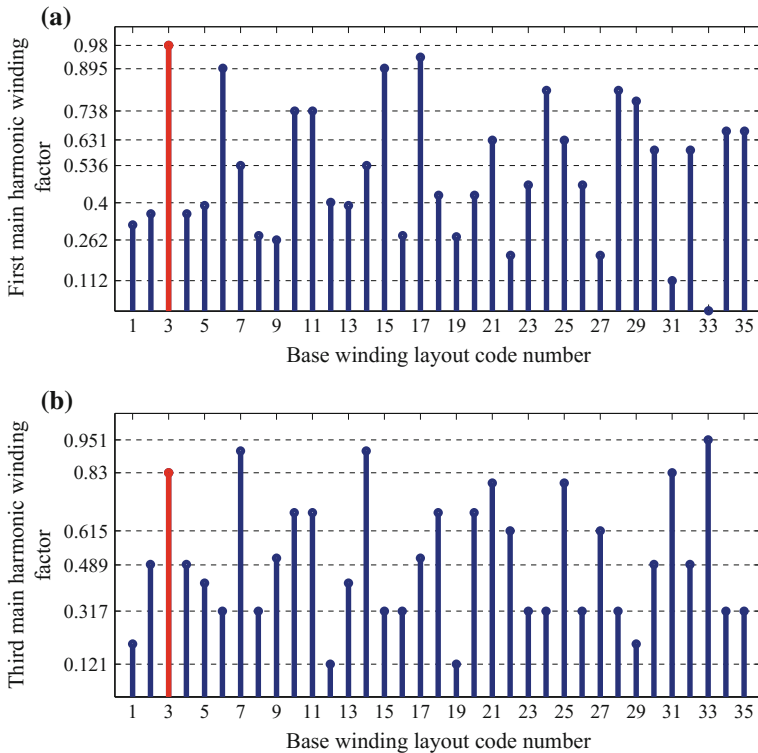


**Fig. 3.15** Valid base winding layouts for the five-phase 3/14 stator class. **a** First main harmonic winding factor. **b** Third main harmonic winding factor

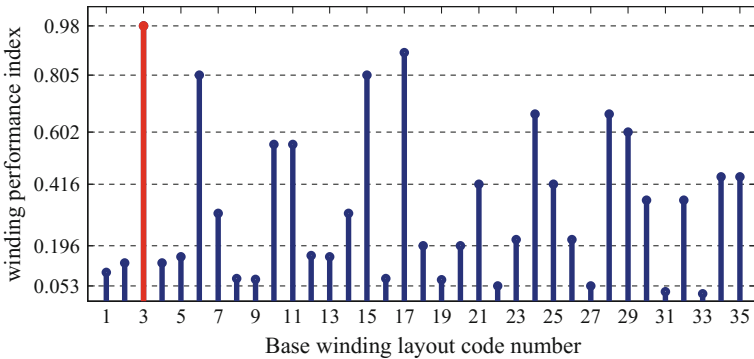


**Fig. 3.16** Winding performance indices (WPI) of the valid base winding layouts for the five-phase 3/14 stator class

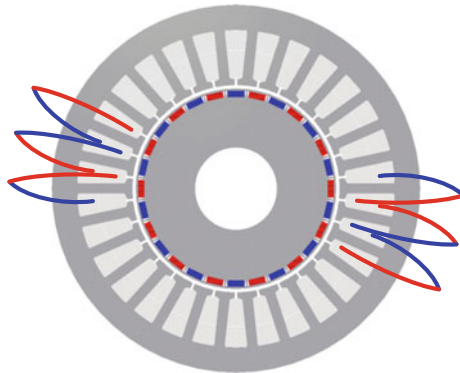


**Fig. 3.17** Single-phase winding layout for the 18-pole 20-slot five-phase FSCW stator obtained using the proposed algorithm. This winding layout represents the base winding layout for the five-phase 2/9 FSCW stator class

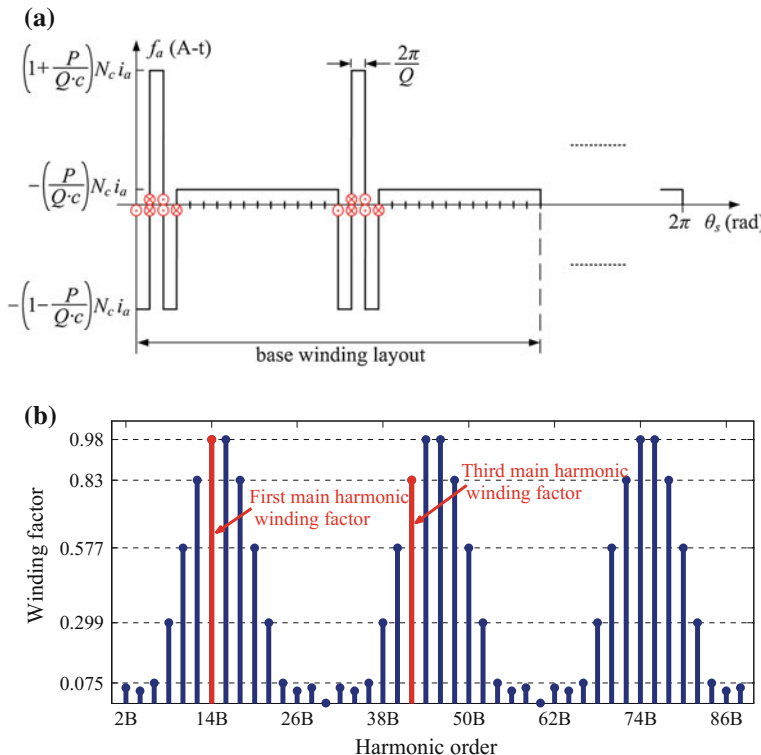


**Fig. 3.18** Five-phase 3/14 FSCW stator with  $P$  poles and  $Q$  slots. **a** Single-phase MMF. **b** Harmonic winding factors, where  $B = P/2c$

A general equation for the harmonic winding factors of a  $Q$ -slot  $P$ -pole FSCW stator of the 3/14 class can be obtained from (3.7), (3.8), and (3.15) as follows:

$$k_{w,n} = \frac{P}{2c} \frac{10}{Q} \sin\left(\frac{n\pi}{Q}\right) \left(1 - 2 \cos\left(\frac{2\pi}{Q}n\right)\right), \quad n = \frac{2P}{2c}, \frac{4P}{2c}, \frac{6P}{2c}, \dots \quad (3.16)$$

### 3.5 Validation of the Results Using FEA and Experiment

The FSCW winding configurations and their characteristics obtained using the proposed heuristic algorithm in the previous sections are simulated using FEA in Maxwell 2D and their performance characteristics are evaluated. Three five-phase designs and one three-phase design are put to test:

- *Design A* and *Design B* of the five-phase 5/24 FSCW stator class with 48 poles and 50 slots,
- The five-phase 2/9 FSCW stator class with 18 poles and 20 slots,
- The three-phase 3/7 FSCW stator class with 14 poles and 18 slots.

The obtained results through FEA and experiment are compared with those predicted by the proposed algorithm which confirms the usefulness and validity of the proposed FSCW stator design technique.

#### 3.5.1 Five-Phase FSCW PMSM with 48 Poles and 50 Slots

The proposed heuristic algorithm was used in Sect. 3.4.2 to obtain *Design A* and *Design B* for the 48-pole 50-slot FSCW PMSM. The stator winding layout, spatial MMF distribution, and harmonic winding factors for these two designs were given in Figs. 3.7, 3.8, 3.9, and 3.10, respectively. Equations for the spatial MMF harmonic amplitudes and the harmonic winding factors for these designs were derived in (3.9)–(3.12). The base speed for the 48-pole machine is:

$$\omega_r = 13.09 \text{ rad/s} = 125 \text{ rpm}$$

FEA models of *Design A* and *Design B* of the 48-slot 50-pole FSCW PMSMs are developed in Maxwell 2D as shown in Fig. 3.19a and b, respectively. In the simulated FSCW PMSMs, the stator and rotor and number of turns in each coil are kept the same for both of the machines. However, the coil arrangement of the stator deviates for *Design A* and *Design B* as evident from Fig. 3.19. Main design parameters for these machines are listed in Table 3.1.

The generated back-EMF by *Design A* and *Design B* FSCW PMSMs when the machine is rotating at the base speed are shown in Fig. 3.20a and b, respectively. Since the rotor of both *Design A* and *Design B* are the same, the airgap PM flux

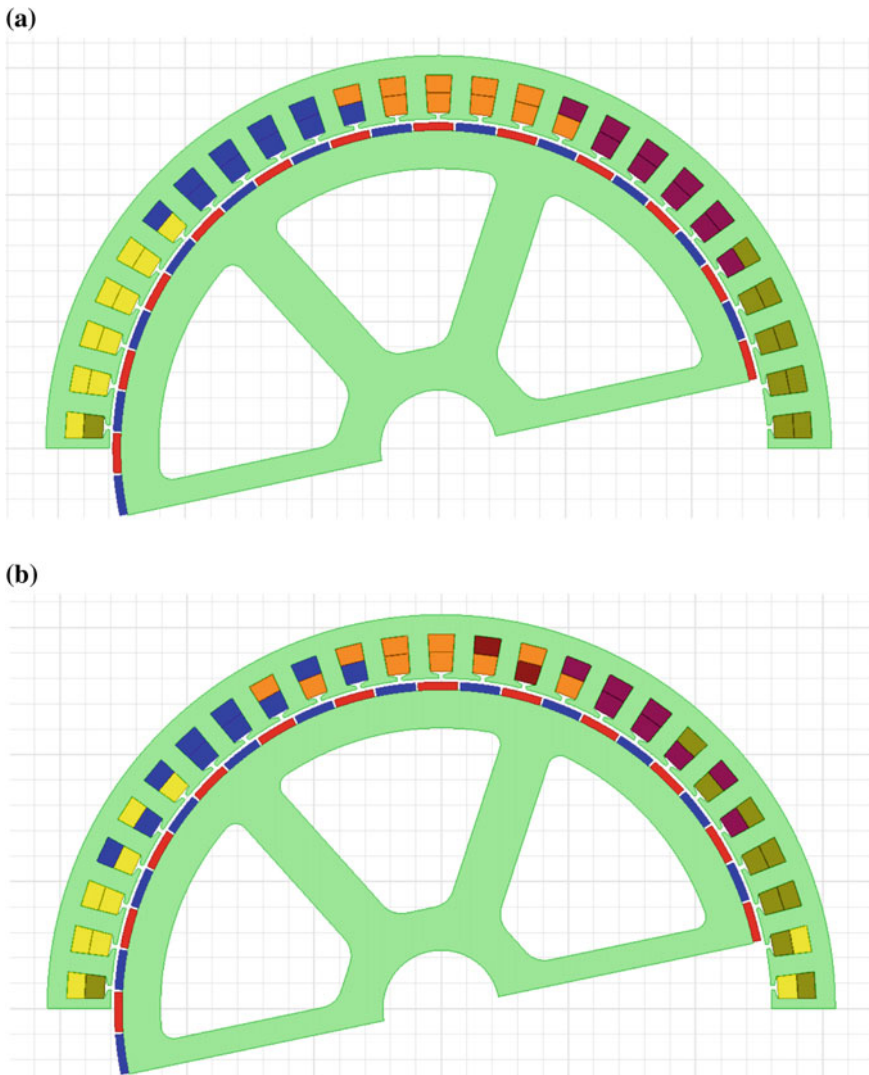


**Fig. 3.19** FEA model of the 48-pole 50-slot 5/24 five-phase FSCW PMSM in Maxwell 2D.  
**a** Design A. **b** Design B

**Table 3.1** Main design parameters of the five-phase 5/24 FSCW PMSM

Quantity	Value
Rotor outer radius	128.5 (mm)
Air-gap length	1.5 (mm)
Axial length, $l_{eff}$	200 (mm)
Number of turns in a coil, $N_c$	50
Rated current	7 (A)

density is the same for both the designs. Therefore, from Chap. 2, the ratio of the back-EMF harmonics in *Design A* and *Design B* are proportional to the ratio of their respective harmonic winding factors. The significant harmonic winding factors of both designs obtained using the proposed algorithm, their ratio, the back-EMF harmonics of both designs obtained using FEA, and their ratio are shown in Table 3.2. It is observed that the fundamental, third and fifth harmonics of the back-EMF for *Design A* are 1.6%, 16% and 62% higher than those of *Design B*, respectively. This is in agreement with the ratio of the harmonic winding factors listed in Table 3.2, validating the proposed algorithm.

In the next step, MTPA technique with third harmonic current injection is utilized. Both the machines are fed by rated currents superimposed by a third harmonic component. The flux lines and flux density distribution of *Design A* and *Design B* are illustrated in Fig. 3.21. The developed torques by both designs are shown in Fig. 3.22. The developed average torque by the *Design A* FSCW PMSM is 269.3 N m, while *Design B* produces an average torque of 264.3 N m. This is in coherence with the results obtained by the proposed algorithm which predicted a lower average torque for the *design B* FSCW PMSM, as a lower *WPI* was

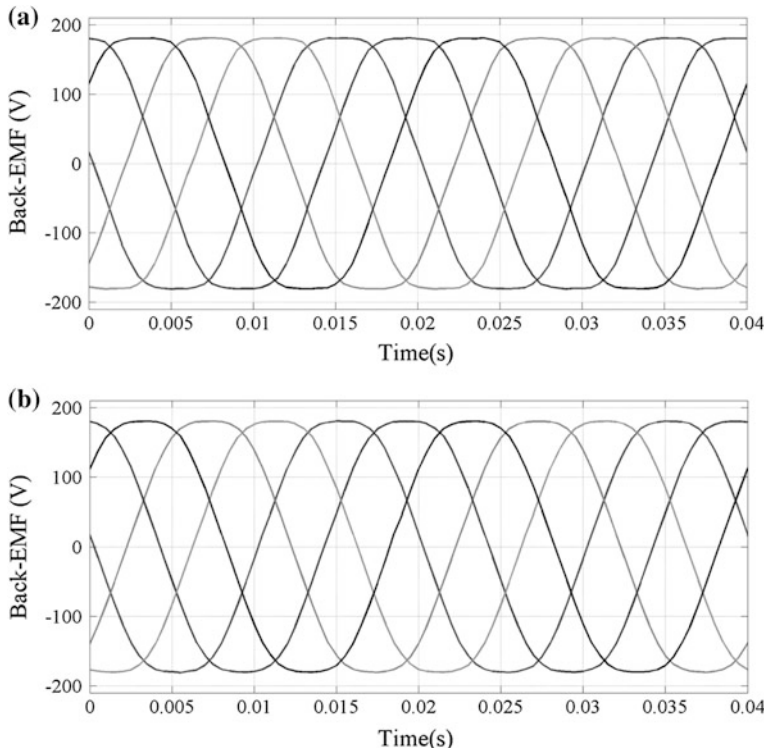
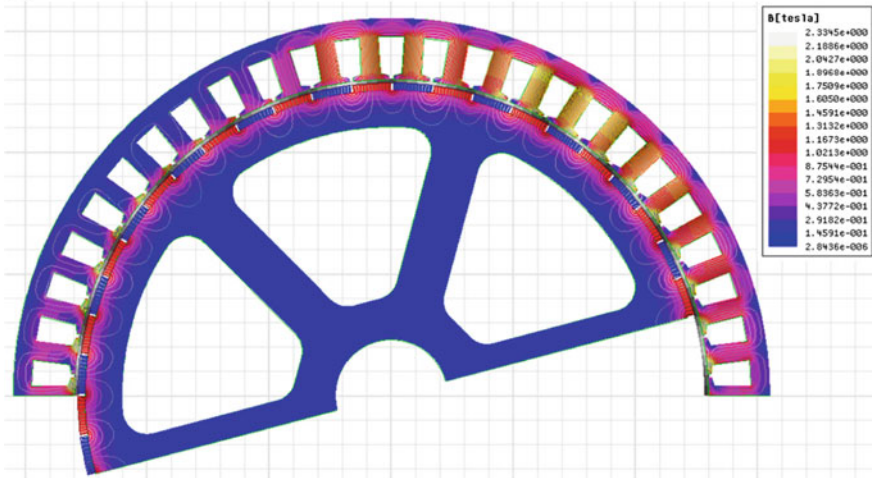


**Fig. 3.20** Generated back-EMF by the 48-pole 50-slot 5/24 five-phase FSCW PMSM in Maxwell 2D. **a** Design A. **b** Design B

**Table 3.2** Ratio of the harmonic winding factors and back-EMF harmonics for *Design A* and *Design B* FSCW PMSMs

	$k_{w,(nP/2)A}$	$k_{w,(nP/2)B}$	$\frac{k_{w,(nP/2)A}}{k_{w,(nP/2)B}}$	$E_{A,n}$	$E_{B,n}$	$\frac{E_{A,n}}{E_{B,n}}$
1st harmonic ( $n = 1$ )	0.9823	0.9668	1.016	180.298	177.4546	1.016
3rd harmonic ( $n = 3$ )	0.8482	0.7291	1.16	41.0081	35.2486	1.16
5th harmonic ( $n = 5$ )	0.6155	0.3804	1.62	10.0634	6.2195	1.62

(a)



(b)

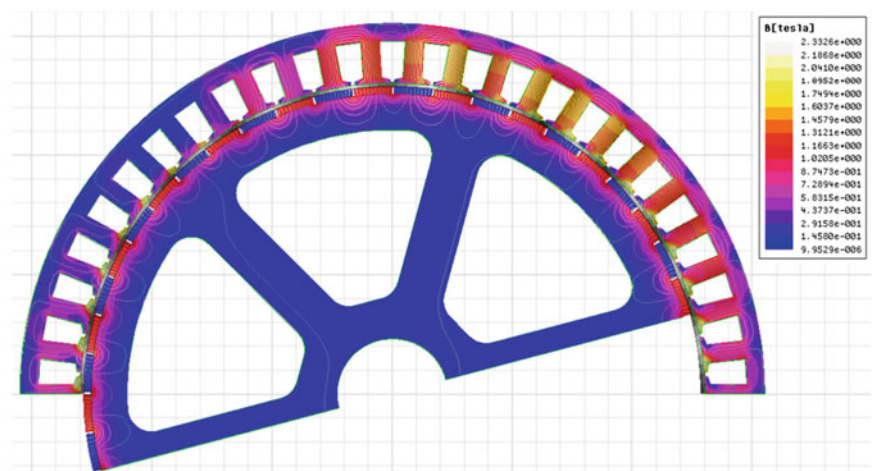


**Fig. 3.21** Flux lines and flux density distribution in the 48-pole 50-slot 5/24 five-phase FSCW PMSM obtained from Maxwell 2D, when supplied with rated currents under an MTPA algorithm. **a** Design A. **b** Design B

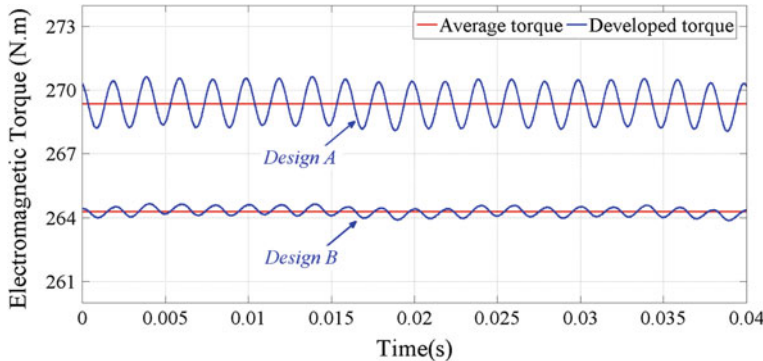


**Fig. 3.22** Developed torque by *Design A* and *Design B* of the 48-pole 50-slot 5/24 FSCW PMSM in Maxwell 2D

calculated for the *Design B* machine compared with that of the *design A* FSCW PMSM. As shown in Fig. 3.22, the torque ripple produced by *Design A* is 2.6 N m while *Design B* produces 0.8 N m. Evidently the developed average torque by *Design A* is 1.9% higher than *Design B*, however, the generated torque tipple by *Design A* is 69.2% higher than *Design B*. The *Design B* FSCW PMSM shows an improvement in the torque ripple at the price of a decrease in the average torque, compared with the *Design A* FSCW PMSM.

### 3.5.2 Five-Phase FSCW PMSM with 18 Poles and 20 Slots

The 18 poles and 20 slots five-phase FSCW PMSM which its winding configuration was previously obtained using the proposed algorithm in Sect. 3.4.3 is developed with FEA in Maxwell 2D in this section. The stator of this machine represents the base winding layout for the five-phase 2/9 FSCW stator class. The winding layout, spatial MMF distribution and harmonic winding factors for this stator are shown in Fig. 3.13 and Fig. 3.14a and b, respectively. General equations for the spatial MMF harmonic amplitudes and harmonic winding factors for this stator class are derived in (3.13)–(3.14).

The developed model of the machine in FEA is given in Fig. 3.23. The main design parameters for this machine are listed in Table 3.3. The base speed for the 18-pole machine is:

$$\omega_r = 34.91 \text{ rad/s} = 333.33 \text{ rpm}$$

The machine is rotated at the base speed and the five-phase back-EMF is obtained as shown in Fig. 3.24. The fundamental, third, and fifth harmonics of the generated back-EMF are 77.52 V, 2.22 V and 2.43 V, respectively. The associated

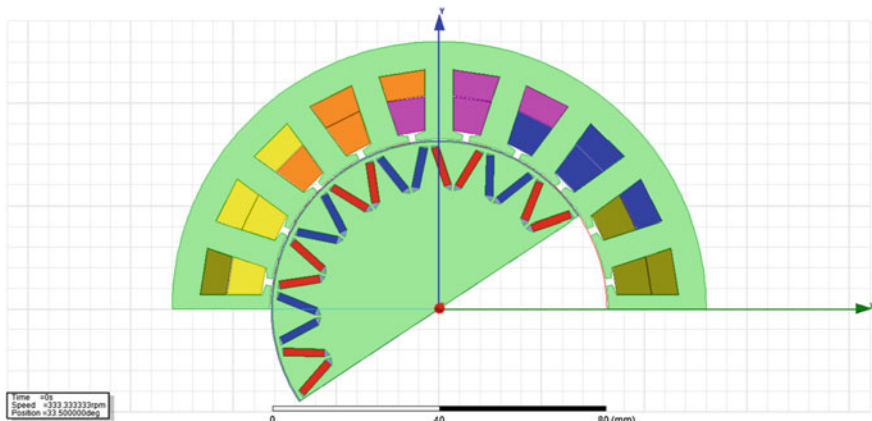


**Fig. 3.23** FEA model of the 18-pole 20-slot 2/9 five-phase FSCW PMSM in Maxwell 2D

**Table 3.3** Main design parameters of the five-phase 5/24 FSCW PMSM

Quantity	Value
Rotor outer radius	40.5 (mm)
Air-gap length	0.7 (mm)
Axial length, $l_{eff}$	89 (mm)
Number of turns in a coil, $N_c$	100
Rated current	3.5 (A)

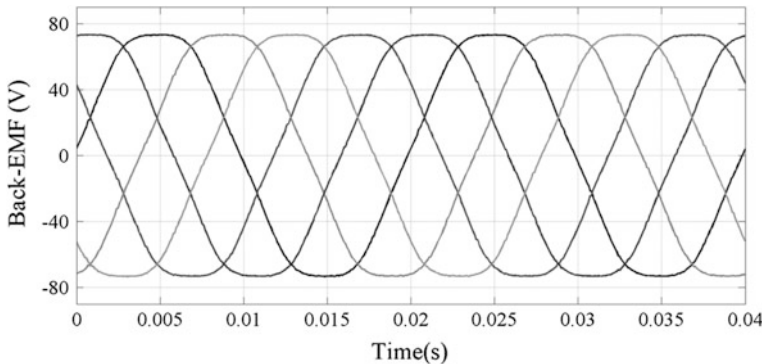


**Fig. 3.24** Generated back-EMF by the 18-pole 20-slot 2/9 five-phase FSCW PMSM in Maxwell 2D

harmonic winding factors obtained using the proposed algorithm are 0.976, 0.794, and 0.5, respectively. The machine is injected with rated currents under an MTPA algorithm with third harmonic injection to obtain the maximum possible torque for

the supplied current amplitude. The flux lines and the distribution of the PM flux density in the iron core under such excitation are shown in Fig. 3.25. The developed electromagnetic torque is illustrated in Fig. 3.26. The average torque is 20.14 N m, while the torque ripple is 0.14 N m which is 0.7% of the average torque. Evidently, a satisfactory torque density is obtained by the a designed FSCW PMSM based on the proposed algorithm. Other winding configuration for the 18-pole 20-slot FSCW PMSM result in a less average torque as predicted by the proposed algorithm.

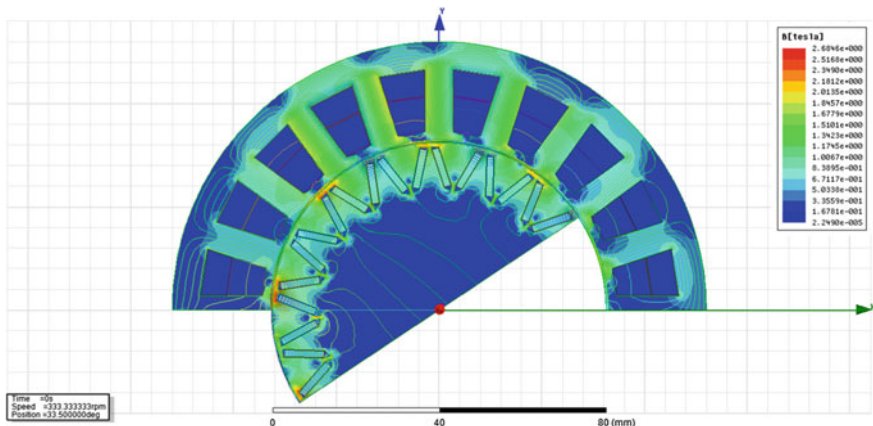


**Fig. 3.25** Flux lines and flux density distribution in the 18-pole 20-slot 2/9 five-phase FSCW PMSM obtained from Maxwell 2D, when supplied with rated currents under an MTPA algorithm

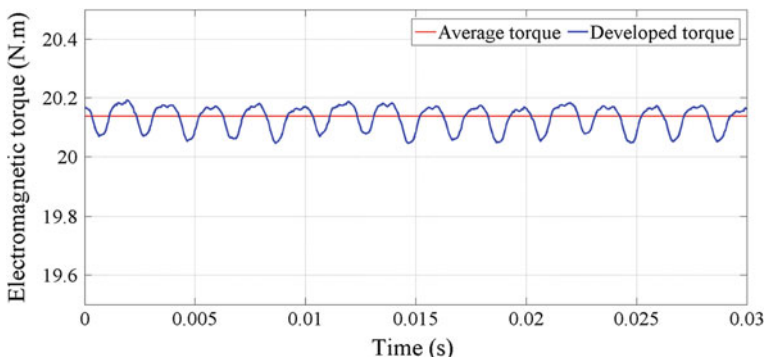


**Fig. 3.26** Developed electromagnetic torque by the 18-pole 20-slot 2/9 FSCW PMSM in Maxwell 2D

### 3.5.3 Three-Phase FSCW PMSM with 14 Poles and 18 Slots

A three-phase 14-pole 18-slot FSCW IPM machine which represents the base winding layout for the 3/7 stator class was designed and manufactured as detailed in [16]. The main design parameters are shown in Table 3.3. The stator winding layout for the prototype machine is according to the optimal layout that was obtained in Sect. 3.4.1 using the proposed heuristic algorithm and shown in Fig. 3.3a. The base speed for the 14-pole machine is:

$$\omega_r = 44.88 \text{ rad/s} = 528.57 \text{ rpm}$$

The FEA model of the prototype machine in CEDRAT FLUX 2D is shown in Fig. 3.27a, and the manufactured rotor and stator are shown in Fig. 3.27b and c, respectively.

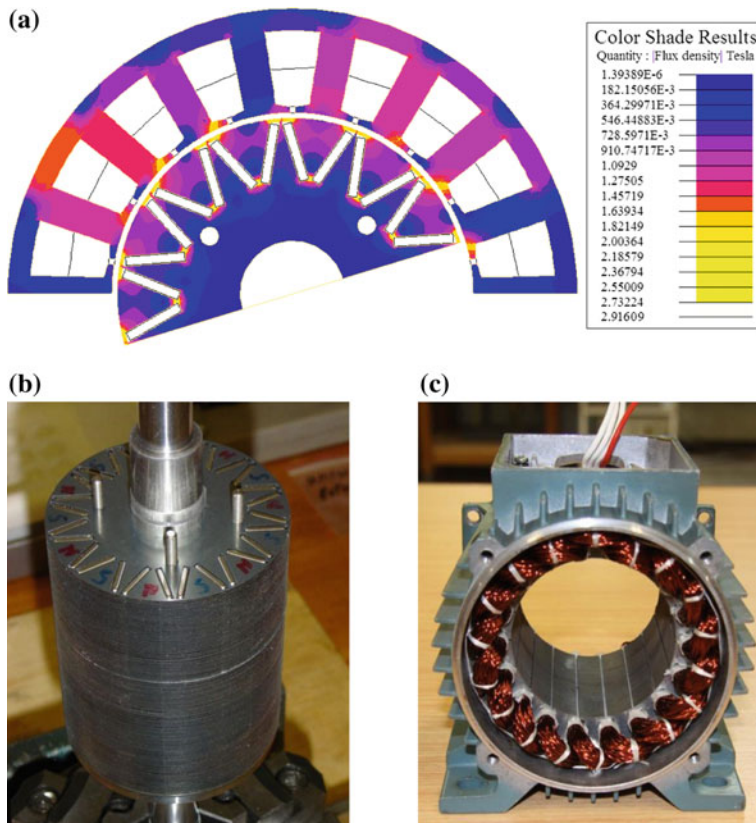


**Fig. 3.27** Prototype 3/7 FSCW IPM machine with 14 poles and 18 slots. **a** FEA model. **b** V-shaped rotor. **c** FSCW stator

The spatial MMF distribution of the prototype machine when it is supplied with a balanced three-phase current with 1 A amplitude and 50 Hz frequency, obtained from FEA is shown in Fig. 3.28. The results are compared with those calculated through the proposed MMF model in Chap. 2 at two arbitrary moments as shown in Fig. 3.28a and b, respectively. The harmonic spectrum of the total MMF is shown in Fig. 3.29. Evidently, the analytical model of the total MMF is in good agreement with the FEA results.

In order to validate the calculated harmonic winding factors of Fig. 3.4 for the 3/7 stator class, their effect on the back-EMF is investigated. The experimental setup for measurement of the back-EMF is shown in Fig. 3.30. A prime-mover is used to rotate the shaft at arbitrary speeds and the back-EMF is measured using a digital oscilloscope.

Figure 3.31 shows the measured back-EMF of the prototype machine at the base speed in comparison with the analytically calculated back-EMF using the obtained harmonic winding factors in Fig. 3.4. Evidently, the measured and calculated line-to-line and line-to-neutral back-EMFs are in good agreement. THD of the measured line-to-neutral and line-to-line back-EMFs are 5.25% and 0.9%, respectively, while for the analytically calculated back-EMFs they are 5.9% and

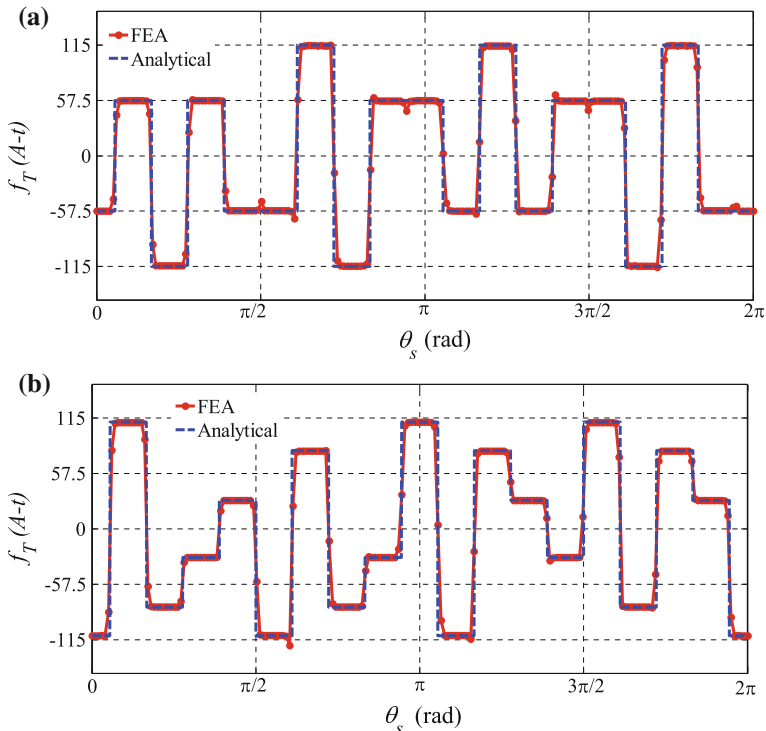


**Fig. 3.28** Total MMF produced by the 14-pole 18-slot FSCW stator. **a** At  $t = 0$  s. **b** At  $t = 5$  ms

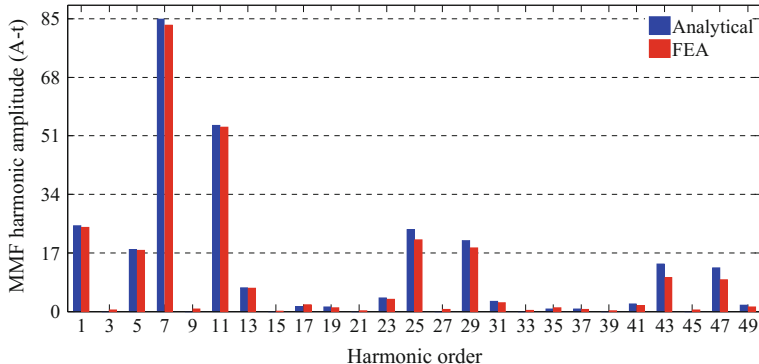


**Fig. 3.29** Spatial harmonic spectrum of the total MMF produced by the 14-pole 18-slot FSCW stator

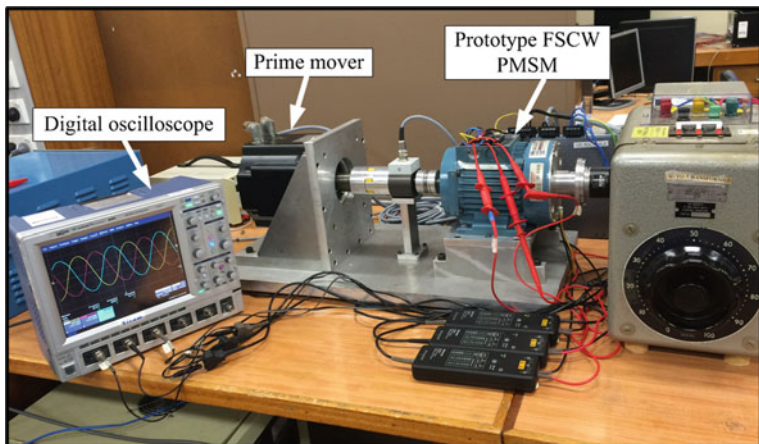


**Fig. 3.30** Experimental setup for measurement of the back-EMF in the prototype FSCW IPM machine

0.95%, respectively. The slight deviations between the analytically calculated and measured back-EMFs are due to neglecting the slotting effects and the imperfections added to the machine in the manufacturing process.

According to (3.2), the back-EMF harmonic amplitudes are directly proportional to their respective harmonic winding factors as well as the rotational speed. The fundamental component and the major harmonics in the line-to-neutral back-EMF which are of the 3rd, 5th, 7th, and 9th order are measured with respect to the rotational speed and compared with the analytical calculations as shown in Fig. 3.32a and b, respectively. As can be seen, the measured back-EMF harmonics are in good agreement with those of the analytically calculated back-EMF using the harmonic winding factors of Fig. 3.4 in (3.2).

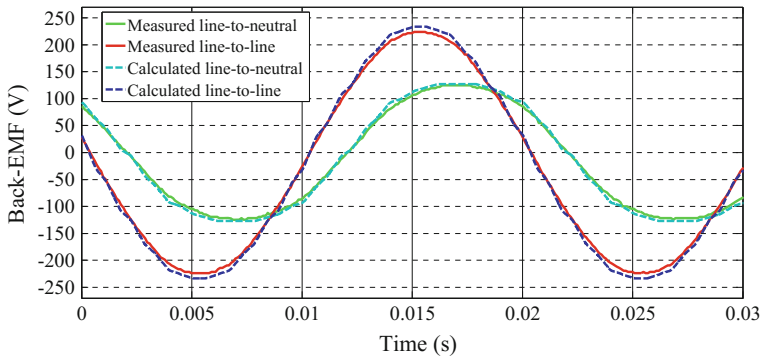


**Fig. 3.31** Experimentally measure and analytically calculated back-EMF for the prototype FSCW IPM machine

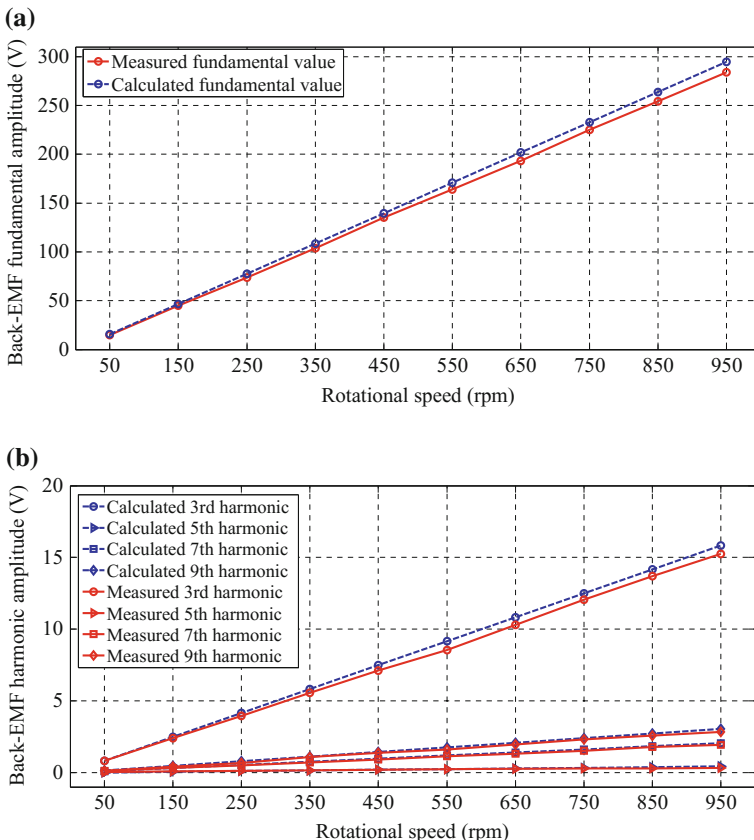


**Fig. 3.32** Experimentally measured and analytically calculated line-to-neutral back-EMF harmonic amplitudes with respect to the rotational speed. **a** Fundamental component. **b** Third, fifth, seventh, and ninth harmonics

The obtained results verify that the proposed technique can correctly predict the spatial MMF distribution, harmonic winding factors, and back-EMF for a given winding layout, which eventually leads to finding the optimal winding layout for a given slot and pole combination.

### 3.6 Conclusion

A systematic technique was proposed in this chapter for determination of the optimal winding layout for multiphase FSCW PMSMs with a given slot and pole combination. The propose heuristic algorithm obtains all the valid winding layouts for a given slot and pole combination, each of them characterized by a winding performance index that describes performance of the layout in terms of torque production ability. Among all the valid layouts, the layout with the highest winding performance index was selected as the optimal winding layout. All the basic characteristics of the optimal winding layout, e.g. the harmonic winding factors and the back-EMF, were also produced by the proposed algorithm.

The proposed winding performance index is based on the rotor design and assists in designing the optimum winding layout such that maximum torque density is produced for a given rotor structure.

Multiple case-studies for designing the optimal winding layouts for multiphase FSCW PMSMs were investigated and the results were validated through FEA and experiments on a prototype FSCW PMSM in the laboratory.

## References

1. A.M. El-Refaie, Fractional-slot concentrated-windings synchronous permanent magnet machines: opportunities and challenges. *IEEE Trans. Ind. Electron.* **57**, 107–121 (2010)
2. A. Mohammadpour, L. Parsa, Asymmetrical multi-lane multi-phase motor drives, in *Proceedings of the APEC* (2014), pp. 2482–2487
3. E. Levi, R. Bojoi, F. Profumo, H.A. Toliyat, S. Williamson, Multiphase induction motor drives—a technology status review. *Electr. Power Appl. IET* **1**, 489–516 (2007)
4. F. Barrero, M.J. Duran, Recent advances in the design, modeling, and control of multiphase machines—Part I. *IEEE Trans. Ind. Electron.* **63**, 449–458 (2016)
5. M.J. Duran, F. Barrero, Recent advances in the design, modeling, and control of multiphase machines—Part II. *IEEE Trans. Ind. Electron.* **63**, 459–468 (2016)
6. E. Levi, Multiphase electric machines for variable-speed applications. *IEEE Trans. Ind. Electron.* **55**, 1893–1909 (2008)
7. W. Jin, Q. Ronghai, Z. Libing, Dual-rotor multiphase permanent magnet machine with harmonic injection to enhance torque density. *IEEE Trans. Appl. Supercond.* **22**, 5202204–5202204 (2012)
8. N. Bianchi, M. Dai Pre, Use of the star of slots in designing fractional-slot single-layer synchronous motors, in *IEE Proceedings on Electric Power Applications*, vol. 153 (2006), pp. 459–466

9. S. Skaar, O. Krovel, R. Nilssen, Distribution, coil-span and winding factors for PM machines with concentrated windings. *ICEM* **2006**, 2–5 (2006)
10. J. Cros, P. Viarouge, Synthesis of high performance PM motors with concentrated windings. *IEEE Trans. Energy Convers.* **17**, 248–253 (2002)
11. A.M. El-Refaie, M.R. Shah, Q. Ronghai, J.M. Kern, Effect of number of phases on losses in conducting sleeves of surface PM machine rotors equipped with fractional-slot concentrated windings. *IEEE Trans. Ind. Appl.* **44**, 1522–1532 (2008)
12. J. Figueroa, J. Cros, P. Viarouge, Generalized transformations for polyphase phase-Modulation motors. *IEEE Trans. Energy Convers.* **21**, 332–341 (2006)
13. L. Parsa, H.A. Toliyat, Five-phase permanent-magnet motor drives. *IEEE Trans. Ind. Appl.* **41**, 30–37 (2005)
14. K. Huilin, Z. Libing, W. Jin, Harmonic winding factors and MMF analysis for five-phase fractional-slot concentrated winding PMSM, in *2013 International Conference on Electrical Machines and Systems (ICEMS)* (2013), pp. 1236–1241
15. N. Bianchi, E. Fornasiero, Index of rotor losses in three-phase fractional-slot permanent magnet machines. *Electr. Power Appl. IET* **3**, 381–388 (2009)
16. R. Dutta, L. Chong, M.F. Rahman, Design and experimental verification of an 18-Slot/14-pole fractional-slot concentrated winding interior permanent magnet machine. *IEEE Trans. Energy Convers.* **28**, 181–190 (2013)

# Chapter 4

## Analytical Modelling of Rotor Magnetic Characteristics in an Interior Permanent Magnet Rotor



### 4.1 Introduction

The flux of the buried magnets inside an IPM rotor leads to a non-uniform distribution of saturation in the rotor magnetic material. This changes the relative permeability of the iron and ultimately the reluctance of the stator flux path which is the determining factor for the machine magnetic characteristics.

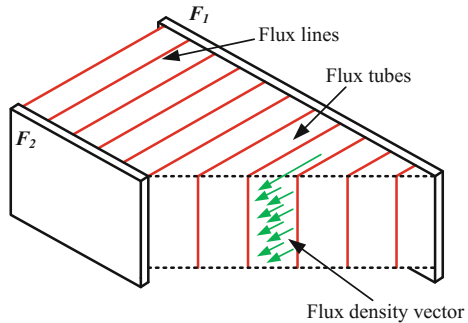
The non-uniform distribution of saturation inside an IPM rotor depends on the rotor geometry and magnet locations buried inside the rotor. In this chapter, a V-shaped IPM rotor is considered and its geometrical relationships are derived. The permanent magnet flux paths inside the rotor iron are then analyzed, upon which a non-uniform local magnetic saturation map in the rotor iron is proposed. The proposed geometrical saturation map is then used in conjunction with the magnetic equivalent circuit of the rotor to propose a mathematical model for the PM flux density in the air-gap of an IPM synchronous machine (Fig. 4.1).

The proposed model takes into account the relative permeability variations with respect to the saturation level at different points of the rotor iron according to its  $B$ - $H$  curve. The proposed theory is validated by FEA and experimental results for a prototype FSCW IPM machine.

### 4.2 Principles of Magnetic Circuits in an IPM Machine

Analysis of rotating machines requires knowledge regarding behaviour of the magnetic flux that links the stator and rotor inside the machine. This section is dedicated to explaining the magnetic flux generation in a magnetic circuit. Elements of a magnetic circuit are introduced and magnetic equivalent circuit (MEC) is explained as a tool for rapid evaluation of simple magnetic circuits.

**Fig. 4.1** Oblique cut through the field between two parallel plates of magnetic potentials  $F_1$  and  $F_2$  [1]



There are three main elements in a loss-less magnetic circuit: magnetic potential, magnetic flux, and magnetic reluctance [2]. In magnetic circuits where a permanent magnet is utilized, a magnetic flux source is used to represent the permanent magnet. Consider two parallel equipotential plates as shown in Fig. 4.5. The magnetic potential on the equipotential plates are  $F_1$  and  $F_2$ , where  $F_1 > F_2$ . The difference in the magnetic potential of the two equipotential plates generates a uniform field in the space between the two plates, in which the flow of flux from the higher potential to the lower potential occurs. The space between the two plates is divided into a number of flux tubes that are perpendicular to the plates. Each flux tube is defined to carry the same amount of flux, thus they have the same flux density. The flux lines as shown in Fig. 4.5 are perpendicular to the plates and in parallel to the flux density vector at each point. The density of the flux lines at every point in the space is proportional to the flux density vector magnitude [1].

In electric machine theory, the magnetic potential due to the current carrying conductors, denoted as MMF, is found using Ampere's law as discussed in Chap. 2. In brief, for an air-gap of length  $g$ , a coil of  $N$  turn that carries current  $I$  produces a magnetic field intensity,  $H$ , which has the following relationship with the MMF:

$$H = \frac{MMF}{g} = \frac{NI}{g} \quad (4.1)$$

The magnetic field intensity is related to the flux density,  $B$ , by the property of the material in which the field exists [3]:

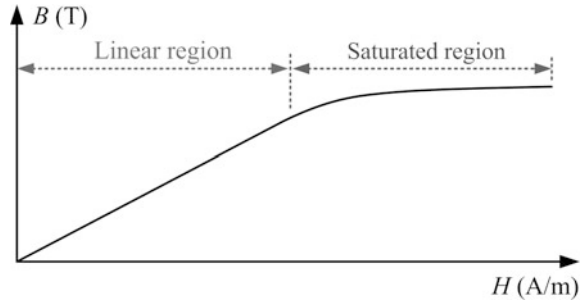
$$B = \mu H \quad (4.2)$$

In the above equation  $\mu$  is the permeability of the material expressed as:

$$\mu = \mu_0 \mu_r \quad (4.3)$$

where  $\mu_0 = 4\pi \times 10^{-7}$  H/m is the permeability of air, and  $\mu_r$  is the relative permeability of the material. Equation (4.2) implies that  $B$  has a linear relationship with  $H$  provided that  $\mu_r$  is constant. In a magnetic material, the relative permeability

**Fig. 4.2** Simplified illustration of the  $B$ - $H$  curve of a magnetic material



is almost constant as long as the material is operating in its linear region well below the saturation knee as shown in Fig. 4.2.

The flux flowing in a flux tube of cross-sectional area  $A$  with the flux density  $B$  is calculated as follows:

$$\varphi = BA \quad (4.4)$$

For an object of non-uniform shape, the flux can be calculated from:

$$\varphi = \int B(A) dA \quad (4.5)$$

where  $dA$  is the surface element parallel to the flux path, and  $B(A)$  is the flux density in the surface element.

Each flux tube represents a magnetic reluctance, which is analogous to resistance in electric circuits. In a magnetic circuit, the amount of flux that flows in a space with reluctance  $\Re$  is obtained from the magnetic potential difference across the reluctance as follows:

$$\varphi = \frac{F_1 - F_2}{\Re} \quad (4.6)$$

Reluctance of an arbitrary non-uniform object can be calculated from:

$$\Re = \int \frac{dl}{\mu(l)A(l)} \quad (4.7)$$

where  $dl$  represents the length element of the object in which the flux is flowing, and  $A(l)$  is the cross-sectional area of the length element, perpendicular to the flux path, and  $\mu(l)$  is the permeability of the length element.

Permeance in a magnetic circuit is defined as:

$$\wp = \frac{1}{\Re} \quad (4.8)$$

Similar to (4.7), an expression for obtaining the permeance is given by:

$$\varphi = \int \frac{\mu(A)}{l(A)} dA \quad (4.9)$$

where  $dA$  is the surface element parallel to the flux path, and  $l(A)$  is the length that the flux travels inside the surface element, and  $\mu(A)$  is the permeability of the surface element. A few examples for calculation of the reluctance and permeance in objects of different shapes are provided in Appendix I.

#### 4.2.1 Properties of the Magnetic Core Material

The flow of flux in a magnetic material and, therefore, performance characteristics of the IPM machine depend on properties of the magnetic core material used in construction of the machine. Finite element model of an unexcited IPM machine is shown in Fig. 4.3. In an IPM rotor the magnets act as individual flux sources. Aimed at maximizing the power density, as it can be observed from Fig. 4.3, the IPM rotor is designed such that it is partially saturated in the bridge areas in order to steer the PM flux into the air-gap. Consequently, the magnetic saturation level and the permeability of the rotor iron vary along the flux paths.

The MEC theory states that the flux distribution in the rotor iron is dependent on the magnetic reluctance of the present routes through which the magnetic flux can close its path. From (4.7), reluctance is inversely proportional with the permeability of the iron core. For a non-uniformly saturated iron, knowledge of the relative permeability at each point of the iron as a function of the flux density is essential to finding the reluctance.

Relative permeability variations with respect to the magnetic saturation level for a common magnetic material M270-35A along with its  $B$ - $H$  curve are shown in

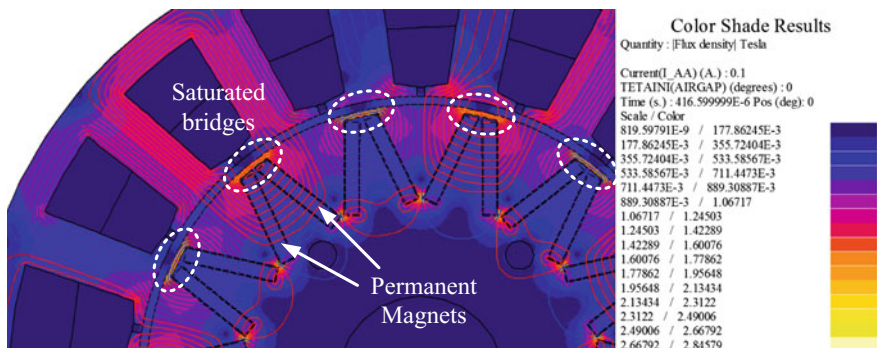


**Fig. 4.3** Finite element analysis model of an unexcited IPM machine

Fig. 4.4. Relative permeability at each point of the steel is a function of the flux density. From Fig. 4.4 it is observed that at low flux densities the relative permeability is high, making the reluctance of the magnetic material negligible. However, as the flux density increases, the relative permeability reduces to small two digit values where the reluctance becomes significant. In the following, an approximation formula is derived for the relative permeability as a function of the flux density in each point of the steel. This formula will be used throughout this chapter for modelling the saturation map of the IPM rotor.

An approximate analytical equation representing the  $B$ - $H$  curve of an isotropic soft magnetic material is given by [4]:

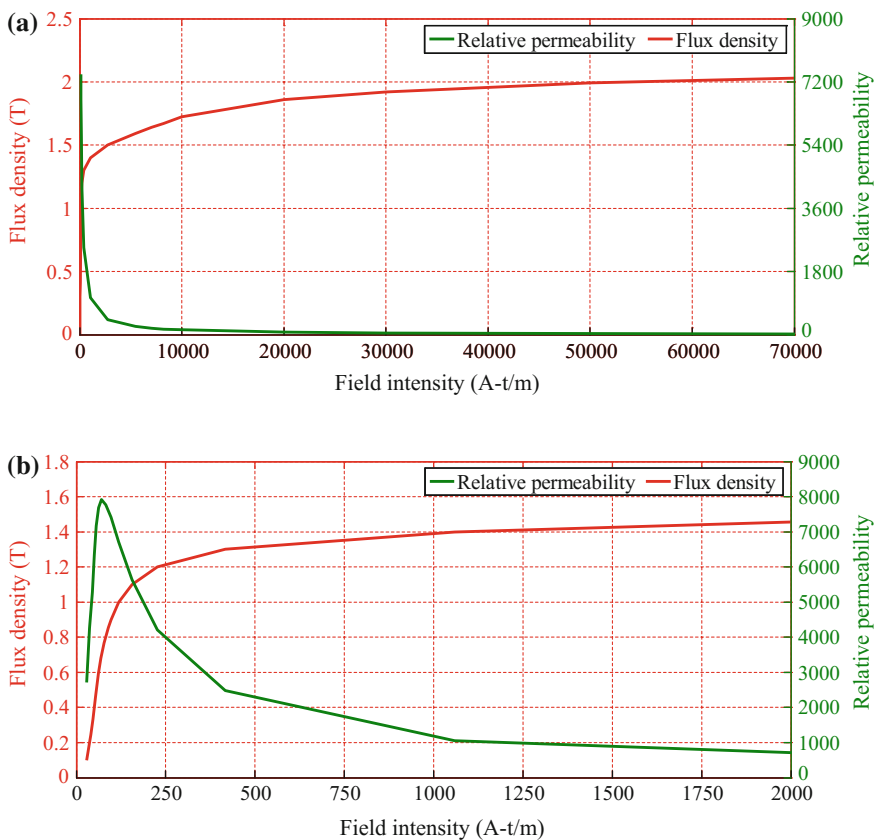


**Fig. 4.4** Variations of the relative permeability with respect to the magnetic saturation level for a common magnetic material M270-35A along with its B-H curve (Manufacturer datasheet). **a** Full range of  $H$ . **b** Zoomed view, limiting  $H$  to 2000  $A\text{-t}/m$

$$B(H) = \mu_0 H + J_s \frac{H_a + 1 - \sqrt{(H_a + 1)^2 - 4H_a(1 - a)}}{2(1 - a)} \quad (4.10)$$

$$H_a = \mu_0 H \frac{\mu_{r0} - 1}{J_s} \quad (4.11)$$

where  $a$  represents the knee adjusting coefficient,  $J_s$  is a coefficient for the saturation magnetization, and  $\mu_{r0}$  indicate the initial relative permeability. These three coefficients should be found such that the produced  $B$ - $H$  curve by (4.10) fits on the experimental  $B$ - $H$  curve of the magnetic material.

From (4.10) and (4.11), after mathematical manipulation,  $H_a$  can be calculated as:

$$H_a = \frac{(\mu_{r0} - 1)(B(2a - 1) - \mu_{r0}(B - J_s))}{2J_s(a - \mu_{r0})} - \frac{(\mu_{r0} - 1)\sqrt{\mu_{r0}^2(B - J_s)^2 - B(2\mu_{r0}(B - J_s) - 4aJ_s(\mu_{r0} - 1) - B)}}{2J_s(a - \mu_{r0})} \quad (4.12)$$

Substitution of (4.12) in (4.11) and rearranging the resultant equation yields the field intensity as a function of the flux density:

$$H = \frac{B(2a - 1) - \mu_{r0}(B - J_s)}{2\mu_0(a - \mu_{r0})} - \frac{\sqrt{\mu_{r0}^2(B - J_s)^2 - B(2\mu_{r0}(B - J_s) - 4aJ_s(\mu_{r0} - 1) - B)}}{2\mu_0(a - \mu_{r0})} \quad (4.13)$$

From (4.2) and (4.3), relative permeability is given by:

$$\mu_r = \frac{B}{\mu_0 H} \quad (4.14)$$

Relative permeability as a function of the flux density can be found by substitution of (4.13) in (4.14) as follows:

$$\mu_r(B) = \frac{2B(a - \mu_{r0})}{B(2a - 1) + \mu_{r0}(J_s - B) - \sqrt{\mu_{r0}^2(J_s - B)^2 + B(2\mu_{r0}(J_s - B) + 4aJ_s(\mu_{r0} - 1) + B)}} \quad (4.15)$$

Now, by calculating the magnetic flux density at each point of the rotor iron, the corresponding relative permeability can be found using (4.15).

### 4.3 Geometrical Relationships in a V-shaped IPM Rotor

Magnetic saturation distribution in an IPM rotor and ultimately the machine characteristics strictly depend on the rotor geometry. In this section, geometrical relationships in a V-shaped IPM rotor are derived which will be used throughout the rest of this chapter for formulation of the non-uniform distribution of magnetic saturation in the iron core.

A V-shaped IPM rotor as illustrated in Fig. 4.5 is considered as a general case. Each pole comprises two magnets that are located in the form of letter “V”. The parameters shown in Fig. 4.5 are:

- $\gamma$  Inner pole-arc, that is defined as the inner width angle of a pole (deg.).
- $\alpha_p$  Outer pole-arc, that is defined as the outer width angle of a pole (deg.).
- $\theta_z$  Pole-pitch, defined as  $360^\circ/P$ , with  $P$  being the number of poles (deg.).
- $B$  V-angle, that is the angle between the two magnets of a pole (deg.).
- $W_{PM}$  Width of the magnet (m).
- $l_{PM}$  Length of the magnet (m).
- $R_r$  Rotor radius (m).
- $C$  Outmost Inner length between the magnet edges in a V-shaped pole (m)
- $l_g$  Inmost Inner length between the two edges of the magnets in a V-shaped pole (m).

A more detailed schematic of a single pole in which the diameters are exaggerated is shown in Fig. 4.6. In this figure the green arc crosses the two outer edges of the magnets and is of radius

$$R_b = R_r - l_1 \quad (4.16)$$

where  $l_1$  is the width of the iron bridge. The angle  $\alpha$  in Fig. 4.6 is the inner angle that the magnet makes with the rotor surface. Most of the geometrical parameters of Fig. 4.6 are interlinked, among which the angles  $\alpha$ ,  $\beta$ , and  $\gamma$  will be derived as a function of the main parameters of Fig. 4.6 which are  $W_{PM}$ ,  $l_{PM}$ ,  $C$ ,  $l_g$ ,  $R_r$  and  $l_1$ .

**Fig. 4.5** Schematic showing the structure and different geometrical parameters for V-shaped IPM rotor with 4 poles

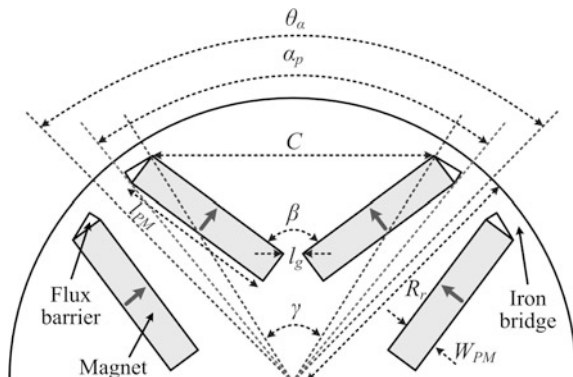
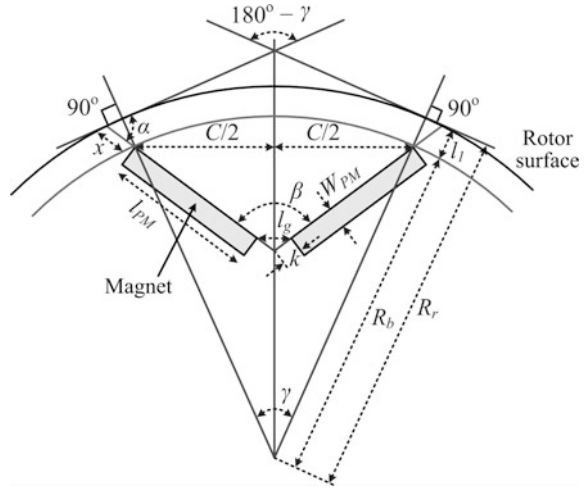


**Fig. 4.6** Geometry of a single V-shaped pole. The diameters are exaggerated



From Fig. 4.6, a system of equations with two variables can be written as:

$$\begin{cases} 2(l_{PM} + k) \sin\left(\frac{\beta}{2}\right) = C \\ 2k \cdot \sin\left(\frac{\beta}{2}\right) = l_g \end{cases} \quad (4.17)$$

Solving (4.17) for  $k$  and  $C$  yields:

$$\begin{cases} k = \frac{l_g}{2 \sin\left(\frac{\beta}{2}\right)} \\ C = 2l_{PM} \sin\left(\frac{\beta}{2}\right) + l_g \end{cases} \quad (4.18)$$

The V-angle,  $\beta$ , can be found from the above equation as:

$$\beta = 2 \sin^{-1} \left( \frac{C - l_g}{2l_{PM}} \right) \quad (4.19)$$

The inner pole-arc angle,  $\gamma$ , can be found from Fig. 4.6 as follows:

$$\gamma = 2 \sin^{-1} \left( \frac{C}{2R_b} \right) \quad (4.20)$$

Substitution of (4.16) in (4.20) gives:

$$\gamma = 2 \sin^{-1} \left( \frac{C}{2(R_r - l_1)} \right) \quad (4.21)$$

All inner angles of a quadrangle sum up to  $360^\circ$ . Therefore, in the inner quadrangle of Fig. 4.6 with the magnets on its edges, the following relationship stands:

$$2\alpha + \beta + 180^\circ - \gamma = 360^\circ \quad (4.22)$$

Hence,

$$\alpha = 90^\circ + \left( \frac{\gamma - \beta}{2} \right) \quad (4.23)$$

Substitution of (4.19) and (4.21) in (4.23) yields:

$$\alpha = 90^\circ + \sin^{-1} \left( \frac{C}{2(R_r - l_1)} \right) - \sin^{-1} \left( \frac{C - l_g}{2l_{PM}} \right) \quad (4.24)$$

The following trigonometric relations hold true:

$$\sin^{-1}(a) + \sin^{-1}(b) = \sin^{-1} \left( a\sqrt{1-b^2} + b\sqrt{1-a^2} \right) \quad (4.25)$$

$$\sin^{-1}(-a) = -\sin^{-1}(a) \quad (4.26)$$

$$\cos^{-1}(a) = 90^\circ - \sin^{-1}(a) \quad (4.27)$$

Note that if  $a > 0$ ,  $b > 0$  and  $\sqrt{a^2+b^2} > 0$ , the left hand term in (4.25) may produce an angle greater than  $90^\circ$  while the right hand term is an angle between  $90^\circ$  and  $-90^\circ$ . Under such conditions (4.25) should be modified as follows:

$$\sin^{-1}(a) + \sin^{-1}(b) = 180^\circ - \sin^{-1} \left( a\sqrt{1-b^2} + b\sqrt{1-a^2} \right) \quad (4.28)$$

From (4.25) and (4.26), the following mathematical manipulations are made:

$$\begin{aligned} & \sin^{-1} \left( \frac{C}{2(R_r - l_1)} \right) - \sin^{-1} \left( \frac{C - l_g}{2l_{PM}} \right) \\ &= \sin^{-1} \left( \frac{C}{2(R_r - l_1)} \right) + \sin^{-1} \left( \frac{l_g - C}{2l_{PM}} \right) \\ &= \sin^{-1} \left( \frac{C}{2(R_r - l_1)} \sqrt{1 - \left( \frac{l_g - C}{2l_{PM}} \right)^2} + \frac{l_g - C}{2l_{PM}} \sqrt{1 - \left( \frac{C}{2(R_r - l_1)} \right)^2} \right) \\ &= \sin^{-1} \left( \frac{C}{2(R_r - l_1)} \sqrt{1 - \frac{(l_g - C)^2}{4l_{PM}^2}} + \frac{l_g - C}{2l_{PM}} \sqrt{1 - \frac{C^2}{4(R_r - l_1)^2}} \right) \end{aligned}$$

$$\begin{aligned}
&= \sin^{-1} \left( \frac{C}{2(R_r - l_1)} \sqrt{\frac{4l_{PM}^2 - (l_g - C)^2}{4l_{PM}^2}} + \frac{l_g - C}{2l_{PM}} \sqrt{\frac{4(R_r - l_1)^2 - C^2}{4(R_r - l_1)^2}} \right) \\
&= \sin^{-1} \left( \frac{C}{4(R_r - l_1)l_{PM}} \sqrt{4l_{PM}^2 - (l_g - C)^2} + \frac{l_g - C}{4(R_r - l_1)l_{PM}} \sqrt{4(R_r - l_1)^2 - C^2} \right) \\
&= \sin^{-1} \left( \frac{1}{4(R_r - l_1)l_{PM}} \left( C \sqrt{4l_{PM}^2 - (l_g - C)^2} + (l_g - C) \sqrt{4(R_r - l_1)^2 - C^2} \right) \right)
\end{aligned} \tag{4.29}$$

Substitution of (4.29) in (4.24) and using (4.27) yields:

$$\alpha = \cos^{-1} \left( \frac{1}{4(l_1 - R_r)l_{PM}} \left( C \sqrt{4l_{PM}^2 - (l_g - C)^2} + (l_g - C) \sqrt{4(l_1 - R_r)^2 - C^2} \right) \right) \tag{4.30}$$

#### 4.4 Geometric Analysis of the PM Flux Paths and Non-uniform Distribution of Saturation in a V-shaped IPM Rotor

The flux of the embedded magnets in an IPM rotor makes it to become non-uniformly saturated. In an IPM rotor, the PM flux is typically dominant and the effect of the stator flux on the non-uniform distribution of saturation is minimal. A detailed analysis of the PM flux paths inside the rotor iron is presented in this section, based on which a magnetic saturation map for the rotor iron is formulated. The V-shaped IPM rotor shown in Fig. 4.5 is considered as a general case.

Each embedded permanent magnet in the IPM rotor is a distinct flux source. MEC theory implies that magnetic flux closes its path through a route with the lowest reluctance. For an object of relative permeability  $\mu_r$ , cross-sectional area  $A$ , and length  $l$ , the magnetic reluctance is found from (4.7) as:

$$\mathfrak{R} = \frac{l}{\mu_0 \mu_r A} \tag{4.31}$$

The flux passing through a flux route in an MEC circuit with many parallel flux routes, is inversely proportional to route reluctance. In Fig. 4.5, the iron bridge in the rotor, if assumed unsaturated, is the flux route with the lowest reluctance. Therefore, a substantial part of each PM flux tangentially crosses the iron bridge, resulting in its saturation. From Fig. 4.4 a high flux density in the bridge area decreases its relative permeability. Accordingly, the bridge area becomes saturated to the point that its magnetic reluctance becomes greater than other available flux routes. Therefore, the remaining residual flux of the magnets passes through

alternative routes proportional to their magnetic reluctance. This explains the reason behind the complicated flux paths in IPM rotors.

An illustrative model for the saturation map of a V-shaped IPM machine and the PM flux paths inside the rotor is shown in Fig. 4.7. In this figure, the flux lines are categorized into 5 different sets:

- Flux lines 1 and 2 represent the leakage flux that goes through the flux barriers. This group partially contributes to saturation of the iron bridge.
- Flux line 3 completely passes through the iron bridge and is the dominant contributor to the iron bridge saturation.
- Flux line 4 is the flux that crosses both the iron bridge and the air-gap, thus it partially contributes to the iron bridge saturation. This flux tangentially crosses the iron bridge, after which it radially passes through the air-gap.
- Flux line 5 goes through the pole-cap area and then crosses the air-gap.

The saturated regions in Fig. 4.7 are shaded with green. The shading intensity indicates the saturation intensity, i.e. magnetic flux density, in the rotor iron. Accordingly, it is observed from Fig. 4.7 that the highest magnetic saturation occurs at the iron bridge, and with an increasing distance from the bridge area the saturation intensity decreases, making the saturation level in the pole-cap area not uniform. Fig. 4.8 details the geometric parameters of Fig. 4.7. In this figure,  $x$  represents the length of a line that extends from the PM edge and criss-crosses the rotor circumference,  $\alpha$  is the angle between the PM edge and the rotor circumference,  $R_1$  indicates distance of the flux barrier edge from the pole-pitch origin, and  $l_1$  and  $l_2$  specify the two different heights of the iron bridge at its edges. In Fig. 4.7 the

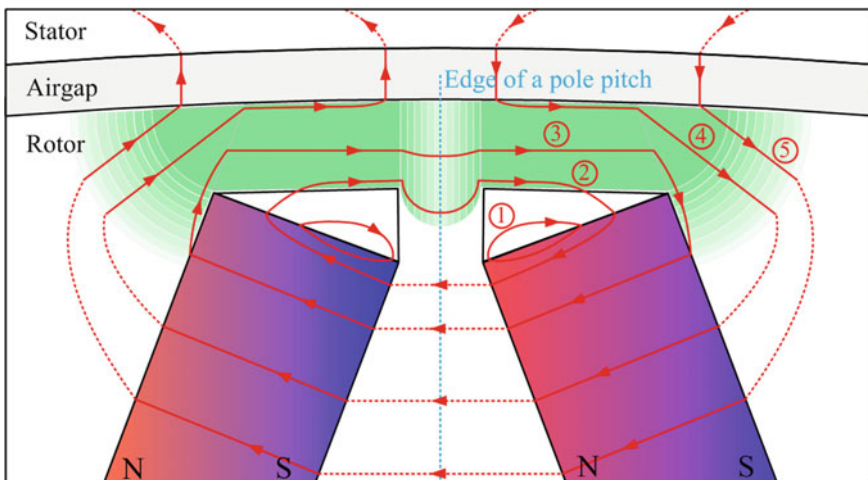


**Fig. 4.7** An illustrative model for the saturation map of a V-shaped IPM machine and the PM flux paths inside the rotor. The green-shaded area indicates magnetic saturation and its intensity

distribution of saturation is symmetrical, thus as shown in Fig. 4.8, the saturated regions are distinguished into four areas:

$$\text{Region 1 : } 0 \leq \theta_r < \theta_1$$

$$\text{Region 2 : } \theta_1 \leq \theta_r < \theta_2$$

$$\text{Region 3 : } \theta_2 \leq \theta_r < \theta_3$$

$$\text{Region 4 : } \theta_3 \leq \theta_r < \theta_4$$

where  $\theta_r$ ,  $\theta_1$ ,  $\theta_2$ ,  $\theta_3$ , and  $\theta_4$  are angles on the rotor circumference measured from the pole-pitch edge in mechanical radians. From Fig. 4.8,  $\theta_1$  indicates the angle for the inner edge of the fully saturated region of the iron bridge denoted by region 2,  $\theta_2$  is the angle at which the line extended from the PM criss-crosses the rotor circumference,  $\theta_3$  is associated with the angle on the rotor circumference at which an arc with radius  $x$  and centering from  $\theta_2$  intersects the rotor circumference, and  $\theta_4$  is the angle at which the magnetic saturation of the rotor iron becomes negligible. Before proceeding with the calculation of the flux density in the specified four regions, the key angles,  $\theta_1$ ,  $\theta_2$ ,  $\theta_3$ , and  $\theta_4$  in Fig. 4.8 are determined. Saturated region 1 stretches from the origin to angle  $\theta_1$  on the rotor circumference, where the saturated region 2 begins. In IPM rotors where the angle  $\theta_1$  is quite small, the following relationship holds true:

$$R_1 \approx \theta_1(R_r - l_1) \quad (4.32)$$

Hence,

$$\theta_1 = \frac{R_1}{R_r - l_1} \quad (4.33)$$

The angle  $\theta_2$  at which the saturated region 2 ends and the saturated region 3 begins, is the intersection angle between the rotor surface and a surface that is extending from the magnet as shown in Figs. 4.6 and 4.8. Region 2 of Fig. 4.8 is

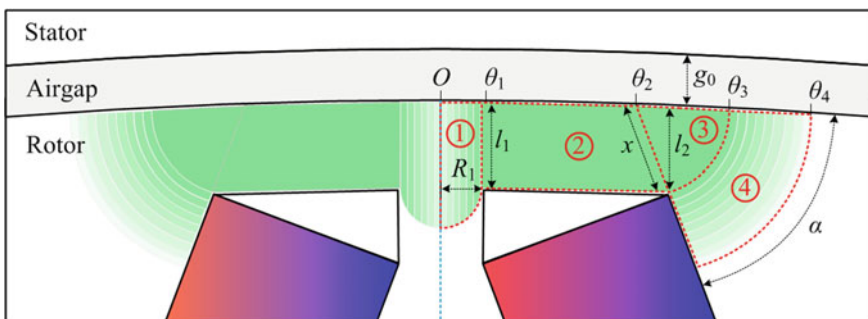
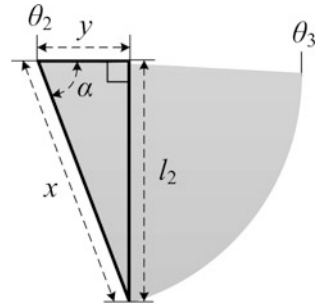


**Fig. 4.8** Classification of the saturated regions in the proposed magnetic saturation model for a V-shaped IPM rotor. The green area indicates the saturation and its intensity

**Fig. 4.9** Dimensions of saturated region 2



redrawn in Fig. 4.9. Side  $y$  of the right triangle of region 2 in Fig. 4.9 is small enough to be approximated by:

$$y = \Delta\theta \cdot R_r \quad (4.34)$$

where  $\Delta\theta$  is the angle on the rotor circumference corresponding to length  $y$ .

In the right triangle of Fig. 4.9,  $y$  can be found by:

$$y = \frac{l_2}{\tan(\alpha)} \quad (4.35)$$

The angle  $\alpha$  can be calculated by (4.30). From (4.34) and (4.35),  $\Delta\theta$  is obtained as:

$$\Delta\theta = \frac{l_2}{R_r \tan(\alpha)} \quad (4.36)$$

According to Figs. 4.5 and 4.8, the angle  $\theta_2$  is equal to:

$$\theta_2 = \frac{\theta_\alpha - \gamma}{2} - \Delta\theta \quad (4.37)$$

Substitution of (4.36) in (4.37) yields:

$$\theta_2 = \frac{\theta_\alpha - \gamma}{2} - \frac{l_2}{R_r \tan(\alpha)} \quad (4.38)$$

Angle  $\theta_3$  in Fig. 4.8 can be found similar to  $\theta_2$  as follows:

$$\theta_3 \approx \theta_2 + \frac{x}{R_r} \quad (4.39)$$

and

$$x = \frac{l_2}{\sin(\alpha)} \quad (4.40)$$

Substitution of (4.38) and (4.40) in (4.39) yields:

$$\theta_3 \approx \frac{\theta_\alpha - \gamma}{2} + \frac{l_2(1 - \cos(\alpha))}{R_r \sin(\alpha)} \quad (4.41)$$

A method for determination of  $\theta_4$  is explained in the following. Among the four specified regions in Fig. 4.8, regions 2 and 3 are fully saturated, such that:

$$B(\theta_r) = B_{sat}, \quad \theta_1 \leq \theta_r < \theta_3 \quad (4.42)$$

where,  $B_{sat}$  is the saturation flux density in the  $B$ - $H$  curve of the utilized magnetic core material in the rotor. As an example,  $B$ - $H$  curve of the sample magnetic core material M270-35A given in Fig. 4.4, has a saturation flux density of  $B_{sat} \approx 2.0$  T. With an increasing distance from regions 2 and 3, the saturation intensity in regions 1 and 4 slowly decreases. These regions are separately shown in Fig. 4.10. According to the proposed saturation map, region 1 is divided into vertical differential sectors, and region 4 comprises radial arcs of differential radius with their center being at  $\theta_2$ . According to (4.4) and (4.5), flux density in region 1 reduces along the flux path relative to the cross-sectional area of the vertical differential sectors, while flux density in region 4 decreases relative to the associated differential arc circumference. In Fig. 4.10b,  $\theta_4$  is the rotor peripheral angle associated with the differential arc at which flux density decreases below the threshold that pushes the iron into saturation. This angle is dependent on the  $B$ - $H$  curve of the rotor magnetic material as well as the geometry of the machine. In areas beyond the differential arc at  $\theta_4$ , relative permeability of the magnetic material becomes high enough for having an insignificant reluctance with a negligible magnetic potential drop across it.

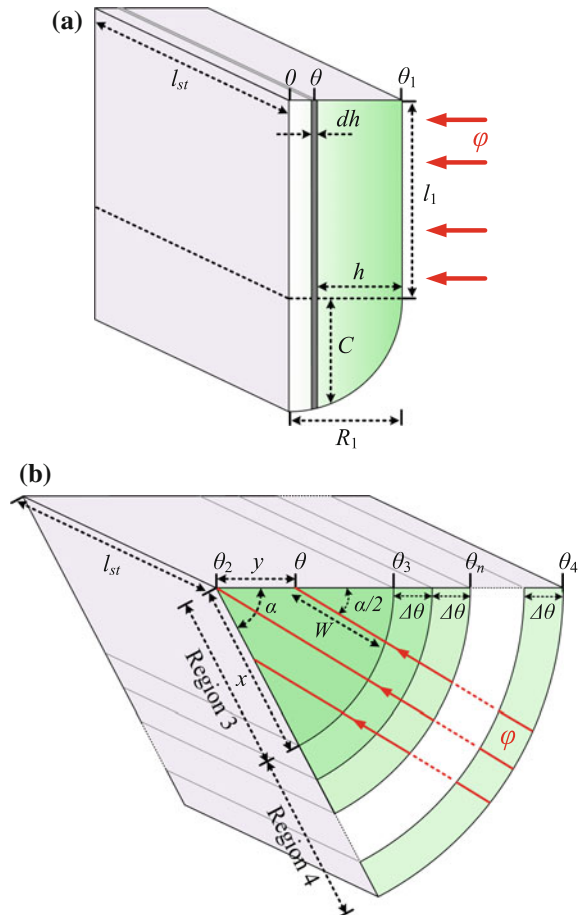
From Fig. 4.10a, flux lines in region 1 of the rotor are tangential and merely sourcing from region 2 with a constant value of  $B_{sat} \cdot l_1 \cdot l_{st}$ , with  $l_{st}$  being the stack length. According to (4.4), in the differential elements of region 1, flux density is found by dividing the passing flux through each element by its cross-section. As  $\theta_r$  gets closer to the origin, flux density reduces due to the increase in the cross-sectional area. Accordingly, for the differential element  $d\theta$  located at angle  $\theta_r$ , with the angular width of  $d\theta$  in region 1, flux density is given by:

$$B(\theta_r) = \frac{\varphi_{in}}{dA(\theta_r)}, \quad 0 \leq \theta_r < \theta_1 \quad (4.43)$$

where  $\varphi_{in}$  is the input flux to region 1,

$$\varphi_{in} = l_1 l_{st} B_{sat}, \quad 0 \leq \theta_r < \theta_1 \quad (4.44)$$

**Fig. 4.10** Saturated regions of the illustrative saturation map for a V-shaped IPM rotor. **a** Saturated region 1. **b** Saturated regions 3 and 4



and  $dA(\theta_r)$  is the differential element cross-sectional area:

$$dA(\theta_r) = (l_1 + C(\theta_r))l_{st}, \quad 0 \leq \theta_r < \theta_1 \quad (4.45)$$

In (4.45),  $C$  as shown in Fig. 4.10a is a function of  $\theta_r$ :

$$C(\theta_r) = \sqrt{h(\theta_r)(2R_1 - h(\theta_r))} \quad (4.46)$$

and  $h$  is

$$h(\theta_r) \approx R_r(\theta_1 - \theta_r). \quad (4.47)$$

Substitution of (4.44)–(4.47) in (4.43) yields:

$$B(\theta_r) = \frac{l_1}{l_1 + \sqrt{R_r(\theta_1 - \theta_r)(2R_1 - R_r(\theta_1 - \theta_r))}} B_{sat}, \quad 0 \leq \theta_r < \theta_1 \quad (4.48)$$

As evident from Fig. 4.10b, saturation intensity in region 4 reduces with increasing distance from the iron bridge. Open-circuit air-gap flux density is the result of the flux that passes through regions 3 and 4, partially crossing the airgap into the stator iron. This yields a trapezoidal form for the open-circuit air-gap flux density as shown in Fig. 4.11 [5]. The angles in Fig. 4.11 can be approximated based on the illustrative model of Fig. 4.7 as  $\delta_1 = \theta_1$ ,  $\delta_1 + \delta_2 = \theta_4$ . Accordingly, these angles can be used in an analytical procedure to obtain the magnitude  $B_m$  in Fig. 4.11, as explained in the following. The air-gap flux density for the region  $(\delta_1, \delta_1 + \delta_2)$  can be expressed as:

$$B_g(\theta_r) = \frac{B_m}{\delta_2} (\theta_r - \delta_1), \quad \delta_1 < \theta_r < \delta_1 + \delta_2 \quad (4.49)$$

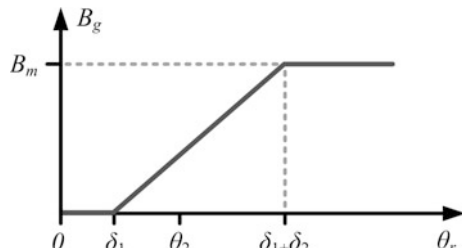
From (4.5), in region 4 of Fig. 4.10b the magnetic flux that crosses the differential arc at angle  $\theta_n$ , is approximated by:

$$\varphi_n(\theta_n) \approx B_{sat} \alpha x l_{st} + \int_{\theta_3}^{\theta_n} B_g(\theta) R_r l_{st} d\theta, \quad \theta_3 \leq \theta_n < \theta_4 \quad (4.50)$$

where  $R_r$  is the rotor radius. In (4.50), the first term represents the flux that passes through region 4 into region 3. This flux is found by multiplying the cross-section of the border of the two regions by  $B_{sat}$ . The second term in (4.50) is the flux that crosses the airgap from region 4 into the stator iron. This flux is found by integrating the air-gap flux density shown in Fig. 4.11. The integral in (4.50) is solved as:

$$\varphi_n(\theta_n) \approx B_{sat} \alpha x l_{st} + \frac{B_m R_r l_{st}}{\delta_2} \left( \frac{1}{2} (\theta_n^2 - \theta_3^2) - \delta_1 (\theta_n - \theta_3) \right), \quad \theta_3 \leq \theta_n < \theta_4 \quad (4.51)$$

**Fig. 4.11** Schematic of the open-circuit air-gap flux density variations in an IPM machine



The cross-section of the differential arc in region 4 at angle  $\theta_n$  is:

$$dA(\theta_n) = \alpha R_r(\theta_n - \theta_2) l_{st} \quad (4.52)$$

For the differential arc located at angle  $\theta_n$ , flux density is found by dividing (4.51) by the cross-section of the differential arc, (4.52):

$$\begin{aligned} B(\theta_n) &= \frac{B_{sat} \alpha x}{\alpha R_r(\theta_n - \theta_2)}, & \theta_3 \leq \theta_n < \theta_4 \\ &+ \frac{B_m}{\delta_2 \alpha (\theta_n - \theta_2)} \left( \frac{1}{2} (\theta_n^2 - \theta_3^2) - \delta_1 (\theta_n - \theta_3) \right) \end{aligned} \quad (4.53)$$

Flux density for every point of a V-shaped IPM rotor, as specified in Fig. 4.7, can now be analytically calculated from (4.42), (4.48) and (4.53). Finding relative permeability at every point of the rotor iron is essential to having complete model for the non-uniform saturation model. By calculating the flux density at every point of the rotor iron, the corresponding relative permeability can be easily found using (4.15). The angle  $\theta_4$  in the saturation model can be found from (4.53) and (4.15), and is the angle at which the relative permeability becomes high enough to yield a negligible reluctance in the differential arcs of region 4. In Chap. 5, the associated reluctance to the differential arcs of region 4 will be calculated and a methodology to determine  $\theta_4$  will be formulated with example study-cases to follow.

It has to be noted that the proposed saturation model for the rotor iron is general and can be applied to any V-shaped IPM rotor regardless of the stator type.

## 4.5 Calculation of the PM Flux Density Distribution in the Air-Gap

Calculation of the PM flux density distribution in the air-gap of PMSMs is essential for the prediction of the machine's performance characteristics such as back-EMF and torque. Three methods exist for obtaining the distribution of the PM flux density in the air-gap:

- Finite-element analysis (FEA),
- Direct analytical methods,
- Magnetic equivalent circuits (MEC).

Among the three mentioned methods, finite-element analysis is most accurate [6], however it is time consuming and not fast and flexible enough for investigating the effect of the machine geometry on the PM flux density. Direct analytical methods are preferred for calculating the flux density distribution in the air-gap by analytically solving the Laplacian or quasi-Poissonian field equations in the air-gap, magnets and slots. This requires knowledge of the boundary conditions for the interface of these regions. Direct analytical techniques have been widely used for

inset PM and surface-mount rotors by assuming negligible magnetic reluctances for the stator and rotor yoke [7–10]. In IPM rotors due to the embedded magnets inside the rotor and existence of the saturated iron bridge, the boundary conditions become too complex, impeding analytical solution of the Laplacian or quasi-Poissonian field equations. Thus, techniques that are based on MEC of the rotor are preferred in IPM machines [11–13]. Analogous to the direct analytical techniques, in methods that are based on MEC, negligible reluctances are often assumed for the stator and rotor yoke for simplicity [11–13]. Moreover, in the magnetic equivalent circuit of an IPM machine, the fully saturated iron bridges are often modelled by flux sources that have a constant flux density of  $B_{sat}$ , obtained from the  $B$ - $H$  curve of the rotor magnetic material. Such assumptions in the calculation of the air-gap PM flux density usually cause negligible errors [11–16].

The state of the art model for the PM flux density, as well as a more accurate model that is based on the proposed saturation map of an IPM rotor in Sect. 4.4, are briefed in the following. Both these models are based on the magnetic equivalent circuit of the PMSM. An example case-study for the calculation of the PM flux density in a prototype IPM machine are also provided.

#### 4.5.1 State of the Art Rectangular Model for PM Flux Density

PM flux density distribution in the air-gap is strictly dependent on the rotor topology. Here only single-layer IPM machines with V-shaped magnets are of interest. For such rotor topologies, the PM flux density is of trapezoidal form [6]. However, in the literature the rectangular PM flux density model that is used for inset and surface-mount PM rotors is commonly adopted for IPM rotors [12, 13, 17]. An IPM rotor topology along with the rectangular PM flux density is shown in Fig. 4.12a and b, respectively.

Assuming a slot-less stator, for a counterclockwise rotating rotor, the rectangular PM flux density as shown in Fig. 4.12b can be expressed using Fourier series as:

$$B_{PM}(t, \theta_s) = \sum_{n=\frac{P}{2}k} B_{max,n} \cos(n\omega_r t - n\theta_s), \quad k = 1, 3, 5, \dots \quad (4.54)$$

where  $\omega_r$  is the mechanical angular speed, and  $B_{max,n}$  is the amplitude of the  $n$ th spatial harmonic component of the PM flux density, given by:

$$B_{max,n} = \frac{P}{2} \frac{4B_m}{n\pi} \sin\left(\frac{n \cdot P}{4}\gamma\right), \quad n = \frac{P}{2}k \quad (4.55)$$

From (4.54) it is observed that all spatial harmonics of the PM flux density are synchronous with the rotor motion.

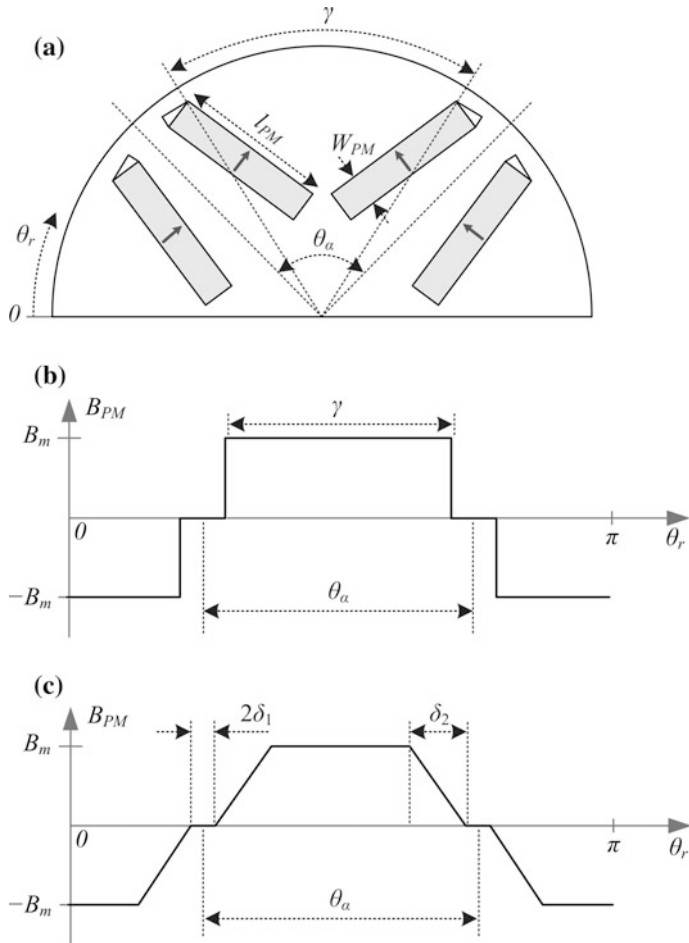


**Fig. 4.12** **a** IPM rotor. **b** Rectangular PM flux density. **c** Trapezoidal PM flux density

The PM flux due to a single magnet that is projected into the air-gap can be calculated from:

$$\varphi_g = \int_0^{2\pi/(2P)} B_g(\theta) \left( R_r + \frac{g}{2} \right) l_{st} d\theta \quad (4.56)$$

Solving the above integral based on Fig. 4.12b gives:

$$\varphi_g = \frac{B_m}{2} \gamma \left( R_r + \frac{g}{2} \right) l_{st} \quad (4.57)$$

The value of  $B_m$  for the rectangular PM flux density can be found by rearranging (4.57) as follows:

$$B_m = \frac{2\varphi_g}{\gamma(R_r + \frac{g}{2})l_{st}} \quad (4.58)$$

In order to find  $B_m$  in Fig. 4.12b and (4.55), the magnetic equivalent circuit of the IPM rotor should be determined. Then by employing an analogy to that of Kirchhoff's current law, the air-gap flux that is being projected out of the rotor into the stator is calculated. The value of  $B_m$  can then be found using (4.58).

#### 4.5.2 Proposed Trapezoidal Model for PM Flux Density

As explained earlier, PM flux density distribution of the IPM rotor of Fig. 4.12a is of a trapezoidal form as shown in Fig. 4.12c. For a counter-clockwise rotor in a slot-less stator, the trapezoidal PM flux density of Fig. 4.12c is described using a Fourier series as:

$$B_{PM}(t, \theta_s) = \sum_{n=\frac{P}{2}k} B_{\max,n} \sin(n\omega_r t - n\theta_s), \quad k = 1, 3, 5, \dots \quad (4.59)$$

where, the amplitude of the  $n$ th spatial harmonic component of the PM flux density,  $B_{\max,n}$  is given by [18, 19]:

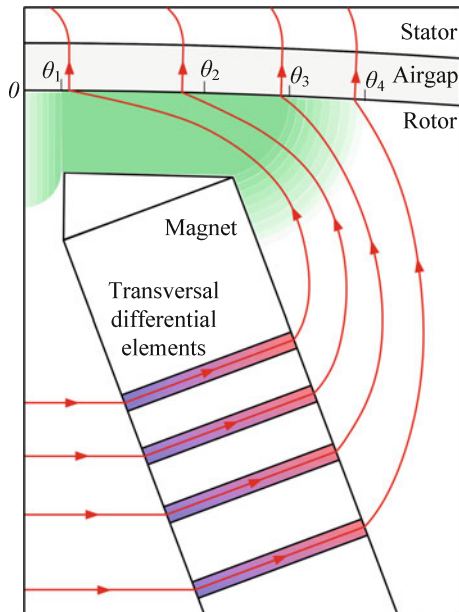
$$B_{\max,n} = \frac{P}{2} \frac{4B_m}{n^2 \pi \delta_2} (\sin(n(\delta_1 + \delta_2)) - \sin(n\delta_1)), \quad n = \frac{P}{2}k \quad (4.60)$$

In (4.60),  $\delta_1$  and  $\delta_2$  are the adjusting coefficients of the trapezoid as shown in Fig. 4.12c. These coefficients have a major impact on the accuracy of the PM flux density model and can be obtained from the proposed non-uniform saturation model in Sect. 4.4. From Fig. 4.12c, it is observed that in the span  $2\delta_1$ , PM flux density is assumed zero. This complies with the region between 0 and  $\theta_1$  in the non-uniform saturation model of Figs. 4.7 and 4.8 where no PM flux leaks into the air-gap. Therefore, a good approximation for  $\delta_1$  is:

$$\delta_1 = \theta_1 \quad (4.61)$$

and  $\theta_1$  is given by (4.33). In the span  $\delta_2$ , the PM flux density increases from zero to its maximum value,  $B_m$ . According to the non-uniform saturation model of Figs. 4.7 and 4.8, this increase is expected in the region starting from  $\theta_1$  and ending at  $\theta_4$ . Assume that the magnets are comprised of transversal differential elements as shown in Fig. 4.13. Each transversal differential element of the magnet is propagating the same amount of flux into the iron. Therefore, all the differential elements

**Fig. 4.13** Non-uniform saturation model of the IPM rotor along with the flux that radially crosses the air-gap. The magnet is divided into differential elements, each of them propagating the same amount of flux into the iron core



are having the same magnetic potential across them. The flux associated with each differential element is shown in Fig. 4.13. Evidently, the flux that is crossing the air-gap closer to  $\theta_1$  is passing through a more saturated region compared with the other flux lines. With distance from  $\theta_1$  toward  $\theta_4$ , as evident from Fig. 4.13, the amount of saturated region that the air-gap flux is passing through decreases. Beyond  $\theta_4$ , the flux that is radially crossing the air-gap passes through no saturated region. Therefore, according to (4.31), the reluctance of the flux path decreases as the peripheral angle  $\theta$ , moves toward  $\theta_4$ . Each transversal differential element of the magnet has the same magnetic potential, therefore, according to (4.6), a decrease in the reluctance of the flux path by moving toward  $\theta_4$  causes the associated flux to increase. Therefore, by moving toward  $\theta_4$  the flux that is being leaked into the air-gap is increasing and beyond  $\theta_4$  it becomes constant. This will be discussed further in Chap. 5. Based on the above explanation, for the trapezoidal air-gap flux density of Fig. 4.12c, we have:

$$\delta_1 + \delta_2 = \theta_4 \quad (4.62)$$

By substituting (4.61) in (4.62),  $\delta_2$  can be found:

$$\delta_2 = \theta_4 - \theta_1 \quad (4.63)$$

Once the adjusting coefficients of the trapezoidal PM flux density are found using the proposed non-uniform saturation model, (4.61) and (4.63), the remaining parameter in (4.60),  $B_m$ , can be calculated. The PM flux due to a single magnet that

is being projected into the air-gap can be found by solving the integral (4.56) for the trapezoidal PM flux density of Fig. 4.12c as follows:

$$\varphi_g = \frac{B_m}{2} \left( \frac{2\pi}{P} - 2\delta_1 - \delta_2 \right) \left( R_r + \frac{g}{2} \right) l_{st} \quad (4.64)$$

Rearranging (4.64) yields  $B_m$  for the trapezoidal PM flux density:

$$B_m = \frac{\varphi_g}{\left( \frac{\pi}{P} - \delta_1 - \frac{\delta_2}{2} \right) \left( R_r + \frac{g}{2} \right) l_{st}} \quad (4.65)$$

In order to find  $B_m$  using (4.65), the air-gap flux density due to a single magnet should be first calculated by employing an analogy to that of Kirchhoff's current law in the magnetic equivalent circuit of the unexcited PMSM. Then, by substituting all the variables in (4.65),  $B_m$  is obtained.

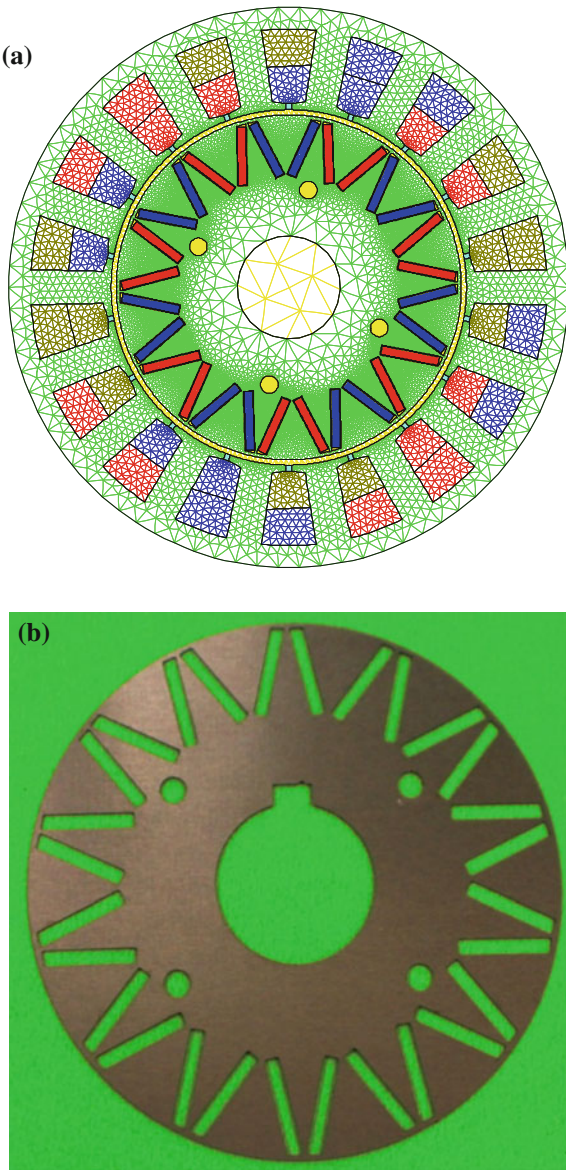
## 4.6 Case-Study: Validation of the Proposed Models

A case-study is presented in this section for calculation of the proposed non-uniform saturation model of a prototype IPM machine. The magnetic equivalent circuit of the prototype machine when it is unexcited is formed. PM flux density distribution in the air-gap is found using the trapezoidal PM flux density model which is based on the non-uniform saturation model and the magnetic equivalent circuit of the IPM machine. The results are compared against the PM flux densities that are obtained based on the prior art rectangular model and the FEA model of the IPM machine in CEDRAT FLUX 2D. Lastly, the generated back-EMF using the calculated PM flux densities are obtained and compared against the experimentally measured back-EMF of the prototype IPM machine.

### 4.6.1 Calculation of the Non-uniform Saturation Model and the PM Flux Density

The FEA model of a prototype 14-pole 18-slot IPM machine and a lamination of the manufactured rotor is shown in Fig. 4.14a and b, respectively. The magnetic core material used in construction of the machine is of type M270-35A with its  $B$ - $H$  curve as shown in Fig. 4.4. Main design parameters of the IPM rotor for use in the non-uniform saturation model based on Figs. 4.5 and 4.6 are listed in Table 4.1. The main angles of the non-uniform saturation model of the rotor iron as shown in Figs. 4.5 and 4.6 are calculated from (4.19), (4.21), (4.30), (4.33), (4.38), and (4.41) using the parameters of Table 4.1 as listed in Table 4.2. The angle  $\theta_4$  in Table 4.2 is found by calculating the reluctance of the flux path associated with each rotor

**Fig. 4.14** Prototype FSCW IPM machine. **a** FEA model. **b** A lamination of the manufactured rotor



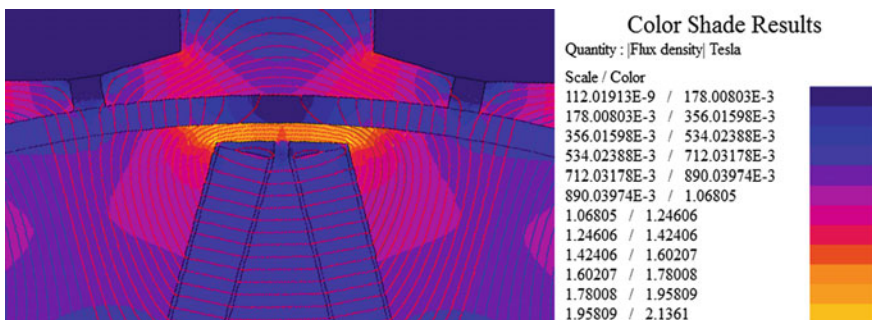
peripheral angle as will be discussed in Chap. 5. Beyond  $\theta_4$  reluctance of the flux paths in the rotor becomes negligible. The saturation map and flux line trajectory for the prototype machine obtained using the FEA model is shown in Fig. 4.15. Evidently, the proposed graphical model of Fig. 4.7 is in close agreement with the FEA results shown in Fig. 4.15.

**Table 4.1** Main design parameters of the prototype FSCW IPM machine

Quantity	Value (m)
$R_r$	$40 \times 10^{-3}$
$l_1$	$0.796 \times 10^{-3}$
$C$	$12.67 \times 10^{-3}$
$l_{PM}$	$12.67 \times 10^{-3}$
$W_{PM}$	$2 \times 10^{-3}$
$l_g$	$0.85 \times 10^{-3}$
$l_{st}$	$79 \times 10^{-3}$
$g$	$1.2 \times 10^{-3}$

**Table 4.2** Main angles for the non-uniform saturation model of the prototype FSCW IPM machine

Quantity	Value
$\alpha$	$72.651^\circ$
$\beta$	$53.920^\circ$
$\gamma$	$18.593^\circ$
$\theta_z$	$25.714^\circ$
$\theta_1$	$0.415^\circ$
$\theta_2$	$3.205^\circ$
$\theta_3$	$4.399^\circ$
$\theta_4$	$4.686^\circ$

**Fig. 4.15** Saturation map and flux line trajectory of the prototype machine obtained by FEA

According to Fig. 4.12c and (4.60), the trapezoidal PM flux density model has three parameters,  $\delta_1$ ,  $\delta_2$  and  $B_m$ . The first two parameters can be found using Table 4.2, (4.61) and (4.63) as follows:

$$\delta_1 = 0.42^\circ$$

$$\delta_2 = 4.27^\circ$$

In order to calculate the remaining parameter,  $B_m$ , the magnetic equivalent circuit of the unexcited machine should be modelled first. This model can be found based on the graphical model of the flux paths as shown in Fig. 4.7. The flux lines associated with a pole-pair of the IPM rotor are shown in Fig. 4.16a and the associated magnetic equivalent circuit is shown in Fig. 4.16b. As can be seen in the magnetic equivalent circuit of Fig. 4.16b, the magnets are represented by constant flux sources in parallel to their reluctance. The reluctances of the magnetic equivalent circuit of Fig. 4.16b are as follows:

$R_r$  Reluctance of the rotor yoke.

$R_s$  Reluctance of the stator yoke.

$R_{PM}$  Reluctance of the permanent magnets.

$R_b$  Reluctance of the flux barrier.

$R_e$  Reluctance of at the end of the permanent magnets.

**Fig. 4.16** A pole-pair in the prototype FSCW IPM machine. **a** Flux paths. **b** MEC model

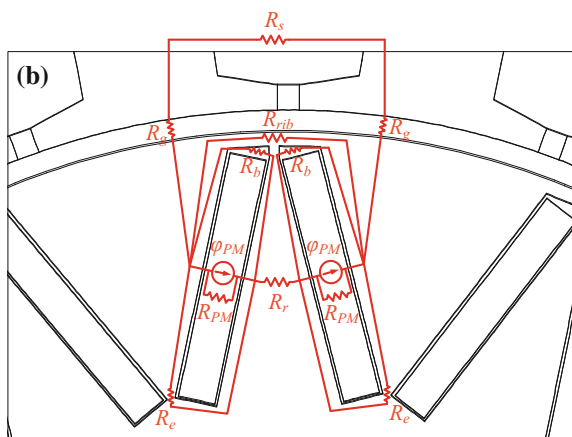
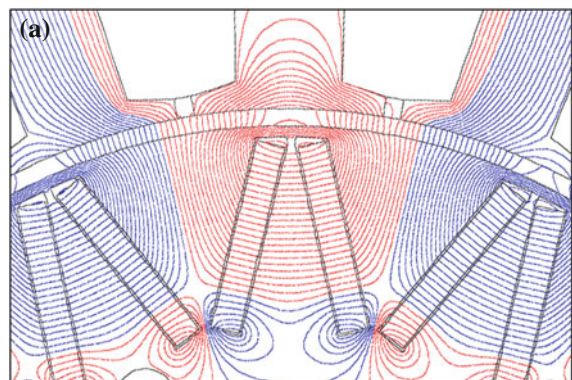
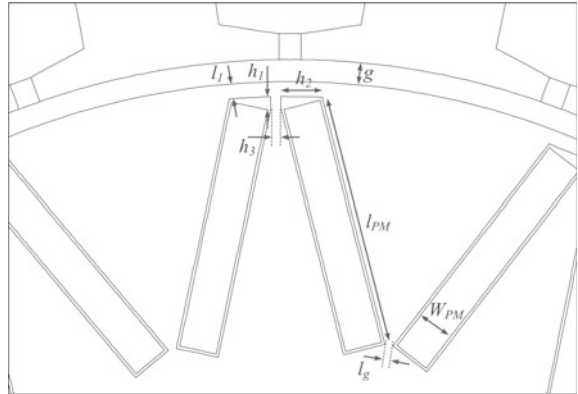


**Fig. 4.17** Geometrical parameters of a pole-pair in the prototype FSCW IPM machine



$R_{rib}$  Reluctance of at inside end of the one pole-pair.

$R_g$  Reluctance of the physical air-gap.

Among the above reluctances,  $R_s$  and  $R_r$  that are associated to the stator and rotor yokes are negligible [7–10]. Geometrical parameters of Fig. 4.16b that are used in the calculation of the MEC elements are shown in Fig. 4.17. Expressions describing the reluctances of the MEC model are:

$$R_{PM} = \frac{W_{PM}}{\mu_0 \mu_r l_{PM} l_{st}} \quad (4.66)$$

$$R_b = \frac{W_{PM}}{\mu_0 \left(\frac{h_1}{2}\right) l_{st}} \quad (4.67)$$

$$R_g = \frac{g}{\mu_0 \frac{\gamma}{2} \left(R_r + \frac{g}{2}\right) l_{st}} \quad (4.68)$$

The IPM rotor is designed such that the bridges are always fully saturated. Hence, the flux that passes through the reluctances  $R_{rib}$  and  $R_e$  can be assumed constant as follows:

$$\varphi_{rib} \approx B_{sat} \cdot A_{rib} \quad (4.69)$$

$$\varphi_e \approx B_{sat} \cdot A_e \quad (4.70)$$

where

$$A_{rib} \approx l_1 \cdot l_{st} \quad (4.71)$$

$$A_e \approx \left(\frac{l_g}{2}\right) \cdot l_{st} \quad (4.72)$$

The value of  $B_{sat}$  in (4.69) and (4.70) are found from the  $B$ - $H$  curve of the iron core. For the magnetic core material M270-35A as shown in Fig. 4.4,  $B_{sat}$  is equal to 2.0T. The magnet flux,  $\varphi_{PM}$  can be found from the residual flux density of the PMs,  $B_r$ , as follows:

$$\varphi_{PM} = B_r \cdot l_{PM} \cdot l_{st} \quad (4.73)$$

Considering negligible values for  $R_s$  and  $R_r$ , magnetic equivalent circuit of Fig. 4.16b simplifies to the circuit shown in Fig. 4.18. Kirchhoff's current law for the magnetic equivalent circuit of Fig. 4.18 gives:

$$\text{Node 1 : } \varphi_{PM} = \varphi_g + \varphi_{rib} + \varphi_{PM\ell} + \varphi_b + \varphi_e \quad (4.74)$$

$$\text{Loop 1 : } \varphi_b R_b - \varphi_{PM\ell} R_{PM} = 0 \quad (4.75)$$

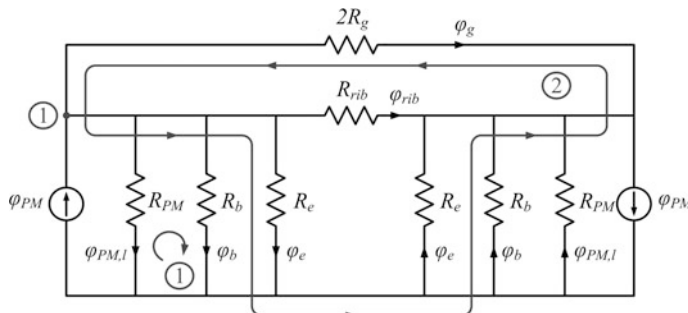
$$\text{Loop 2 : } \varphi_b R_b - \varphi_g R_g = 0 \quad (4.76)$$

Solving the above system of three equations for the air-gap flux,  $\varphi_g$ , yields:

$$\varphi_g = \frac{R_b R_{PM}}{R_b R_g + R_b R_{PM} + R_g R_{PM}} (\varphi_{PM} - \varphi_{rib} - \varphi_e) \quad (4.77)$$

Numerical values, Table 4.3, for the parameters of the magnetic equivalent circuit of Fig. 4.18 are obtained using the above equations. The value of  $B_m$  for the trapezoidal flux density of Fig. 4.12c can now be found by substituting all the variables in (4.65) that were previous calculated, as follows:

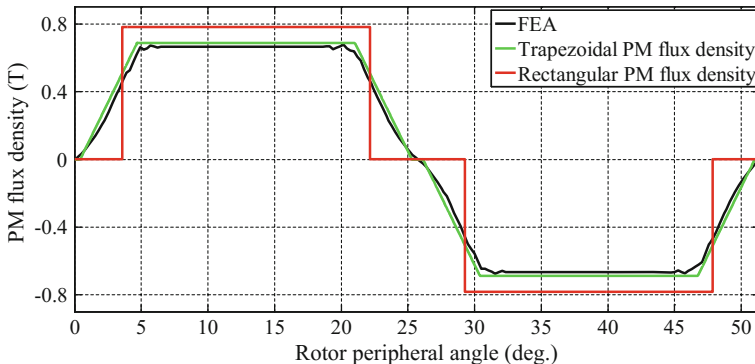
$$B_m = 0.688 \text{ T} \quad [\text{Trapezoidal PM flux density}]$$



**Fig. 4.18** Simplified magnetic equivalent circuit of the prototype FSCW IPM machine

**Table 4.3** Numerical values for the parameters of the magnetic equivalent circuit of 4.18

Quantity	Value
$R_{PM}$	$1.42124 \times 10^6$ (A/Wb)
$R_b$	$76.60151 \times 10^6$ (A/Wb)
$R_g$	$1.83498 \times 10^6$ (A/Wb)
$\varphi_{PM}$	$1.16249 \times 10^{-3}$ (Wb)
$\varphi_{rib}$	$0.12577 \times 10^{-3}$ (Wb)
$\varphi_e$	$94.09999 \times 10^{-6}$ (Wb)
$\varphi_g$	$0.40721 \times 10^{-3}$ (Wb)

**Fig. 4.19** PM flux density in the air-gap of a slot-less IPM machine. Trapezoidal PM flux density versus rectangular PM flux density versus PM flux density obtained by FEA

For the prior art rectangular PM flux density of Fig. 4.12b, the value of  $B_m$  is found using (4.58):

$$B_m = 0.782 \text{ T} \quad [\text{Rectangular PM flux density}]$$

The proposed trapezoidal PM flux density and the prior art rectangular PM flux density that are obtained based on the above calculations along with the PM flux density obtained from FEA are shown in Fig. 4.19. Evidently, the proposed method for calculation of the PM flux density based on the non-uniform saturation model of the IPM rotor yields results much closer to the FEA. However, there is a significant discrepancy between the prior art rectangular PM flux density and the FEA results. Such error in calculation of the PM flux density could lead to wrong estimation of the machine output characteristics such as the back-EMF as will be discussed in the following sections.

### 4.6.2 Estimation of the Back-EMF Based on the Calculated PM Flux Densities

The analytical equation for calculating the back-EMF due to the trapezoidal PM flux density was derived in Chap. 2 as follows:

$$e_j = \sum_k E_{\max,k} \cos(k\omega_e t - k\theta_{j,e}), \quad k = 1, 3, 5, \dots \quad (4.78)$$

$$E_{\max,k} = -2 r_g l_{eff} \omega_r k_{w,(P/2)k} N_j B_{\max,(P/2)k} \quad (4.79)$$

where the phase angle  $\theta_{j,e}$  in three-phase system is equal to 0,  $2\pi/3$  and  $-2\pi/3$  for phase  $a$ ,  $b$ , and  $c$ , respectively, and:

$$\omega_e = \frac{P}{2} \omega_r \quad (4.80)$$

For the rectangular PM flux density, (4.78) should be modified as follows:

$$e_j = \sum_k E_{\max,k} \sin(k\omega_e t - k\theta_{j,e}), \quad k = 1, 3, 5, \dots \quad (4.81)$$

From (4.79) it is observed that voltage harmonic of order  $k$  in the back-EMF is generated due to the PM flux density harmonic of order  $n = kP/2$ . For the 14-pole prototype IPM machine, the fundamental harmonic of the back-EMF is generated due to the interaction between the 7th harmonic winding factor and the 7th harmonic of the PM flux density. An 18-slot double-layer three-phase FSCW stator is used with the 14-pole rotor. The harmonic winding factors for this type of stator was derived in Chap. 2 as follows:

$$k_{w,n} = \frac{P}{2c} \frac{6}{Q} \sin\left(\frac{n\pi}{Q}\right) \left(1 + 2 \cos\left(\frac{10\pi}{Q}n\right)\right), \quad n = \frac{P}{2c}, \frac{3P}{2c}, \frac{5P}{2c}, \dots \quad (4.82)$$

The prototype machine is coupled with a prime mover. The prime mover is rotating at 428 rpm and the back-EMF of the prototype machine is experimentally measured. The back-EMF is also calculated using (4.78)–(4.81) for the trapezoidal and rectangular PM flux densities that were obtained in Sect. 4.6.1. The results are shown in Fig. 4.20. Evidently, the back-emf that was calculated based on the proposed trapezoidal PM flux density is much closer to the experimentally measured back-EMF. On the contrary, as can be seen in Fig. 4.20, the back-EMF obtained from the prior art rectangular PM flux density exhibits significant discrepancy from the experimentally measured back-EMF. Therefore, unlike the proposed trapezoidal PM flux density, the prior art rectangular back-EMF is not a good estimator of machine performance characteristics such as back-EMF.

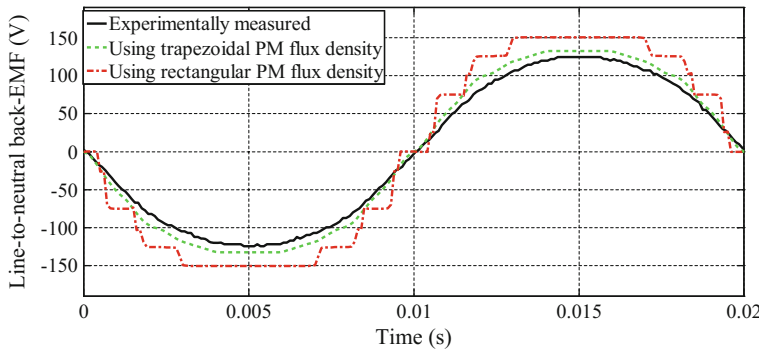


**Fig. 4.20** Line-to-neutral back-EMF of the 14-pole 18-slot prototype FSCW IPM machine. Experimentally measured back-EMF versus analytically calculated back-EMF using the proposed trapezoidal PM flux density and the prior art rectangular PM flux density

A few remarks can be made regarding the trapezoidal PM flux density model:

- In the trapezoidal model,  $B_m$ ,  $\delta_1$  and  $\delta_2$  are functions of the IPM rotor geometry.
- The value of the PM residual flux density,  $B_r$ , has negligible effect on  $\delta_1$  and  $\delta_2$ , and only affects  $B_m$ .
- If the iron bridge is too thick, most of the PM flux will pass through this region and make it saturated, causing in a decrease in the amount of flux that crosses the air-gap.
- The harmonics in the back-EMF are strictly dependent on  $\delta_1$  and  $\delta_2$  in the PM flux density.

## 4.7 Conclusion

The residual flux of the magnets buried inside the rotor cause the rotor iron to become non-uniformly saturated. A geometry-based mathematical model for the non-uniform distribution of magnetic saturation in an IPM rotor was proposed in this chapter. It was shown that the distribution of the magnetic saturation in the rotor iron is solely dependent on its geometry. PM flux density in the air-gap due to an IPM rotor was then modelled using a trapezoidal waveform whose parameters were found based on the proposed non-uniform saturation model and the magnetic equivalent circuit of the machine.

A case-study for calculating the PM flux density and back-EMF of a prototype FSCW IPM machine was investigated. The non-uniform saturation model and the trapezoidal PM flux density for this machine were mathematically calculated and compared against the prior art rectangular PM flux density model and FEA results. Moreover, the back-EMF of the prototype machine was analytically calculated using the obtained PM flux densities and was compared with the experimentally

measure back-EMF. It was shown that the proposed method yields significantly closer results to the FEA and experiment.

The proposed approach in this chapter can aid in analysis of the fields inside the machine and provides a quick tool for saturation analysis of the rotor based on its geometry and the nonlinear  $B$ - $H$  curve of the it's magnetic material. Moreover, it can be used as a tool for rapid obtaining preliminary designs for an IPM machine with desired characteristics.

## References

1. A.J. Baden Fuller, *Engineering Field Theory* (Pergamon Press, 1973)
2. E.R. Laithwaite, Magnetic equivalent circuits for electrical machines, in *Proceedings of the Institution of Electrical Engineers*, vol. 114 (1967), pp. 1805–1809
3. N. Mohan, T.M. Undeland, *Power Electronics: Converters, Applications, and Design* (Wiley, 2007)
4. *User guide Flux® 11.2—Physical Description, Solving & Postprocessing*, vol. 2 (CEDRAT, 2013)
5. M. Farshadnia, R. Dutta, J.E. Fletcher, K. Ahsanullah, M.F. Rahman, H.C. Lovatt, Analysis of MMF and back-EMF waveforms for fractional-slot concentrated-wound permanent magnet machines, in *Proceedings of the ICEM* (2014), pp. 1976–1982
6. K. Ahsanullah, R. Dutta, M.F. Rahman, Investigation of flat and V-shaped magnets in interior permanent magnet machine for direct drive wind turbine application, in *2013 IEEE ECCE Asia Downunder (ECCE Asia)* (2013), pp. 208–213
7. A.B. Proca, A. Keyhani, A. El-Antably, L. Wenzhe, D. Min, Analytical model for permanent magnet motors with surface mounted magnets. *IEEE Trans. Energy Convers.* **18**, 386–391 (2003)
8. D. Zarko, D. Ban, T.A. Lipo, Analytical calculation of magnetic field distribution in the slotted air gap of a surface permanent-magnet motor using complex relative air-gap permeance. *IEEE Trans. Magn.* **42**, 1828–1837 (2006)
9. A. Rahideh, M. Mardaneh, T. Korakianitis, Analytical 2-D calculations of torque, inductance, and back-EMF for brushless slotless machines with surface inset magnets. *IEEE Trans. Magn.* **49**, 4873–4884 (2013)
10. A. Rahideh, T. Korakianitis, Analytical magnetic field calculation of slotted brushless permanent-magnet machines with surface inset magnets. *IEEE Trans. Magn.* **48**, 2633–2649 (2012)
11. M. Chunting, M. Filippa, L. Weiguo, M. Ruiqing, Analytical method for predicting the air-gap flux of interior-type permanent-magnet machines. *IEEE Trans. Magn.* **40**, 50–58 (2004)
12. G. Dajaku, D. Gerling, Stator slotting effect on the magnetic field distribution of salient pole synchronous permanent-magnet machines. *IEEE Trans. Magn.* **46**, 3676–3683 (2010)
13. Z. Li, S.Z. Jiang, Z.Q. Zhu, C.C. Chan, Analytical modeling of open-circuit air-gap field distributions in multisegment and multilayer interior permanent-magnet machines. *IEEE Trans. Magn.* **45**, 3121–3130 (2009)
14. T. Wen-Bin, C. Ting-Yu, Analysis of flux leakage in a brushless permanent-magnet motor with embedded magnets. *IEEE Trans. Magn.* **35**, 543–547 (1999)
15. H. Chang-Chou, Y.H. Cho, Effects of leakage flux on magnetic fields of interior permanent magnet synchronous motors. *IEEE Trans. Magn.* **37**, 3021–3024 (2001)
16. E.C. Lovelace, T.M. Jahns, J.H. Lang, A saturating lumped-parameter model for an interior PM synchronous machine. *IEEE Trans. Ind. Appl.* **38**, 645–650 (2002)

17. R. Dutta, M.F. Rahman, L. Chong, Winding inductances of an interior permanent magnet (IPM) machine with fractional slot concentrated winding. *IEEE Trans. Magn.* **48**, 4842–4849 (2012)
18. W. Jie, W. Yunyan, L. Xinhua, Z. Jie, W. Tiezhou, Effect of parameters on back-EMF in permanent magnet brushless DC motor with concentrated winding, in *World Automation Congress, 2008, WAC 2008* (2008), pp. 1–4
19. T.J.E. Miller, R. Rabinovici, Back-EMF waveforms and core losses in brushless DC motors. *IEE Proc. Electr. Power Appl.* **141**, 144–154 (1994)

# Chapter 5

## Calculation of Airgap Function and Inductance in Fractional-Slot Concentrated-Wound Interior Permanent Magnet Machines



### 5.1 Introduction

The non-uniform distribution of saturation due to the buried magnets inside the rotor of an IPM machine affects the reluctance that the stator flux path is facing. The reluctance of the stator flux path varies from the  $d$ -axis alignment to the  $q$ -axis alignment of the rotor resulting in machine saliency. Saliency decreases when a fractional-slot concentrated-wound stator is utilized [1, 2].

In this chapter the stator flux paths inside the non-uniformly saturated IPM rotor, developed and modelled in Chap. 4, are analyzed and an equivalent airgap function is proposed. The inductance of the machine is then analytically calculated using the winding function formulated in Chap. 2 and the proposed airgap function in this chapter. Relative permeability variations with the varying saturation intensity at different rotor regions are included in the proposed equivalent airgap function. FEA simulation tool and experimental results from a prototype FSCW IPM machine are used to validate the proposed theory.

### 5.2 Inductances in FSCW PMSMs

Inductance of a winding is an indicator of the induced EMF of the winding due to the changing flux linking its coils. If the flux linking the coils is produced by the winding itself, the inductance is referred to as self-inductance, while for the flux that is produced by another winding, the inductance is referred to as mutual inductance. In an electric machine, the total flux produced by a phase winding can be categorized into two general groups [3]:

- The flux portion that radially crosses the airgap.
- The flux portion that does not cross the airgap.

The flux components that radially cross the airgap link the stator and rotor electromagnetically. This group is calculated from the spatial MMF distribution of a winding in the airgap and comprises the following components:

- Magnetizing flux—which is due to the main spatial harmonic of the MMF.
- Airgap leakage flux—which is associated to the remaining spatial harmonics of the MMF.

The magnetizing flux yields the “*magnetizing flux linkage*”,  $\lambda_m$ , while the airgap leakage flux produces the “*airgap leakage flux linkage*”,  $\lambda_{ag}$ .

The flux portion that does not cross the airgap has no participation in the electromagnetic energy conversion process and yield the “*leakage flux linkage*”,  $\lambda_l$ . These flux components can be categorized in the following groups [3]:

- Tooth-tip leakage flux
- Slot leakage flux
- End-winding leakage flux

Sum of the aforementioned flux linkages comprise the total flux linkage of a phase winding, as follows [3]:

$$\lambda = \lambda_R + \lambda_l = \lambda_m + \lambda_{ag} + \lambda_l \quad (5.1)$$

where the flux linkage  $\lambda_R$  indicates the total flux linkage due to the flux that radially crosses the airgap.

In an electric machine, the magnetizing flux contributes to the magnetizing inductance,  $L_m$ . The airgap leakage flux and yields the airgap leakage inductance,  $L_{ag}$ . The leakage flux portion that does not cross the airgap creates the tooth-tip leakage inductance,  $L_{tt}$ , slot leakage inductance,  $L_u$ , and end-winding leakage inductance,  $L_{ew}$ . Thereby, total inductance should be expressed as the sum of all these sub-components as follows:

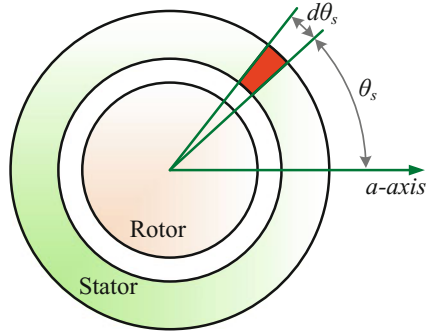
$$L_s = L_m + L_{ag} + L_u + L_{tt} + L_{ew} \quad (5.2)$$

The above terms are formulated on terms of the machine design parameters in the following sections.

### 5.2.1 Magnetizing Inductance and Airgap Leakage Inductance

Magnetizing inductance and airgap leakage inductance are the result of the radial flux that is produced by the spatial MMF distribution in the airgap. In an electric machine, the phase windings are distributed along the stator peripheral angle. For a differential element of angular width  $d\theta_s$  located at the stator peripheral angle  $\theta_s$

**Fig. 5.1** Differential element of width  $d\theta_s$  located at the stator peripheral angle  $\theta_s$  with reference to the stator *a*-axis



with reference to the stator *a*-axis as shown in Fig. 5.1, the flux linking phase *k* winding due to the flux produced in the airgap by phase *j* winding, is given by [4]:

$$d\lambda_{R,jk}(t, \theta_s) = w_k(\theta_s) d\varphi_j(t, \theta_s) \quad (5.3)$$

where  $w_k$  is the winding function of phase *k*, and  $d\varphi_j$  is the flux due to phase *j* in the differential element, given by:

$$d\varphi_j(t, \theta_s) = \frac{f_j(t, \theta_s)}{d\mathfrak{R}(\theta_r)} \quad (5.4)$$

In (5.4),  $f_j$  is the MMF produced by phase *j* in the airgap, expressed using the winding function of phase *j* winding as follows:

$$f_j(t, \theta_s) = w_j(\theta_s) i_j(t) \quad (5.5)$$

and  $d\mathfrak{R}$  is the reluctance of the flux path for  $d\varphi_j$ :

$$d\mathfrak{R}(\theta_r) = \frac{g_{eq}(\theta_r)}{\mu_0 dA} \quad (5.6)$$

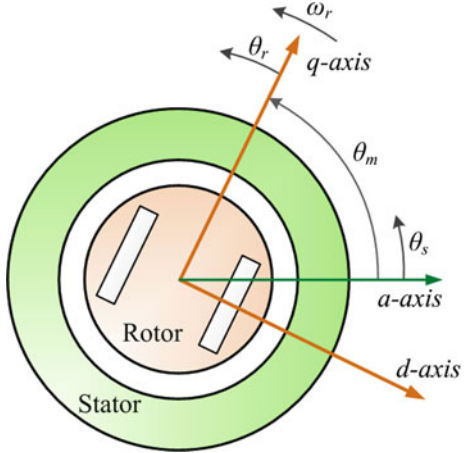
where  $g_{eq}$  is the equivalent airgap length and conventionally is a function of the rotor peripheral angle,  $\theta_r$ , which is measured with respect to the rotor *q*-axis, and  $dA$  is the cross-sectional area of the differential element:

$$dA = r_g l_{eff} d\theta_s \quad (5.7)$$

In a machine with its rotor rotating at the angular speed  $\omega_r$ , as shown in Fig. 5.2, the rotor peripheral angle can be expressed in terms of the stator peripheral angle and the rotor angular speed as follows:

$$\theta_r = \theta_s - \theta_m \quad (5.8)$$

**Fig. 5.2** Key angles in the formulation of the inductances



where  $\theta_m$  is the rotor position:

$$\theta_m = \omega_r t \quad (5.9)$$

Substitution of (5.4)–(5.9) in (5.3) yields:

$$d\lambda_{R,jk}(t, \theta_s) = \mu_0 r_g l_{eff} w_k(\theta_s) \frac{w_j(\theta_s)}{g_{eq}(\theta_s - \theta_m)} d\theta_s i_j(t) \quad (5.10)$$

The total flux linkage,  $\lambda_{R,jk}$ , is obtained by the summation of the flux linkages due to all the differential elements along the peripheral angle in the airgap, therefore:

$$\lambda_{R,jk}(t) = \mu_0 r_g l_{eff} i_j(t) \int_0^{2\pi} \frac{w_k(\theta_s) w_j(\theta_s)}{g_{eq}(\theta_s - \theta_m)} d\theta_s \quad (5.11)$$

Inductance between the windings of phases  $j$  and  $k$  due to  $\lambda_{R,jk}$  is given by:

$$L_{m,jk} + L_{ag,jk} = \frac{\lambda_{R,jk}(t)}{i_j(t)} \quad (5.12)$$

where the subscript  $j$  and  $k$  represent phase  $j$  and  $k$  windings. Substitution of (5.11) in (5.12) yields:

$$L_{m,jk} + L_{ag,jk} = \mu_0 r_g l_{eff} \int_0^{2\pi} \frac{w_k(\theta_s) w_j(\theta_s)}{g_{eq}(\theta_s - \theta_m)} d\theta_s \quad (5.13)$$

If  $j = k$  in the above equation it represents the self-inductance, while for  $j \neq k$  (5.13) yields the mutual inductance. The equivalent airgap function is determined by the stator and rotor design and geometry, and will vary with respect to the rotor angular position in machines utilizing IPM rotors. Hence, the magnetizing and air-gap leakage inductances vary with the rotor angular position in IPM machines. This does not apply to the slot leakage inductance, tooth-tip leakage inductance, and end-winding leakage inductance. These leakage inductance components are not dependent on the rotor angular position.

The magnetizing inductance in (5.13) is the result of the main harmonic of the winding functions, while the airgap leakage inductance is due to the remaining harmonics of the winding function. Detailed parametric formulas for these inductances can be obtained by solving the integral in (5.13), as will be provided in Chap. 6.

### 5.2.2 Slot Leakage Inductance

Slot leakage inductance contributes to a significant portion of the synchronous inductance in FSCW machines [5]. The following assumptions are made in calculation of the slot leakage inductance:

- Permeability of the magnetic core material is infinite.
- The magnetic field lines are straight and parallel to the width of the slot.

The slot leakage inductance is calculated using a 2-D model that is based on the stored energy in the magnetic circuit of the slot. General expressions for the self- and mutual slot leakage inductances are respectively of the forms [3, 6]:

$$L_u = \frac{12}{Q} \mu_0 l_{st} N_s^2 \lambda_{Su} \quad (5.14)$$

$$M_u = -\frac{12}{Q} \mu_0 l_{st} N_s^2 \lambda_{Mu} \quad (5.15)$$

where  $\lambda_u$  is the slot permeance factor, and  $N_s$  is the total number of turns per phase. The slot permeance factor is a function of the slot geometry and the number of winding layers in the slot. For a horizontally-filled double-layer slot with an equal height of the coils as shown in Fig. 5.3, the slot permeance factor for the self- and mutual slot leakage inductance are given by [3, 6]:

$$\lambda_{Su} = k_{S1} \frac{h_4 - h'}{3b_4} + k_{S2} \left( \frac{h_3}{b_4} + \frac{h_1}{b_1} + \frac{h_2}{b_4 - b_1} \ln \frac{b_4}{b_1} \right) + \frac{h'}{4b_4} \quad (5.16)$$

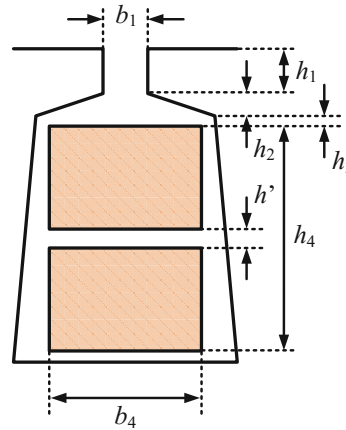


**Fig. 5.3** Key dimensions of a horizontally-filled double-layer slot with equal coil heights

$$\lambda_{uM} = k_{M1} \frac{h_4 - h'}{3b_4} + k_{M2} \left( \frac{h_3}{b_4} + \frac{h_1}{b_1} + \frac{h_2}{b_4 - b_1} \ln \frac{b_4}{b_1} \right) \quad (5.17)$$

where coefficients  $k_{S1}$ ,  $k_{S2}$ ,  $k_{M1}$  and  $k_{M2}$  are:

$$k_{S1} = 1 - \frac{9}{8}\varepsilon \quad (5.18)$$

$$k_{S2} = 1 - \frac{3}{2}\varepsilon \quad (5.19)$$

$$k_{S1} = \frac{9}{16}\varepsilon \quad (5.20)$$

$$k_{M2} = \frac{3}{4}\varepsilon \quad (5.21)$$

and

$$\varepsilon = 1 - \frac{W_{cs}}{\tau_p} \quad (5.22)$$

where  $W_{cs}$  is the coil span, and  $\tau_p$  is the pole pitch, both in meters.

A more detailed approach for calculation of the slot leakage inductance, based on the solution of the 2-D Poisson equation for FSCW machines, is given in [7].

### 5.2.3 Tooth-Tip Leakage Inductance

The slot openings in the stator provide additional leakage paths for the flux. The flux in the slot opening is due to the magnetic potential difference across the slot opening permeance. This flux component does not cross the airgap, and its magnitude depends on the slot opening width  $b_1$ , and the physical airgap length  $g_0$ .

The tooth-tip leakage inductance is associated with the slot opening leakage flux. This inductance subcomponent is obtained similar to the slot leakage inductance, given by [3]:

$$L_{tt} = \frac{12}{Q} \mu_0 I_{st} N_s^2 \lambda_{tt} \quad (5.23)$$

where,  $\lambda_{tt}$  is the tooth-tip permeance factor, expressed by:

$$\lambda_{tt} = k_2 \frac{5g_0/b_1}{5 + 4g_0/b_1} \quad (5.24)$$

### 5.2.4 End-Winding Leakage Inductance

End-winding leakage flux is sourcing from the current flow in the stator end windings. Accurate value of the end winding leakage inductance can only be obtained using a 3-D FEA solution of the machine. As this is time-consuming, empirical permeance factors are often used instead. For a winding with the mean dimensions as shown in Fig. 5.4, the end winding leakage inductance can be approximated by [3]:

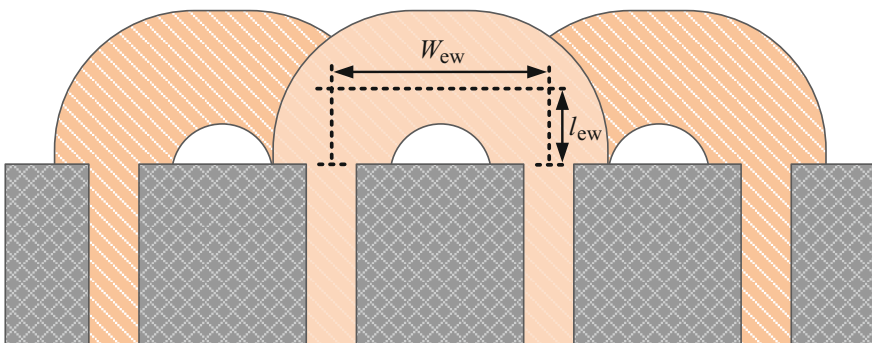


**Fig. 5.4** Mean dimensions of the end winding in a FSCW stator

$$L_{ew} = \frac{12}{Q} S_{pp} \mu_0 N_s^2 (2l_{ew} \lambda_{lew} + W_{ew} \lambda_w) \quad (5.25)$$

Here the empirical permeance factors  $\lambda_{lew}$  and  $\lambda_w$  depend on the winding structure and can be chosen according to the criteria given in [3].

### 5.3 Modelling of the Equivalent Airgap Function

Inductance variations with respect to the rotor angular position are due to the change in the permeance of the stator flux path. This permeance is dependent on the physical air-gap length, the width of the magnets, the slot openings, and saturation of the iron core. For calculation simplicity, the effect of all the aforementioned parameters is included in an equivalent airgap function,  $g_{eq}$ , which aims at representing the magnetic permeance variations. The equivalent airgap function can be used in (5.13) to obtain the inductance. In this section, the state of the art equivalent airgap function for IPM machines is first explored and its limitations and are discussed. Accordingly, an equivalent airgap function is then proposed for FSCW IPM machines that considers both the complicated flux path in an FSCW machine, and the non-uniform magnetic saturation of the IPM rotor magnetic material. Compared with the prior-art method, the proposed equivalent airgap function produces better estimate for the machine characteristics according to experimental results.

#### 5.3.1 State of the Art Equivalent Airgap Function

Permeance of an object of cross-sectional area  $A$ , length  $l$ , and relative permeability  $\mu_r$  is expressed by:

$$\wp = \frac{\mu_0 \mu_r A}{l} \quad (5.26)$$

Relative permeability of a magnet is close to that of air. In a PMSM, depending on the rotor angular position, the magnets may lie in the path of the flux produced by a phase winding of the stator and yield a decrease the permeance of the flux path. The most popular rotor topologies for PMSMs are illustrated in Fig. 5.5. In an SPM rotor, Fig. 5.5a, PMs are exposed to air and the magnetic flux is assumed to radially cross the airgap. In this case, the effect of the magnets on the inductance is obtained by calculating the cumulative permeance of the air-gap and the magnets together. Hence, an equivalent airgap function can be derived for use in (5.13) [8]. The same technique is used for the inset-PM machine of Fig. 5.5b. Accordingly, the

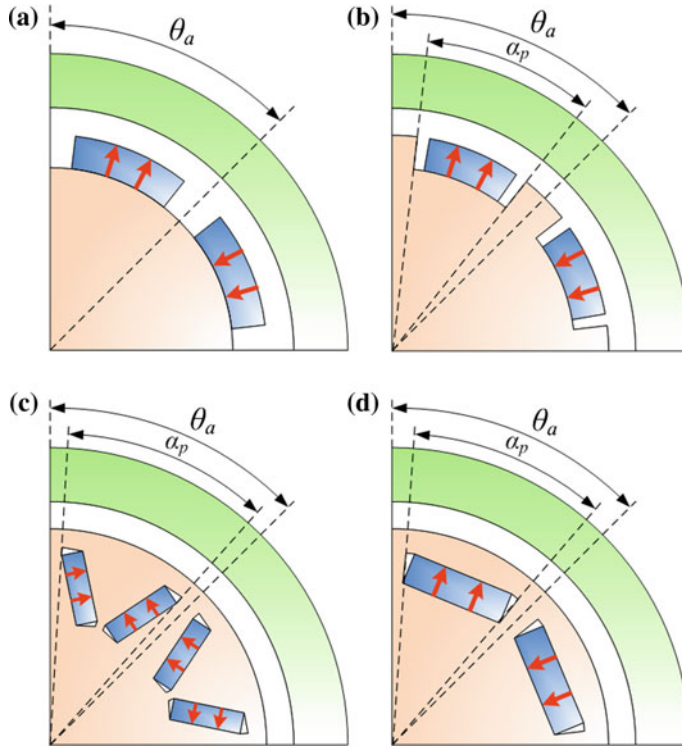


**Fig. 5.5** Most popular PM rotor topologies. **a** Surface PM rotor. **b** Inset PM rotor. **c** V-shaped interior PM rotor. **d** Flat-shaped interior PM rotor

equivalent air-gap function for an inset PM machine, for one pole pitch,  $\theta_a$ , is expressed by [9]:

$$g_{eq}^{inset}(\theta_r) = \begin{cases} g_0 & 0 < \theta_r \leq \frac{2\pi}{2P} - \frac{\alpha_p}{2} \\ g_0 + \frac{W_{PM}}{\mu_r} & \frac{2\pi}{2P} - \frac{\alpha_p}{2} < \theta_r \leq \frac{2\pi}{2P} + \frac{\alpha_p}{2} \\ g_0 & \frac{2\pi}{2P} + \frac{\alpha_p}{2} < \theta_r \leq \frac{2\pi}{P} \end{cases} \quad (5.27)$$

In (5.27)  $W_{PM}$  is the width of the magnets,  $\alpha_p$  is the pole arc angle as shown in Fig. 5.5b. From (5.13) and (5.27) it is observed that variations of the equivalent airgap length with the rotor peripheral angle,  $\theta_r$ , is the main cause of the saliency. In (5.27), the slot openings effect can be included by multiplying the Carter coefficient,  $K_C$  in the physical airgap [10]:

$$g_{0,C} = K_C \cdot g_0 \quad (5.28)$$

Equation (5.27) indicates a square wave. In order to have the equivalent airgap function for the whole mechanical cycle, (5.27) needs to be repeated  $P$  times. The complete airgap function can be expressed using a Fourier series as:

$$g_{eq}^{inset}(\theta_r) = \beta_1 + \sum_{i=1}^{\infty} \beta_{2i} \cos 2\theta_r \quad (5.29)$$

where  $\beta_1$  and  $\beta_{2i}$  are coefficients that are calculated using the MEC model of the machine, as detailed in [2, 9]. The effect of the iron saturation can be included in  $\beta_1$  and  $\beta_{2i}$ . However, a uniform saturation should be assumed. The same concept is used in the literature for the IPM machines shown in Fig. 5.5c, d to find the equivalent airgap function [2, 11]. The main drawbacks of such adoption are:

- The non-uniform distribution of magnetic saturation in the rotor magnetic material is not taken into account. Unlike inset-PM rotors, this phenomenon is a determining factor in IPM machines and should not be neglected.
- The complicated stator flux paths in an IPM rotor are not taken into account.
- The effect of the stator teeth and the IPM rotor geometry are not accounted for in the stator flux path permeance.

Added to the abovementioned shortcomings, the existing airgap function in the literature just a function of the rotor peripheral angle. It will be proved in the next section does not hold true for FSCW IPM machines. Hence, the state of the art method does not provide an accurate model for the equivalent airgap function in FSCW IPM machines. In the next section, the specific properties of a FSCW IPM machine will be investigated and used to propose a novel model for the equivalent airgap function of an IPM machine.

### 5.3.2 *Proposed Equivalent Airgap Function Taking into Account the Non-uniformly Saturated Stator*

The flux of the embedded magnets results in non-homogeneous saturation of the rotor magnetic material. In an IPM rotor, the PM flux is typically dominant and the effect of the stator flux on the non-uniform distribution of saturation is minimal. A saturation map for the IPM rotor was proposed in Chap. 4 as shown in Fig. 5.6. This map is used here to analyze the effect of the non-uniform distribution of saturation on the stator flux and to propose an equivalent airgap function for the FSCW IPM machine. A V-shaped IPM rotor is considered as a general case.

In an FSCW IPM machine, the stator flux projects outward from the stator teeth and radially crosses the airgap into the IPM rotor. As shown in Fig. 5.6, the stator flux in an IPM rotor passes through regions with various saturation intensities and geometries. This needs to be considered in the equivalent air-gap function for this type of machine.

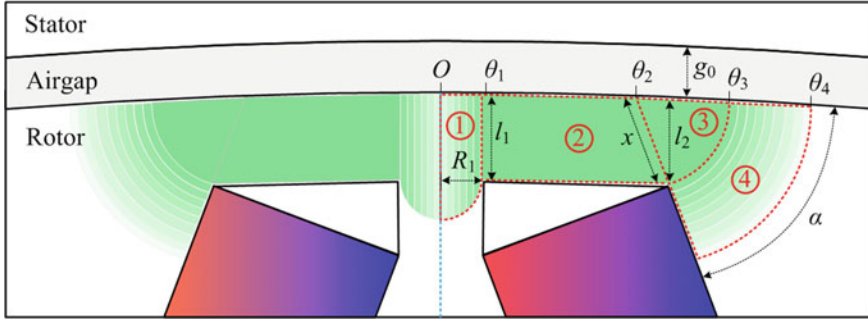


**Fig. 5.6** Non-uniform distribution of magnetic saturation in an IPM rotor due to the magnet flux: classification of the saturated regions

In the IPM rotor the stator flux tends to pass through a route that has the smallest magnetic reluctance. Thus, because of the non-homogeneously saturated rotor, the stator flux path in the rotor iron becomes dependent on the rotor angular position. Fig. 5.7 shows the stator flux path at two different rotor angular positions,  $\theta_m$ . In Fig. 5.7a,  $q$ -axis of the IPM rotor is aligned with the  $a$ -axis of the FSCW stator. Evidently, in this situation the stator flux is bypassing the magnets. By counter-clockwise rotation of the rotor by 90 electrical degrees and aligning its  $d$ -axis with the  $a$ -axis of the stator, as shown in Fig. 5.7b the stator flux will travel through the magnets. The terms “ $q$ -axis alignment” and “ $d$ -axis alignment” will be used throughout the rest of this chapter for scenarios in which the rotor is positioned such that its  $q$ - and  $d$ -axes are aligned with the stator  $a$ -axis, respectively.

In different rotor positions, as shown in Fig. 5.7a, b, the stator flux in the IPM rotor is passing through saturated regions with different relative permeability. Furthermore, the flux is passing through regions with different geometry and cross-sectional area. From (5.26), permeance of the flux path needs to include the cumulative effect for the variations of the cross-sectional area, the physical length for the flux path, and relative permeability.

Figure 5.8a illustrates the stator flux path inside the rotor at a random angular rotor position. When magnetic saturation of the rotor is neglected, the simple illustration shown in Fig. 5.8b describes the magnetic circuit for the flux that is radially passing the airgap into the rotor iron. In this figure,  $\mu_0$  is the free space permeability,  $F_1$  is the magnetic potential on the tooth surface and  $F_2$  is the magnetic potential at the point of symmetry of the flux path, and  $g_0$  is the physical airgap length. Equation (5.13) for the calculating the inductance was derived based on the flux density in the airgap. For Fig. 5.8b the airgap flux density can be obtained as:

$$B_0 = \mu_0 \frac{F_1 - F_2}{g_0} \quad (5.30)$$

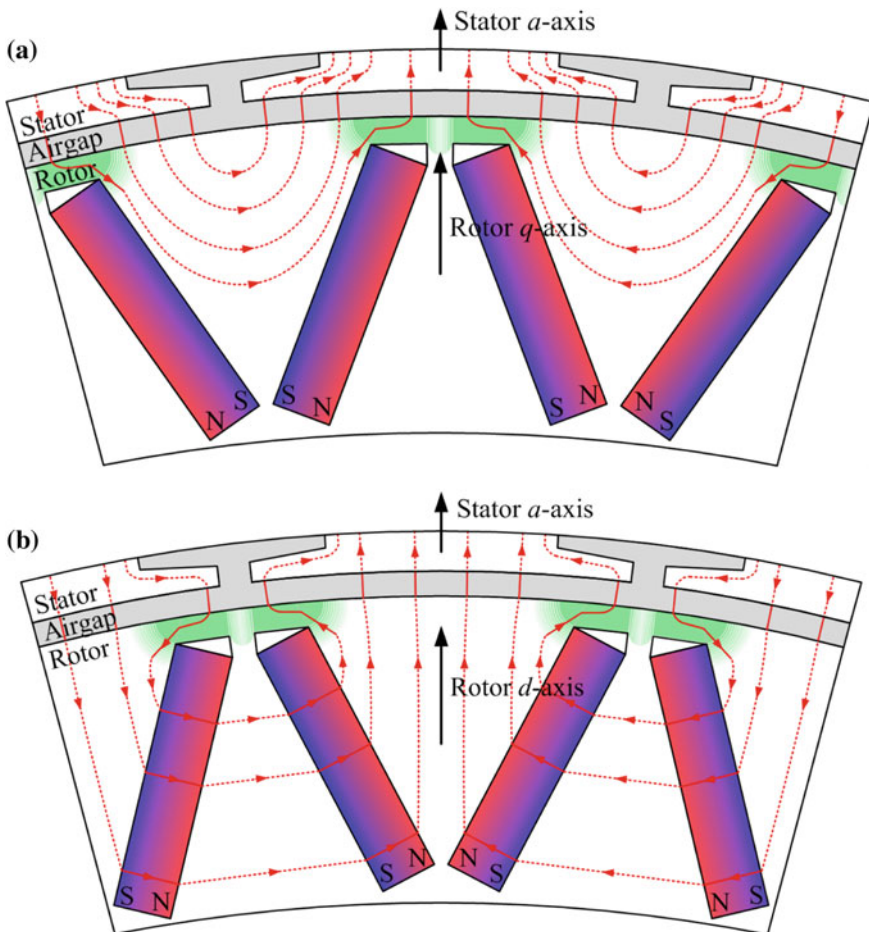


**Fig. 5.7** Pattern of the stator flux lines in an IPM rotor. **a** IPM rotor *q*-axis is aligned with the *a*-axis of the stator ( $\theta_m = 0$  Elec. Rad.). **b** IPM rotor *d*-axis is aligned with the *a*-axis of the stator ( $\theta_m = -\pi/2$  Elec. Rad.)

For the case in which the non-uniform magnetic saturation of the rotor iron is present, as shown in Fig. 5.8a, the simplified magnetic circuit of the stator flux path is as shown in Fig. 5.8c. Evidently, the stator flux is projecting out of the tooth surface with area  $A_0$  and travels through the air-gap,  $g_0$ , to cross through  $n$  sections with lengths  $g_1, g_2, \dots, g_n$ , cross-sectional areas  $A_1, A_2, \dots, A_n$ , and relative permeability  $\mu_{r,1}, \mu_{r,2}, \dots, \mu_{r,n}$ . In the airgap, indicated by region “0” in Fig. 5.8c, flux can be derived from the reluctances of different saturated regions as follows:

$$\varphi = \frac{F_1 - F_2}{\mathfrak{R}_0 + \mathfrak{R}_1 + \dots + \mathfrak{R}_n} \quad (5.31)$$

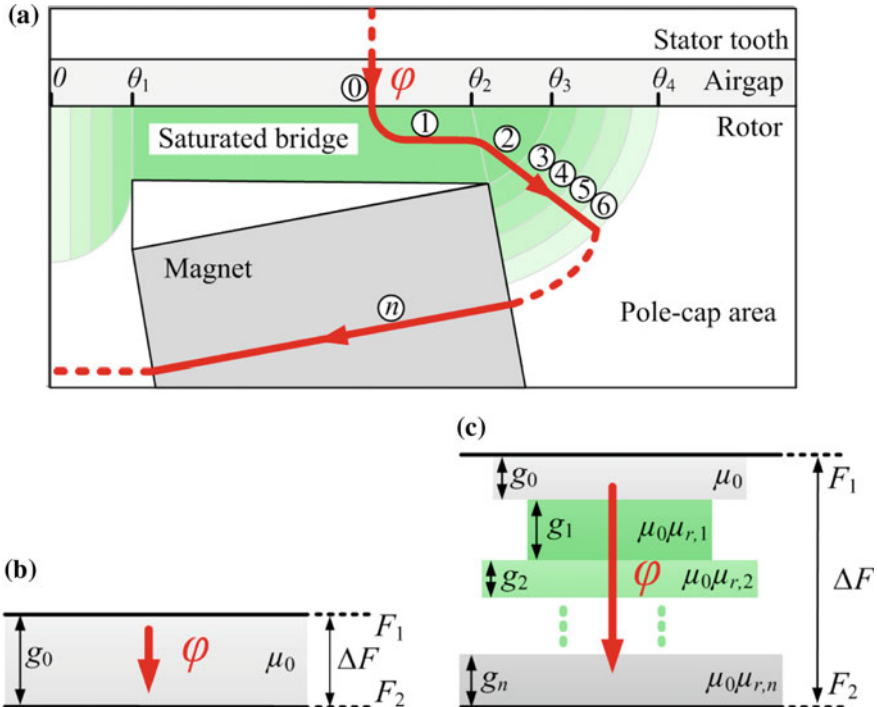


**Fig. 5.8** Derivation of the equivalent airgap function **a** Example case of the stator flux passing through the saturated regions in a CW IPM machine. **b** Simple illustration of the radial flux path based on the state of the art model. **c** Simple illustration of the flux that passes through different saturated regions based on the proposed model

Replacing the reluctances by their detailed expression yields:

$$\varphi = \frac{F_1 - F_2}{\frac{g_0}{\mu_0 A_0} + \frac{g_1}{\mu_0 \mu_1 A_1} + \dots + \frac{g_n}{\mu_0 \mu_n A_n}} \quad (5.32)$$

In region “0”, airgap flux density is given by:

$$B_0 = \frac{\varphi}{A_0} \quad (5.33)$$

Substitution of (5.32) in (5.33) after a few mathematical steps gives:

$$B_0 = \mu_0 \frac{F_1 - F_2}{g_0 + \frac{A_0 g_1}{A_1 \mu_1} + \dots + \frac{A_0 g_n}{A_n \mu_n}} \quad (5.34)$$

By comparing (5.30) and (5.34), the denominator in (5.34) can be identified as the equivalent airgap function:

$$g_{eq}(\theta_r, \theta_m) = g_0 + \sum_n MCL_n \quad (5.35)$$

In (5.35), *MCL* is short for the effective *magnetic circuit length* of the stator flux path, expressed by:

$$MCL_n = \frac{A_0}{A_n} \frac{g_n}{\mu_{r,n}} \quad (5.36)$$

Equation (5.36) implies that variations of the iron permeability and rotor geometry along the stator flux path, considerably affects the equivalent airgap function. By finding the equivalent airgap function using (5.35), the inductances associated with the FSCW IPM machine can be found from (5.13).

Magnetic saturation in the rotor magnetic material, as previously formulated in Chap. 4, is dependent on the rotor peripheral angle. As earlier discussed, the flow of the stator flux path in the rotor iron is determined based on the rotor angular position which affects the total reluctance that along the flux path. Therefore, the proposed equivalent airgap function for FSCW IPM machines, (5.35), is a function of the rotor angular position,  $\theta_m$ , as well as the rotor peripheral angle,  $\theta_r$ .

The parameters in (5.36) for obtaining the *MCL* are functions of the rotor circumferential angle  $\theta_r$ . Relative permeability  $\mu_{r,n}$  is a function of the flux density along the flux path and can be found using the formula that was derived in Chap. 4 based on the *B-H* curve of the magnetic core material:

$$\mu_r(B) = \frac{2B(a - \mu_{r0})}{B(2a - 1) + \mu_{r0}(J_s - B) - \sqrt{\mu_{r0}^2(J_s - B)^2 + B(2\mu_{r0}(J_s - B) + 4aJ_s(\mu_{r0} - 1) + B)}} \quad (5.37)$$

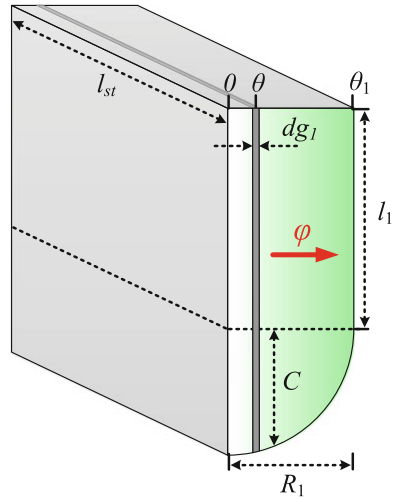
Flux density at every point of the rotor iron core for use in (5.37) can be found as a function of  $\theta_r$  which was formulated in the non-uniform saturation model of the IPM rotor in Chap. 4.

The total *MCL* along the stator flux path in the non-uniformly saturated areas of the saturation model of Fig. 5.6 is formulated in the follows. In these derivations the PMs are approached as separate regions.

### 5.3.2.1 Region 1

From Fig. 5.7a, the flux that sources from the stator and enters region 1 of Fig. 5.6, tangentially passes through this region to reach region 2. Detailed illustration of Region 1 is shown in Fig. 5.9. In this figure, the distance that the stator flux is

**Fig. 5.9** Calculation of the MCL for stator flux in region 1



travelling in the differential element  $dg_1$ , located at peripheral angle  $\theta$  in region 1 can be expressed by:

$$dg_1 = R_r d\theta \quad (5.38)$$

From Chap. 4, the cross-section of the differential element is given by:

$$A_1(\theta) = (l_1 + C(\theta))l_{st} \quad (5.39)$$

where  $C$  is a function of the rotor peripheral angle and is formulated in Chap. 4. In region 1, the total *MCL* of the stator flux that goes from angle  $\theta$  to  $\theta_1$  can be obtained by summing the *MCL* of the flux path in all the differential elements, calculated from (5.36) as follows:

$$MCL_1(\theta) = \int_{\theta}^{\theta_1} \frac{A_0^1}{A_1(\theta')} \frac{R_r d\theta'}{\mu_r(B(\theta'))}, \quad 0 \leq \theta < \theta_1 \quad (5.40)$$

In (5.40),  $A_0^1$  represents the area on the rotor surface that the stator flux is passing through from the airgap into region 1.

### 5.3.2.2 Region 2

Region 2 is redrawn in Fig. 5.10. In this region, the stator flux enters the rotor at circumferential angle  $\theta$  and cross it tangentially into region 3. Assuming  $l_1 = l_2$  in Fig. 5.10, region 2 can be divided into two sections: a rectangle and a triangle. The physical length that the flux in traveling in the rectangular region is:

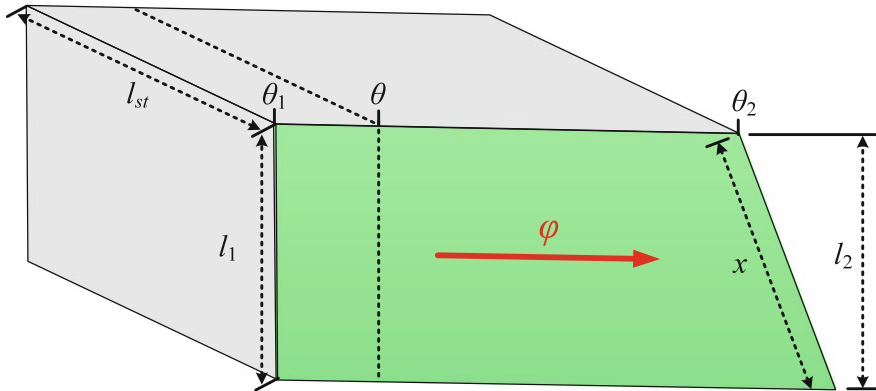


**Fig. 5.10** Calculation of the *MCL* for stator flux in region 2

$$g'_2 = (\theta_2 - \theta)R_r \quad (5.41)$$

While, for the triangular region, the average physical length is found to be:

$$g''_2 = \frac{\sqrt{x^2 - l_1^2}}{2} \quad (5.42)$$

Accordingly, the average distance that the stator flux is traveling in region 2 before reaching region 3 is approximated by summing (5.41) and (5.42), as follows:

$$g_2(\theta) = (\theta_2 - \theta)R_r + \frac{\sqrt{x^2 - l_1^2}}{2} \quad (5.43)$$

The average cross-sectional area that the stator flux is facing in this region is obtained by dividing the volume of the geometrical mass of Fig. 5.10 by the average travelled distance of (5.43), as follows:

$$A_2(\theta) = \frac{g'_2 l_1 l_{st} + g''_2 \frac{\sqrt{x^2 - l_1^2}}{2} l_1 l_{st}}{(\theta_2 - \theta)R_r + \frac{\sqrt{x^2 - l_1^2}}{2}} \quad (5.44)$$

Manipulating the above equation yields:

$$A_2(\theta) = \frac{\left( (\theta_2 - \theta)R_r + \frac{x^2 - l_1^2}{4} \right) l_1 l_{st}}{(\theta_2 - \theta)R_r + \frac{\sqrt{x^2 - l_1^2}}{2}} \quad (5.45)$$

Finally, the *MCL* of the stator flux that enters region 2 at the circumferential angle  $\theta$  can be found by substituting (5.43) and (5.45) into (5.36) as follows:

$$MCL_2(\theta) = \frac{A_0^2}{A_2(\theta) \mu_r(B_{sat})}, \quad \theta_1 \leq \theta < \theta_2 \quad (5.46)$$

where  $A_0^2$  represents the area on the rotor surface that the stator flux is passing through from the airgap into region 2.

### 5.3.2.3 Region 3

As illustrated in Fig. 5.11, inside regions 3 and 4 of the saturation model, the average angle that the stator flux is making with the rotor surface is equal to  $\alpha/2$ . For the stator flux line that enters region 3 at the peripheral angle  $\theta$  and travels through this region into region 4, as shown in Fig. 5.11, the average physical traveled length is equal to:

$$W(\theta) = \sqrt{(\theta_3 - \theta_2)^2 R_r^2 - y^2(\theta) \sin^2\left(\frac{\alpha}{2}\right)} - y(\theta) \cos\left(\frac{\alpha}{2}\right) \quad (5.47)$$

where:

$$y(\theta) = (\theta - \theta_2)R_r \quad (5.48)$$

The average length of the stator flux path entering region 3 at the peripheral angle  $\theta$ , for calculation of the flux path reluctance, can be approximated by:

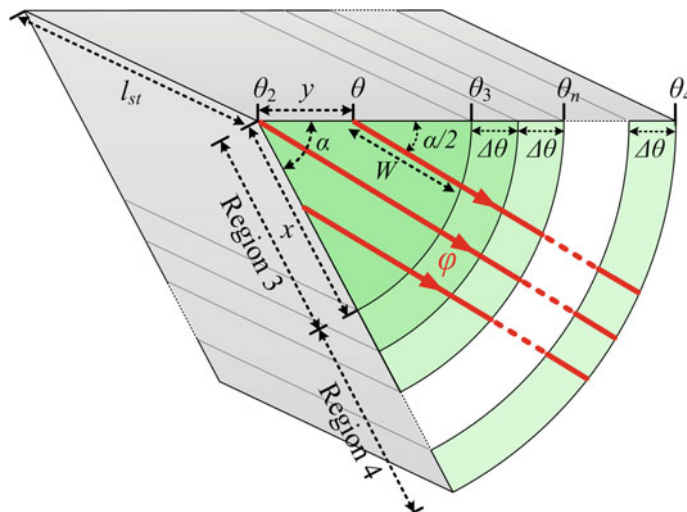


**Fig. 5.11** Calculation of the  $MCL$  for stator flux in regions 3 and 4

$$g_3(\theta) = \frac{2 \int_{\theta_2}^{\theta_3} W(\theta') d\theta'}{(\theta_3 - \theta_2) R_r \sin\left(\frac{z}{2}\right)} - \frac{2 \int_{\theta_2}^{\theta} W(\theta') d\theta'}{(\theta - \theta_2) R_r \sin\left(\frac{z}{2}\right)} \quad (5.49)$$

In (5.49), the first term represents the average travelled distance between  $\theta_2$  to  $\theta_3$  for the stator flux in region 3, calculated by adding the length of the infinite flux lines in this section and averaging the result. Likewise, the second term in (5.49) indicates the average travelled distance of the stator flux between  $\theta_2$  and  $\theta$ . Deducting the second term in (5.49) from the first term, gives the average stator flux path between  $\theta$  and  $\theta_3$ .

In region 3, for the stator flux entering the rotor peripheral angle  $\theta$ , the average cross-sectional area is equal to:

$$A_3(\theta) = \frac{1}{2} (\alpha(\theta_3 - \theta_2) R_r + \alpha(\theta - \theta_2) R_r) l_{st} \quad (5.50)$$

The *MCL* for the stator flux that enters region 3 at the circumferential angle  $\theta$  can now be found by substituting (5.49) and (5.50) into (5.36) as follows:

$$MCL_3(\theta) = \frac{A_0^3}{A_3(\theta)} \frac{g_3(\theta)}{\mu_r(B_{sat})}, \quad \theta_2 \leq \theta < \theta_3 \quad (5.51)$$

where  $A_0^3$  represents the area on the rotor surface that the stator flux is passing through from the airgap into region 3.

### 5.3.2.4 Region 4

In order to simplify the calculations, as evident from Fig. 5.11 region 4 is assumed to comprise differential arcs of  $\Delta\theta$ . Similar to region 3, the average physical length of airgap flux entering the differential arc located at an angle  $\theta_n = \theta_3 + n\Delta\theta$  in region 4 can be obtained using (5.47) as follows:

$$g_{4n}(\theta_n) = \frac{2 \int_{\theta_2}^{\theta_n + \Delta\theta} W(\theta') d\theta'}{(\theta_n + \Delta\theta - \theta_2) R_r \sin\left(\frac{z}{2}\right)} - \frac{2 \int_{\theta_2}^{\theta_n} W(\theta') d\theta'}{(\theta_n - \theta_2) R_r \sin\left(\frac{z}{2}\right)} \quad (5.52)$$

The average cross-sectional area through which the flux is passing in the differential arc is given by:

$$A_{4n}(\theta_n) = \frac{1}{2} (\alpha(\theta_n - \theta_2) R_r + \alpha(\theta_n - \Delta\theta - \theta_2) R_r) l_{st} \quad (5.53)$$

The total *MCL* of the stator flux flowing into region 4 at the circumferential angle  $\theta_n = \theta_3 + n\Delta\theta$  can be obtained using (5.36) by adding the *MCL* associated to all the differential arcs of region 4 through which the flux is passing:

$$MCL_4 = \int_{\theta_n}^{\theta_4} \frac{A_0^4}{A_{4n}(\theta')} \frac{g_{4n}(\theta')}{\mu_r(B(\theta'))} d\theta', \quad \theta_3 \leq \theta < \theta_4 \quad (5.54)$$

where  $A_0^4$  represents the area on the rotor surface that the stator flux is passing through from the airgap into region 4.

It has to be noted that  $\theta_4$  is the rotor peripheral angle of the differential arc where the flux density decreases to a point that saturation of the rotor iron becomes negligible. This angle depends on the geometry of the rotor and the  $B$ - $H$  curve of its magnetic material. Beyond this point, the relative permeability of the rotor magnetic material becomes high enough to make its magnetic reluctance negligible. This leads to the  $MCL$  beyond  $\theta_4$  to converge to a fixed value as will be observed in the example study case presented in the next section.

### 5.3.2.5 Region 5

As shown in Fig. 5.7, based on the rotor angular position, stator flux might travel through the PMs. If this happens, the  $MCL$  in the PMs needs to be considered in the calculations. For a PM, the associated  $MCL$  is:

$$MCL_5 = \frac{A_0^5}{l_{PM} l_{st}} \frac{W_{PM}}{\mu_{r_{PM}}} \quad (5.55)$$

where  $A_0^5$  represents the area on the rotor surface on which the stator flux passing through the magnets (region 5) is entering the rotor.

$A_0$  is dependent on the rotor angular position and the rotor peripheral angle and is different for each saturated region. The following average values are used for  $A_0$ :

$$A_0^{1-4} = \theta_4 R_r l_{st} \quad (5.56)$$

$$A_0^5 = k\pi R_r l_{st} / Q \quad (5.57)$$

where the superscripts indicate the rotor regions,  $k = 0$  when the rotor  $q$ -axis aligns with the stator  $a$ -axis, and  $k = 1$  when the rotor  $d$ -axis aligns with the  $a$ -axis of the stator.

From (5.35), for each value of  $\theta_r$ , the  $MCL$ s for all the rotor regions that the flux is passing through need to be obtained and added to give the total equivalent airgap length. Consequently, for a FSCW IPM machine, the equivalent airgap function is found by substituting (5.40), (5.46), (5.51), (5.54) and (5.55) in (5.35).

The proposed saturation model for an IPM rotor in Chap. 4 is general and can be applied to any V-shaped IPM rotor regardless of the stator type. Consequently the, the proposed equivalent airgap function in this chapter which uses the saturation model of Chap. 4 is valid for any FSCW IPM machine.

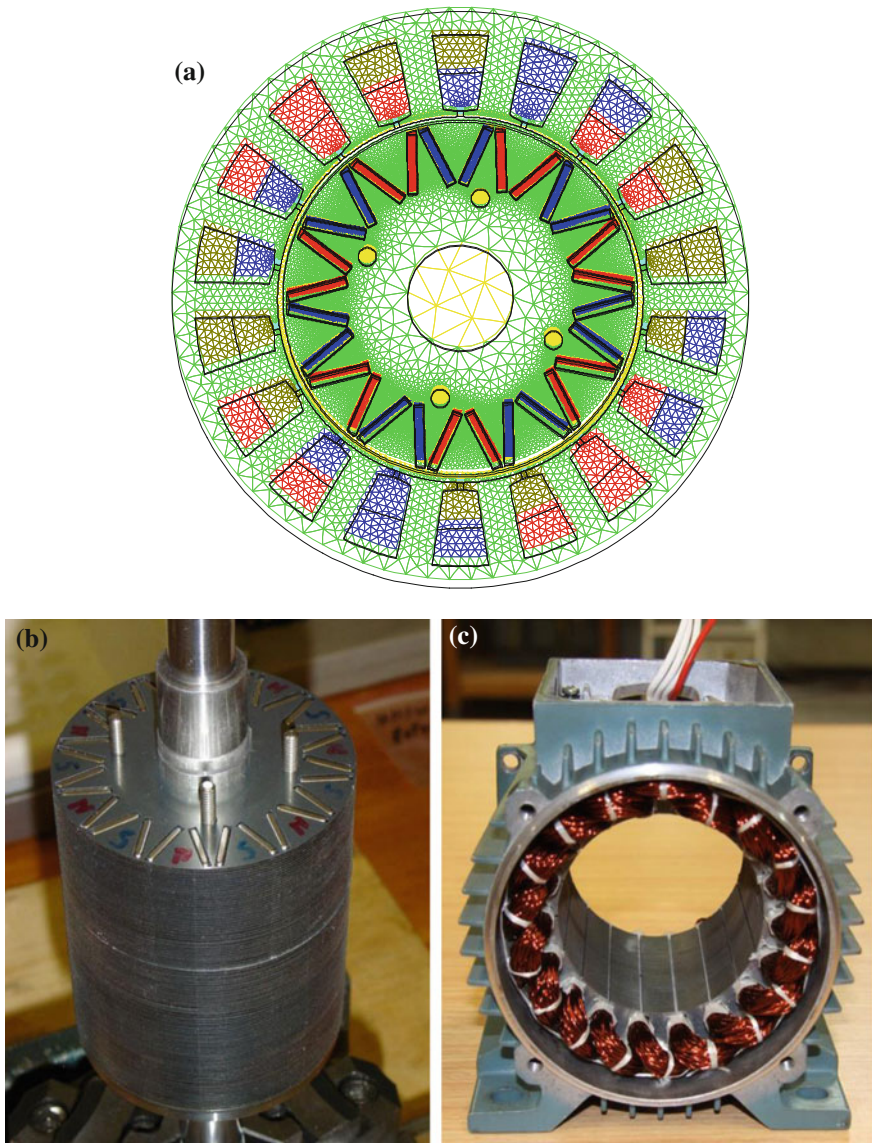
In the next section the proposed methodology will be applied to a prototype FSCW IPM machine and the results will be validated through FEA and experiments.

## 5.4 Case-Study: Validation of the Proposed Airgap Function

The proposed methodology for analytical calculation of the equivalent air-gap function and the inductance based on the proposed saturation model in Chap. 4 are evaluated in this section. A 800 W, 14-pole 18-slot prototype FSCW IPM machine that its stator is based on the optimal layout found in Chap. 3 is used for the experimental evaluations. The design procedure for this 3/7 configuration is detailed in [12]. The FEA model for the prototype machine in CEDRAT FLUX 2D is given in Fig. 5.12a. The FEA model is solved by CEDRAT SOLVER 2D in which the solver precision is set to 0.0001. The manufactured FSCW stator and V-shaped IPM rotor are given in Fig. 5.12b and c, respectively. The main design parameters for the prototype FSCW IPM machine are listed in Table 5.1.

A program is developed in Matlab for the proposed method to calculate variations of the equivalent airgap function with the rotor peripheral angle,  $\theta_r$ , for two distinct rotor angular positions: when the  $q$ -axis of the rotor is aligned with the stator  $a$ -axis where  $\theta_m = 0$  elec. rad. ( $q$ -axis alignment), and the case where  $d$ -axis of the rotor is aligned with the stator  $a$ -axis, where  $\theta_m = -\pi/2$  elec. rad. ( $d$ -axis alignment). The developed code can be found in Appendix II. Figure 5.13 shows a comparison between the obtained equivalent airgap functions by the proposed and conventional methods for the IPM rotor. In this figure only one pole pair is considered. For the complete rotor, the equivalent airgap function of Fig. 5.13 should be repeated 7 times. As previously stated, the conventional equivalent airgap function is adopted from the theory of inset-PM machines [9] in which at the  $q$ -axis a minimum airgap length is assumed, while the maximum airgap length is expected to occur at the  $d$ -axis, independent of the rotor angular position. Nevertheless, as shown in Fig. 5.13, the obtained equivalent airgap function for an IPM machine using the proposed methodology changes with the rotor angular position. Hence, in contrast to common belief, the equivalent airgap length is a function of both the rotor peripheral angle,  $\theta_r$ , and the rotor position,  $\theta_m$ . Thus, the equivalent airgap function at the  $q$ -axis alignment becomes different than that of the  $d$ -axis alignment.

From Fig. 5.13, in all rotor positions, highest value of the equivalent airgap length always occurs at the  $q$ -axis of the rotor, indicating the saturated iron bridge. As shown in Fig. 5.7, in regardless of the rotor alignment, the flux that travels through the iron bridge faces a relatively high reluctance caused by the high saturation of this region. This in turn, causes an increase in the equivalent airgap length on the iron bridge. This explains the higher value of the equivalent airgap length under the  $q$ -axis in Fig. 5.13. Nevertheless, the equivalent airgap length in

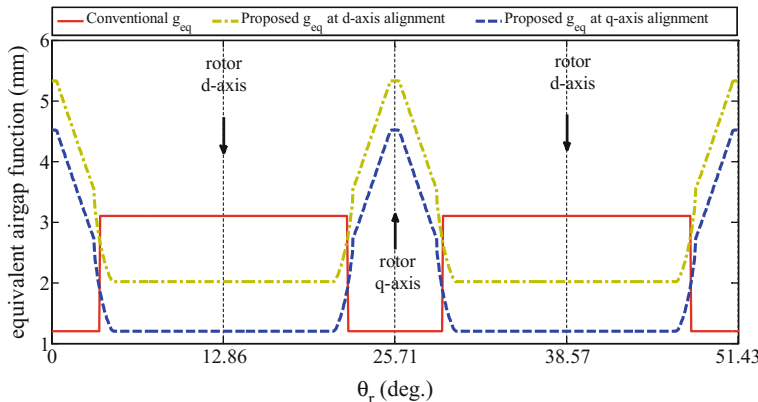


**Fig. 5.12** Prototype FSCW IPM machine. **a** FEA model. **b** Manufactured rotor. **c** Manufactured stator

the  $d$ -axis and  $q$ -axis of the IPM rotor is dependent on the rotor angular position, i.e. the  $q$ -axis and  $d$ -axis alignments of the rotor. In general, the average equivalent airgap function in the  $d$ -axis alignment where the flux travels through the PMs is higher than that of the  $q$ -axis alignment. From (5.13), this causes the inductance

**Table 5.1** Main design parameters of the prototype FSCW IPM machine

Quantity	Value
$g_0$	$1.2 \times 10^{-3}$ (m)
$l_{st}$	$79.0 \times 10^{-3}$ (m)
$W_{PM}$	$2.0 \times 10^{-3}$ (m)
$l_{PM}$	$13.5 \times 10^{-3}$ (m)
$R_r$	$40.0 \times 10^{-3}$ (m)
$N_c$	115 (turns)

**Fig. 5.13** Proposed equivalent airgap function for the prototype FSCW IPM machine along with the state of the art equivalent airgap function

value in the IPM rotor  $q$ -axis to be larger than that of the IPM rotor  $d$ -axis. This complies with the actual phenomena happening in an IPM machine and the theory surrounding it.

From Fig. 5.13 it is observed that by moving from the  $q$ -axis to the  $d$ -axis the proposed equivalent airgap length gradually reduces until a point where it converges to a fixed value. The point of conversion is the angle  $\theta_4$  in Fig. 5.6. A closer view of the proposed equivalent airgap function at the  $q$ -axis alignment is illustrated in Fig. 5.14. Evidently, as explained earlier, beyond the rotor peripheral angle  $\theta_4$ , the effect of the iron saturation on the  $MCL$  becomes negligible, and thereby the proposed equivalent airgap function converges to a fixed value. The illustrated equivalent airgap functions in Fig. 5.13 should be replicated  $P/2$  times to account for a full mechanical cycle.

From (5.13), apart from the equivalent airgap function the winding function of the FSCW machine is also required to obtain the inductance. From Chap. 2, the winding function for the prototype 3/7 FSCW machine is expressed by:

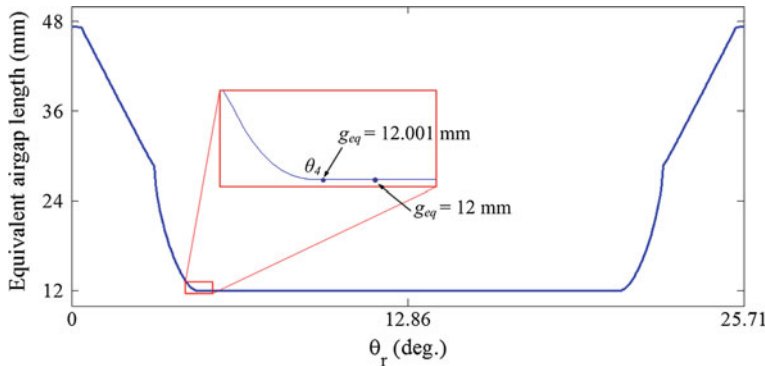


**Fig. 5.14** Convergence of the equivalent airgap function to a fixed value at the rotor peripheral angle  $\theta_4$

$$w_j(\theta_s) = \sum_n W_n \cos(n\theta_s - n\theta_j), \quad n = \frac{P}{2c}, \frac{3P}{2c}, \frac{5P}{2c}, \dots \quad (5.58)$$

$$W_n = \frac{2}{3} \frac{QN_c}{n\pi} k_{w,n} \quad (5.59)$$

$$k_{w,n} = \frac{P}{2c} \frac{6}{Q} \sin\left(\frac{n\pi}{Q}\right) \left(1 + 2 \cos\left(\frac{10\pi}{Q}n\right)\right) \quad (5.60)$$

The winding function of the 3/7 FSCW machine obtained by both analytical equations from Chap. 2 and the FEA model is shown in Fig. 5.15.

Assuming the stator is excited with current  $i_x$ , the flux density in the airgap generated by phase  $x$  of the stator can be obtained using the equivalent airgap function and winding function as follows:

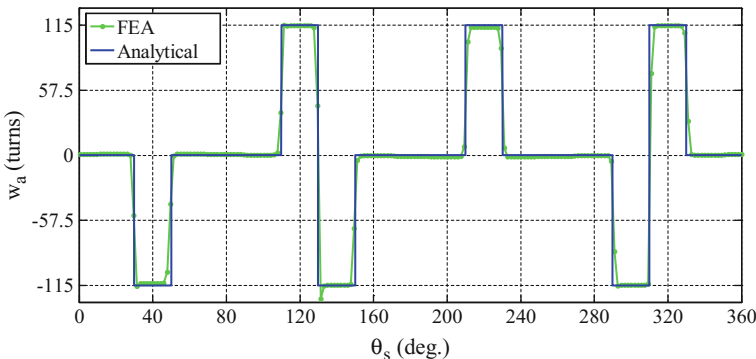


**Fig. 5.15** Winding function for the prototype FSCW IPM machine: analytical calculation versus FEA results

$$B_x(\theta_s) = \mu_0 \frac{i_x w_x}{g_{eq}} \quad (5.61)$$

In order to validate the proposed equivalent airgap function, phase  $a$  of the stator is considered and its flux density,  $B_a$ , is theoretically calculated by both the conventional airgap function and the proposed equivalent airgap function. The results are compared with those obtained by FEA as shown in Fig. 5.16. Two rotor positions are considered, the  $q$ -axis alignment with the stator  $a$ -axis, and the  $d$ -axis alignment with the stator  $a$ -axis. In order to observe the effect of the non-homogenous rotor iron on the stator flux in Fig. 5.16, the saturation caused by the stator current should be avoided. Therefore, in the FEA simulations the stator is fed with 20% of the rated current. It is clear from Fig. 5.16 that the stator flux obtained by the conventional equivalent airgap function has significant errors, whereas, that obtained from the proposed equivalent airgap function is fairly similar to the FEA results. In Fig. 5.16, the notches in the stator flux obtained by both the

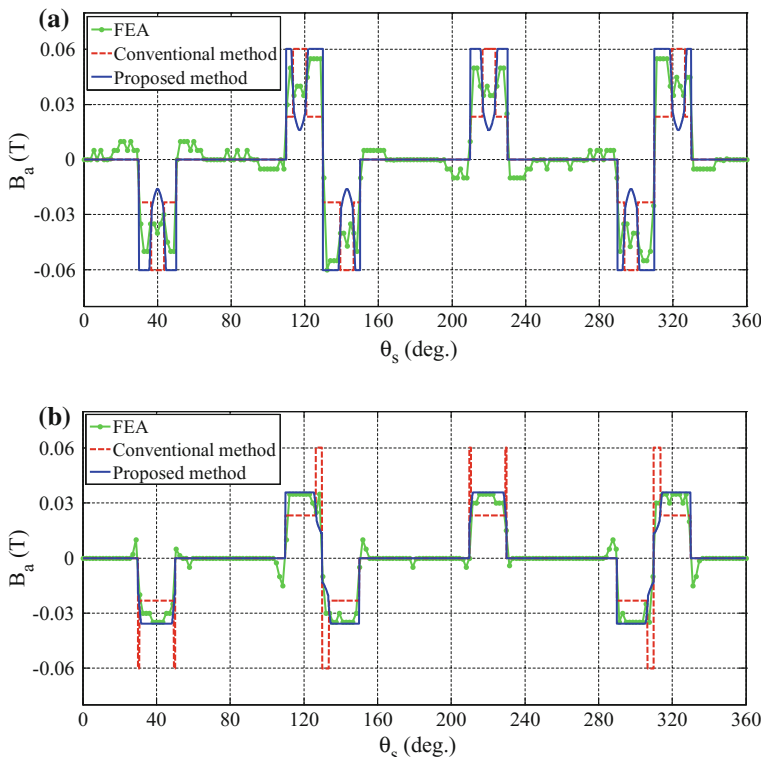


**Fig. 5.16** Airgap flux density of phase  $a$  for the prototype FSCW stator supplied by 20% of the rated current. **a**  $q$ -axis alignment of the rotor with respect to the stator  $a$ -axis. **b**  $d$ -axis alignment of the rotor with respect to the stator  $a$ -axis

**Table 5.2** Analytically calculated inductance subcomponents using the proposed approach

Quantity	Value (mH)
$L_m + L_{ag}$	$L_0 = 61.5 \Delta L = 19.5$
$L_u$	57.6
$L_{tt}$	0.405
$L_{ew}$	4.8

proposed approach and FEA, are caused by the higher value of the equivalent airgap length at the  $q$ -axis of the rotor. From (5.61), a higher equivalent airgap length at the rotor  $q$ -axis leads to a lower flux density.

The self-inductance is calculated from the winding function and equivalent airgap function using (5.13). Both the proposed equivalent airgap function and the conventional equivalent airgap function as shown in Fig. 5.13 are used for the inductance calculation. The minimum and maximum values of the self-inductance take place at the rotor  $d$ -axis and  $q$ -axis alignments, respectively. Therefore, the equivalent airgap functions at these rotor alignments are used in (5.13) to find the lumped inductance comprised of the magnetizing inductance and airgap leakage inductance. The slot-leakage, tooth-tip leakage and end-winding leakage inductances are also calculated from (5.14), (5.23) and (5.25), respectively. The obtained values are listed in Table 5.2. In this table,  $L_0$  is the inductance mean value and  $\Delta L$  indicates the variation in the inductance amplitude.

Self-inductance is a sinusoidal function of  $P\theta_m$  [4]. Accordingly, the computed values for the inductance at the  $d$ -axis and  $q$ -axis alignments are employed in plotting the complete inductance waveforms as a function of the rotor angular position. The results are illustrated in Fig. 5.17 and compared with the inductances obtained by FEA and experiment.

The ac standstill test is used for experimental measurement of the inductance. In this method, a constant ac current is flowed in one phase, while the other two phases are open-circuit. The self-inductance is then obtained using the rms voltage,  $V_s$ , and rms current,  $I_s$ , measured at different rotor positions [13]:

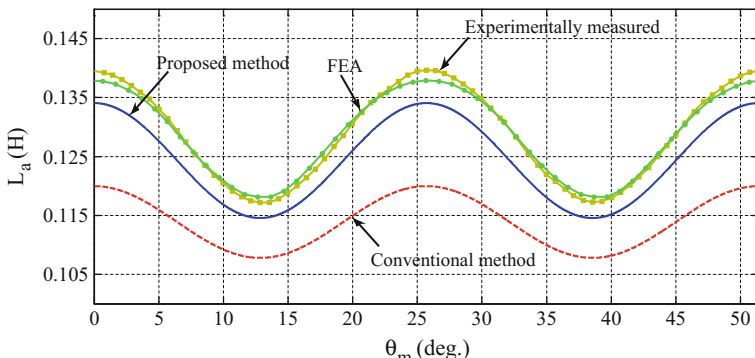


**Fig. 5.17** A comparison between the self-inductances obtained by experimental measurements, FEA, and analytical calculations

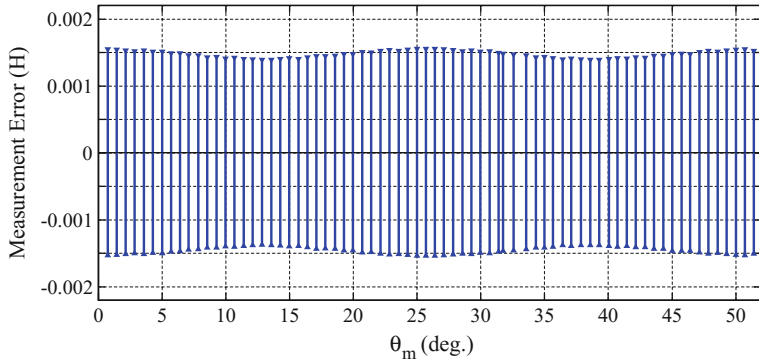


**Fig. 5.18** Error bars associated to the experimental inductance measurements

$$L_s(\theta_m) = \frac{\sqrt{(V_s/I_s)^2 - R_s^2}}{2\pi f} \quad (5.62)$$

In (5.62),  $R_s$  is the phase resistance, and  $f$  is the frequency. It is important to consider the possible measurement errors in the experimental results of Fig. 5.17. The associated error bars to the experimental inductance measurements are shown in Fig. 5.18. Evidently, maximum possible error for the measured inductance is found to be around  $\pm 1.5$  mH which is insignificant. A comprehensive discussion on experimental measurement of the machine inductances is provided in Appendix III.

For the inductances of Fig. 5.17, their mean value and their oscillation amplitude are found and compared in Table 5.3. Clearly, the values reported for the inductance computed using the proposed analytical approach is closer to those of FEA and the experiment. On the other hand, a considerable discrepancy is observed between the FEA and experimental results with the inductance that is analytically calculated using the conventional equivalent airgap function. This discrepancy can be associated to inability of the conventional equivalent airgap function to account for the actual flux paths, geometry, and the non-uniformly saturated iron in a FSCW IPM machine. In Fig. 5.17, the calculated inductance using the proposed approach is in good agreement with the FEA results and the measurements. The slight deviation between the measured values and the analytically computed

**Table 5.3** Specifications of the inductances in Fig. 5.17

	$L_0$ (mH)	$\Delta L$ (mH)
Experimentally measured inductance	128.4	22.3
Inductance obtained from FEA	128.9	19.8
Calculated inductance based on the proposed method	124.3	19.5
Calculated inductance based on prior-art method	113.9	12.2

inductance by the proposed methodology is caused by the imperfections added to the FSCW IPM prototype in the manufacturing procedure, errors in the leakage inductance calculations, and the simplifications made to the stator flux paths in formulating the *MCLs*.

The demonstrated results prove that the proposed saturation model and equivalent airgap function can accurately predict the non-uniform distribution of saturation in the IPM rotor magnetic material. Accordingly, the proposed equivalent airgap function is computing the magnetic circuit length with a high accuracy in FSCW IPM machines, resulting in a more accurate estimation of the stator flux density in the airgap. Hence, it results in a more relevant value for the inductance compared with the conventional method.

## 5.5 Conclusion

With the purpose of calculating the inductance, different inductance components in a FSCW IPM machine were investigated. It was shown that for accurate analytical calculation of the inductance, the equivalent airgap function of the machine should be first obtained. To this aim, the stator flux lines in an IPM rotor at different angular positions was investigated. An equivalent airgap function was then proposed for the V-shaped FSCW IPM machine that was based on the formulated saturation map for the non-uniform distribution of magnetic saturation for the IPM rotor in Chap. 4. The effect of the concentrated-wound stator was taken into account in the proposed approach, considering the actual flux path inside the saturated rotor. The *B-H* curve of the rotor iron and the machine geometry are the fundamentals based on which the proposed equivalent airgap function is formulated. The proposed equivalent airgap function can be adopted in the standard formula for obtaining the inductance.

The rigorous mathematical analysis in this chapter shows that contrary to the conventional model for a FSCW IPM machine, the proposed equivalent airgap length is a function of both the rotor peripheral angle and the rotor angular position.

The prior-art and the proposed equivalent airgap functions were used to analytically calculate the stator airgap flux density and the inductance in a prototype FSCW IPM machine. The obtained results were compared against those obtained through FEA and experimental measurements, proving that compared with the conventional model, the proposed technique result in more accurate predictions for the machine characteristics.

The inductance of a prototype FSCW IPM machine was experimentally measured and compared with the results obtained by the proposed analytical technique and FEA. It was found that the proposed approach delivers results in a closer agreement with the experimental findings when compared with the state of the art. This analytical approach for inductance calculation is of prime importance as it eliminates the need for exhaustive and time-consuming FEA analysis involved in the typical machine analysis and design processes. Therefore, the proposed

approach provides a quick tool for saturation analysis of the rotor as well as analytical estimation of the inductances based on the IPM rotor geometry, the FSCW stator topology, and the  $B$ - $H$  curve of the rotor iron. This tool can aid in optimization of the saliency during the machine design phase.

## References

1. P.B. Reddy, A.M. El-Refaie, K.K. Huh, J.K. Tangudu, T.M. Jahns, Comparison of interior and surface PM machines equipped with fractional-slot concentrated windings for hybrid traction applications. *IEEE Trans. Energy Convers.* **27**, 593–602 (2012)
2. R. Dutta, M.F. Rahman, L. Chong, Winding inductances of an interior permanent magnet (IPM) machine with fractional slot concentrated winding. *IEEE Trans. Magn.* **48**, 4842–4849 (2012)
3. J. Pyrhonen, T. Jokinen, V. Hrabovcová, *Design of Rotating Electrical Machines* (Wiley, 2009)
4. P.C. Krause, O. Wasyczuk, S.D. Sudhoff, S. Pekarek, *Analysis of Electric Machinery and Drive Systems*, vol. 75 (Wiley, 2013)
5. A.M. El-Refaie, Z.Q. Zhu, T.M. Jahns, D. Howe, Winding inductances of fractional slot surface-mounted permanent magnet brushless machines, in *Industry Applications Society Annual Meeting, 2008, IAS '08* (IEEE, 2008), pp. 1–8
6. J. Staszak, Determination of slot leakage inductance for three-phase induction motor winding using an analytical method. *Arch. Electr. Eng.* **62**, 569–591 (2013)
7. B. Prieto, M. Martínez-Iturralde, L. Fontan, I. Elosegui, Analytical calculation of the slot leakage inductance in fractional-slot concentrated-winding machines. *IEEE Trans. Ind. Electron.* 2742–2752 (2015)
8. B.N. Cassimere, S.D. Sudhoff, D.H. Sudhoff, Analytical design model for surface-mounted permanent-magnet synchronous machines. *IEEE Trans. Energy Convers.* **24**, 347–357 (2009)
9. G. Dajaku, D. Gerling, Stator slotting effect on the magnetic field distribution of salient pole synchronous permanent-magnet machines. *IEEE Trans. Magn.* **46**, 3676–3683 (2010)
10. X. Hung Vu, D. Lahaye, H. Polinder, J.A. Ferreira, Influence of stator slotting on the performance of permanent-magnet machines with concentrated windings. *IEEE Trans. Magn.* **49**, 929–938 (2013)
11. L. Qi, F. Tao, W. Xuhui, Armature-reaction magnetic field analysis for interior permanent magnet motor based on winding function theory. *IEEE Trans. Magn.* **49**, 1193–1201 (2013)
12. L. Chong, R. Dutta, M.F. Rahman, Design of a highly efficient 1 kW concentric wound IPM machine with a very wide constant power speed range, in *Proceedings of the IPEC* (2010), pp. 1956–1961
13. IEEE standard procedure for obtaining synchronous machine parameters by standstill frequency response testing, in *IEEE Standard 115A-1987*, ed.

# Chapter 6

## Detailed Analytical Modelling of Inductances and Electromagnetic Torque in Fractional-Slot Concentrated-Wound Interior Permanent Magnet Machines Under Healthy and Open-Phase Fault Conditions



### 6.1 Introduction

Electromagnetic torque in an electric machine is the direct result of the interaction between the stator and rotor magnetic fields. This chapter builds upon the modelling of the stator and rotor magnetic characteristics performed in Chaps. 2, 4 and 5, based on which a rigorous mathematical modelling is conducted leading to detailed analytical formulae for the electromagnetic torque in a FSCW IPM machine operating under healthy and open-phase fault conditions.

Electromagnetic torque in IPM machines consists of the alignment torque and the reluctance torque that are originated from the rotor PM flux density and the machine magnetic saliency, respectively. Magnetic saliency represents the machine inductances which are conventionally assumed sinusoidal leading to calculation of a smooth reluctance torque. In the general treatment performed in this chapter, detailed analytical formulae are proposed for the inductances showing that the assumption of sinusoidal machine parameters does not hold true for FSCW IPM machines.

The detailed model for the rotor PM flux density proposed in Chap. 4 and the derived formulae for the self- and mutual inductances in this chapter are used to propose detailed formulae for the torque subcomponents. The average electromagnetic torque and the torque ripple are formulated in terms of the machine design parameters. Non-idealities in the machine variables are taken into account in the formulation of the torque subcomponents, making them adoptable for most synchronous machines.

In next sections of this chapter, an open-phase fault condition is considered and detailed models are proposed for the torque components under such conditions. The proposed formulae are then used to optimize the current phase angles for MTPA operation under an open phase fault condition. The proposed MTPA model for the

open-phase fault condition also leads to minimized torque ripple compared with standard control methods for open-phase fault conditions.

The proposed models in this chapter give insight into the parameters that affect the inductances and torque under different conditions in an electric machine and can aid in prediction of the machine operational characteristics in the design process.

## 6.2 Detailed Modelling of FSCW IPM Machine Operational Inductances

Self- and mutual inductances in an electric machine are the result of the interaction between the winding function of the machine phases with the permeance function of the machine. Detailed analytical models are proposed in this section for the machine inductances based on the machine design parameters.

### 6.2.1 Analytical Model of the Self-inductance

Self-inductance of phase  $j$  in an electric machine is a function of the rotor angular position,  $\theta_m$ , described by [1]:

$$L_j(\theta_m) = \int_0^{2\pi} w_j^2(\theta_s) \wp(\theta_r) d\theta_s \quad (6.1)$$

where  $w_j$  is the winding function of phase  $j$ , and  $\wp$  stands for the permeance function. The rotor motion should be accounted for in the above equation. The relationship between  $\theta_s$ ,  $\theta_m$ , and  $\theta_r$  when the rotor rotates at  $\omega_m$  mechanical rad/s are shown in Fig. 6.1. In this figure,  $a$ -axis is fixed in the stator and used as the reference for determining  $\theta_s$  and  $\theta_m$ . The  $d$ - and  $q$ -axes in Fig. 6.1 are fixed in the rotor frame, and the latter axis is used as the reference for measuring  $\theta_r$ . According to Fig. 6.1, the relationship between  $\theta_s$ ,  $\theta_m$ , and  $\theta_r$  can be written as:

$$\theta_s = \theta_m + \theta_r \quad (6.2)$$

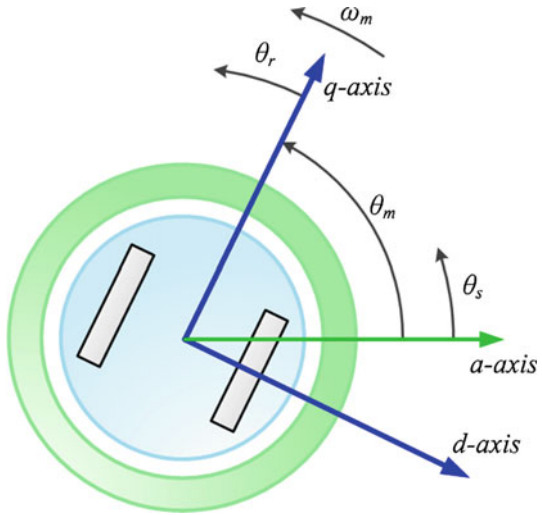
and

$$\theta_m = \omega_m t \quad (6.3)$$

Substitution of  $\theta_r$  from (6.2) in (6.1) gives:

$$L_j(\theta_m) = \int_0^{2\pi} w_j^2(\theta_s) \wp(\theta_s - \theta_m) d\theta_s \quad (6.4)$$

**Fig. 6.1** Relationship between the angles  $\theta_r$ ,  $\theta_s$ , and  $\theta_m$



From Chap. 2, Sect. 2.3.2 winding function of phase  $j$  is expressed by:

$$w_j(\theta_s) = \sum_n W_n \cos(n\theta_s - n\theta_j), \quad n = \frac{kP}{2c} \quad (6.5)$$

where:

$k = 1, 3, 5, \dots$  if the machine has an odd number of pole pairs, and  
 $k = 2, 4, 6, \dots$  if the machine has an even number of pole pairs,

and  $\theta_j$  is equal to 0,  $+2\pi/3$  and  $-2\pi/3$ , for phase  $a$ ,  $b$ , and  $c$ , respectively. The  $n$ th harmonic amplitude of the winding function,  $W_n$ , in (6.5) was computed in terms of the winding factor as:

$$W_n = \frac{2QN_c}{3n\pi} k_{w,n} \quad (6.6)$$

Before solving the integral in (6.4), the square root of the winding function should be calculated. This yields the following general expression:

$$w_j^2(\theta_s) = Y_0 + \sum_n^\infty Y_n \cos(n\theta_s - n\theta_j), \quad n = \frac{2P}{2c}, \frac{4P}{2c}, \frac{6P}{2c}, \dots \quad (6.7)$$

The most common topologies of FSCW machines are considered here and  $Y_0$  and  $Y_n$  are calculated using the Fourier series.

For category “C” FSCW Stators where  $S_{pp} = 2/(6k \pm 1)$  and  $k = 1, 3, 5, \dots$ ,  $Y_0$  and  $Y_n$  are calculated as:

$$Y_0 = \frac{1}{3} N_c^2 \quad (6.8)$$

$$Y_n = N_c^2 \frac{2}{n\pi c} \frac{P}{c} \sin\left(\frac{n\pi}{Q}\right) \left( 2 \cos\left(\frac{7\pi}{Q} n\right) \right) \quad (6.9)$$

For category “D” FSCW Stators where  $S_{pp} = 3/(9k \pm 2)$  and  $k = 1, 3, 5, \dots$ ,  $Y_0$  and  $Y_n$  are formulated as:

$$Y_0 = \frac{1}{3} N_c^2 \quad (6.10)$$

$$Y_n = N_c^2 \frac{2}{n\pi c} \frac{P}{c} \sin\left(\frac{n\pi}{Q}\right) \left( 1 + 2 \cos\left(\frac{10\pi}{Q} n\right) \right) \quad (6.11)$$

For category “D” FSCW Stators where  $S_{pp} = 3/(9k \pm 1)$  and  $k = 1, 3, 5, \dots$ ,  $Y_0$  and  $Y_n$  can be given by:

$$Y_0 = \frac{26}{81} N_c^2 \quad (6.12)$$

$$Y_n = N_c^2 \frac{P}{c} \frac{2}{9n\pi} \sin\left(\frac{n\pi}{Q}\right) \left( 11 + 14 \cos\left(\frac{2n\pi}{Q}\right) \right) \quad (6.13)$$

Conventionally, the permeance function can be approximated by a trapezoidal form, as shown in Fig. 6.2, expressed using Fourier series as:

$$\wp(\theta_r) = \wp_0 + \sum_{n=kP}^{\infty} \wp_n \cos(n\theta_r), \quad k = 1, 2, 3, \dots \quad (6.14)$$

where

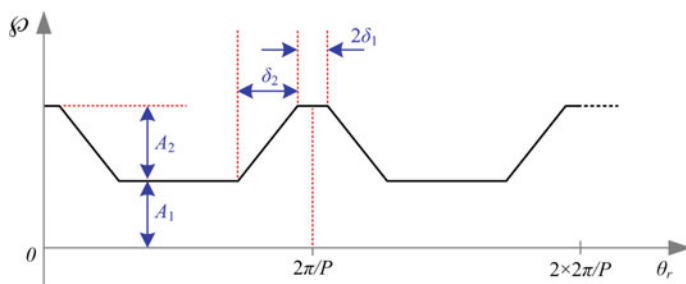


**Fig. 6.2** Permeance function of a PMSM, showing its main parameters

$$\wp_0 = A_1 + \frac{PA_2}{2\pi} (2\delta_1 + \delta_2) \quad (6.15)$$

$$\wp_n = \frac{4PA_2}{n^2\pi\delta_2} \sin\left(\frac{n\delta_2}{2}\right) \sin\left(\frac{n}{2}(2\delta_1 + \delta_2)\right) \quad (6.16)$$

The parameters in (6.15) and (6.16) should be obtained from Fig. 6.2 based on the analysis performed in Chaps. 4 and 5. Substitution of (6.7) and (6.14) in (6.4) yields:

$$L_j(\theta_m) = \int_0^{2\pi} \left( Y_0 + \sum_{n=\frac{P}{c}, \frac{2P}{c}, \frac{3P}{c}, \dots}^{\infty} Y_n \cdot \cos(n\theta_s - n\theta_j) \right) \times \left( \wp_0 + \sum_{n=P, 2P, 3P, \dots}^{\infty} \wp_n \cos(n\theta_s - n\theta_m) \right) d\theta_s \quad (6.17)$$

Thus:

$$\begin{aligned} L_j(\theta_m) &= \int_0^{2\pi} Y_0 \wp_0 d\theta_s \\ &+ Y_0 \int_0^{2\pi} \sum_{n=P, 2P, 3P, \dots}^{\infty} \wp_n \cos(n\theta_s - n\theta_m) d\theta_s \\ &+ \wp_0 \int_0^{2\pi} \sum_{n=P, 2P, 3P, \dots}^{\infty} \wp_n \cos(n\theta_s - n\theta_m) d\theta_s \\ &+ \int_0^{2\pi} \sum_{n=P, 2P, 3P, \dots}^{\infty} \wp_n \cos(n\theta_s - n\theta_m) \sum_{n=\frac{P}{c}, \frac{2P}{c}, \frac{3P}{c}, \dots}^{\infty} Y_n \cdot \cos(n\theta_s - n\theta_j) d\theta_s \end{aligned} \quad (6.18)$$

The second and third terms in the above equation return a zero value. Solving the integrals in the first term and fourth term in (6.18) gives:

$$\int_0^{2\pi} d\theta_s = 2\pi Y_0 \wp_0 \quad (6.19)$$

$$\begin{aligned} & \int_0^{2\pi} \sum_{n=P,2P,3P,\dots}^{\infty} \wp_n \cos(n\theta_s - n\theta_m) \sum_{n=\frac{P}{c},\frac{2P}{c},\frac{3P}{c},\dots}^{\infty} Y_n \cdot \cos(n\theta_s - n\theta_j) d\theta_s \\ &= \pi \sum_{n=P,2P,3P,\dots}^{\infty} Y_n \wp_n \cos(n\theta_m - n\theta_j) \end{aligned} \quad (6.20)$$

Therefore, (6.18) simplifies to:

$$L_j(\theta_m) = 2\pi Y_0 \wp_0 + \pi \sum_n^{\infty} Y_n \wp_n \cos(n\theta_m - n\theta_j), \quad n = P, 2P, 3P, \dots \quad (6.21)$$

Evidently, the self-inductance comprises a *dc* value with superimposed spatial harmonics of order  $n = P, 2P, 3P, \dots$ . The oscillatory part of the self-inductance is a function of the rotor angular position,  $\theta_m$ , in mechanical radians. The rotor angular position can be expressed in terms of electrical radians as follows:

$$\theta_{m,e} = \frac{P}{2} \theta_m \quad (6.22)$$

Substitution of (6.22) into (6.21) yields:

$$L_j(\theta_{m,e}) = 2\pi Y_0 \wp_0 + \pi \sum_n^{\infty} Y_{n \cdot P} \wp_{n \cdot P} \cos(n\theta_{m,e} - n\theta_j), \quad n = 2, 4, 6, \dots \quad (6.23)$$

It has to be noted that the complete formula for the self-inductance is obtained by adding the *dc* self-inductance leakage term,  $L_{ls}$ , to (6.23) as calculated in Chap. 5. Accordingly, the self-inductance can be cumulated in the following general form:

$$L_j(\theta_{m,e}) = L_0 + \sum_n^{\infty} L_n \cos(n\theta_{m,e} - n\theta_j), \quad n = 2, 4, 6, \dots \quad (6.24)$$

where

$$L_0 = L_{ls} + 2\pi Y_0 \wp_0 \quad (6.25)$$

$$L_n = \pi Y_{n \cdot P} \wp_{n \cdot P}. \quad (6.26)$$

### 6.2.2 Analytical Model of the Mutual Inductance

Mutual inductance between phases  $j$  and  $z$  in an electric machine is a function of the rotor angular position,  $\theta_m$ , and is described by [1]:

$$M_{jz}(\theta_m) = \int_0^{2\pi} w_j(\theta_s) w_z(\theta_s) \wp(\theta_r) d\theta_s \quad (6.27)$$

It is observed that the mutual inductance between two phase windings has a direct relationship with the multiplication of their winding functions. From Chap. 2, the winding functions of the phase windings in an FSCW stator overlap only in the stator topologies where the number of pole pairs in their base winding layout is an even number. In stator topologies that have an odd number of pole pairs in their base winding layout, the winding functions of different phase windings do not overlap, thus according to (6.27) the mutual inductance is expected to be zero. However, due to the wide slots of a FSCW stator, the winding function is more of a trapezoidal shape rather than the commonly used square shape. Thus in a double-layer FSCW configuration with an odd number of pole pairs in its base winding layout, a small overlap in the winding functions underneath the slots is expected, leading to a small value for the mutual inductance. Based on these explanations, the integral in (6.27) is solved. Substitution of  $\theta_r$  from (6.2) in (6.27) yields:

$$M_{jz}(\theta_m) = \int_0^{2\pi} w_j(\theta_s) w_z(\theta_s) \wp(\theta_s - \theta_m) d\theta_s \quad (6.28)$$

Similar to the procedure for obtaining the self-inductance detailed expression, after some mathematical simplifications, (6.28) solves to the following compact form:

$$M_{jz}(\theta_m) = \begin{cases} \pi \wp_0 \sum_{n=\frac{kP}{2c}}^{\infty} W_n^2 \cos(n(\theta_z - \theta_j)) & k = \text{odd number} \\ + \frac{\pi}{2} \sum_{n=P,3P,5P,\dots}^{\infty} W_{(n/2)}^2 \wp_n \cos(n\theta_m - \frac{n}{2}(\theta_z + \theta_j)) \\ \pi \wp_0 \sum_{n=\frac{kP}{2c}}^{\infty} W_n^2 \cos(n(\theta_z - \theta_j)) & k = \text{even number} \\ + \frac{\pi}{2} \sum_{n=P,2P,3P,\dots}^{\infty} W_{(n/2)}^2 \wp_n \cos(n\theta_m - \frac{n}{2}(\theta_z + \theta_j)) \end{cases} \quad (6.29)$$

The above equations can be expressed in terms of electrical radians by substituting the rotor angular position in mechanical radians,  $\theta_m$  with its equivalent in electrical radians, (6.22), as follows:

$$M_{jz}(\theta_{m,e}) = \begin{cases} \pi\varphi_0 \sum_{n=\frac{kP}{2c}}^{\infty} W_n^2 \cos(n(\theta_z - \theta_j)) & k = \text{odd number} \\ + \frac{\pi}{2} \sum_{n=2,6,10,\dots}^{\infty} W_{(n\cdot P/2)}^2 \varphi_{n\cdot P} \cos(n\theta_{m,e} - \frac{n}{2}(\theta_z + \theta_j)) \\ \pi\varphi_0 \sum_{n=\frac{kP}{2c}}^{\infty} W_n^2 \cos(n(\theta_z - \theta_j)) & k = \text{even number} \\ + \frac{\pi}{2} \sum_{n=2,4,6,\dots}^{\infty} W_{(n\cdot P/2)}^2 \varphi_{n\cdot P} \cos(n\theta_{m,e} - \frac{n}{2}(\theta_z + \theta_j)) \end{cases} \quad (6.30)$$

It is observed from (6.30) that similar to the self-inductance, regardless of the number of pole pairs, the mutual inductance comprises a *dc* term with superimposed spatial harmonics of even order.

It has to be noted that the complete formula for the mutual inductance should include the leakage mutual inductance terms which were calculated in Chap. 5. Accordingly, these leakage mutual inductance terms should be mathematically added to (6.30). Consequently, the mutual inductance in a FSCW PMSM can be cumulated in the following general form:

$$M_{jz}(\theta_{m,e}) = M_0 + \sum_n^{\infty} M_n \cos(n\theta_{m,e} - n\theta_{jz}), \quad n = 2, 4, 6, \dots \quad (6.31)$$

where

$$M_0 = L_{lm} + \pi\varphi_0 \sum_{n=\frac{kP}{2c}}^{\infty} W_n^2 \cos\left(\frac{2n\pi}{3}\right) \quad (6.32)$$

$$M_n = \frac{\pi}{2} W_{(n\cdot P/2)}^2 \varphi_{n\cdot P} \quad (6.33)$$

and  $\theta_{jz}$  is equal to  $+\pi/3$ ,  $-\pi/3$ , and  $-\pi$  for phase *ab*, *ac*, and *bc*, respectively.

### 6.3 Detailed Modelling of FSCW IPM Machine Electromagnetic Torque Under Normal Operating Condition

The generated torque in a FSCW PMSM consists of three main components, as follows:

$$T_{em}(t) = T_{align}(t) + T_{rel}(t) + T_{cog}(t) \quad (6.34)$$

The first term in (6.34) is the alignment torque, the second term is the reluctance torque, and the last term is the cogging torque. The alignment and reluctance torques are the only components that contribute to average torque production in a PMSM. Thus, only these components are of interest here. Cogging torque only contributes to the torque ripple and is due to the interaction of the rotor PM flux with the stator slots. This torque ripple component is negligible in a well-designed FSCW PMSM [2, 3].

The FSCW PMSM is assumed to be supplied with a balanced three-phase current set with amplitude  $I_m$  and frequency  $\omega_e$  as follows:

$$\begin{aligned} i_a(t) &= I_m \cos(\omega_e t + \gamma) \\ i_b(t) &= I_m \cos(\omega_e t - \frac{2\pi}{3} + \gamma) \\ i_c(t) &= I_m \cos(\omega_e t + \frac{2\pi}{3} + \gamma) \end{aligned} \quad (6.35)$$

The current phase angle  $\gamma$  in (6.35) indicates the phase angle of the current with respect to the back-EMF. In electric drives, zero-crossing of the back-EMF is taken as a reference for measuring the current angle as shown in Fig. 6.3. As a reference, zero-crossing of the back-EMF occurs at  $t = 0$  s. For this purpose, an initial rotor position,  $\theta_{0,m}$ , will be included in the analytical torque calculations which is measured with respect to the stator  $a$ -axis and should be determined such that the rotor  $d$ -axis and the stator  $a$ -axis are aligned. Under such alignment the zero-crossing of the back-EMF occurs at time  $t = 0$  s.

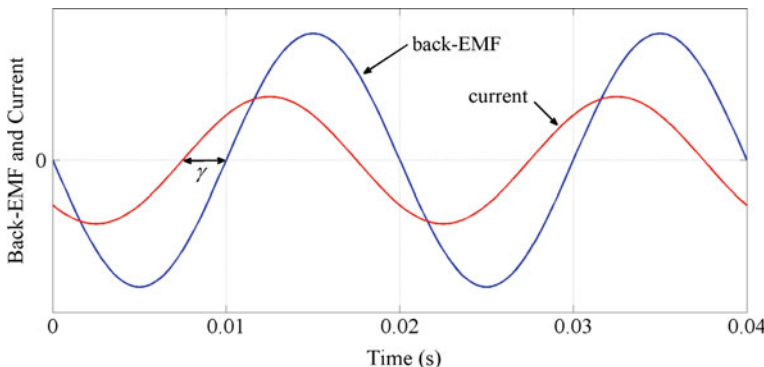


**Fig. 6.3** Illustration of the supplied current leading the back-EMF by  $\gamma$  radians for maximum torque per ampere scheme

### 6.3.1 Formulation of Alignment Torque

In a PMSM, Alignment torque is the result of the interaction between the stator and rotor spatial MMF distributions. The stator MMF originates from the supplied current, while the rotor MMF is generated due to the residual flux of the embedded magnets in the rotor. The alignment torque can be calculated by integrating Lorentz's force density around the airgap [4, 5]:

$$T_{align}(t) = r_g l_{eff} \int_0^{2\pi} B_{ag}(t, \theta_s) \frac{df_s(t, \theta_s)}{d\theta_s} d\theta_s \quad (6.36)$$

where,  $B_{ag}$  is the net flux density in the airgap as a function of time and the angle along the stator circumference, and is due to the interaction between the stator and rotor magnetic fields. According to the theory of magnetic equivalent circuits,  $B_{ag}$  is obtained from the MMF drop across the physical airgap as follows:

$$B_{ag}(t, \theta_s) = \mu_0 \frac{f_r(t, \theta_s) - f_s(t, \theta_s)}{g} \quad (6.37)$$

where  $f_r$  and  $f_s$  are the MMFs on the rotor and stator surfaces, respectively. Substitution of (6.37) in (6.36) yields:

$$T_{align}(t) = \frac{\mu_0 r_g l_{eff}}{g} \left( \int_0^{2\pi} f_r(t, \theta_s) \frac{df_s(t, \theta_s)}{d\theta_s} d\theta_s - \int_0^{2\pi} f_s(t, \theta_s) \frac{df_s(t, \theta_s)}{d\theta_s} d\theta_s \right) \quad (6.38)$$

The second integral in the above equation returns a zero value:

$$\int_0^{2\pi} f_s(t, \theta_s) \frac{df_s(t, \theta_s)}{d\theta_s} d\theta_s = \frac{1}{2} f_s(t, \theta_s) \Big|_0^{2\pi} = 0 \quad (6.39)$$

Hence, (6.38) simplifies to:

$$T_{align}(t) = \frac{\mu_0 r_g l_{eff}}{g} \int_0^{2\pi} f_r(t, \theta_s) \frac{df_s(t, \theta_s)}{d\theta_s} d\theta_s \quad (6.40)$$

From Chap. 2, for a FSCW PMSM that is being supplied with the balanced three-phase current, (6.35), the stator MMF is expressed by:

$$\begin{aligned} f_s(t, \theta_s) = & \sum_{n=\frac{P}{2c}(6k+b)} f_{ccw,n}(t, \theta_s) \\ & + \sum_{n=\frac{P}{2c}(6k-b)} f_{cw,n}(t, \theta_s), \quad k = 0, 1, 2, 3, \dots \end{aligned} \quad (6.41)$$

where

$$f_{ccw,n}(t, \theta_s) = F_n \cos(\omega_e t - n\theta_s + \gamma) \quad (6.42)$$

$$f_{cw,n}(t, \theta_s) = F_n \cos(\omega_e t + n\theta_s + \gamma) \quad (6.43)$$

and

$$F_n = \frac{QN_c}{n\pi} k_{w,n} I_m. \quad (6.44)$$

The embedded magnets in an IPM rotor creates a magnetic potential on the rotor surface and the airgap. The role of the rotor magnetic potential is similar to that of the stator MMF, thus it will be termed *rotor MMF*. The flux of the embedded magnets in an IPM rotor causes a non-uniform saturation in the rotor iron. This makes the magnetic potential on the rotor surface to be non-uniform. This phenomenon complicates direct analytical calculation of the rotor MMF on the surface of an IPM rotor. However, the rotor MMF can be indirectly computed using the open-circuit airgap PM flux density, as explained in the following:

$$f_r(t, \theta_s) = \frac{g}{\mu_0} B_{PM}(t, \theta_s) \quad (6.45)$$

where  $B_{PM}$  is the open-circuit airgap PM flux density for the rotating rotor. From Chap. 2, open-circuit PM flux density can be expressed as a function of time and the angle subtended along the stator circumference, and for a counter-clockwise rotating rotor is expressed using Fourier series as:

$$B_{PM}(t, \theta_s) = \sum_{n=\frac{P}{2d}}^{\infty} B_{max,n} \sin(n\omega_m t - n\theta_s - n\theta_{0,m}), \quad d = 1, 3, 5, \dots \quad (6.46)$$

where  $B_{max,n}$  is the amplitude of the  $n$ th harmonic of the airgap PM flux density, and  $\theta_{0,m}$  is the initial mechanical position of the rotor with respect to the stator. It is common to express the rotor MMF as a function of the PM flux linkage. From Chap. 2, the PM flux linkage is expressed by:

$$\lambda_{PM,j} = \sum_d \lambda_{max,d} \sin(d\omega_e t - d\theta_j), \quad d = 1, 3, 5, \dots \quad (6.47)$$

$$\lambda_{\max,d} = r_g l_{eff} \frac{4}{Pd} N_j k_{w,(P/2)d} B_{\max,(P/2)d} \quad (6.48)$$

where  $\lambda_{\max,k}$  is the amplitude of the  $k$ th PM flux linkage harmonic, and  $\omega_e$  is the rotational speed in electrical rad/s (equal to the supply frequency), and can be expressed as:

$$\omega_e = \frac{P}{2} \omega_m \quad (6.49)$$

The rotor MMF can be found as a function of the PM flux linkage by rearranging (6.48) for the PM flux density amplitude and replacing it in (6.46). Replacing the result in (6.45) yields the rotor MMF as follows:

$$f_r(t, \theta_s) = \sum_{n=\frac{P}{2}d}^{\infty} f_{r,\max,n} \sin(n\omega_m t - n\theta_s - n\theta_{0,m}), \quad d = 1, 3, 5, \dots \quad (6.50)$$

$$f_{r,\max,n} = \frac{g}{\mu_0} \frac{1}{2r_g l_{eff} N_j} \frac{n\lambda_{\max,n/(P/2)}}{k_{w,n}} \quad (6.51)$$

Substitution of the rotor MMF, (6.50), and the derivative of the stator MMF, (6.41), in the alignment torque equation, (6.40), gives:

$$\begin{aligned} T_{align}(t) &= \frac{\mu_0 r_g l_{eff}}{g} \int_0^{2\pi} \left[ \sum_{n=\frac{P}{2}d}^{\infty} f_{r,\max,n} \sin(n\omega_m t - n\theta_s - n\theta_{0,m}) \right] \\ &\quad \times \left[ \sum_{n=\frac{P}{2c}(6k+b)} n F_n \sin(\omega_e t - n\theta_s + \gamma) - \sum_{n=\frac{P}{2c}(6k-b)} n F_n \sin(\omega_e t + n\theta_s + \gamma) \right] d\theta_s \\ &= \frac{\mu_0 r_g l_{eff}}{g} \int_0^{2\pi} \sum_{n=\frac{P}{2}d}^{\infty} f_{r,\max,n} \sin(n\omega_m t - n\theta_s - n\theta_{0,m}) \\ &\quad \times \sum_{n=\frac{P}{2c}(6k+b)} n F_n \sin(\omega_e t - n\theta_s + \gamma) d\theta_s \\ &\quad - \frac{\mu_0 r_g l_{eff}}{g} \int_0^{2\pi} \sum_{n=\frac{P}{2}d}^{\infty} f_{r,\max,n} \sin(n\omega_m t - n\theta_s - n\theta_{0,m}) \\ &\quad \times \sum_{n=\frac{P}{2c}(6k-b)} n F_n \sin(\omega_e t + n\theta_s + \gamma) d\theta_s \end{aligned} \quad (6.52)$$

The integral terms in (6.53) return a nonzero value, if

$$n = \frac{P}{2}d = \frac{P}{2c}(6k \pm b), \quad d = 1, 3, 5, 7, \dots \quad k = 0, 1, 2, 3, \dots \quad (6.53)$$

Taking into account the condition of (6.53), solutions to the integrals in (6.52) yield:

$$\begin{aligned} & \int_0^{2\pi} \sin(n\omega_m t - n\theta_s - n\theta_{0,m}) \cdot \sin(\omega_e t - n\theta_s + \gamma) d\theta_s \\ &= \int_0^{2\pi} \sin(k\omega_e t - \frac{P}{2}k\theta_s - \frac{P}{2}k\theta_{0,m}) \cdot \sin(\omega_e t - \frac{P}{2}k\theta_s + \gamma) d\theta_s \\ &= \pi \cos\left((k-1)\omega_e t - \gamma - \frac{P}{2}k\theta_{0,m}\right), \quad k = 6q+1, \quad q = 0, 1, 2, 3, \dots \end{aligned} \quad (6.54)$$

$$\begin{aligned} & \int_0^{2\pi} \sin(n\omega_m t - n\theta_s - n\theta_{0,m}) \cdot \sin(\omega_e t + n\theta_s + \gamma) d\theta_s \\ &= \int_0^{2\pi} \sin(k\omega_e t - \frac{P}{2}k\theta_s - \frac{P}{2}k\theta_{0,m}) \cdot \sin(\omega_e t + \frac{P}{2}k\theta_s + \gamma) d\theta_s \\ &= -\pi \cos\left((k+1)\omega_e t + \gamma - \frac{P}{2}k\theta_{0,m}\right), \quad k = 6q-1, \quad q = 1, 2, 3, \dots \end{aligned} \quad (6.55)$$

Substitution of (6.54) and (6.55) into (6.52) gives:

$$\begin{aligned} T_{align}(t) &= \frac{\mu_0 \pi r_g l_{eff}}{g} \frac{P}{2} \left( \sum_{k=6q+1}^{\infty} k F_{(P/2)k} f_{r,\max,(P/2)k}, \quad q = 0, 1, 2, 3, \dots \right. \\ &\quad \times \cos\left((k-1)\omega_e t - \gamma - \frac{P}{2}k\theta_{0,m}\right) \\ &\quad \left. + \sum_{k=6q-1}^{\infty} k F_{(P/2)k} f_{r,\max,(P/2)k} \right. \\ &\quad \left. \times \cos\left((k+1)\omega_e t + \gamma - \frac{P}{2}k\theta_{0,m}\right) \right) \end{aligned} \quad (6.56)$$

Substitution of the stator and rotor MMF amplitudes, (6.44) and (6.51), into (6.56) yields:

$$\begin{aligned} T_{align}(t) &= \frac{3P}{2} I_m \left( \sum_{k=6q+1}^{\infty} k \lambda_{\max,k} \cos\left((k-1)\omega_e t - \gamma - \frac{P}{2}k\theta_{0,m}\right) \right. \\ &\quad \left. + \sum_{k=6q-1}^{\infty} k \lambda_{\max,k} \cos\left((k+1)\omega_e t + \gamma - \frac{P}{2}k\theta_{0,m}\right) \right), \\ q &= 0, 1, 2, 3, \dots \end{aligned} \quad (6.57)$$

The PM flux linkage harmonic amplitudes,  $\lambda_{max,k}$ , in (6.57) can either be measured directly from the machine, or calculated using (6.48) from the harmonic winding factors and PM flux density, for which analytical treatments are proposed in Chap. 4 and Chap. 2, respectively.

From (6.57), the average torque and the torque ripple of the alignment torque are found as follows:

$$T_{align,ave} = \frac{3P}{2} \frac{I_m}{2} \lambda_{max,1} \cos(\gamma + \frac{P}{2} \theta_{0,m}) \quad (6.58)$$

$$\begin{aligned} T_{align,ripple}(t) &= \frac{3P}{2} \frac{I_m}{2} \left( \sum_{k=6q+1}^{\infty} k \lambda_{max,k} \cos\left((k-1)\omega_e t - \gamma - \frac{P}{2} k \theta_{0,m}\right) \right. \\ &\quad \left. + \sum_{k=6q-1}^{\infty} k \lambda_{max,k} \cos\left((k+1)\omega_e t + \gamma - \frac{P}{2} k \theta_{0,m}\right) \right), \\ q &= 1, 2, 3, \dots \end{aligned} \quad (6.59)$$

and  $\lambda_{max,k}$  is given in (6.48).

It is clear from (6.58) that the alignment torque is directly proportional with the supply current amplitude. The only PM flux linkage component that participates in the average alignment torque generation is the fundamental component. This component is proportional to the fundamental component of the back-EMF, which is turn is the result of the PM flux density harmonic of order  $P/2$ . The remaining harmonics of the PM flux linkage only participate in generating the alignment torque ripple as seen in (6.59). From (6.58), the maximum average alignment torque occurs when the *cosine* function returns unity. Assuming  $\theta_{0,m} = 0$ , the maximum average reluctance torque occurs at  $\gamma = 90^\circ$ . Eq. (6.59) implies that the alignment torque ripple contains harmonics with their order being an integer multiple of 6.

### 6.3.2 Formulation of Reluctance Torque Equation

Reluctance torque is the result of the non-uniform equivalent airgap in an IPM machine. This torque component is developed on account of the stator field trying to align the rotor in such a way that the magnetic reluctance of the stator flux paths becomes minimum. Therefore, this torque component is generated by the interaction of the stator spatial MMF distribution with the rotor magnetic saliency which is represented by the machine inductances. Reluctance torque of a  $P$ -pole machine can be found from the partial derivative of the reluctance co-energy caused by the magnetic saliency of the machine [1]:

$$T_{rel}(t) = \left(\frac{P}{2}\right) \frac{\partial W_{c,rel}}{\partial \theta_{m,e}} \quad (6.60)$$

where  $W_{c,rel}$  represents the reluctance co-energy. This term can be expressed as a function of the machine inductances and supplied currents as follows [12]:

$$W_{c,rel} = L_a i_a^2 + L_b i_b^2 + L_c i_c^2 + M_{ab} i_a i_b + M_{ac} i_a i_c + M_{bc} i_b i_c \quad (6.61)$$

Thus:

$$\begin{aligned} T_{rel}(t) &= \frac{P}{2} \left( \frac{1}{2} i_a^2 \frac{dL_a}{d\theta_{m,e}} + \frac{1}{2} i_b^2 \frac{dL_b}{d\theta_{m,e}} + \frac{1}{2} i_c^2 \frac{dL_c}{d\theta_{m,e}} \right. \\ &\quad \left. + i_a i_b \frac{dM_{ab}}{d\theta_{m,e}} + i_a i_c \frac{dM_{ac}}{d\theta_{m,e}} + i_b i_c \frac{dM_{bc}}{d\theta_{m,e}} \right) \end{aligned} \quad (6.62)$$

Taking into account that  $\theta_{m,e} = \omega_e t$ , and considering the initial rotor position,  $\theta_{0,m}$ , substitution of the detailed expressions for the self- and mutual inductances, (6.24) and (6.31), and the three-phase currents, (6.35), in (6.62) yields:

$$\begin{aligned} T_{rel}(t) &= -\frac{P}{2} I_m^2 \left( \frac{1}{2} \sum_{n=2,4,6,\dots}^{\infty} n L_n \cos^2(\omega_e t + \gamma) \sin(n\omega_e t - n \frac{P}{2} \theta_{0,m}) \right. \\ &\quad + \frac{1}{2} \sum_{n=2,4,6,\dots}^{\infty} n L_n \cos^2(\omega_e t - \frac{2\pi}{3} + \gamma) \sin(n\omega_e t - n \frac{2\pi}{3} - n \frac{P}{2} \theta_{0,m}) \\ &\quad + \frac{1}{2} \sum_{n=2,4,6,\dots}^{\infty} n L_n \cos^2(\omega_e t + \frac{2\pi}{3} + \gamma) \sin(n\omega_e t + n \frac{2\pi}{3} - n \frac{P}{2} \theta_{0,m}) \\ &\quad + \sum_{n=2,4,6,\dots}^{\infty} n M_n \cos(\omega_e t + \gamma) \cos(\omega_e t - \frac{2\pi}{3} + \gamma) \\ &\quad \times \sin(n\omega_e t - n \frac{\pi}{3} - n \frac{P}{2} \theta_{0,m}) \\ &\quad + \sum_{n=2,4,6,\dots}^{\infty} n M_n \cos(\omega_e t + \gamma) \cos(\omega_e t + \frac{2\pi}{3} + \gamma) \\ &\quad \times \sin(n\omega_e t + n \frac{\pi}{3} - n \frac{P}{2} \theta_{0,m}) \\ &\quad + \sum_{n=2,4,6,\dots}^{\infty} n M_n \cos(\omega_e t - \frac{2\pi}{3} + \gamma) \cos(\omega_e t + \frac{2\pi}{3} + \gamma) \\ &\quad \times \sin(n\omega_e t + n\pi - n \frac{P}{2} \theta_{0,m}) \left. \right) \end{aligned} \quad (6.63)$$

or

$$\begin{aligned}
 T_{rel}(t) = & -\frac{1}{2} \frac{P}{2} I_m^2 \left( \frac{1}{2} \sum_{n=2,4,6,\dots}^{\infty} n L_n \left( (1 + \cos 2(\omega_e t + \gamma)) \sin(n\omega_e t - n \frac{P}{2} \theta_{0,m}) \right. \right. \\
 & + \left( 1 + \cos 2(\omega_e t - \frac{2\pi}{3} + \gamma) \right) \times \sin(n\omega_e t - n \frac{2\pi}{3} - n \frac{P}{2} \theta_{0,m}) \\
 & + \left( 1 + \cos 2(\omega_e t + \frac{2\pi}{3} + \gamma) \right) \times \sin(n\omega_e t + n \frac{2\pi}{3} - n \frac{P}{2} \theta_{0,m}) \\
 & + \sum_{n=2,4,6,\dots}^{\infty} n M_n \left( \left( \cos(\frac{2\pi}{3}) + \cos(2\omega_e t + 2\gamma - \frac{2\pi}{3}) \right) \right. \\
 & \times \sin(n\omega_e t - n \frac{\pi}{3} - n \frac{P}{2} \theta_{0,m}) \\
 & + \left( \cos(\frac{2\pi}{3}) + \cos(2\omega_e t + 2\gamma + \frac{2\pi}{3}) \right) \\
 & \times \sin(n\omega_e t + n \frac{\pi}{3} - n \frac{P}{2} \theta_{0,m}) \\
 & + \left( \cos(\frac{4\pi}{3}) + \cos(2\omega_e t + 2\gamma + 2\pi) \right) \\
 & \times \sin(n\omega_e t + n\pi - n \frac{P}{2} \theta_{0,m}) \Big) \Big) \\
 \end{aligned} \tag{6.64}$$

The following mathematical manipulations are used:

$$\begin{aligned}
 & \sum_{n=2,4,6,\dots}^{\infty} n L_n \left( (1 + \cos 2(\omega_e t + \gamma)) \sin(n\omega_e t - n \frac{P}{2} \theta_{0,m}) \right. \\
 & + \left( 1 + \cos 2(\omega_e t - \frac{2\pi}{3} + \gamma) \right) \sin(n\omega_e t - n \frac{2\pi}{3} - n \frac{P}{2} \theta_{0,m}) \\
 & + \left. \left( 1 + \cos 2(\omega_e t + \frac{2\pi}{3} + \gamma) \right) \sin(n\omega_e t + n \frac{2\pi}{3} - n \frac{P}{2} \theta_{0,m}) \right) \\
 = & \frac{3}{2} \left( \sum_{n=2,8,14,\dots}^{\infty} n L_n \sin \left( (n-2)\omega_e t - 2\gamma - n \frac{P}{2} \theta_{0,m} \right) \right. \\
 & + \sum_{n=6,12,18,\dots}^{\infty} 2 n L_n \sin(n\omega_e t - n \frac{P}{2} \theta_{0,m}) \\
 & + \left. \left. \sum_{n=4,10,16,\dots}^{\infty} n L_n \sin \left( (n+2)\omega_e t + 2\gamma - n \frac{P}{2} \theta_{0,m} \right) \right) \right) \\
 \end{aligned} \tag{6.65}$$

and

$$\begin{aligned}
& \sum_{n=2,4,6,\dots}^{\infty} nM_n \left( \left( \cos\left(\frac{2\pi}{3}\right) + \cos(2\omega_e t + 2\gamma - \frac{2\pi}{3}) \right) \sin(n\omega_e t - n\frac{\pi}{3} - n\frac{P}{2}\theta_{0,m}) \right. \\
& + \left( \cos\left(\frac{2\pi}{3}\right) + \cos(2\omega_e t + 2\gamma + \frac{2\pi}{3}) \right) \sin(n\omega_e t + n\frac{\pi}{3} - n\frac{P}{2}\theta_{0,m}) \\
& + \left. \left( \cos\left(\frac{4\pi}{3}\right) + \cos(2\omega_e t + 2\gamma + 2\pi) \right) \sin(n\omega_e t + n\pi - n\frac{P}{2}\theta_{0,m}) \right) \\
& = \frac{3}{2} \left( \sum_{n=2,8,14,\dots}^{\infty} nM_n \sin((n-2)\omega_e t - 2\gamma - n\frac{P}{2}\theta_{0,m}) \right. \\
& - \sum_{n=6,12,18,\dots}^{\infty} nM_n \sin(n\omega_e t - n\frac{P}{2}\theta_{0,m}) \\
& \left. + \sum_{n=4,10,16,\dots}^{\infty} nM_n \sin((n+2)\omega_e t + 2\gamma - n\frac{P}{2}\theta_{0,m}) \right) \tag{6.66}
\end{aligned}$$

Based on (6.65) and (6.66), the reluctance torque equation, (6.64), simplifies to:

$$\begin{aligned}
T_{rel}(t) &= -\frac{3P}{4}I_m^2 \left( \sum_{n=2,8,14,\dots}^{\infty} \frac{n}{2}(L_n + 2M_n) \sin((n-2)\omega_e t - 2\gamma - n\frac{P}{2}\theta_{0,m}) \right. \\
& + \sum_{n=4,10,16,\dots}^{\infty} \frac{n}{2}(L_n + 2M_n) \sin((n+2)\omega_e t + 2\gamma - n\frac{P}{2}\theta_{0,m}) \\
& \left. + \sum_{n=6,12,18,\dots}^{\infty} n(L_n - M_n) \sin(n\omega_e t - n\frac{P}{2}\theta_{0,m}) \right) \tag{6.67}
\end{aligned}$$

From (6.67), the average reluctance torque and the reluctance torque ripple are:

$$T_{rel,ave} = \frac{3P}{4}I_m^2(L_2 + 2M_2) \sin(2\gamma - P\theta_{0,m}) \tag{6.68}$$

$$\begin{aligned}
T_{rel,ripple}(t) &= -\frac{3P}{4}I_m^2 \left( \sum_{n=6k+2}^{\infty} \frac{n}{2}(L_n + 2M_n) \sin((n-2)\omega_e t - 2\gamma - n\frac{P}{2}\theta_{0,m}) \right. \\
& + \sum_{n=6k-2}^{\infty} \frac{n}{2}(L_n + 2M_n) \sin((n+2)\omega_e t + 2\gamma - n\frac{P}{2}\theta_{0,m}) \\
& \left. + \sum_{n=6k}^{\infty} n(L_n - M_n) \sin(n\omega_e t - n\frac{P}{2}\theta_{0,m}) \right), \quad k = 1, 2, 3, \dots \tag{6.69}
\end{aligned}$$

It is observed that the reluctance torque is directly proportional to the square of the supply current amplitude. From (6.68), the maximum average reluctance torque occurs when the *sine* function returns unity. The only inductance harmonics that participate in generation of the average reluctance torque are the fundamental components of the self- and mutual inductances. Other harmonics of the machine inductances contribute only to the torque ripple ad can be seen in (6.69). Assuming  $\theta_{0,m} = 0$ , the maximum average reluctance torque occurs at  $\gamma = 45^\circ$ . It is observed from (6.69) that similar to the alignment torque ripple, the reluctance torque ripple comprises harmonics that their order is an integer multiple of 6.

### 6.3.3 Complete Torque Equation

According to (6.34), the complete torque equation in an FSCW IPM machine is obtained by summing the alignment torque, (6.63), and the reluctance torque, (6.67). This yields the total average torque,  $T_{ave}$ , and the total torque ripple,  $T_{ripple}$ , as follows:

$$T_{ave} = \frac{3P}{4} \underbrace{\left( 2I_m \lambda_{\max,1} \cos\left(\gamma + \frac{P}{2}\theta_{0,m}\right) \right)}_{\text{Field-alignment torque}} + \underbrace{\left( I_m^2 (L_2 + 2M_2) \sin(2\gamma - P\theta_{0,m}) \right)}_{\text{Reluctance torque}} \quad (6.70)$$

$$\begin{aligned} T_{ripple}(t) = & \frac{3P}{2} \left\{ I_m \left( \sum_{n=6k+1}^{\infty} n \lambda_{\max,n} \cos\left((n-1)\omega_e t - \gamma - \frac{P}{2}n\theta_{0,m}\right) \right. \right. \\ & + \sum_{n=6k-1}^{\infty} n \lambda_{\max,n} \cos\left((n+1)\omega_e t + \gamma - \frac{P}{2}n\theta_{0,m}\right) \Big) \\ & - \frac{1}{2} I_m^2 \left( \sum_{n=6k+2}^{\infty} \frac{n}{2} (L_n + 2M_n) \sin\left((n-2)\omega_e t - 2\gamma - n\frac{P}{2}\theta_{0,m}\right) \right. \\ & + \sum_{n=6k-2}^{\infty} \frac{n}{2} (L_n + 2M_n) \sin\left((n+2)\omega_e t + 2\gamma - n\frac{P}{2}\theta_{0,m}\right) \Big) \\ & \left. \left. + \sum_{n=6k}^{\infty} n (L_n - M_n) \sin(n\omega_e t - n\frac{P}{2}\theta_{0,m}) \right) \right\}, \\ k = & 1, 2, 3, \dots \end{aligned} \quad (6.71)$$

where  $\lambda_{\max,n}$ ,  $L_n$ , and  $M_n$  were derived in (6.48), (6.26) and (6.33), respectively. The supply current angle,  $\gamma$ , which is measured with respect to the zero-crossing of the back-EMF is a control parameter and should be calculated as a function of the current amplitude,  $I_m$ , such that MTPA condition is achieved. The average torque, (6.70), originates from the fundamental components of the PM flux linkage and

machine inductances, while their harmonics only contribute to the torque ripple generation. From (6.71) it is observed that harmonics of  $6k$  order are present in the total torque ripple.

### 6.3.4 Validation Through Finite Element Analysis

Results from FEA are used here to validate the derived detailed torque Eqs. (6.70) and (6.71). The 800 W 14-pole 18-slot FSCW IPM machine that was previously described in Chaps. 2–5 is used here for evaluation purposes. The stator MMF, PM flux density and the inductance of this machine were analytically calculated in Chaps. 3, 5, and Sect. 6.2, respectively. These results are used in (6.70) and (6.71) to analytically compute the optimal current angle trajectory and the electromagnetic torque for this machine. The results are compared with those obtained from FEA.

Generation of MTPA is performed by adjusting the current angle,  $\gamma$ , to its optimum value in (6.35) for different current amplitudes. Variation of the developed average torque with respect to the current angle for different current amplitudes obtained from (6.70) is shown in Fig. 6.4. Evidently, as the current amplitude increases,  $\gamma$  should increase so that the developed average torque is always at its maximum value. The variation of optimum  $\gamma$  with respect to the current amplitude is referred to as the “MTPA trajectory” as shown with respect to the developed torque in Fig. 6.4. MTPA trajectory for the current angle with respect to the current amplitude obtained based on (6.70) is shown in Fig. 6.5. Evidently with an increase in the torque demand, the current amplitude increases leading to an increase in the current angle such that the torque always remains at its maximum value for the given current amplitude. From Fig. 6.5, the optimum current angle for maximum average torque at the rated current of 3.6 A is  $9.68^\circ$ .

Variations of the average alignment torque, reluctance torque, and the cumulative developed torque with respect to the current angle at the rated current obtained

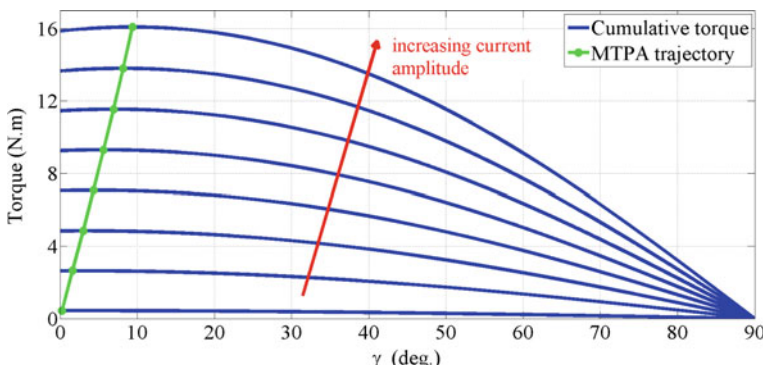


**Fig. 6.4** Developed average torque profile as a function of the current angle

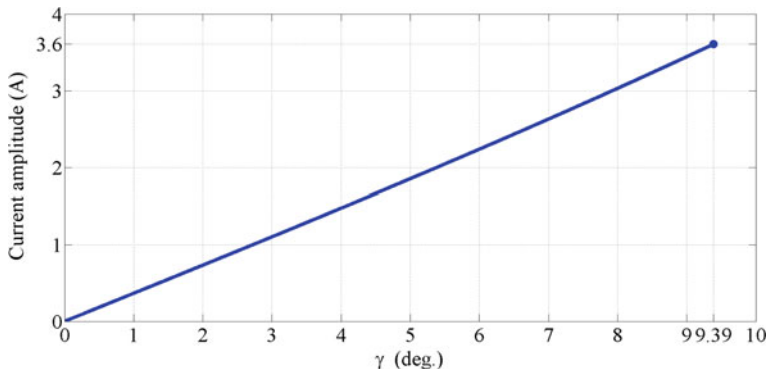


**Fig. 6.5** Variations of the optimum current angle with respect to the current amplitude (MTPA trajectory)

from (6.58), (6.68), and (6.70) are shown in Fig. 6.6. Evidently, the maximum average alignment torque occurs at  $\gamma = 0^\circ$ , the maximum average reluctance torque occurs at  $\gamma = 45^\circ$ , while the maximum average cumulative electromagnetic torque is generated at a current angle between  $0^\circ$  and  $45^\circ$ . From Fig. 6.6, the alignment torque is the dominant component, while the reluctance torque makes a small contribution to the total average torque. From (6.68), this is due to the small fundamental components of the self- and mutual inductances, which according to (6.26) and (6.33) are proportional to the spatial MMF harmonic of order  $P/2$ . Thus one of the challenges in designing FSCW IPM machines is optimizing the spatial harmonic content of the MMF such that reluctance torque is increased.

In order to validate the above analytical results, the profile of the generated electromagnetic torque is obtained from FEA and compared with the analytical results at 25, 50 and 100% of the full load as shown in Fig. 6.7. It is observed that the analytically computed torque including the average torque and torque ripple is in close agreement with the results obtained from FEA. The analytically obtained

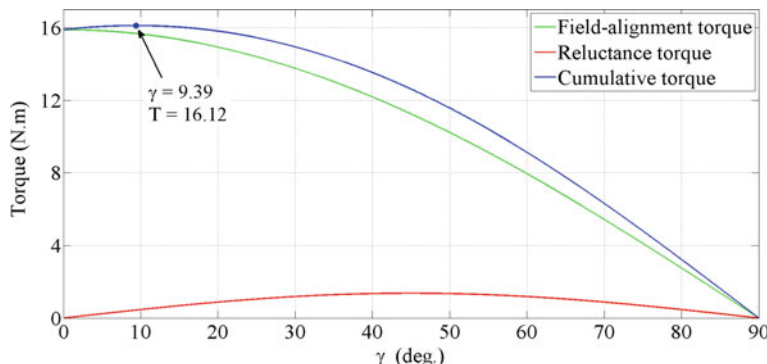


**Fig. 6.6** Variations of different average torque components with respect to the current angle at rated current

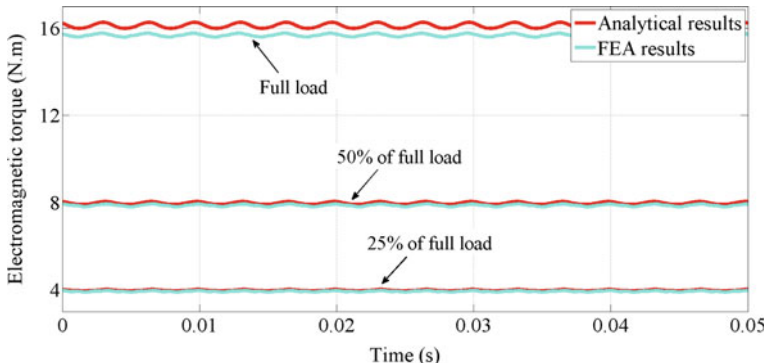


**Fig. 6.7** Developed electromagnetic torque in the 14-pole 18-slot FSCW IPM machine: comparison between the analytical calculations and the FEA results

torque has a slightly higher value compared with the result from FEA. The reason for this discrepancy is the higher amplitude of the analytically calculated PM flux density, as observed in Chap. 4. Moreover, the effect of the slot-openings on the PM flux density and the developed torque are neglected in the computations, leading to the analytical torque to be higher than the FEA results. The latter effect is less significant as the number of slots is low in the studied FSCW machine.

## 6.4 Detailed Modelling of FSCW IPM Machine Electromagnetic Torque Under an Open-Phase Fault Condition

FSCW IPM machines are subject to many mechanical and electrical faults, such as bearing failure, eccentricity fault, PM demagnetization faults, short-circuit faults, and open-circuit faults. Only the latter is of interest here, as the performance of the machine can be enhanced using a suitable control scheme under such condition.

In FSCW IPM machines, the stator MMF contains a wide range of spatial harmonics with significant amplitudes. This high harmonic content in the stator spatial MMF distribution is one of the main causes of torque ripple in such machines. When an open-phase fault is present, the fundamental stator MMF harmonic is reduced and the amplitudes of the other stator MMF harmonics are affected; additionally, triplen spatial harmonics, which are not normally present under healthy condition, will appear in the stator MMF. These phenomena results in a considerable increase in the torque ripple and also a decrease in the average torque.

Many literatures have addressed the open-phase fault condition of PMSMs and have proposed post-fault strategies for improving the output torque characteristics [6–13]. From these studies, torque ripple under an open-phase fault becomes so severe that the instantaneous electromagnetic torque crosses into the negative

region. In order to compensate for this, a pre-firing angle is introduced in drive systems that use a three-leg inverter shown in Fig. 6.8a. Nevertheless, in a star-connected stator that is subject to an open-phase fault, the currents in the two remaining phases become  $180^\circ$  apart, limiting the post-fault control strategies [6–8]. Realizing independent control of the remaining phase currents is the key to having a more effective post-fault control strategy that leads to a higher average torque and a lower torque ripple. For this purpose, the simplest type of inverter uses four legs as shown in Fig. 6.8b, with the fourth leg connected to the center of the star connection. Nevertheless, such inverter has limitation on its output voltage capability. The most reliable topology for operation of the PMSM under fault would be to use modular-fed three-lane inverters that completely isolate the three windings, providing full control over their currents [8–11].

Accurate and efficient control of the machine under an open-phase fault requires an accurate model that accounts for the machine dynamics. This is to achieve a high average torque with a low torque ripple under such condition. Many researchers have addressed this need and have proposed models for the machine under an open-phase fault [6, 12–14]. However, these models assume sinusoidal parameters for the PMSM, including the MMF, PM flux linkages, self- and mutual inductances. This

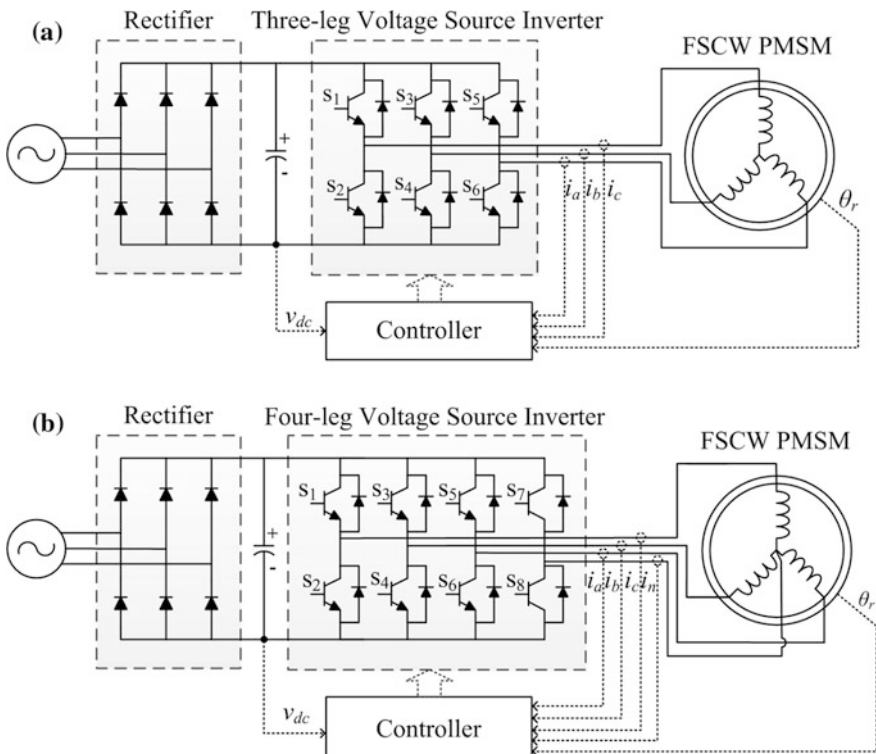


**Fig. 6.8** Drive system topologies: **a** Three-leg voltage source inverter supplying a three-phase PMSM. **b** Four-leg voltage source inverter supplying a three-phase PMSM

assumption is flawed as the MMF in general is not sinusoidal, especially in FSCW machines. Furthermore, all these models are based on the assumption of injecting a balanced current set, limiting their application for individual control of the winding currents. Accordingly, a detailed analytical model for PMSMs with non-sinusoidal parameters that operate under an open-phase fault has not yet been proposed that takes into account all the machine non-idealities. Moreover, detailed equations are required for the electromagnetic torque components under such operating conditions.

In a PMSM, only the stator MMF is affected by the open-phase fault, and the rotor MMF remains unchanged. In the following, a general analytical model is first proposed for the stator MMF that is fed with custom currents. This model along with the model that was previously obtained in Sect. 6.3.1 for the rotor MMF are used to analytically calculate the reluctance torque, the alignment torque, their average values and ripple components in a FSCW IPM machine that operates under an open-phase fault. The complete harmonic spectrum of the spatial MMF distribution and the machine non-sinusoidal parameters are taken into account in the proposed model. This model is used to obtain the optimal currents for MTPA operation of the machine with maximum possible average torque and minimum torque ripple. Study-cases are used for better understanding of the proposed model.

#### 6.4.1 Stator MMF Under an Open-Phase Fault Condition

A post-fault strategy for the drive system under an open-phase fault condition is to inject two individual currents into the remaining phase windings of the stator, expressed by:

$$\begin{aligned} i_a &= I_m \cos(\omega_e t + \alpha) \\ i_b &= I_m \cos(\omega_e t + \beta) \\ i_c &= 0 \end{aligned} \quad (6.72)$$

where  $\alpha$  and  $\beta$  are the current phase angles, with their reference being the zero-crossing of the back-EMF. These angles need to be calculated for all operating points with the objective of maximizing the average torque and minimizing the torque ripple. From the analysis performed in Chap. 2, the total stator MMF under an open-phase fault condition is expressed by:

$$f_s(t, \theta_s) = f_a(t, \theta_s) + f_b(t, \theta_s) \quad (6.73)$$

Substituting the single-phase MMFs in (6.73) yields:

$$\begin{aligned} f_s(t, \theta_s) &= F_{a,n} \cos(n\theta_s) + F_{b,n} \cos(n\theta_s - n\frac{2\pi}{3}) \\ &= \sum_{n=\frac{kP}{2c}} W_n \left( i_a \cos(n\theta_s) + i_b \cos(n\theta_s - n\frac{2\pi}{3}) \right) \end{aligned} \quad (6.74)$$

where

- $k = 1, 3, 5, \dots$  when  $c$  is an odd number  
 $k = 2, 4, 6, \dots$  when  $c$  is an even number

Substituting the instantaneous currents from (6.72) in (6.74) gives:

$$f_s(t, \theta_s) = \frac{2}{3} \sum_{n=\frac{kP}{2c}} F_n (\cos(\omega_e t + \alpha) \cos(n\theta_s) + \cos(\omega_e t + \beta) \cos(n\theta_s - n\frac{2\pi}{3})) \quad (6.75)$$

Mathematical manipulation of the above expression yields the total stator MMF for a FSCW machine that is operating under an open-phase fault condition and is being fed with the current set (6.72):

$$\begin{aligned} f_s(t, \theta_s) &= f_{s,a}(t, \theta_s) + f_{s,b}(t, \theta_s) \\ &= \sum_{n=\frac{P}{2c}} f_{ccw,n}(t, \theta_s) + \sum_{n=\frac{P}{2c}} f_{cw,n}(t, \theta_s) \end{aligned} \quad (6.76)$$

In (6.76), the subscripts  $cw$  and  $ccw$  indicate the clockwise and counter-clockwise rotation of harmonics in the spatial MMF distribution, respectively. These components for the total spatial MMF of (6.76) are given by:

$$\begin{aligned} f_{ccw,n}(t, \theta_s) &= \frac{2}{3} F_n \cos\left(\frac{\pi}{3}n - \frac{\alpha - \beta}{2}\right) \\ &\times \cos\left(\omega_e t - n\theta_s + \frac{\pi}{3}n + \frac{\alpha + \beta}{2}\right) \end{aligned} \quad (6.77)$$

$$\begin{aligned} f_{cw,n}(t, \theta_s) &= \frac{2}{3} F_n \cos\left(\frac{\pi}{3}n + \frac{\alpha - \beta}{2}\right) \\ &\times \cos\left(\omega_e t + n\theta_s - \frac{\pi}{3}n + \frac{\alpha + \beta}{2}\right) \end{aligned} \quad (6.78)$$

From the above expressions it is observed that in a FSCW stator the total spatial MMF is consisted of spatial harmonics of order  $n = k P/2c$ . From (6.76) to (6.78) it can be seen that for each harmonic order two spatial harmonics are present in the airgap that are rotating in the opposite direction, each of which having their own time independent magnitude and phase angle. The angular speed of the  $n$ th MMF harmonic in mechanical radians per second is given by:

$$\omega_n = \begin{cases} \frac{\omega_e}{n} & \text{for counterclockwise-rotating harmonics} \\ -\frac{\omega_e}{n} & \text{for clockwise-rotating harmonics} \end{cases}$$

Each harmonic of the total stator MMF can be imagined as a number of virtual alternate magnets that rotate in the airgap with their pole-pair number being equal to their harmonic order. In a PMSM, the rotor which has  $P/2$  pole-pairs is locked to the main stator MMF harmonic of order  $v = P/2$ , synchronously rotates with it, and leads to the average torque production. Evidently, all other spatial MMF harmonics are rotating asynchronously with the rotor and do not produce an average torque, rather they lead to torque ripple, saturation of the machine magnetic material and core losses [15].

### 6.4.2 Alignment Torque in a FSCW IPM Machine Operating Under an Open-Phase Fault Condition

Alignment torque is obtained by substituting the rotor MMF, (6.50), and the stator MMF, (6.76), in (6.40):

$$\begin{aligned}
 T_{align,OPF}(t) &= \frac{\mu_0 r_g l_{eff}}{g} \int_0^{2\pi} f_r(t, \theta_s) \frac{df_s(t, \theta_s)}{d\theta_s} d\theta_s \\
 &= \frac{2 \mu_0 r_g l_{eff}}{3 g} \int_0^{2\pi} \left( \sum_{n=\frac{P}{2}k}^{\infty} f_{r,max,n} \sin(n\omega_m t - n\theta_s - n\theta_{0,m}) \right) \\
 &\quad \times \left( \sum_{n=\frac{P}{2}k}^{\infty} nF_n \cos\left(\frac{\pi}{3}n - \frac{\alpha - \beta}{2}\right) \times \sin\left(\omega_e t - n\theta_s + \frac{\pi}{3}n + \frac{\alpha + \beta}{2}\right) \right. \\
 &\quad \left. - \sum_{n=\frac{P}{2}k}^{\infty} nF_n \cos\left(\frac{\pi}{3}n + \frac{\alpha - \beta}{2}\right) \times \sin\left(\omega_e t + n\theta_s - \frac{\pi}{3}n + \frac{\alpha + \beta}{2}\right) \right) d\theta_s
 \end{aligned} \tag{6.79}$$

The integral terms in (6.53) return a nonzero value, only when

$$n = \frac{P}{2}k, \quad k = 1, 3, 5, \dots$$

Substitution of the above relation in (6.79) and converting all the mechanical parameters into their electrical equivalent leads to the following simplifications:

$$\begin{aligned}
 &\int_0^{2\pi} \sin(k\omega_e t - \frac{P}{2}k\theta_s - \frac{P}{2}k\theta_{0,m}) \cdot \sin\left(\omega_e t - \frac{P}{2}k\theta_s + \frac{\pi P}{3}k + \frac{\alpha + \beta}{2}\right) d\theta_s \\
 &= \pi \cos\left((k-1)\omega_e t - \frac{\pi P}{3}k - \frac{\alpha + \beta}{2} - \frac{P}{2}k\theta_{0,m}\right)
 \end{aligned} \tag{6.80}$$

$$\begin{aligned} & \int_0^{2\pi} \sin(k\omega_e t - \frac{P}{2}k\theta_s - \frac{P}{2}k\theta_{0,m}) \cdot \sin\left(\omega_e t + \frac{P}{2}k\theta_s - \frac{\pi P}{3}k + \frac{\alpha + \beta}{2}\right) d\theta_s \\ &= -\pi \cos\left((k+1)\omega_e t - \frac{\pi P}{3}k + \frac{\alpha + \beta}{2} - \frac{P}{2}k\theta_{0,m}\right) \end{aligned} \quad (6.81)$$

Substitution of the integral terms in (6.79) with their solutions according to (6.80) and (6.81), the detailed expression for the alignment torque under an open-phase fault is found as follows:

$$\begin{aligned} T_{align,OPF}(t) &= \frac{\mu_0 r_g l_{eff}}{g} \int_0^{2\pi} f_r(t, \theta_s) \frac{df_s(t, \theta_s)}{d\theta_s} d\theta_s \\ &= \frac{P}{2} \frac{2\pi \mu_0 r_g l_{eff}}{3g} \sum_{k=1,3,5,\dots} k f_{r,max,(P/2)k} F_{(P/2)k} \cos\left(\frac{\pi P}{3}k - \frac{\alpha - \beta}{2}\right) \\ &\quad \times \cos\left((k-1)\omega_e t - \frac{\pi P}{3}k - \frac{\alpha + \beta}{2} - \frac{P}{2}k\theta_{0,m}\right) \\ &+ \frac{P}{2} \frac{2\pi \mu_0 r_g l_{eff}}{3g} \sum_{k=1,3,5,\dots} k f_{r,max,(P/2)k} F_{(P/2)k} \cos\left(\frac{\pi P}{3}k + \frac{\alpha - \beta}{2}\right) \\ &\quad \times \cos\left((k+1)\omega_e t - \frac{\pi P}{3}k + \frac{\alpha + \beta}{2} - \frac{P}{2}k\theta_{0,m}\right) \end{aligned} \quad (6.82)$$

Substitution of  $f_{r,max,n}$  and  $F_n$  from (6.51) and (6.44) into (6.82) gives the alignment torque as a function of the PM flux linkage:

$$\begin{aligned} T_{align,OPF}(t) &= \frac{P}{2} I_m \sum_{k=1,3,5,\dots} k \lambda_{max,k} \left[ \cos\left(\frac{\pi P}{6}k - \frac{\alpha - \beta}{2}\right) \right. \\ &\quad \times \cos\left((k-1)\omega_e t - \frac{\pi P}{6}k - \frac{\alpha + \beta}{2} - \frac{P}{2}k\theta_{0,m}\right) \\ &\quad \left. + \cos\left(\frac{\pi P}{6}k + \frac{\alpha - \beta}{2}\right) \right. \\ &\quad \left. \times \cos\left((k+1)\omega_e t - \frac{\pi P}{6}k + \frac{\alpha + \beta}{2} - \frac{P}{2}k\theta_{0,m}\right) \right] \end{aligned} \quad (6.83)$$

The average value of the alignment torque found from (6.83) is:

$$\begin{aligned} T_{align,ave,OPF}(t) &= \frac{P}{2} I_m \lambda_{max,1} \cos\left(\frac{\pi P}{6} - \frac{\alpha - \beta}{2}\right) \\ &\quad \times \cos\left(\frac{\pi P}{6} + \frac{\alpha + \beta}{2} + \frac{P}{2}\theta_{0,m}\right) \end{aligned} \quad (6.84)$$

From (6.84) it is observed that the average alignment torque is a function the fundamental harmonic of the PM flux linkage, the supplied current amplitude, and the current phase angles. Evidently, PM flux linkage harmonics other than the fundamental do not contribute to the average torque production, rather they only contribute to torque ripple.

Equation (6.83) implies that the alignment torque under the open-phase fault condition comprises even torque harmonics. It can be seen that PM flux linkage harmonic of order  $n = 2k \pm 1$  contributes to torque harmonics of order  $2k$ ,  $k = 1, 2, 3, \dots$ . These PM flux linkage harmonics are generated by the interaction between common harmonics of order  $n = (P/2) \cdot (2k \pm 1)$  in both the rotor PM flux density and the stator spatial MMF. Any other spatial harmonics that are not common in both the stator MMF and rotor PM flux density do not participate in torque production and only contribute to increasing the core losses.

### 6.4.3 Reluctance Torque in a FSCW IPM Machine Operating Under an Open-Phase Fault Condition

Reluctance torque under an open-phase fault condition can be found by substituting the machine self- and mutual inductances, (6.24) and (6.31), and the supplied current (6.72) in the reluctance torque Eq. (6.62):

$$\begin{aligned} T_{rel,OPF}(t) &= \frac{P}{2} \frac{1}{2} I_m^2 \left( \sum_{n=2,4,6,\dots}^{\infty} nL_n \cos^2(\omega_e t + \alpha) \sin(n\omega_e t) \right. \\ &\quad + \sum_{n=2,4,6,\dots}^{\infty} nL_n \cos^2(\omega_e t + \beta) \sin\left(n\omega_e t - \frac{2\pi}{3}n\right) \\ &\quad \left. + 2 \sum_{n=2,4,6,\dots}^{\infty} nM_n \cos(\omega_e t + \alpha) \cos(\omega_e t + \beta) \sin\left(n\omega_e t + \frac{2\pi}{3}n\right) \right) \end{aligned} \quad (6.85)$$

The following simplifications are used:

$$\begin{aligned} &\sum_{n=2,4,6,\dots}^{\infty} \cos^2(\omega_e t + \alpha) \sin(n\omega_e t) + \cos^2(\omega_e t + \beta) \sin\left(n\omega_e t - \frac{2\pi}{3}n\right) \\ &= \frac{1}{2} \sum_{n=2,4,6,\dots}^{\infty} \left[ \cos\left(\alpha - \beta - \frac{n\pi}{3}\right) \cdot \sin\left((n-2)\omega_e t - (\alpha + \beta) - \frac{n\pi}{3}\right) \right. \\ &\quad \left. + 2 \cos\left(\frac{n\pi}{3}\right) \sin\left(n\omega_e t - \frac{n\pi}{3}\right) \right. \\ &\quad \left. + \cos\left(\alpha - \beta + \frac{n\pi}{3}\right) \cdot \sin\left((n+2)\omega_e t + (\alpha + \beta) - \frac{n\pi}{3}\right) \right] \end{aligned} \quad (6.86)$$

$$\begin{aligned}
& \sum_{n=2,4,6,\dots}^{\infty} \cos(\omega_e t + \alpha) \cos(\omega_e t + \beta) \sin\left(n\omega_e t + \frac{2\pi}{3}n\right) \\
& = \frac{1}{4} \sum_{n=2,4,6,\dots}^{\infty} \left[ \sin\left((n-2)\omega_e t - (\alpha + \beta) - \frac{n\pi}{3}\right) \right. \\
& \quad \left. + 2 \cos(\alpha - \beta) \sin\left(n\omega_e t - \frac{n\pi}{3}\right) \right. \\
& \quad \left. + \sin\left((n+2)\omega_e t + (\alpha + \beta) - \frac{n\pi}{3}\right) \right]
\end{aligned} \tag{6.87}$$

Substitution of (6.86) and (6.87) in (6.85) and subsequent manipulation gives the detailed reluctance torque expression under an open-phase fault:

$$\begin{aligned}
T_{rel,OPF}(t) & = \frac{P_1}{24} I_m^2 \left\{ \sum_{n=2,4,6,\dots}^{\infty} \left[ n \left( L_n \cdot \cos\left(\alpha - \beta - \frac{n\pi}{3}\right) + M_n \right) \right. \right. \\
& \quad \times \sin\left((n-2)\omega_e t - (\alpha + \beta) - \frac{n\pi}{3}\right) \\
& \quad + 2n \left( L_n \cdot \cos\left(\frac{n\pi}{3}\right) + M_n \cdot \cos(\alpha - \beta) \right) \\
& \quad \times \sin\left(n\omega_e t - \frac{n\pi}{3}\right) \\
& \quad + n \left( L_n \cdot \cos\left(\alpha - \beta + \frac{n\pi}{3}\right) + M_n \right) \\
& \quad \times \left. \sin\left((n+2)\omega_e t + (\alpha + \beta) - \frac{n\pi}{3}\right) \right] \right\}
\end{aligned} \tag{6.88}$$

From (6.88), the average reluctance torque can be computed as follows:

$$T_{rel,ave,OPF} = -\frac{P_1}{22} I_m^2 \left( L_2 \cdot \cos\left(\alpha - \beta - \frac{2\pi}{3}\right) + M_2 \right) \sin\left(\alpha + \beta + \frac{2\pi}{3}\right) \tag{6.89}$$

From Eq. (6.89), the average reluctance torque is a function of the square of the current amplitude, the current phase angles, and the fundamental components of the inductances,  $L_2$  and  $M_2$ . Inductance harmonics other than the fundamental do not contribute to the average reluctance torque production and only lead to torque ripple as shown in (6.88).

Equation (6.88) implies that under the open-phase fault, reluctance torque only comprises even harmonics. Evidently, the second harmonic of the reluctance torque is generated by the 2nd and 4th harmonics in the self- and mutual inductances. Accordingly, harmonics in the reluctance torque which are of order  $2k$ ,  $k = 2, 3, \dots$  originate from harmonics in the self- and mutual inductance which are of order  $n = 2k$  and  $n = 2k \pm 2$ .

#### 6.4.4 Complete Torque Equation Under an Open-Phase Fault

According to (6.34) the complete torque equation under an open-phase fault condition is found by summing the alignment torque, (6.83), and the reluctance torque, (6.88). The resultant expression is a function of time, current amplitude and current phase angles:

$$T_{OPF}(t) = T_{align,OPF}(t) + T_{re,OPF}(t) \quad (6.90)$$

The average developed torque under an open-phase fault condition can be obtained from (6.90) by summing the average alignment torque, (6.84), and the average reluctance torque, (6.89), as follows:

$$\begin{aligned} T_{ave,OPF} = & \frac{P}{2} I_m \lambda_{max,1} \cos\left(\frac{\pi P}{6} - \frac{\alpha - \beta}{2}\right) \cos\left(\frac{\pi P}{6} + \frac{\alpha + \beta}{2} + \frac{P}{2} \theta_{0,m}\right) \\ & - \frac{P}{2} \frac{1}{2} I_m^2 \left( L_2 \cdot \cos(\alpha - \beta - \frac{2\pi}{3}) + M_2 \right) \sin\left(\alpha + \beta + \frac{2\pi}{3}\right) \end{aligned} \quad (6.91)$$

It is observed from (6.91) that only the main harmonic of the PM flux linkage and the fundamental harmonic of the self- and mutual inductances contribute to the average torque production.

The second harmonic in the torque ripple is the dominant component under an open-phase fault condition. An expression for the second harmonic of the torque ripple can be found from (6.90), (6.83), and (6.88) as follows:

$$\begin{aligned} T_{2,OPF}(t) = & \frac{P}{2} I_m \left[ \lambda_{max,1} \cos\left(\frac{\pi P}{6} + \frac{\alpha - \beta}{2}\right) \cos\left(2\omega_e t - \frac{\pi P}{6} + \frac{\alpha + \beta}{2} - \frac{P}{2} \theta_{0,m}\right) \right. \\ & + 3\lambda_{max,3} \cos\left(\frac{\pi P}{2} - \frac{\alpha - \beta}{2}\right) \cos\left(2\omega_e t - \frac{\pi P}{2} - \frac{\alpha + \beta}{2} - \frac{3P}{2} \theta_{0,m}\right) \left. \right] \\ & + \frac{P}{2} I_m^2 \left[ \left( L_4 \cdot \cos(\alpha - \beta - \frac{4\pi}{3}) + M_4 \right) \sin\left(2\omega_e t - (\alpha + \beta) - \frac{4\pi}{3}\right) \right. \\ & \left. + \left( L_2 \cdot \cos\left(\frac{2\pi}{3}\right) + M_2 \cdot \cos(\alpha - \beta) \right) \sin\left(2\omega_e t - \frac{2\pi}{3}\right) \right] \end{aligned} \quad (6.92)$$

where  $\lambda_{max,n}$ ,  $L_n$ , and  $M_n$  were derived in (6.48), (6.26) and (6.33), respectively. Evidently, the first and third harmonics of the PM flux linkage contribute to the second harmonic of the torque ripple. Likewise, the fundamental harmonics of the self- and mutual inductances also take part in generation of the second harmonic of the torque ripple. This explains the high amplitude of the second harmonic torque ripple, as the flux linkage and inductance components that contribute in the generation of the average torque, also are the main cause of the torque ripple.

The supply current angles,  $\alpha$  and  $\beta$ , which are measured with respect to the zero-crossing of the back-EMF are control parameters and should be calculated as a function of the current amplitude,  $I_m$ , such that MTPA condition is guaranteed as will be seen in the next section.

#### 6.4.5 Validation Through Finite Element Analysis

The proposed MMF and torque models for an FSCW PMSM that is being fed with custom currents, (6.72), under an open-phase fault condition and the resultant MTPA trajectory are validated in this section. The 14-pole 18-slot FSCW IPM machine with a rated torque of 16.1 N m at 2.55 Arms that had its characteristics under normal operating condition presented in Sect. 6.3.4, is examined here. The PM flux density and the inductance of this machine were analytically calculated in Chaps. 4 and 5, respectively. These results are used in (6.48) and (6.91) to analytically compute the optimal current angles,  $\alpha$  and  $\beta$ , that lead to maximum average torque for different loadings under an open-phase fault condition. The results are compared with those obtained from FEA.

The developed average torque from a PMSM, as derived in (6.91), is a function of the current amplitude,  $I_m$ , and the current phase angles,  $\alpha$  and  $\beta$ . Variations of the average electromagnetic torque with the current phase angles,  $\alpha$  and  $\beta$ , for the studied FSCW IPM machine when it is being supplied with rated current under an open-phase fault condition is obtained from (6.91) and is shown in Fig. 6.9. It can be seen from Fig. 6.9 that for the sinusoidal current set (6.72), maximum possible average torque is achievable only when  $\alpha$  and  $\beta$  are adopted to be  $120^\circ$  apart. Clearly, the average torque will drop if any other values for  $\alpha$  and  $\beta$  are adopted.

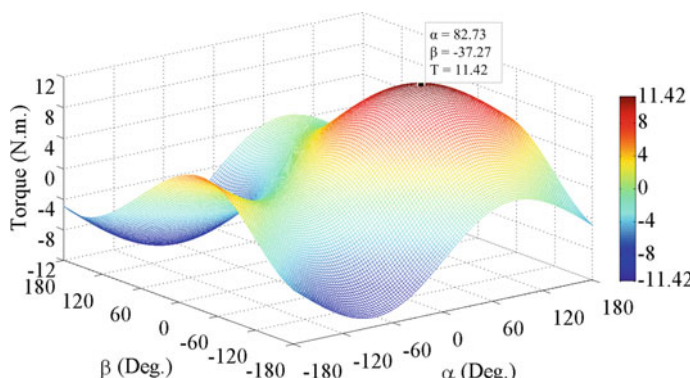


**Fig. 6.9** Variations of the average electromagnetic torque with current phase angles at rated current for the studied FSCW IPM machine. This graph is generated using the proposed analytical model for the electromagnetic torque under an open-phase fault condition

Two case-studies are presented in the following. In the first case-study, the FSCW IPM machine is connected to a three-leg inverter as shown in Fig. 6.8a and its performance is studied. In the second case-study, a four-leg inverter with the fourth leg connected to the center of the star connection is assumed, as shown in Fig. 6.8b. In the presented case-studies, the current angles  $\alpha$  and  $\beta$  in the current set (6.72) are found using the proposed average torque equation under an open-phase fault condition, (6.91), such that MTPA for a given current amplitude is guaranteed. Torque ripple is computed for the presented case-studies and compared, as defined by:

$$T_{\text{ripple}} = \frac{T_{\max} - T_{\min}}{T_{\text{ave}}} \times 100 \quad (\%) \quad (6.93)$$

where  $T_{\min}$  and  $T_{\max}$  are the minimum and maximum values for the instantaneous torque.

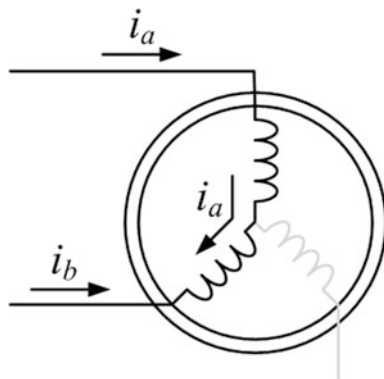
#### 6.4.5.1 Case-Study 1: Drive System with a Three-Leg Inverter

When an open-phase fault occurs in a FSCW IPM machine that is being driven by a three-leg inverter, the two healthy windings are placed in series, resulting in the same current passing through them, as shown in Fig. 6.10. Under such condition, the currents in the windings will have phase angles that are  $180^\circ$  apart; therefore, the following relation will hold true for the current angles,  $\alpha$  and  $\beta$  in (6.72):

$$\beta = \alpha - \pi \quad (6.94)$$

If  $\alpha$  is assumed to be zero, the resultant stator spatial MMF distribution at  $t = 0$  is found from (6.76) to (6.78) and shown in Fig. 6.11 along with that obtained from FEA. It can be seen that the analytically calculated stator spatial MMF distribution using the proposed expressions is in good agreement with that obtained by FEA.

**Fig. 6.10** Currents in a PMSM when being supplied by a three-leg inverter under an open-phase fault condition



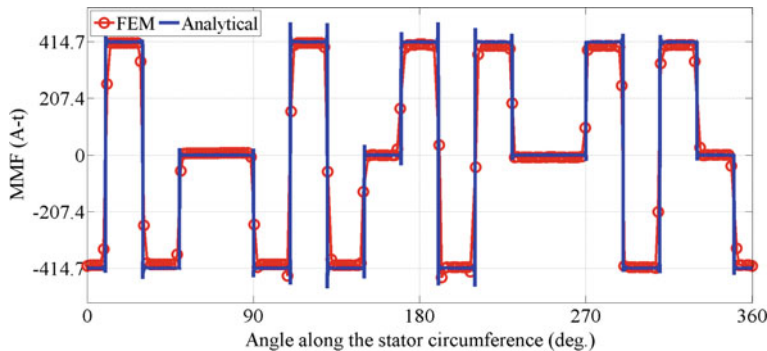


**Fig. 6.11** Stator MMF around the airgap at  $t = 0$  for the studied FSCW IPM machine under an open-phase fault condition when the machine is driven by a three-leg inverter. The current angles are assumed  $180^\circ$  apart: analytical results obtained from the proposed model versus FEA

From (6.91), when operating under and open-phase fault, depending on the current amplitude,  $I_m$ , optimal values for the current angles,  $\alpha$  and  $\beta$ , need to be obtained to generate the maximum possible average torque. For the current phase angle  $\alpha$ , its optimal value that yields MTPA for a given current amplitude,  $I_m$ , is computed by replacing (6.94) in (6.91) as shown in Fig. 6.12 along with the resultant average torque and dominant torque ripple harmonic. By having the value of  $\alpha$ , the phase angle  $\beta$  can be found based on (6.94). From (6.91), torque is directly proportional to the current amplitude and its square, thus as shown in Fig. 6.12, an increase in the demand for torque leads to an increase in the current amplitude. Accordingly, as shown in Fig. 6.12 as the current amplitude increases, the current phase angle needs to be decreased so that MTPA condition is always guaranteed.

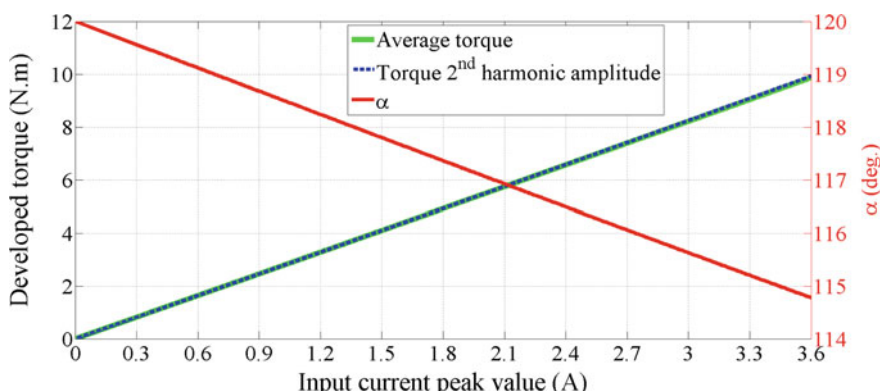


**Fig. 6.12** Torque versus current angle versus current amplitude under maximum torque per ampere (MTPA) condition when the machine is subject to an open-phase fault. The current angles are assumed  $180^\circ$  apart

When operating under an open-phase fault, the dominant torque ripple harmonic is of second order. Figure 6.12 shows the generated average torque and the amplitude of the second torque harmonic with respect to the phase angle,  $\alpha$ , and amplitude of the supplied current. Clearly, the average torque is increasing with the increasing current amplitude. Nevertheless, the second torque harmonic is also increasing with the current amplitude, having a high value close to the average torque at different current amplitudes. This is expected since according to the derived expression for the second harmonic torque ripple, (6.92), it originates from the fundamental component of the PM flux linkage which has a high value and is also responsible for generating the average torque. When the current angles are  $180^\circ$  apart, the multipliers of  $\lambda_{max,1}$  in both the average torque and second harmonic torque ripple, become closer. Moreover, the third harmonic of the PM flux linkage has a strong contribution to the torque ripple, and according to (6.92) it affects the second harmonic torque ripple by a multiple of 3. All this leads to an increase in the amplitude of the second harmonic torque.

From Fig. 6.12 it is clear that for the FSCW IPM machine that is being driven under MTPA condition by a three-leg inverter, when an open-phase fault occurs torque ripple increases to around 200% of the average torque, regardless of the current amplitude.

The optimal current angles for generating maximum average torque at the rated current,  $I_m = 3.6$  A, can be obtained from Fig. 6.12 and (6.94) as follows:

$$\alpha = 114.8^\circ \quad \beta = -65.2^\circ$$

The instantaneous developed torque by the machine can be obtained by substituting the above current phase angles in the proposed electromagnetic torque model for the machine operating under an open-phase fault, (6.90), (6.83) and (6.88), as shown and compared with FEA results in Fig. 6.13. Clearly, the obtained torque using the proposed analytical model is in close agreement with that obtained

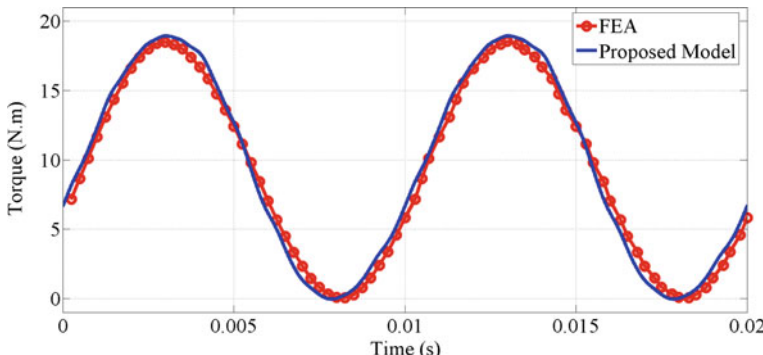


**Fig. 6.13** Developed torque by the studied FSCW IPM machine when it is connected to a three-leg inverter and operates under an open-phase fault. The supplied currents to the machine are  $180^\circ$  apart

from FEA. From Fig. 6.13 an average torque of 9.88 N m is being generated under an open-phase fault condition which is equal to 61.29% of the rated three-phase torque. Nevertheless, torque ripple under such condition is around 200%.

#### 6.4.5.2 Case-Study 2: Drive System with a Four-Leg Inverter

The drive topology for a FSCW PMSM that is being supplied by a four-leg inverter is shown in Fig. 6.8b. In such a topology, after the occurrence of an open-phase fault, the two remaining phase currents can be controlled independently as shown in Fig. 6.14. Thus, the current angles in (6.72) should be determined such that maximum average torque is generated.

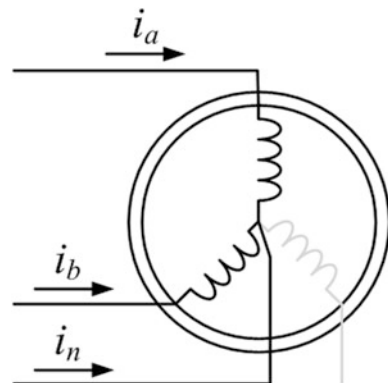
From Fig. 6.9 it can be observed that when subject to an open-phase fault, the three-phase PMSM can generate maximum possible average torque only when the currents in its two remaining phases are  $120^\circ$  apart:

$$\beta = \alpha - \frac{2\pi}{3} \quad (6.95)$$

By assuming  $\alpha$  to be zero, if the current phase angles in (6.72) satisfy the condition in (6.95), the stator MMF at  $t = 0$  obtained from (6.76) to (6.78) will be as shown in Fig. 6.15. This figure also shows the stator MMF obtained by FEA. Evidently, the obtained MMF by the proposed model and FEA are in good agreement.

Equation (6.91) implies that the average torque demand is a determining factor for the supplied current amplitude. The current phase angle  $\alpha$  at each current amplitude needs to be found such that generation of the maximum average torque is guaranteed. Optimal value of this current angle can be obtained through substitution of (6.95) in (6.91) and finding the operating points at which maximum average torque is generated for a given current amplitude (MTPA condition). The obtained

**Fig. 6.14** Currents in a PMSM under an open-phase fault condition, when the machine is being supplied by a four-leg inverter



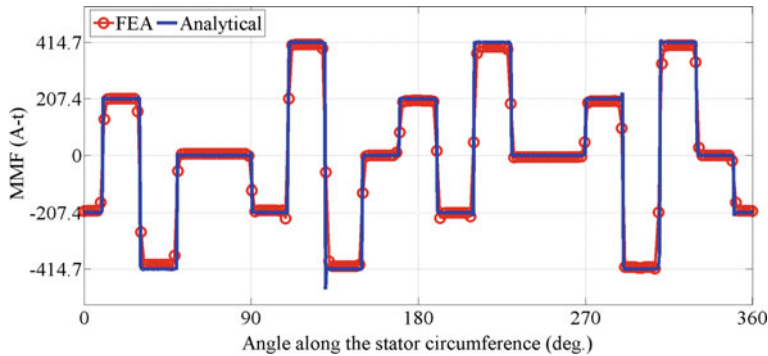


**Fig. 6.15** Stator MMF around the airgap at  $t = 0$  for the studied FSCW IPM machine under an open-phase fault condition when the machine is driven by a four-leg inverter. The current angles are assumed  $120^\circ$  apart: analytical results obtained from the proposed model versus FEA

MTPA trajectory is shown in Fig. 6.16 along with the developed average torque and the second harmonic torque ripple as a function of the current phase angle,  $\alpha$ , and the current amplitudes. Equation (6.95) can be used to obtain the current phase angle  $\beta$ . Figure 6.16 implies that similar to the case of a PMSM with a three-leg inverter, when using a four-leg inverter under the MTPA condition, the second order harmonic in the electromagnetic torque is the main contributor to torque ripple. In this case, the torque ripple obtained from (6.93) and Fig. 6.16 is around 96% of the average torque. By comparing Figs. 6.16 and 6.12 it is observed that using a four-leg inverter under the proposed MTPA condition increases the average torque by 16%, while the torque ripple is significantly reduced by 52%. This

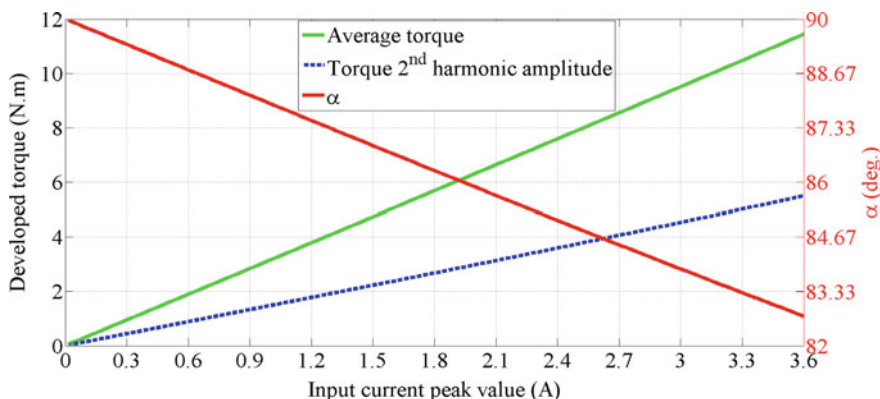


**Fig. 6.16** Torque versus current angle versus current amplitude under maximum torque per ampere (MTPA) condition when the machine is subject to an open-phase fault. The current angles are assumed  $120^\circ$  apart

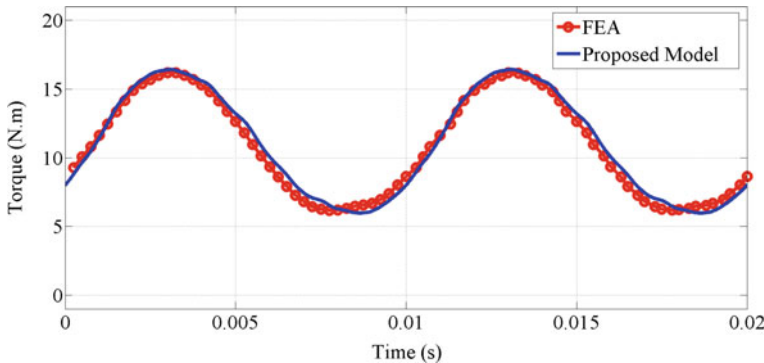


**Fig. 6.17** Developed torque by the studied FSCW IPM machine when it is connected to a three-leg inverter and operates under an open-phase fault. The supplied currents to the machine are  $120^\circ$  apart

indicates a significant improvement in the torque profile when the current angles in the healthy windings of the faulty machine are individually controlled to be  $120^\circ$  apart.

The optimal current angles for generating maximum average torque at the rated current,  $I_m = 3.6$  A, can be obtained from Fig. 6.16 and (6.95) as follows:

$$\alpha = 82.73^\circ \quad \beta = -37.27^\circ$$

The instantaneous torque can be obtained by using the above current angles in the proposed torque model, (6.90), (6.83), and (6.88) as shown in Fig. 6.17 in comparison with the FEA results. Evidently, the analytically calculated torque is in good agreement with the FEA results, validating the proposed model and its accuracy. From Fig. 6.17, an average torque of  $11.42$  N m is generated at the rated current. This is  $70.84\%$  of the rated torque of the machine under healthy condition. Moreover, torque ripple is around  $96\%$ . The same results are predicted in Fig. 6.16 for the proposed MTPA under an open-phase fault condition.

## 6.5 Comparison of the FSCW IPM Machine Performance Under Normal and Open-Phase Fault Conditions

Based on the analytical results obtained in the previous sections, a comparison is made here for the performance of the 14-pole 18-slot FSCW IPM machine under normal and open-phase fault conditions.

A comparison between the MMF harmonic content, average torque, and torque ripple of the test machine is shown in Table 6.1. Evidently, when subjected to an open-phase fault, all odd harmonics are present in the MMF harmonic spectrum,

**Table 6.1** A comparison between the performance characteristics of the test FSCW IPM machine under healthy and faulty condition

Quantity	Operating condition			
	Normal condition	Open-phase fault condition (Three-leg VSI)	Open-phase fault condition (Four-leg VSI)	
Current phase angle difference	120°	180°	120°	
Present stator MMF harmonics	All odd harmonics excluding triplen harmonics	All odd harmonics	All odd harmonics	
MMF main harmonic amplitude (7th harmonic)	306.16 (A-t) 100 (%)	176.77 (A-t) 57.74 (%)	204.1 (A-t) 66.66 (%)	
Average torque at full load (MTPA)	16.12 (N m) 100 (%)	9.88 (N m) 61.29 (%)	11.42 (N m) 70.84 (%)	
Torque ripple at full load (MTPA)	1.74 (%)	200 (%)	96 (%)	

while, in a machine operating under normal condition the triplen harmonics are cancelled. When the machine is being supplied through a three-phase voltage-source inverter (VSI), under an open-phase fault condition the current phase angles are 180° apart and the amplitude of the main harmonic of the MMF is 57.74% of the normal operating condition and the developed average torque is 61.29% of the normal condition. In a machine supplied by a four-leg VSI, under an open-phase fault condition using the proposed MTPA algorithm, the supplied currents are 120° apart, the amplitude of the main MMF harmonic is 66.66% of that under the normal operating condition, and the developed average torque is 70.84% of the normal operating condition which is 15.6% higher than when the machine is supplied by a three-leg VSI.

Apart from the significant improvement in the average torque under an open phase fault condition using the four-leg VSI and the proposed MTPA approach compared with the three-phase VSI, the torque ripple also reduces from 200% to 96% of the average torque. It is noteworthy that using an open-ended structure, the same results as the four-leg inverter could be achieved.

## 6.6 Conclusion

In this chapter, the self- and mutual inductances, and the spatial MMF distribution of the stator and rotor of an FSCW IPM machine under healthy and open-phase fault conditions were analytically modelled. Accordingly, general equations were derived for the electromagnetic torque and torque ripple which detailed the different

contributors to the average torque and torque ripple components. The proposed models were used to derive an MTPA trajectory for the machine operating under an open-phase fault such that maximum possible torque with minimum torque ripple was always guaranteed. It was concluded that if a four-leg inverter is used instead of a three-leg inverter, independent currents can be supplied into the machine phases in accordance to the proposed algorithm, resulting a higher average torque and a significantly lower torque ripple.

The proposed models are beneficial to investigating the effect of the machine design parameters such as its dimensions and geometry on its output characteristics under normal and open-phase fault condition. Moreover, the proposed analytical expressions can be used to evaluate different FSCW topologies with respect to their performance under different operating conditions. Furthermore, they can be used for the design of advanced control fault-tolerant drive systems.

## References

1. P.C. Krause, O. Wasyczuk, S.D. Sudhoff, S. Pekarek, *Analysis of Electric Machinery and Drive Systems*, vol. 75 (Wiley, 2013)
2. S. Jang Ho, C. Hong Soon, Analytical modeling for calculating cogging torque in interior permanent magnet machine with multi flux-barriers. *IEEE Trans. Appl. Superconduct.* **24**, 1–4 (2014)
3. Z. Azar, Z.Q. Zhu, G. Ombach, Influence of electric loading and magnetic saturation on cogging torque, back-EMF and torque ripple of PM machines. *IEEE Trans. Magn.* **48**, 2650–2658 (2012)
4. H. Seok-Hee, T.M. Jahns, W.L. Soong, M.K. Guven, M.S. Illindala, Torque ripple reduction in interior permanent magnet synchronous machines using stators with odd number of slots per pole pair. *IEEE Trans. Energy Convers.* **25**, 118–127 (2010)
5. J.P. Karunadasa, A.C. Renfrew, Analysis of torque production in brushless DC and AC motor drives, in *Fourth International Conference on Power Electronics and Variable-Speed Drives, 1991* (1990), pp. 451–456
6. B.A. Welchko, T.M. Jahns, S. Hiti, IPM synchronous machine drive response to a single-phase open circuit fault. *IEEE Trans. Power Electron.* **17**, 764–771 (2002)
7. A. Kontarcek, P. Bajec, M. Nemec, V. Ambrozic, D. Nedeljkovic, Cost-effective three-phase PMSM drive tolerant to open-phase fault. *IEEE Trans. Ind. Electron.* **62**, 6708–6718 (2015)
8. B.A. Welchko, T.A. Lipo, T.M. Jahns, S.E. Schulz, Fault tolerant three-phase AC motor drive topologies: a comparison of features, cost, and limitations. *IEEE Trans. Power Electron.* **19**, 1108–1116 (2004)
9. F. Meinguet, J. Gyselinck, Control strategies and reconfiguration of four-leg inverter PMSM drives in case of single-phase open-circuit faults, in *Electric Machines and Drives Conference, 2009, IEMDC '09. IEEE International* (2009), pp. 299–304
10. A. Mohammadpour, L. Parsa, Asymmetrical multi-lane multi-phase motor drives, in *Proceedings of the APEC* (2014), pp. 2482–2487
11. J.W. Bennett, G.J. Atkinson, B.C. Mecrow, D.J. Atkinson, Fault-tolerant design considerations and control strategies for aerospace drives. *IEEE Trans. Ind. Electron.* **59**, 2049–2058 (2012)
12. A. Gaeta, G. Scelba, A. Consoli, Sensorless vector control of PM synchronous motors during single-phase open-circuit faulted conditions. *IEEE Trans. Ind. Appl.* **48**, 1968–1979 (2012)

13. A. Gaeta, G. Scelba, A. Consoli, Modeling and control of three-phase PMSMs under open-phase fault. *IEEE Trans. Ind. Appl.* **49**, 74–83 (2013)
14. M. Fei, R. Zanasi, F. Grossi, Modeling of multi-phase permanent magnet synchronous motors under open-phase fault condition, in *2011 9th IEEE International Conference on Control and Automation (ICCA)* (2011), pp. 59–64
15. L. Alberti, M. Barcaro, N. Bianchi, Design of a low-torque-ripple fractional-slot interior permanent-magnet motor. *IEEE Trans. Ind. Appl.* **50**, 1801–1808 (2014)

# Chapter 7

## An Extended $dq$ Model for Fractional-Slot Concentrated-Wound Interior Permanent Magnet Machines Considering Non-ideal Machine Parameters



### 7.1 Introduction

The main parameters in the  $dq$  model of a PMSM are the self- and mutual inductances and the PM flux linkages. Self- and mutual inductances are the product of the interaction between the equivalent airgap function and the stator MMF, while PM flux linkages originate from the interaction between the PM flux density and the stator MMF. In the standard  $dq$  model, these machine parameters are assumed sinusoidal, leading to a smooth estimated torque for the machine. This assumption can be justified for PMSMs with ideal DW stators where the spatial MMF distribution of the stator is sinusoidal, leading to sinusoidal inductances and PM flux linkages. However, as seen in Chap. 2, for a PMSM utilizing a non-ideal stator such as a FSCW stator the spatial MMF distribution of the stator contains a wide range of spatial harmonics and cannot be considered sinusoidal, leading to non-sinusoidal machine parameters. This is the main cause of torque ripple in such machines [1–4]. Thus, the use of the standard  $dq$  model for evaluation of FSCW PMSMs is expected to yield in inaccurate results [5].

This chapter builds upon the results of Chaps. 2–6 in which the non-sinusoidal machine parameters were modelled. In order to address the deficiency in the standard  $dq$  model, an extended  $dq$  model is proposed that considers the non-sinusoidal machine parameters. The proposed extended  $dq$  model contains new parameters. Methods for experimental measurement of these parameters are described. Detailed expressions for the electromagnetic torque components are derived based on the proposed extended  $dq$  model. These expressions quantify different subcomponents of the developed torque as a function of the new parameters in the proposed extended  $dq$  model. In order to validate the proposed model, its parameters are experimentally measured for a prototype FSCW PMSM. The obtained parameters are used in the proposed extended  $dq$  model to estimate the

average torque and torque ripple in the prototype. FEA is used to validate the results.

## 7.2 Standard $dq$ Model of PMSMs

Parameters of a PMSM are assumed sinusoidal in the standard  $dq$  model. This yields constant values for the  $dq$  inductances, PM flux linkages, and ultimately a smooth developed torque with no torque ripple [6, 7]. The standard  $dq$  model is derived in this section.

### 7.2.1 Machine Model in the abc-System

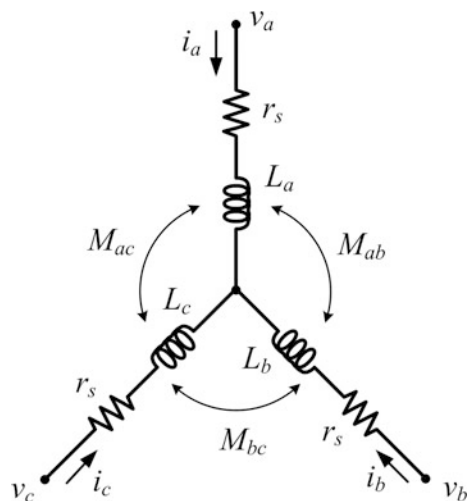
A schematic of the three-phase windings in a PMSM is shown in Fig. 7.1. Evidently, the electrical part of the PMSM is a first order system, with its dynamic equations in the  $abc$ -system given by [6]:

$$\mathbf{v}_{abc} = \mathbf{r}_s \mathbf{i}_{abc} + \frac{d\lambda_{abc}}{dt} \quad (7.1)$$

$$\lambda_{abc} = \mathbf{L}_s \mathbf{i}_{abc} + \lambda_{pm,abc} \quad (7.2)$$

where  $\mathbf{i}_{abc}$ ,  $\mathbf{v}_{abc}$ ,  $\lambda_{abc}$ , and  $\lambda_{pm,abc}$  are vectors for the stator currents, stator voltages, stator flux linkages, and PM flux linkages respectively,  $\mathbf{r}_s$  is a diagonal matrix for

**Fig. 7.1** Schematic of the three-phase windings in a PMSM



the stator resistance, and  $\mathbf{L}_s$  is the inductance matrix, comprised of self- and mutual inductances:

$$\mathbf{v}_{abc} = \begin{bmatrix} v_a \\ v_b \\ v_c \end{bmatrix}, \mathbf{i}_{abc} = \begin{bmatrix} i_a \\ i_b \\ i_c \end{bmatrix}, \boldsymbol{\lambda}_{abc} = \begin{bmatrix} \lambda_a \\ \lambda_b \\ \lambda_c \end{bmatrix}, \boldsymbol{\lambda}_{pm,abc} = \begin{bmatrix} \lambda_{pm,a}(\theta_{m,e}) \\ \lambda_{pm,b}(\theta_{m,e}) \\ \lambda_{pm,c}(\theta_{m,e}) \end{bmatrix},$$

$$\mathbf{r}_s = \begin{bmatrix} r_s & 0 & 0 \\ 0 & r_s & 0 \\ 0 & 0 & r_s \end{bmatrix}$$

In the PM flux linkage vector,  $\lambda_{pm,x}$  is phase  $x$  PM flux linkage and varies with the rotor angular position in electrical radians,  $\theta_{m,e}$ . For a PMSM with an ideal DW stator, PM flux linkage is assumed sinusoidal and expressed by:

$$\lambda_{pm,x}(\theta_{m,e}) = \lambda_{pm} \sin(\theta_{m,e} + \theta_x) \quad (7.3)$$

and

$$\theta_{m,e} = \omega_{m,e}t = \left(\frac{P}{2}\right)\omega_m t \quad (7.4)$$

where  $\omega_{m,e}$  is the rotor angular speed electrical rad/s,  $\omega_m$  is the rotor angular speed in mechanical rad/s,  $\lambda_{pm}$  is the amplitude for the PM flux linkage, and  $\theta_x$  represents the phase angle for phase winding  $x$  and for phases  $a$ ,  $b$ , and  $c$  is equal to 0,  $-2\pi/3$  and  $+2\pi/3$ , respectively.

The inductance matrix in (7.2) is expressed by [6]:

$$\mathbf{L}_s = \begin{bmatrix} L_a(\theta_{m,e}) & M_{ab}(\theta_{m,e}) & M_{ac}(\theta_{m,e}) \\ M_{ab}(\theta_{m,e}) & L_b(\theta_{m,e}) & M_{bc}(\theta_{m,e}) \\ M_{ac}(\theta_{m,e}) & M_{bc}(\theta_{m,e}) & L_c(\theta_{m,e}) \end{bmatrix} \quad (7.5)$$

In (7.5),  $L_x$  is the self-inductance for phase  $x$  winding, and  $M_{xy}$  is the mutual inductance between phase  $x$  winding and phase  $y$  winding. Self- and mutual inductances in a PMSM with an ideal DW stator are assumed sinusoidal and dependent on the angular position of the rotor, expressed by:

$$L_x(\theta_{m,e}) = L_{ls} + L_0 + L_2 \cos 2(\theta_{m,e} - \theta_x) \quad (7.6)$$

$$M_{xy}(\theta_{m,e}) = -\frac{1}{2}L_0 + L_2 \cos 2(\theta_{m,e} - \theta_{xy}) \quad (7.7)$$

where  $L_{ls}$  is the leakage inductance,  $L_0$  is the mean value of the self-inductance,  $L_2$  is the amplitude for the second spatial harmonic of the self-inductance, and  $\theta_{xy}$  is the phase angle for the mutual inductance between phase  $x$  and phase  $y$  windings

and equal to  $-\pi/3$ ,  $+\pi/3$ , and  $\pi$  for  $ab$ ,  $ac$ , and  $bc$ , respectively. Equations (7.1)–(7.7) represent the standard dynamic model in the  $abc$ -system for a PMSM with an ideal DW stator.

### 7.2.2 Transformation of the Machine Model to the $qd0$ -Reference Frame

Transformation of the machine dynamic Eqs. (7.1)–(7.7) from the  $abc$ -system to the  $qd0$ -reference frame by employing the Park transformation matrix, gives [8]:

$$\mathbf{K}_s = \frac{2}{3} \begin{bmatrix} \cos \theta_{m,e} & \cos(\theta_{m,e} - \frac{2\pi}{3}) & \cos(\theta_{m,e} + \frac{2\pi}{3}) \\ \sin \theta_{m,e} & \sin(\theta_{m,e} - \frac{2\pi}{3}) & \sin(\theta_{m,e} + \frac{2\pi}{3}) \\ 1/2 & 1/2 & 1/2 \end{bmatrix} \quad (7.8)$$

The inverse Park transformation is given by:

$$\mathbf{K}_s^{-1} = \begin{bmatrix} \cos \theta_{m,e} & \sin \theta_{m,e} & 1 \\ \cos(\theta_{m,e} - \frac{2\pi}{3}) & \sin(\theta_{m,e} - \frac{2\pi}{3}) & 1 \\ \cos(\theta_{m,e} + \frac{2\pi}{3}) & \sin(\theta_{m,e} + \frac{2\pi}{3}) & 1 \end{bmatrix} \quad (7.9)$$

Multiplying both sides of (7.1) by (7.8) yields:

$$\mathbf{K}_s \begin{bmatrix} v_a \\ v_b \\ v_c \end{bmatrix} = \mathbf{K}_s \begin{bmatrix} r_s & 0 & 0 \\ 0 & r_s & 0 \\ 0 & 0 & r_s \end{bmatrix} \mathbf{K}_s^{-1} \begin{bmatrix} i_q \\ i_d \\ i_0 \end{bmatrix} + \mathbf{K}_s \frac{d}{dt} \left( \mathbf{K}_s^{-1} \begin{bmatrix} \lambda_q \\ \lambda_d \\ \lambda_0 \end{bmatrix} \right) \quad (7.10)$$

The following mathematical manipulations are used:

$$\mathbf{K}_s \begin{bmatrix} r_s & 0 & 0 \\ 0 & r_s & 0 \\ 0 & 0 & r_s \end{bmatrix} \mathbf{K}_s^{-1} = \begin{bmatrix} r_s & 0 & 0 \\ 0 & r_s & 0 \\ 0 & 0 & r_s \end{bmatrix} \quad (7.11)$$

$$\begin{aligned} \mathbf{K}_s \frac{d}{dt} \left( \mathbf{K}_s^{-1} \begin{bmatrix} \lambda_q \\ \lambda_d \\ \lambda_0 \end{bmatrix} \right) &= \mathbf{K}_s \frac{d}{dt} (\mathbf{K}_s^{-1}) \begin{bmatrix} \lambda_q \\ \lambda_d \\ \lambda_0 \end{bmatrix} + \mathbf{K}_s \mathbf{K}_s^{-1} \frac{d}{dt} \begin{bmatrix} \lambda_q \\ \lambda_d \\ \lambda_0 \end{bmatrix} \\ &= \omega_{m,e} \begin{bmatrix} 0 & -1 & 0 \\ 1 & 0 & 0 \\ 0 & 0 & 0 \end{bmatrix} \begin{bmatrix} \lambda_q \\ \lambda_d \\ \lambda_0 \end{bmatrix} + \frac{d}{dt} \begin{bmatrix} \lambda_q \\ \lambda_d \\ \lambda_0 \end{bmatrix} \end{aligned} \quad (7.12)$$

Thus, (7.10) simplifies to:

$$\begin{bmatrix} v_q \\ v_d \\ v_0 \end{bmatrix} = \begin{bmatrix} r_s & 0 & 0 \\ 0 & r_s & 0 \\ 0 & 0 & r_s \end{bmatrix} \begin{bmatrix} i_q \\ i_d \\ i_0 \end{bmatrix} + \omega_{m,e} \begin{bmatrix} \lambda_d \\ -\lambda_q \\ 0 \end{bmatrix} + \frac{d}{dt} \begin{bmatrix} \lambda_q \\ \lambda_d \\ \lambda_0 \end{bmatrix} \quad (7.13)$$

The  $qd0$  flux linkage column vector in (7.13) can be obtained by multiplying both sides of (7.2) by (7.8) as follows:

$$\begin{aligned} \mathbf{K}_s \mathbf{K}_s^{-1} \begin{bmatrix} \lambda_q \\ \lambda_d \\ \lambda_0 \end{bmatrix} &= \mathbf{K}_s \begin{bmatrix} L_a(\theta_{m,e}) & M_{ab}(\theta_{m,e}) & M_{ac}(\theta_{m,e}) \\ M_{ab}(\theta_{m,e}) & L_b(\theta_{m,e}) & M_{bc}(\theta_{m,e}) \\ M_{ac}(\theta_{m,e}) & M_{bc}(\theta_{m,e}) & L_c(\theta_{m,e}) \end{bmatrix} \mathbf{K}_s^{-1} \begin{bmatrix} i_q \\ i_d \\ i_0 \end{bmatrix} \\ &\quad + \mathbf{K}_s \begin{bmatrix} \lambda_{pm,a}(\theta_{m,e}) \\ \lambda_{pm,b}(\theta_{m,e}) \\ \lambda_{pm,c}(\theta_{m,e}) \end{bmatrix} \end{aligned} \quad (7.14)$$

The following mathematical manipulations are used:

$$\begin{aligned} \mathbf{K}_s \begin{bmatrix} L_a(\theta_{m,e}) & M_{ab}(\theta_{m,e}) & M_{ac}(\theta_{m,e}) \\ M_{ab}(\theta_{m,e}) & L_b(\theta_{m,e}) & M_{bc}(\theta_{m,e}) \\ M_{ac}(\theta_{m,e}) & M_{bc}(\theta_{m,e}) & L_c(\theta_{m,e}) \end{bmatrix} \mathbf{K}_s^{-1} \\ = \begin{bmatrix} L_{ls} + \frac{3}{2}(L_0 + L_2) & 0 & 0 \\ 0 & L_{ls} + \frac{3}{2}(L_0 - L_2) & 0 \\ 0 & 0 & L_{ls} \end{bmatrix} \end{aligned} \quad (7.15)$$

$$\mathbf{K}_s \begin{bmatrix} \lambda_{pm,a}(\theta_{m,e}) \\ \lambda_{pm,b}(\theta_{m,e}) \\ \lambda_{pm,c}(\theta_{m,e}) \end{bmatrix} = \begin{bmatrix} 0 \\ \lambda_{pm} \\ 0 \end{bmatrix} \quad (7.16)$$

Thus, (7.15) simplifies to:

$$\begin{bmatrix} \lambda_q \\ \lambda_d \\ \lambda_0 \end{bmatrix} = \begin{bmatrix} L_{ls} + \frac{3}{2}(L_0 + L_2) & 0 & 0 \\ 0 & L_{ls} + \frac{3}{2}(L_0 - L_2) & 0 \\ 0 & 0 & L_{ls} \end{bmatrix} \begin{bmatrix} i_q \\ i_d \\ i_0 \end{bmatrix} + \begin{bmatrix} 0 \\ \lambda_{pm} \\ 0 \end{bmatrix} \quad (7.17)$$

The standard  $dq$  model can now be written in the following matrix form:

$$\mathbf{v}_{qd0} = \mathbf{r}_s \mathbf{i}_{qd0} + \omega_m \boldsymbol{\lambda}_{dq} + \frac{d \boldsymbol{\lambda}_{qd0}}{dt} \quad (7.18)$$

$$\boldsymbol{\lambda}_{qd0} = \mathbf{L}_{qd0} \mathbf{i}_{qd0} + \boldsymbol{\lambda}_{pm,qd0} \quad (7.19)$$

where

$$\mathbf{v}_{qd0} = \begin{bmatrix} v_q \\ v_d \\ v_0 \end{bmatrix}, \mathbf{i}_{qd0} = \begin{bmatrix} i_q \\ i_d \\ i_0 \end{bmatrix}, \boldsymbol{\lambda}_{qd0} = \begin{bmatrix} \lambda_q \\ \lambda_d \\ \lambda_0 \end{bmatrix}, \boldsymbol{\lambda}_{dq} = \begin{bmatrix} \lambda_d \\ -\lambda_q \\ 0 \end{bmatrix}.$$

The inductance matrix,  $\mathbf{L}_{qd0}$ , and the PM flux linkage vector,  $\boldsymbol{\lambda}_{pm,qd0}$ , in the *qd0*-reference frame are derived as follows:

$$\mathbf{L}_{qd0} = \begin{bmatrix} L_q & 0 & 0 \\ 0 & L_d & 0 \\ 0 & 0 & L_0 \end{bmatrix} \quad (7.20)$$

$$\boldsymbol{\lambda}_{pm,qd0} = \begin{bmatrix} 0 \\ \lambda_{pm} \\ 0 \end{bmatrix} \quad (7.21)$$

and

$$L_q = L_{ls} + \frac{3}{2}(L_0 + L_2) \quad (7.22)$$

$$L_d = L_{ls} + \frac{3}{2}(L_0 - L_2) \quad (7.23)$$

$$L_0 = L_{ls} \quad (7.24)$$

Evidently, the inductance matrix and the PM flux linkage vector in the *qd0*-reference frame are *dc* terms and independent of time and position. From (7.18) to (7.19) the standard *dq* model in expanded form can be written as:

$$v_q = r_s i_q + i_q \frac{dL_q}{dt} + \omega_{m,e} \lambda_d \quad (7.25)$$

$$v_d = r_s i_d + i_d \frac{dL_d}{dt} - \omega_{m,e} \lambda_q \quad (7.26)$$

$$v_0 = r_s i_0 + i_0 \frac{dL_0}{dt} \quad (7.27)$$

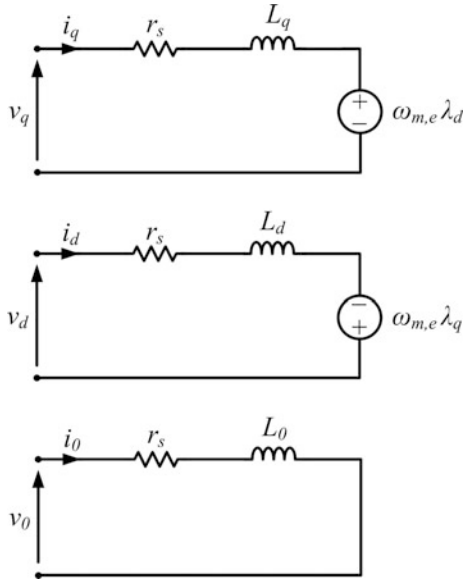
where

$$\lambda_q = L_q i_q \quad (7.28)$$

$$\lambda_d = L_d i_d + \lambda_{pm} \quad (7.29)$$

The equivalent circuit of the standard *dq* model based on (7.25)–(7.27) is shown in Fig. 7.2.

**Fig. 7.2** Equivalent circuit of the standard  $dq$  model, containing constant inductances and flux linkages



### 7.2.3 Electromagnetic Torque in the $qd0$ -Reference Frame

In the  $qd0$ -reference frame, the instantaneous active power is given by [6]:

$$p = \frac{3}{2} (v_q i_q + v_d i_d + 2v_0 i_0) \quad (7.30)$$

Substituting (7.18)–(7.19) in (7.30) yields:

$$\begin{aligned} p = & \underbrace{\frac{3}{2} (r_s i_q^2 + r_s i_d^2 + 2r_s i_0^2)}_{\text{Resistive losses}} + \underbrace{\frac{3}{2} \omega_{m,e} (\lambda_d i_q - \lambda_q i_d)}_{\text{Electromechanical power}} \\ & + \underbrace{\frac{3}{2} \left( i_q \frac{d\lambda_q}{dt} + i_d \frac{d\lambda_d}{dt} + 2i_0 \frac{d\lambda_0}{dt} \right)}_{\text{Rate of change of the stored energy}} \end{aligned} \quad (7.31)$$

The first term in (7.31) is the resistive losses, the second term is electromechanical power and is the power that contributes to the energy conversion process, and the last term represents the rate of change for the stored energy in the airgap.

Electromagnetic torque is obtained by dividing the electromechanical power by the rotational speed in mechanical rad/s [6]:

$$T_e = \frac{p}{\omega_m} = \left( \frac{P}{2} \right) \frac{p}{\omega_{m,e}} \quad (7.32)$$

Thus by neglecting the resistive losses, the developed torque for a  $P$ -pole PMSM using the standard *dq* model is obtained as follows:

$$T_e = \frac{3}{2} \frac{P}{2} (\lambda_d i_q - \lambda_q i_d) \quad (7.33)$$

Substituting  $\lambda_d$  and  $\lambda_q$  from (7.19) in (7.33) yields:

$$T_e = \frac{3}{2} \frac{P}{2} (\lambda_{pm} i_q + (L_d - L_q) i_q i_d) \quad (7.34)$$

The first term in (7.34) is the alignment torque which is generated by the interaction between the stator MMF and the PM flux density. The second term in (7.34) represents the reluctance torque which originates from the machine saliency. Since the inductances and PM flux linkages in the standard *dq* model are *dc* values, according to (7.34), the developed electromagnetic torque becomes constant.

### 7.3 Proposed Extended *dq* Model for FSCW PMSMs

Torque ripple in PMSMs that utilize DW stators with non-sinusoidal parameters is generated by the interaction of the harmonics in the back-EMF and self- and mutual inductances with the current that flows in the stator windings [3–7]. The literatures that have analyzed the sources of torque ripple, have not investigated the reason behind the non-sinusoidal nature of the machine parameters. Furthermore, a detailed *dq* model that accounts for all the non-sinusoidal parameters of a PMSM is yet to be proposed. Such detailed model is of significance in designing efficient control systems. From the study performed in [8], in a PMSM with a non-sinusoidal spatial MMF distribution, measurement of the *dq* inductances based on the standard *dq* model leads to inaccurate results. This necessitates the need for a comprehensive *dq* model that considers all the machine non-idealities.

Motivated by the abovementioned gap in the existing knowledge, this section proposes an extended *dq* model for PMSMs that utilize a stator with a non-sinusoidal MMF distribution, e.g. a FSCW stator. Accordingly, the detailed expressions of the PM flux linkages, and the self- and mutual inductances in the *abc*-system that were previously formulated in Chaps. 2 and 6 are used here to form the detailed machine model in the *abc*-system. Subsequently, this model is transformed to the *qd0*-reference frame to yield the proposed extended *dq* model. Accordingly, detailed equations are derived for the average developed torque and torque ripple. Experimental tests for measuring the parameters of the proposed extended *dq* model are also described.

### 7.3.1 Detailed Machine Model in the abc-System

The three-phase PMSM is a first order system with its schematic diagram as shown in Fig. 7.1. General equations governing the machine model in the  $abc$ -system are the same as (7.1) and (7.2) as follows:

$$\mathbf{v}_{abc} = \mathbf{r}_s \mathbf{i}_{abc} + \frac{d\lambda_{abc}}{dt} \quad (7.35)$$

$$\lambda_{abc} = \mathbf{L}_s \mathbf{i}_{abc} + \lambda_{pm,abc} \quad (7.36)$$

A general equation for the detailed inductance matrix for a FSCW PMSM was derived in Chap. 6 as follows:

$$\mathbf{L}_s = \begin{bmatrix} L_a(\theta_{m,e}) & M_{ab}(\theta_{m,e}) & M_{ac}(\theta_{m,e}) \\ M_{ab}(\theta_{m,e}) & L_b(\theta_{m,e}) & M_{bc}(\theta_{m,e}) \\ M_{ac}(\theta_{m,e}) & M_{bc}(\theta_{m,e}) & L_c(\theta_{m,e}) \end{bmatrix} \quad (7.37)$$

where

$$L_j(\theta_{m,e}) = L_0 + \sum_n^{\infty} L_n \cos(n\theta_{m,e} - n\theta_j), \quad n = 2, 4, 6, \dots \quad (7.38)$$

$$M_{jz}(\theta_{m,e}) = M_0 + \sum_n^{\infty} M_n \cos(n\theta_{m,e} - n\theta_{jz}), \quad n = 2, 4, 6, \dots \quad (7.39)$$

In the above equations  $\theta_j$  is equal to 0,  $+2\pi/3$  and  $-2\pi/3$ , for phase  $a$ ,  $b$ , and  $c$ ; and  $\theta_{jz}$  is equal to  $+\pi/3$ ,  $-\pi/3$ , and  $-\pi$  for phase  $ab$ ,  $ac$ , and  $bc$ , respectively.

The general equation for the detailed PM flux linkage column vector for a FSCW PMSM as derived in Chap. 2 is:

$$\lambda_{pm,abc} = \begin{bmatrix} \lambda_{pm,a}(\theta_{m,e}) \\ \lambda_{pm,b}(\theta_{m,e}) \\ \lambda_{pm,c}(\theta_{m,e}) \end{bmatrix} \quad (7.40)$$

where

$$\lambda_{pm,j}(\theta_{m,e}) = \sum_n^{\infty} \lambda_{pm,n} \sin(n\theta_{m,e} - n\theta_j), \quad n = 1, 3, 5, \dots \quad (7.41)$$

Evidently, the detailed machine model is based on the harmonics in the machine inductances and flux-linkages, which could be either calculated as shown in Chaps. 2–6, or obtained experimentally as described in the next sections.

### 7.3.2 Transformation of the Detailed Machine Model to the $qd0$ -Reference Frame

In this section, the detailed machine model expressed in (7.35)–(7.41) is transformed from the  $abc$ -system to the  $qd0$ -reference frame by using the Park transformation matrix, (7.8). Accordingly, the obtained voltage and flux linkage equations will have a similar form to (7.18)–(7.19):

$$\mathbf{v}_{qd0} = \mathbf{r}_s \dot{\mathbf{i}}_{qd0} + \omega_m \boldsymbol{\lambda}_{dq} + \frac{d\boldsymbol{\lambda}_{qd0}}{dt} \quad (7.42)$$

$$\boldsymbol{\lambda}_{qd0} = \mathbf{L}_{qd0} \mathbf{i}_{qd0} + \boldsymbol{\lambda}_{pm,qd0} \quad (7.43)$$

Nevertheless, in the above equations, the inductance matrix and the PM flux linkage vector in the  $qd0$ -reference frame need to be found based on their detailed expressions.

#### 7.3.2.1 Detailed Inductance Matrix in the $qd0$ -Reference Frame

The detailed inductance matrix in the  $abc$ -system described by (7.37)–(7.39) is transformed to the  $qd0$ -reference frame as follows:

$$\begin{aligned} \mathbf{L}_{qd0} &= \mathbf{K}_s \begin{bmatrix} L_a(\theta_{m,e}) & M_{ab}(\theta_{m,e}) & M_{ac}(\theta_{m,e}) \\ M_{ab}(\theta_{m,e}) & L_b(\theta_{m,e}) & M_{bc}(\theta_{m,e}) \\ M_{ac}(\theta_{m,e}) & M_{bc}(\theta_{m,e}) & L_c(\theta_{m,e}) \end{bmatrix} \mathbf{K}_s^{-1} \\ &= \begin{bmatrix} L_q(\theta_{m,e}) & M_{qd}(\theta_{m,e}) & M_{q0}(\theta_{m,e}) \\ M_{qd}(\theta_{m,e}) & L_d(\theta_{m,e}) & M_{d0}(\theta_{m,e}) \\ M_{q0}(\theta_{m,e}) & M_{d0}(\theta_{m,e}) & L_0(\theta_{m,e}) \end{bmatrix} \end{aligned} \quad (7.44)$$

In the above matrix, the diagonal elements are referred to as the *qd0 self-inductances*; similarly, the non-diagonal elements are the *qd0 mutual inductances*.

The self-inductances in (7.44) are given by:

$$L_q(\theta_{m,e}) = L_{q,0} + \sum_{n=6k} \bar{L}_{q,n} \cos(n\theta_{m,e}), \quad k = 1, 2, 3, \dots \quad (7.45)$$

$$L_d(\theta_{m,e}) = L_{d,0} + \sum_{n=6k} \bar{L}_{d,n} \cos(n\theta_{m,e}), \quad k = 1, 2, 3, \dots \quad (7.46)$$

$$L_0(\theta_{m,e}) = L_{0,0} + \sum_{n=6k} \bar{L}_{0,n} \cos(n\theta_{m,e}), \quad k = 1, 2, 3, \dots \quad (7.47)$$

where

$$L_{q,0} = (L_0 - M_0) + \frac{1}{2}(L_2 + 2M_2) \quad (7.48)$$

$$L_{q,n} = \frac{1}{2}[(L_{n-2} + 2M_{n-2}) + 2(L_n - M_n) + (L_{n+2} + 2M_{n+2})] \quad (7.49)$$

$$L_{d,0} = (L_0 - M_0) - \frac{1}{2}(L_2 + 2M_2) \quad (7.50)$$

$$L_{d,n} = -\frac{1}{2}[(L_{n-2} + 2M_{n-2}) - 2(L_n - M_n) + (L_{n+2} + 2M_{n+2})] \quad (7.51)$$

$$L_{0,0} = L_0 + 2M_0 \quad (7.52)$$

$$L_{0,n} = L_n + 2M_n \quad (7.53)$$

The mutual inductances in (7.44) are formulated as follows:

$$M_{qd}(\theta_{m,e}) = \sum_{n=6k} M_{qd,n} \sin(n\theta_{m,e}), \quad k = 1, 2, 3, \dots \quad (7.54)$$

$$M_{q0}(\theta_{m,e}) = \sum_{n=3k} M_{q0,n} \sin(n\theta_{m,e}), \quad k = 1, 3, 5, \dots \quad (7.55)$$

$$M_{d0}(\theta_{m,e}) = \sum_{n=3k} M_{d0,n} \sin(n\theta_{m,e}), \quad k = 1, 3, 5, \dots \quad (7.56)$$

$$M_{0q}(\theta_{m,e}) = \frac{1}{2} M_{q0}(\theta_{m,e}) \quad (7.57)$$

$$M_{0d}(\theta_{m,e}) = \frac{1}{2} M_{d0}(\theta_{m,e}) \quad (7.58)$$

where

$$M_{qd,n} = \frac{1}{2}[(L_{n-2} + 2M_{n-2}) - (L_{n+2} + 2M_{n+2})] \quad (7.59)$$

$$M_{q0,n} = (L_{n-1} - M_{n-1}) + (L_{n+1} - M_{n+1}) \quad (7.60)$$

$$M_{d0,n} = (L_{n-1} - M_{n-1}) - (L_{n+1} - M_{n+1}) \quad (7.61)$$

From (7.45) to (7.47), the  $qd0$  self-inductances consist of spatial harmonics of order  $6k$ ,  $k = 1, 2, 3, \dots$  superimposed on an average inductance value. On the other hand, for the  $qd0$  mutual inductances given in (7.54)–(7.58), the average value is zero and only spatial harmonics are present. Accordingly,  $M_{qd}$  consists of harmonics of order  $6k$ ,  $k = 1, 2, 3, \dots$  and  $M_{0q}$ ,  $M_{0d}$ ,  $M_{q0}$  and  $M_{d0}$  comprise spatial harmonics of order  $3k$ ,  $k = 1, 3, 5, \dots$ .

### 7.3.2.2 Detailed PM Flux Linkage Column Vector in the $qd0$ -Reference Frame

The detailed PM flux linkage vector given by (7.40) and (7.41) is transformed to the  $qd0$ -reference frame from the  $abc$ -system as follows:

$$\lambda_{pm,qd0} = \begin{bmatrix} \lambda_{pm,q}(\theta_{m,e}) \\ \lambda_{pm,d}(\theta_{m,e}) \\ \lambda_{pm,0}(\theta_{m,e}) \end{bmatrix} \quad (7.62)$$

where

$$\lambda_{pm,q}(\theta_{m,e}) = \sum_{n=6k} \lambda_{pm,q,n} \sin(n\theta_{m,e}), \quad k = 1, 2, 3, \dots \quad (7.63)$$

$$\lambda_{pm,d}(\theta_{m,e}) = \lambda_{pm,d,0} - \sum_{n=6k} \lambda_{pm,d,n} \cos(n\theta_{m,e}), \quad k = 1, 2, 3, \dots \quad (7.64)$$

$$\lambda_{pm,0}(\theta_{m,e}) = \sum_{n=3k} \lambda_{pm,0,n} \sin(n\theta_{m,e}), \quad k = 1, 3, 5, \dots \quad (7.65)$$

and

$$\lambda_{pm,q,n} = \lambda_{pm,n-1} + \lambda_{pm,n+1} \quad (7.66)$$

$$\lambda_{pm,d,0} = \lambda_{pm,1} \quad (7.67)$$

$$\lambda_{pm,d,n} = \lambda_{pm,n-1} - \lambda_{pm,n+1} \quad (7.68)$$

$$\lambda_{pm,0,n} = \lambda_{pm,n}. \quad (7.69)$$

It can be observed that PM flux linkage in the  $d$ -axis consists of spatial harmonics of order  $6k$ ,  $k = 1, 2, 3, \dots$  superimposed on an average value. However, for the PM flux linkages in the  $q$ - and  $0$ -axis the average value is zero and only spatial harmonics of order  $6k$ ,  $k = 1, 2, 3, \dots$ , and  $3k$ ,  $k = 1, 3, 5, \dots$  are present, respectively.

### 7.3.2.3 Formulation of the Proposed Extended $dq$ Model

As seen in Sect. 7.3.2, the  $qd0$  inductances and PM flux linkages in the detailed  $dq$  model are dependent on the rotor angular position. This is unlike the standard  $dq$  model where these parameters are position-independent. Furthermore, the non-diagonal inductances in the  $qd0$  inductance matrix of the detailed  $dq$  model are not zero.

Substitution of the detailed  $qd0$  inductance matrix and detailed  $qd0$  PM flux linkage vector in (7.42) and (7.43) yields:

$$\mathbf{v}_{qd0} = \mathbf{r}_s \mathbf{i}_{qd0} + \omega_{m,e} \boldsymbol{\lambda}_{dq} + \frac{d\mathbf{L}_{qd0}}{dt} \mathbf{i}_{qd0} + \mathbf{L}_{qd0} \frac{d\mathbf{i}_{qd0}}{dt} + \frac{d\boldsymbol{\lambda}_{pm,qd0}}{dt} \quad (7.70)$$

where

$$\boldsymbol{\lambda}_{dq} = \begin{bmatrix} \lambda_d(\theta_{m,e}) \\ -\lambda_q(\theta_{m,e}) \\ 0 \end{bmatrix} \quad (7.71)$$

The proposed extended  $dq$  model is obtained by mathematical manipulation of (7.70) as follows:

$$v_q = r_s i_q + \omega_{m,e} \lambda_d(\theta_{m,e}) + L_q(\theta_{m,e}) \frac{di_q}{dt} + v_{\Delta L,q} + v_{\Delta \lambda,q} + v_{\Delta i,q} \quad (7.72)$$

$$v_d = r_s i_d - \omega_{m,e} \lambda_q(\theta_{m,e}) + L_d(\theta_{m,e}) \frac{di_d}{dt} + v_{\Delta L,d} + v_{\Delta \lambda,d} + v_{\Delta i,d} \quad (7.73)$$

$$v_0 = r_s i_0 + L_0(\theta_{m,e}) \frac{di_0}{dt} + v_{\Delta L,0} + v_{\Delta \lambda,0} + v_{\Delta i,0} \quad (7.74)$$

In (7.72)  $v_{\Delta L,q}$  represents the  $q$ -axis voltage generated due to the dependency of  $L_q$ ,  $M_{qd}$  and  $M_{q0}$  on the rotor angular position:

$$v_{\Delta L,q} = \frac{dL_q(\theta_{m,e})}{dt} i_q + \frac{dM_{qd}(\theta_{m,e})}{dt} i_d + \frac{dM_{q0}(\theta_{m,e})}{dt} i_0, \quad (7.75)$$

$v_{\Delta \lambda,q}$  represents the  $q$ -axis voltage generated due to the dependency of the  $q$ -axis PM flux density on the rotor angular position:

$$v_{\Delta \lambda,q} = \frac{d}{dt} \lambda_{pm,q}(\theta_{m,e}), \quad (7.76)$$

and  $v_{\Delta i,q}$  indicates the  $q$ -axis voltage generated due to the  $d$ -axis and 0-axis currents being a function of time:

$$v_{\Delta i,q} = M_{qd}(\theta_{m,e}) \frac{di_d}{dt} + M_{q0}(\theta_{m,e}) \frac{di_0}{dt}. \quad (7.77)$$

Similarly, the  $d$ -axis voltages  $v_{\Delta L,d}$ ,  $v_{\Delta \lambda,d}$  and  $v_{\Delta i,d}$ , and The 0-axis voltages  $v_{\Delta L,0}$ ,  $v_{\Delta \lambda,0}$  and  $v_{\Delta i,0}$  are expressed by:

$$v_{\Delta L,d} = \frac{dM_{qd}(\theta_{m,e})}{dt} i_q + \frac{dL_d(\theta_{m,e})}{dt} i_d + \frac{dM_{d0}(\theta_{m,e})}{dt} i_0 \quad (7.78)$$

$$v_{\Delta \lambda,d} = \frac{d}{dt} \lambda_{pm,d}(\theta_{m,e}) \quad (7.79)$$

$$v_{\Delta i,d} = M_{qd}(\theta_{m,e}) \frac{di_q}{dt} + M_{d0}(\theta_{m,e}) \frac{di_0}{dt} \quad (7.80)$$

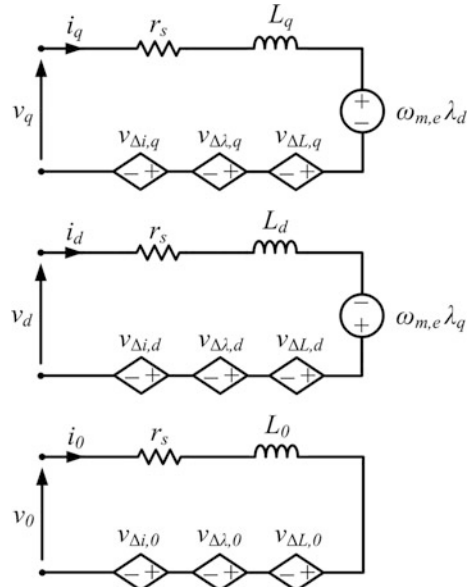
$$v_{\Delta L,0} = \frac{dM_{0q}(\theta_{m,e})}{dt} i_q + \frac{dM_{0d}(\theta_{m,e})}{dt} i_d + \frac{dL_0(\theta_{m,e})}{dt} i_0 \quad (7.81)$$

$$v_{\Delta \lambda,0} = \frac{d}{dt} \lambda_{pm,0}(\theta_{m,e}) \quad (7.82)$$

$$v_{\Delta i,0} = M_{0q}(\theta_{m,e}) \frac{di_q}{dt} + M_{0d}(\theta_{m,e}) \frac{di_d}{dt} \quad (7.83)$$

An equivalent circuit describing the proposed extended  $dq$  model based on (7.72)–(7.74) is shown in Fig. 7.3.

**Fig. 7.3** Equivalent circuit describing the proposed extended  $dq$  model



### 7.3.3 Formulation of the Electromagnetic Torque Using the Proposed Extended $dq$ Model

A detailed expression for the instantaneous active power as a function of the extended  $dq$  model parameters can be found by substituting  $v_q$ ,  $v_d$  and  $v_0$  expressed by (7.72)–(7.74) in (7.30). Mathematical manipulation of the result gives:

$$\begin{aligned} p &= \frac{3}{2} (v_q i_q + v_d i_d + 2v_0 i_0) \\ &= \frac{3}{2} \left[ \left( r_s i_q^2 + r_s i_d^2 + 2r_s i_0^2 \right) + \omega_m (\lambda_d i_q - \lambda_q i_d) \right. \\ &\quad + \omega_m [i_q \quad i_d \quad 2i_0] \left( \frac{d\mathbf{L}_{qd0}}{d\theta_{m,e}} \mathbf{i}_{qd0} + \frac{d\lambda_{pm,qd0}}{d\theta_{m,e}} \right) \\ &\quad \left. + [i_q \quad i_d \quad 2i_0] \mathbf{L}_{qd0} \frac{d\mathbf{i}_{qd0}}{dt} \right] \end{aligned} \quad (7.84)$$

In (7.84), the first term is the ohmic losses, the second and third terms indicate the instantaneous power that participate in the energy conversion and are the main contributors to the developed torque. The last term in (7.84) represents the rate of change of the energy stored in the magnetic field.

Under steady-state condition, the developed torque in a PMSM can be obtained as a function of the proposed extended  $dq$  model parameters by dividing the second and third terms in (7.84) by the rotor angular speed [9, 10]:

$$T_e = \frac{3P}{2} \left[ (\lambda_d i_q - \lambda_q i_d) + [i_q \quad i_d \quad 2i_0] \left( \frac{d\mathbf{L}_{qd0}}{d\theta_{m,e}} \mathbf{i}_{qd0} + \frac{d\lambda_{pm,qd0}}{d\theta_{m,e}} \right) \right] \quad (7.85)$$

By substituting the inductances and flux linkages in (7.85) by their detailed expressions, detailed equation for the developed torque can be obtained as:

$$T_e = T_{ave} + T_{r,rel} + T_{r,\lambda} \quad (7.86)$$

where  $T_{ave}$  is the average torque,  $T_{r,rel}$  is the reluctance torque ripple originating from the machine saliency, and  $T_{r,\lambda}$  is the alignment torque ripple originating from the PM flux linkages. Detailed expressions for the torque subcomponents in (7.86) are given by:

$$T_{ave} = \frac{3P}{2} (\lambda_{pm,d,0} i_q + (L_{d,0} - L_{q,0}) i_q i_d) \quad (7.87)$$

$$\begin{aligned}
T_{r,rel} = & \frac{3P}{22} \left[ (i_q^2 - i_d^2) \sum_{n=6,12,18,\dots} M_{qd,n} \sin(n\theta_m) \right. \\
& - \sum_{n=6,12,18,\dots} n(L_{q,n}i_q^2 + L_{d,n}i_d^2 + 2L_{0,n}i_0^2) \sin(n\theta_m) \\
& + i_0 \sum_{n=1,9,15,\dots} (M_{d0,n}i_q - M_{q0,n}i_d) \sin(n\theta_m) \\
& + i_q i_d \sum_{n=6,12,18,\dots} (L_{d,n} - L_{q,n} + 2nM_{qd,n}) \cos(n\theta_m) \\
& \left. + 2i_0 \sum_{n=3,9,15,\dots} n(M_{q0,n}i_q + M_{d0,n}i_d) \cos(n\theta_m) \right]
\end{aligned} \tag{7.88}$$

$$\begin{aligned}
T_{r,\lambda} = & -\frac{3P}{22} \left[ i_q \sum_{n=6,12,18,\dots} (\lambda_{pm,d,n} - n\lambda_{pm,q,n}) \cos(n\theta_m) \right. \\
& + i_d \sum_{n=6,12,18,\dots} (\lambda_{pm,q,n} - n\lambda_{pm,d,n}) \sin(n\theta_m) \\
& \left. - 2i_0 \sum_{n=3,9,15,\dots} n\lambda_{pm,0,n} \cos(n\theta_m) \right]
\end{aligned} \tag{7.89}$$

In the average torque expression (7.87), the first and second terms indicate the average alignment and reluctance torques, respectively. Evidently, the mean value of the *d*-axis PM flux linkage is the sole contributor to the average alignment torque, whereas the mean *q*- and *d*-axis inductances are the main sources of the average reluctance torque.

It is observed from (7.88) and (7.89) that the interaction of the supplied current with the harmonics in the *qd0* inductances and PM flux linkages are the main source of torque ripple. Evidently, torque harmonics (7.88) and (7.89) can be categorized into harmonics of order  $n = 6, 12, 18, \dots$  and harmonics of order  $n = 3, 9, 15, \dots$ . Clearly, the latter group of harmonics exists only when zero sequence currents are present.

In general, PM flux linkage harmonics are the main contributor to torque ripple dominating the effect of the inductance harmonics [11]. Hence, reluctance torque ripple,  $T_{r,rel}$ , in (7.86) can be neglected and the detailed torque ripple equation can be limited to alignment torque ripple,  $T_{r,\lambda}$ , only.

### 7.3.4 Experimental Tests for Determination of the Parameters in the Proposed Extended *dq* Model

In order to use the proposed extended *dq* model for a PMSM, its parameters need to be experimentally measured. These parameters include the *qd0* PM flux linkages

and inductances. From (7.45) to (7.61) and (7.63) to (7.69), parameters of the proposed model can be obtained from the  $abc$  PM flux linkage harmonics and the harmonics in the  $abc$  self- and mutual inductances. Experimental methods for measurement of these harmonics are described in the following.

### 7.3.4.1 Measurement of the Self- and Mutual Inductances

AC standstill test is the most common method for measuring the self- and mutual inductances [12]. This test is performed by injecting a constant AC current in one of the machine windings while the rotor is locked and the other machine windings are open-circuit. In order to obtain the inductances as a function of the rotor angular position, the voltage across all the windings at different lock position of the rotor, in one electrical cycle, are recorded. The inductances for each rotor position are then obtained by:

$$L_j = \frac{\sqrt{(V_j/I_j)^2 - r_s^2}}{2\pi f} \quad (7.90)$$

$$M_{jk} = \frac{V_k}{2\pi f I_j} \quad (7.91)$$

In the above equations  $V_j$  and  $V_k$  are phase  $j$  and  $k$  line-to-neutral voltages, respectively,  $I_j$  is the injected current in phase  $j$ , and  $f$  is the frequency of the injected current.

After obtaining the spatial waveforms of the self- and mutual inductances in one electrical cycle, Fast Fourier Transform (FFT) analysis can be used to obtain the mean value and harmonics amplitudes of the inductances.

### 7.3.4.2 Measurement of the PM Flux Linkage Harmonics

PM flux linkage for phase  $j$  in a PMSM can be obtained from its respective phase-to-neutral back-EMF. From Chap. 2, when a PMSM is rotating at angular speed  $\omega_{m,e}$  in electrical rad/s, phase  $j$  back-EMF has the following harmonic model:

$$\begin{aligned} e_j(t) &= -\frac{d}{dt} \left( \sum_n^{\infty} \lambda_{pm,n} \sin(n\omega_{m,e}t - n\theta_j) \right) \\ &= -\sum_{n=1,3,5,\dots}^{\infty} \underbrace{n\omega_{m,e}\lambda_{pm,n}}_{E_n} \cos(n\omega_{m,e}t - n\theta_j) \end{aligned} \quad (7.92)$$

where  $E_n$  is the  $n$ th harmonic amplitude for the back-EMF. According to (7.92), the PM flux linkage harmonic of order  $n$  can be obtained from the phase-to-neutral back-EMF harmonic of the same order, as follows:

$$\lambda_{pm,n} = \frac{E_n}{n\omega_{m,e}}, \quad n = 1, 3, 5, \dots \quad (7.93)$$

The above equation can be used to find the PM flux linkage harmonic by measuring the back-EMF harmonics at an arbitrary angular speed  $\omega_{m,e}$ . Similar to obtaining the inductance harmonics, an FFT analysis is required here for obtaining the harmonic spectrum of the measured back-EMF.

## 7.4 Experimental Results and Discussion

The 1 kW, 2.55 Arms 14-pole 18-slot prototype FSCW IPM machine that was studied in the previous chapters is used in this section to evaluate the proposed extended  $dq$  model. To this aim, parameters of the proposed extended  $dq$  model are first measured for the prototype machine. These parameters are then used in the derived detailed torque expressions to estimate the developed average torque and torque ripple.

### 7.4.1 Measurement of the Extended $dq$ Model Parameters

AC standstill test as described in Sect. 7.3.4 is used here to measure the inductances of the prototype FSCW IPM machine. Five current amplitudes are assumed: 1, 1.4, 1.8, 2.2, 2.5 A. The measured self- and mutual inductances with respect to the rotor angular position are shown in Fig. 7.4. It is observed that increasing the amplitude of the injected current which increases the saturation level of the machine magnetic material, causes the self-inductance to decrease. Whereas, mutual inductance is almost not affected the current amplitude. FFT analysis is used to obtain the harmonic content of the measured inductances as listed in Table 7.1. The data of this table are used in (7.45)–(7.61) to obtain the elements of the inductance matrix in the extended  $dq$  model as shown in Figs. 7.5 and 7.6.

From Fig. 7.5a, b, the measured  $L_d$ ,  $L_q$ , and  $L_0$  for the extended  $dq$  model have harmonics of order  $6k$ ,  $k = 1, 2, 3, \dots$  superimposed on a non-zero average value. The mutual inductances  $M_{qd}$ ,  $M_{q0}$ , and  $M_{d0}$ , as shown in Fig. 7.6a, b, contain harmonics with a zero mean value. Accordingly,  $M_{qd}$  contain  $6k$ ,  $k = 1, 2, 3, \dots$  harmonic orders, whereas harmonics in  $M_{q0}$ , and  $M_{d0}$  are of order  $3k$ ,  $k = 1, 3, 5, \dots$ . The design objective for the prototype FSCW IPM machine is to have the minimum possible torque ripple [13]. According to (7.88), such a design objective

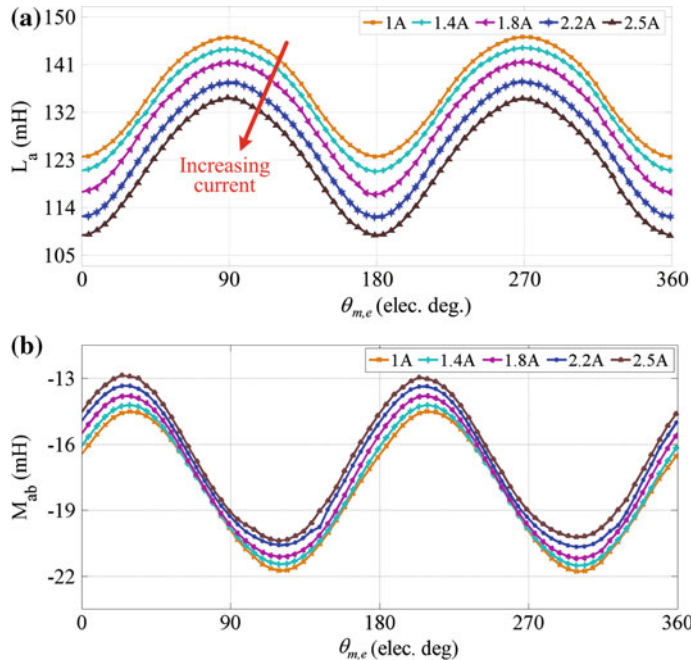


**Fig. 7.4** Inductances of the prototype FSCW IPM machine at different current amplitudes. **a** Self-inductance. **b** Mutual inductance

**Table 7.1** Harmonic amplitudes for the measured self- and mutual inductances

Inductance (mH)	Harmonic order				
	dc	2	4	6	8
$L_a$ 1A	135.742	11.322	0.902	0.161	0.068
$L_a$ 1.4A	133.594	11.489	1.141	0.153	0.014
$L_a$ 1.8A	130.421	12.068	1.371	0.213	0.057
$L_a$ 2.2A	126.112	12.446	1.240	0.261	0.106
$L_a$ 2.5A	122.614	12.676	0.987	0.160	0.117
$M_{ab}$ 1A	-18.15	3.568	0.022	0.006	0.003
$M_{ab}$ 1.4A	-17.955	3.609	0.107	0.003	0.014
$M_{ab}$ 1.8A	-17.622	3.685	0.165	0.059	0.002
$M_{ab}$ 2.2A	-17.175	3.674	0.203	0.089	0.003
$M_{ab}$ 2.5A	-16.789	3.685	0.184	0.071	0.002

decreases the higher order harmonics in the self-and mutual inductances, decreasing the harmonic amplitudes in the  $qd0$  inductances, as can be seen in Figs. 7.5 and 7.6.

Harmonic amplitudes for the PM flux linkage of the prototype FSCW IPM machine in the  $abc$ -system are found according to the methodology described in Sect. 7.3.4.2. Accordingly, the machine is rotated at the synchronous speed and its

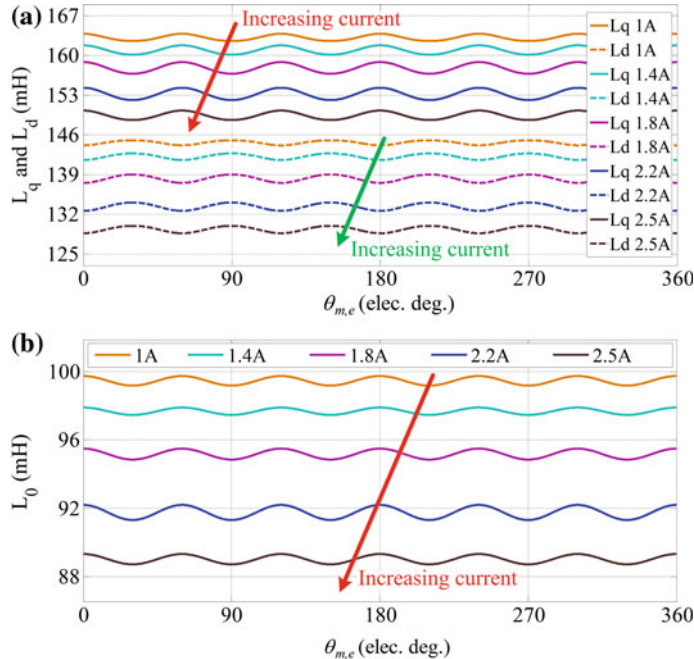


**Fig. 7.5** Variations of the diagonal elements of the detailed  $qd0$  inductance matrix with respect to current amplitude. **a**  $d$ - and  $q$ -axis self-inductances. **b** 0-axis self-inductance

back-EMF is measured as shown in Fig. 7.7. FFT analysis is performed on the measured back-EMF to find its harmonic amplitudes and subsequently the PM flux linkage harmonics using (7.93) as listed in Table 7.2. The detailed  $qd0$  PM flux linkages are calculated as shown in Fig. 7.8 by substituting the data of Table 7.2 in (7.63)–(7.69).

In Fig. 7.8, PM flux linkage for the  $d$ -axis contains harmonics of order  $6k$ ,  $k = 1, 2, 3, \dots$  that are superimposed on the average value of the inductance. However, PM flux linkage for the  $q$ -axis has a zero average value and only contains harmonics of order  $6k$ ,  $k = 1, 2, 3, \dots$ . For the  $0$ -axis PM flux linkage as shown in Fig. 7.8b, only harmonics of order  $3k$ ,  $k = 1, 3, 5, \dots$  exist with a zero average value.

#### 7.4.2 Estimation of the Average Torque and Torque Ripple for the Prototype FSCW IPM Machine

The value of torque and torque ripple are estimated in this section for the prototype FSCW IPM machine using the obtained parameters for the proposed extended  $dq$  model. It is assumed that the prototype is under full load condition and operating on an MTPA trajectory. From (7.87), average torque originates from the average

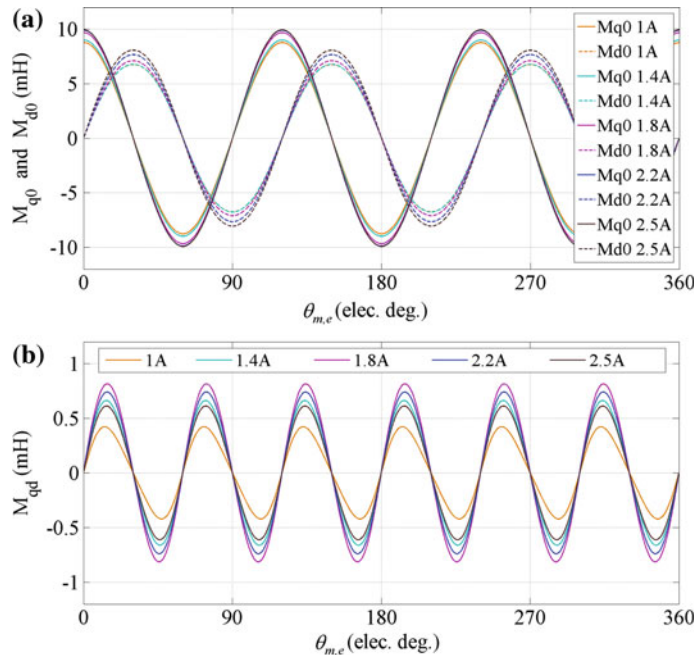


**Fig. 7.6** Variations of the non-diagonal elements of the detailed  $qd0$  inductance matrix with respect to current amplitude. **a** Mutual inductance for the  $d$ - and  $0$ -axes. **b** Mutual inductance for the  $d$ - and  $q$ -axes

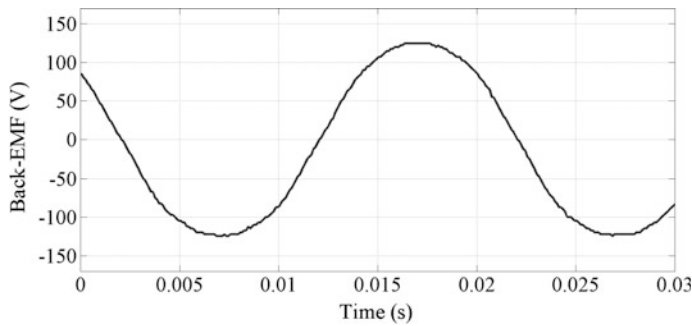


**Fig. 7.7** Measured back-EMF at the synchronous speed for the prototype FSCW PMSM

**Table 7.2** Harmonic content of the measured back-EMF and PM flux linkage

	Harmonic order					
	$dc$	1	3	5	7	9
$E_a$ (V)	0	127.38	7.06	0.08	0.78	0.91
$\lambda_{pm,a}$ (mWb)	0	405.48	7.49	0.05	0.35	0.32

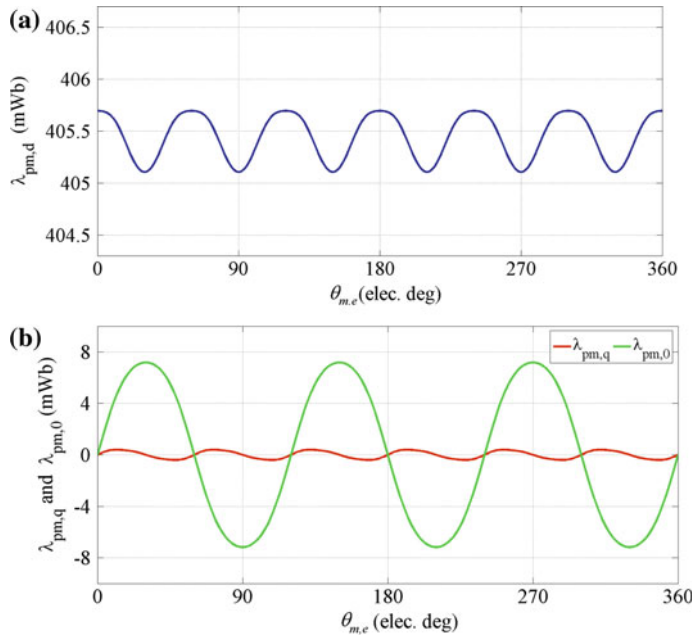


**Fig. 7.8**  $qd0$  PM flux linkages for the proposed extended  $dq$  model. **a**  $d$ -axis PM flux linkage. **b**  $q$ -axis and 0-axis PM flux linkages

values of the  $qd0$  inductances and PM flux linkages. Accordingly, in order to find the required  $dq$  currents to operate the machine at full load under MTPA condition, the average values of the machine parameters are used in the MTPA trajectory expression to determine  $i_d$  and  $i_q$  currents as follows:  $i_q = 3.5$  A,  $i_d = -0.6$  A.

The developed electromagnetic torque and torque ripple by the prototype FSCW IPM machine are estimated by substituting  $i_d$  and  $i_q$  in the derived torque equations in Sect. 7.3.3. The estimated torque using the proposed extended  $dq$  model, along with those obtained from the standard  $dq$  model and FEA are shown in Fig. 7.9. Evidently, the estimated torque by the proposed extended  $dq$  model is close to that obtained from the FEA model. The obtained torque ripple by the extended  $dq$  model is 1.1% of the average developed torque which is in close agreement with that obtained from FEA. From Fig. 7.9 it is observed that the standard  $dq$  model cannot estimate the torque ripple in the prototype machine. Moreover, the estimated average torque by the standard  $dq$  model is 2.6% higher than that estimated by the proposed extended  $dq$  model.

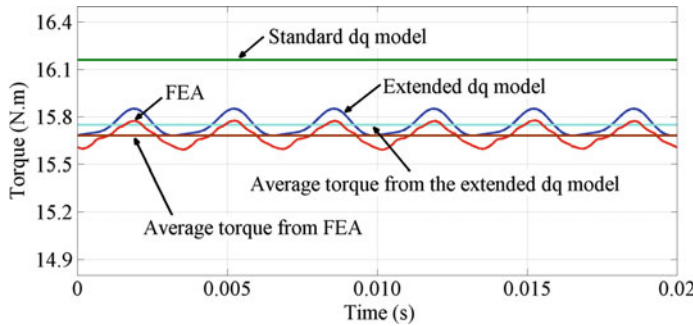


**Fig. 7.9** Estimation of electromagnetic torque for the prototype FSCW IPM machine running under MTPA algorithm at full load: results obtained through the proposed extended  $dq$  model, standard  $dq$  model, and FEA

## 7.5 Conclusion

An extended  $dq$  model for non-salient pole FSCW PMSMs was proposed in this chapter that accounts for the non-idealities in the machine parameters, i.e. non-sinusoidal MMF, back-EMF, inductances, and PM flux density. The proposed extended  $dq$  model was derived based on the detailed machine model in the  $abc$ -system which was transformed to the  $qd0$ -reference frame. Tests were described to experimentally measure the new parameters in the proposed extended  $dq$  model. The proposed model was used to derive detailed expressions for the developed torque, showing the different sources that contribute to the average torque and torque ripple. It was shown that the fundamental harmonics of the inductances and PM flux linkages in the  $abc$ -system are the sole contributors to the average torque. Torque ripple originates from the non-fundamental harmonics of the inductances and PM flux linkages.

A prototype FSCW IPM machine was used to validate the proposed extended  $dq$  model. First, parameters of the prototype machine for the proposed extended  $dq$  model were experimentally measured. These parameters were then used in the derived detailed torque expression to estimate the developed average torque and torque ripple. The obtained results through the proposed extended  $dq$  model were compared with those obtained from the standard  $dq$  model and FEA. It was shown that the proposed model could accurately estimate the average torque and torque ripple. However, the estimated average torque by standard  $dq$  model was inaccurate; moreover, it was unable to estimate the torque ripple.

## References

1. H.R. Bolton, R.A. Ashen, Influence of motor design and feed-current waveform on torque ripple in brushless DC drives. *Proc. Elect. Power Appl.* **131**, 82–90 (1984)
2. M. Farshadnia, R. Dutta, J.E. Fletcher, K. Ahsanullah, M.F. Rahman, H.C. Lovatt, Analysis of MMF and back-EMF waveforms for fractional-slot concentrated-wound permanent magnet machines, in *Proceedings of the ICEM* (2014), pp. 1976–1982
3. L. Alberti, M. Barcaro, N. Bianchi, Design of a low-torque-ripple fractional-slot interior permanent-magnet motor. *IEEE Trans. Ind. Appl.* **50**, 1801–1808 (2014)
4. F. Meier, J. Soulard,  $dq$  theory applied to a permanent magnet synchronous machine with concentrated windings, in *Proceedings of the PEMD* (2008), pp. 194–198
5. A. Chiba, F. Nakamura, T. Fukao, M. Azizur Rahman, Inductances of cageless reluctance-synchronous machines having nonsinusoidal space distributions. *IEEE Trans. Ind. Appl.* **27**, 44–51 (1991)
6. P.C. Krause, O. Wasynczuk, S.D. Sudhoff, S. Pekarek, *Analysis of Electric Machinery and Drive Systems*, vol. 75 (Wiley, 2013)
7. T. Sebastian, G. Slemmon, M. Rahman, Modelling of permanent magnet synchronous motors. *IEEE Trans. Magn.* **22**, 1069–1071 (1986)
8. R.H. Park, Two-reaction theory of synchronous machines generalized method of analysis—Part I. *AIEEE Trans.* **48**, 716–727 (1929)
9. C. Se-Kyo, K. Hyun-Soo, K. Chang-Gyun, Y. Myung-Joong, A new instantaneous torque control of PM synchronous motor for high-performance direct-drive applications. *IEEE Trans. Power Electron.* **13**, 388–400 (1998)
10. L. Yong, Z.Q. Zhu, D. Howe, Direct torque control of brushless DC drives with reduced torque ripple. *IEEE Trans. Ind. Appl.* **41**, 599–608 (2005)
11. B.H. Ng, M.F. Rahman, T.S. Low, K.W. Lim, An investigation into the effects of machine parameters on torque pulsations in a brushless Dc drive, in *Proceedings of the IECON* (1988), pp. 749–754
12. I. S. 115A-1987, IEEE standard procedure for obtaining synchronous machine parameters by standstill frequency response testing (1987)
13. L. Chong, R. Dutta, M.F. Rahman, Design of a highly efficient 1 kW concentric wound IPM machine with a very wide constant power speed range, in *Proceedings of the IPEC* (2010), pp. 1956–1961

# Chapter 8

## Conclusions and Future Works



### 8.1 Conclusions

The research reported in this thesis proposed a systematic analytical approach for the analysis and modelling of the magnetic and electrical characteristics of various double-layer FSCW IPM machines. The outcome of this study offers new insight into FSCW IPM machines with a V-shaped rotor and is of prime importance in the design, modelling, and control of application-oriented FSCW IPM machines.

The proposed methods and theories in this thesis were organized in three main sectors: the stator magnetic characteristics, the rotor magnetic characteristics, and the overall performance characteristics of the machine due to the interaction of the stator and rotor magnetic characteristics. A brief review of the contributions and achievements of this thesis follows.

#### 8.1.1 *Stator Magnetic Characteristics*

At first the spatial distribution of the magnetic field developed by FSCW stators, represented by the developed MMF, was analyzed and an analytical approach developed. The results of this analysis led to a systematic approach for formulation of the spatial MMF distribution in the airgap. Moreover, they were used to classify FSCW stators into different stator “*classes*” and “*categories*”, for which, lumped analytical formulae were derived for their spatial MMF distribution and harmonic winding factors.

The proposed systematic approach for computing the spatial MMF distribution of airgap was used to propose a heuristic algorithm for designing the optimal winding layout in multiphase FSCW PMSMs. A “*winding performance index*” was proposed to evaluate the performance of different winding layouts in terms of torque production ability for different FSCW stator classes.

The proposed methods for calculating the stator MMF distribution in the airgap and obtaining the optimal winding layout with maximum torque density in multi-phase machines were validated through FEA and experiment.

### **8.1.2 Rotor Magnetic Characteristics**

The buried magnets in an IPM rotor cause a non-homogenous magnetic saturation in the rotor core which deeply affects the spatial distribution of the rotor magnetic field in the airgap and the reluctance of the stator flux paths. These magnetic quantities are represented by the PM flux density in the airgap and the equivalent airgap function, respectively. With the purpose of proposing accurate analytical models for the rotor PM flux density and equivalent airgap function, an analytical model was proposed for calculating the non-homogenous saturation in different regions of the iron core. A dynamic relative permeability was used in the calculations to take the non-linear  $B$ - $H$  curve of the iron core into account. In contrast with the conventional equivalent airgap function which is just a function of the angle subtended along the rotor circumference, the proposed equivalent airgap length for FSCW IPM machines is a function of both the rotor angular position and the angle subtended along the rotor circumference. The proposed equivalent airgap function was used to accurately compute the machine inductances and the spatial distribution of the stator flux density in the airgap. Validations through FEA and experiment showed that the proposed models for the PM flux density and equivalent airgap function were more accurate compared with their respective conventional models.

### **8.1.3 Overall Performance Characteristics for the Machine**

Based on the proposed analysis and models for the magnetic characteristics of FSCW IPM machine, detailed analytical models in the *abc*-system for the self- and mutual inductances, back-EMFs, field-alignment torque, reluctance torque, and torque ripple were proposed. MTPA trajectory was calculated through the proposed analytical formulae and the developed torque was analytically calculated. The results were validated through FEA.

In the next step an open-phase fault condition was investigated. A four-leg inverter that enables injection of custom currents with adjustable phase angles into the FSCW IPM machine was considered. Detailed models were proposed through rigorous mathematical calculations for the developed field-alignment torque, reluctance torque, and torque ripple under the mentioned open-phase fault condition. It was shown through the proposed torque models that maximum average torque occurs if the two remaining phase windings of the machine are supplied with currents that their phase angles are 120 electrical degrees apart. MTPA trajectory

was analytically calculated through the proposed models for the open-phase fault conditions. It was shown that compared with the conventional methods for controlling the machine under an open-phase fault condition, supplying currents to the machine according to the proposed model results in a significant decrease in the torque ripple along with a significant increase in the average torque. The results were validated through FEA.

In the last step in analytical modelling of FSCW IPM machines, based on the proposed detailed models of the machine in the *abc*-system, an extended *dq* model was proposed that accounts for all the non-idealities in the machine parameters. Tests were described to experimentally measure the new parameters in the proposed extended *dq* model. The proposed extended *dq* model was then used to formulate detailed expressions for the developed average torque and torque ripple in the *dq* reference frame. Parameters of the proposed extended *dq* model were experimentally measured for a prototype FSCW IPM machine. Torque and torque ripple of the prototype machine were estimated through the proposed model and the results were validated through FEA.

## 8.2 Suggestions for Future Work

This thesis focused on analytical modelling of the performance characteristics of a FSCW IPM machine with a V-shaped rotor operating under healthy and open-phase fault conditions. The derived equations were functions of the machine geometrical parameters. A heuristic algorithm was also proposed for designing the optimal FSCW winding layout with maximum torque density for multiphase double-layer FSCW stators. Lastly, an extended *dq* model was proposed for FSCW IPM machines.

The proposed theories and methods are advised to be extended in the following areas:

- Designing application-oriented V-shaped FSCW IPM machines with desirable performance, under both healthy and open-phase fault conditions, using the proposed models for the machine performance characteristics, i.e. stator MMF, rotor PM flux density, equivalent airgap function, inductances, torque, and torque ripple.
- Extension of the proposed method for modelling the machine characteristics to other types of FSCW IPM machines, including machines with multi-layer rotors and four-layer stators.
- The use of the proposed machine model and MTPA trajectory for an open-phase faulted machine to design controllers that can achieve maximum average torque per ampere for the FSCW IPM machine under an open-phase fault condition.
- The use of the proposed machine model and MTPA trajectory for an open-phase faulted machine to design controllers that can suppress the torque ripple to a minimum under an open-phase fault condition.

- Extension of the proposed heuristic algorithm for designing double-layer FSCW winding layouts to four-layer FSCW stators.
- The use of the proposed extended  $dq$  model and torque equations to design controllers for suppressing the torque ripple caused by the inductance and back-EMF harmonics.
- Accurate on-line parameter estimation of the machine parameters using the proposed extended  $dq$  model.
- Designing FSCW IPM machines with desired saliency and characteristic current using the correct formulas of  $L_d$ ,  $L_q$ ,  $\lambda_d$ , and  $\lambda_q$  from the proposed extended  $dq$  model.

# Appendix A

## Analytical Calculation of Magnetic Reluctance and Magnetic Permeance in Objects of Different Geometrical Shapes

### A.1 Introduction

Examples are presented in this Appendix for analytical formulation of the reluctance and permeance of objects with different geometrical shapes.

Magnetic reluctance of an object represents the magnetic resistance against the flow of flux in that object and depends on the direction of the flux lines. A general formula for calculating the reluctance of a non-uniform object is given by:

$$\mathfrak{R} = \int \frac{dl}{\mu(l)A(l)} \quad (\text{A.1})$$

where  $dl$  represents the length element of the object in which the flux is flowing, and  $A(l)$  is the cross-sectional area of the length element, perpendicular to the flux path, and  $\mu(l)$  is the permeability of the length element.

Magnetic permeance is defined as:

$$\wp = \frac{1}{\mathfrak{R}} \quad (\text{A.2})$$

Similar to (A.1), an expression for obtaining the permeance is given by:

$$\wp = \int \frac{\mu(A)}{l(A)} dA \quad (\text{A.3})$$

where  $dA$  is the surface element parallel to the flux path, and  $l(A)$  is the length that the flux that travels inside the surface element, and  $\mu(A)$  is the permeability of the surface element.

Similar to electric circuit theory, for magnetic reluctances that are in series,  $\mathfrak{R}_1$ ,  $\mathfrak{R}_2$ ,  $\mathfrak{R}_3$ , ..., the total reluctance is:

$$\mathfrak{R}_T = \mathfrak{R}_1 + \mathfrak{R}_2 + \mathfrak{R}_3 + \dots \quad (\text{A.4})$$

Similarly, for magnetic permeances that are in parallel,  $\wp_1$ ,  $\wp_2$ ,  $\wp_3$ , ... the total permeance can be found from:

$$\wp_T = \wp_1 + \wp_2 + \wp_3 + \dots \quad (\text{A.5})$$

A few examples for analytical formulation of the magnetic reluctance and permeance in different objects are given in the following.

## A.2 Example-Case 1

In this example-case, the object shown in Fig. A.1 is considered. The flux is entering from the top and passes through the object. Equation (A.1) is used to formulate the magnetic reluctance of this object against the flux lines entering from the top of the object. The object is assumed to be uniform having the same relative permeability in all regions.

From (A.1), the object should be divided into differential elements with their cross-sectional area perpendicular to the flux path, as shown in Fig. A.1. The reluctance of these differential elements are in series, which is in accordance with (A.1).

The cross-sectional area of the differential length element is:

$$A = L \times w \quad (\text{A.6})$$

According to (A.1), the cross-sectional area of the differential length element should be found as a function of  $l$ . To this aim, the width of the differential element,  $w$ ,

**Fig. A.1** Geometry and flux direction in the object of example-case 1

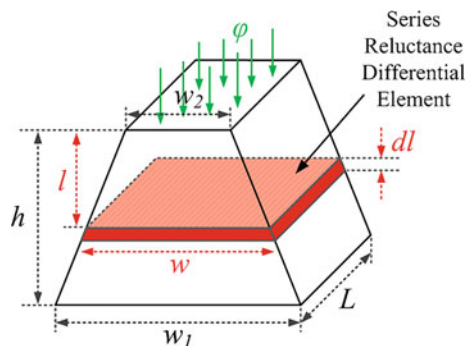
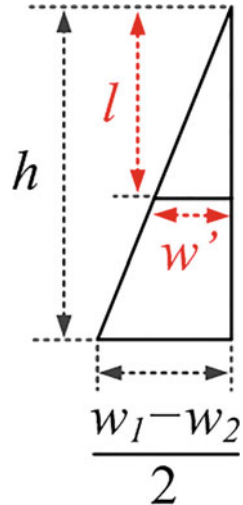


**Fig. A.2** Geometrical relations in the object of example-case 1



should be found as a function of  $l$  and replaced in (A.6). From Fig. A.2 it can be written:

$$w = w_2 + 2w' \quad (\text{A.7})$$

and

$$w' = \frac{l}{h} \left( \frac{w_1 - w_2}{2} \right) \quad (\text{A.8})$$

Thus:

$$w = w_2 + (w_1 - w_2) \frac{l}{h} \quad (\text{A.9})$$

Replacing (A.9) in (A.6) yields:

$$A = L \left( w_2 + (w_1 - w_2) \frac{l}{h} \right) \quad (\text{A.10})$$

The reluctance of the flux path can now be found by substituting (A.6) in (A.1) and solving the integral:

$$\begin{aligned}
 \mathfrak{R} &= \frac{1}{\mu} \int_0^h \frac{dl}{A(l)} \\
 &= \frac{1}{\mu L} \int_0^h \frac{dl}{w_2 + (w_1 - w_2) \frac{l}{h}} \\
 &= \frac{1}{\mu L} \frac{h}{w_1 - w_2} \ln \left( \frac{w_1}{w_2} \right)
 \end{aligned} \tag{A.11}$$

The permeance of this object can be found from (A.2) as follows:

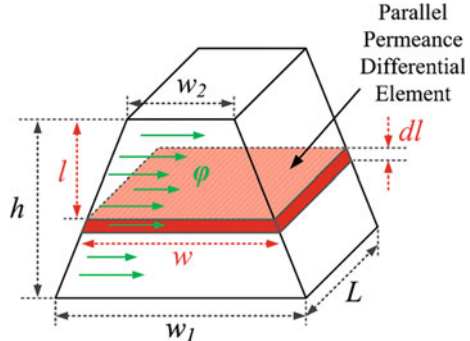
$$\wp = \mu L \frac{w_1 - w_2}{h} \frac{1}{\ln \left( \frac{w_1}{w_2} \right)} \tag{A.12}$$

### A.3 Example-Case 2

The object in this example-case is similar to example-case 1, however, the flux is passing the object from the sides as shown in Fig. A.3. For this case it is easier to calculate the permeance using (A.3) from the parallel differential elements shown in Fig. A.3. The surface element  $dA$  is found from Fig. A.3 as:

$$dA = L \times dl \tag{A.13}$$

**Fig. A.3** Geometry and flux direction in the object of example-case 2



Substitution of (A.13) in (A.3) yields:

$$\wp = \mu L \int_0^h \frac{1}{w(l)} dl \quad (\text{A.14})$$

where  $w$  is the length that the flux travels in the differential elements and is a function of  $l$ , given by (A.9). Substitution of (A.9) in (A.14) and solving the integral yields the lumped permeance formula:

$$\begin{aligned} \wp &= \mu L \int_0^h \frac{1}{w_2 + (w_1 - w_2) \frac{l}{h}} dl \\ &= \mu L \frac{h}{w_2 - w_1} \ln\left(\frac{w_2}{w_1}\right) \end{aligned} \quad (\text{A.15})$$

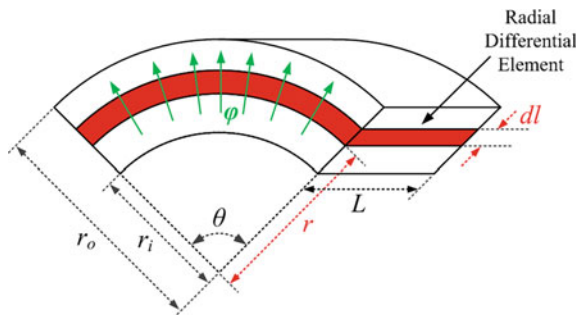
The reluctance can be found by substituting (A.15) in (A.2) as follows:

$$\mathfrak{R} = \frac{1}{\mu L} \frac{w_2 - w_1}{h} \frac{1}{\ln\left(\frac{w_2}{w_1}\right)} \quad (\text{A.16})$$

## A.4 Example-Case 3

In this example-case, the object for which the reluctance is being calculated is an arc through which the flux is passing radially. An example for this type of object is a magnet that is being used on the surface of an SPM rotor. A schematic for this object is shown in Fig. A.4.

**Fig. A.4** Geometry and flux direction in the object of example-case 3



The radial differential element for calculating the reluctance of the arc using (A.1) is shown Fig. A.4. Evidently, the radial flux is perpendicular to the surface of the differential element. The cross-sectional area of the differential element is given by:

$$A = \theta r L \quad (\text{A.17})$$

The length of the travelled flux through the differential element is:

$$dl = dr \quad (\text{A.18})$$

Substitution of (A.17) and (A.18) into (A.1) yields:

$$\begin{aligned} \Re &= \frac{1}{\mu} \int_{r_i}^{r_o} \frac{dl}{A(l)} \\ &= \frac{1}{\mu} \int_{r_i}^{r_o} \frac{dr}{\theta r L} \\ &= \frac{1}{\mu \theta L} \ln\left(\frac{r_o}{r_i}\right) \end{aligned} \quad (\text{A.19})$$

The permeance of the arc can be found by substituting (A.19) into (A.2):

$$\wp = \mu \theta L \frac{1}{\ln\left(\frac{r_o}{r_i}\right)} \quad (\text{A.20})$$

# Appendix B

## Developed Code in Matlab for Computing the Proposed Equivalent Airgap Function

### B.1 Introduction

The code written in Matlab for calculation of the proposed equivalent airgap function based on the proposed saturation model for the iron core as described in Chaps. 4 and 5 is demonstrated in the following. The *MCL* of different saturated rotor regions of Figs. 5.6 and 5.7 are first coded as separate Matlab functions as follows.

### B.2 Code for Calculation of *MCL* in Region 1

For the stator flux line entering region 1 at angle  $\theta_r$  and crossing this region and entering region 2 at angle  $\theta_1$ , the *MCL* is calculated through the following function:

```
function f = MCL_region_1(theta_r)

MCL = 0;

for theta_temp = theta_r:theta_resolution:theta_1

    h_pole = (theta_1 - theta_temp) * Rr;

    C_pole = 2 * sqrt(h_pole * (2*R_pole - h_pole));

    B_h_pole = (11/(11+(C_pole/2)))*B_sat;

    A_pole = (11 + (C_pole/2)) * lst;

    MCL = MCL + ((theta_resolution*Rr) / (mu_r(B_h_pole)) * A0/A_pole));

end

f = MCL;
```

### B.3 Code for Calculation of MCL in Region 2

For the stator flux line entering region 2 at angle  $\theta_r$ , and crossing through this region into region 3 at angle  $\theta_2$ , the MCL is calculated through the following function:

```
function f = MCL_region_2(theta_r)

A_rib_ave = (((theta_2-theta_r)*Rr)*l2*lst + sqrt((x ^ 2) - (l2 ^ 2))
              /2*lst*l2/2) / ((theta_2-theta_r)*Rr + sqrt((x ^ 2) - (l2 ^ 2))/2);

f = (((theta_2-theta_r)*Rr + sqrt((x ^ 2) - (l2 ^ 2))/2)
      / (mu_r(B_sat))) * (A0/A_rib_ave);
```

### B.4 Code for Calculation of MCL in Region 3

For the stator flux line entering region 3 at angle  $\theta_r$ , and crossing through this region into region 4 at angle  $\theta_3$ , the *MCL* is calculated through the following function:

```
function f = MCL_region_3(theta_r)

syms k;

if theta_r <= theta_2

    W = @(l) (sqrt(((theta_3-theta_2)*Rr)^2 - l^2) - (l *
        cos(alpha/2)/sin(alpha/2)));
    W_ave = 2 * double(symsum(W(k/1000000), [0,floor(1000000 *
        x*sin(alpha/2))]))/floor(1000000 * x*sin(alpha/2));
    A_x = (alpha*x/2) * lst;
    MCL = (A0/A_x) * W_ave/mu_r(B_sat);

else

    W = @(l) (sqrt(((theta_3-theta_2)*Rr)^2 - l^2) - (l *
        cos(alpha/2)/sin(alpha/2)));
    W_ave_1 = 2 * double(symsum(W(k/1000000), [0,floor(1000000 *
        ((theta_3-theta_2)*Rr)*sin(alpha/2))]))/floor(1000000 *
        ((theta_3-theta_2)*Rr)*sin(alpha/2));
```

```

W = @(l) (sqrt(((theta_r-theta_2)*Rr)^2 - l^2) - (l * 
    cos(alpha/2)/sin(alpha/2)));

W_ave_2 = 2 * double(symsum(W(k/1000000), [0,floor(1000000 * 
    ((theta_r-theta_2)*Rr)*sin(alpha/2))])/floor(1000000 * 
    ((theta_r-theta_2)*Rr)*sin(alpha/2));

W_ave_total = W_ave_1 - W_ave_2;

A_x = ((alpha*(theta_r - theta_2)*Rr + alpha*x)/2) * lst;

MCL = (A0/A_x) * W_ave_total/mu_r(B_sat);

end

f = MCL;

```

## B.5 Code for Calculation of *MCL* in Region 4

Before calculating the *MCL* of flux lines in region 4, the following function should be run in order to obtain the flux density at different radial arcs of differential radius centering at  $\theta_3$ :

```

function f = MCL_region_4_pre_run_data_generation

%% calculation of B on the circumference of inner circles
corresponding to alpha, until the circle at which B = B_mu_r_100

nnn = 0;
B_r_theta_temp = 100;

while B_r_theta_temp >= B_mu_r_100

    nnn = nnn+1;

    theta_IC(nnn) = theta_3 + nnn*theta_resolution;
        % angle in the airgap corresponding to the intersection
        % of the n'th inner circle and rotor circumference

    r(nnn) = Rr*(theta_IC(nnn) - theta_2);
        % radius of the n'th inner circle

    phi(nnn) = B_sat*alpha*x + (Bm*Rr/delta_2)*
        (0.5*(theta_IC(nnn) ^ 2 - theta_3 ^ 2)-delta_1*
        (theta_IC(nnn) - theta_3)) - Br*(r(nnn) -
        Rr*(theta_3 - theta_2));
        % the passing flux through n'th inner circle,
        % assuming it is radial in the inner circles

```

```

B_nnn(nnn) = phi(nnn)/(alpha*r(nnn));
    % B at the circumference of the n'th inner circle

B_r_theta_temp = B_nnn(nnn);

end

theta_mu_r_100 = theta_IC(nnn);

%% calculation of the average lengths

syms k;

W = @(l) (sqrt((x)^2 - l^2) - (l * cos(alpha/2)/sin(alpha/2)));

W_0 = 2 * double(symsum(W(k/1000000), [0,floor(1000000 * x
    * sin(alpha/2))]))/floor(1000000 * x*sin(alpha/2));

for j=1:nnn

    W = @(l) (sqrt(r(j)^2 - l^2) - (l * cos(alpha/2)/sin(alpha/2)));

    W_calc(j) = 2 * double(symsum(W(k/1000000), [0,floor(1000000 *
        r(j)*sin(alpha/2))]))/floor(1000000 * r(j) *
        sin(alpha/2));

end

```

For the stator flux line entering region 4 at angle  $\theta_r$  and crossing through this region, the *MCL* is calculated through the following function:

```

function f = MCL_region_4(theta_r)

if theta_r < theta_3

    for j=1:nnn

        if j==1

            W_ave(j) = W_calc(j)-W_0;

            A_IC(j) = ((alpha*r(j) + alpha*x)/2) * lst;

            MCL = (A0/A_IC(j))*W_ave(j)/mu_r(B_nnn(j));

        elseif j>1

```

```

W_ave(j) = W_calc(j)-W_calc(j-1);

A_IC(j) = ((alpha*r(j-1) + alpha*r(j))/2) * lst;

MCL = MCL + (A0/A_IC(j))*W_ave(j)/mu_r(B_nnn(j));
% valid for when theta_r < theta_3

end
end

if theta_r >= theta_3

MCL = 0;

i=1;
t=0;

while t~=1
    if theta_IC(i)>theta_r
        t=1;
    else
        i=i+1;
    end
end

for j=i:nnn

if j==1

W_ave(j) = W_calc(j)-W_0;

A_IC(j) = ((alpha*r(j) + alpha*x)/2) * lst;

MCL = (A0/A_IC(j))*W_ave(j)/mu_r(B_nnn(j));

elseif j>1

W_ave(j) = W_calc(j)-W_calc(j-1);

A_IC(j) = ((alpha*r(j-1) + alpha*r(j))/2) * lst;

MCL = MCL + (A0/A_IC(j))*W_ave(j)/mu_r(B_nnn(j));

end

end

f = MCL;

```

## B.6 Code for Computing the Proposed Equivalent Airgap Function

The code for computing the proposed equivalent airgap function is provided in the following which is based on the method described in Chap. 5 and the corresponding functions as defined in Sects. B.2–B.5. Note that for obtaining the equivalent airgap function in the  $d$ -axis alignment of the rotor the parameter II should be set to 1, while for the  $q$ -axis alignment of the rotor, II should be set to 0.

```

II=0      % II=0 for q-axis position and II = 1 for d-axis position

% Core magnetic material data

mu_0=4*pi*(10^-7);
Js=1.55;
mu_r_0=5000;
a=0.403743;
B_sat = 2;
B_mu_r_100 = 1.553;      % B at the at mu_r = 100 for the core material

% PM data

Br = 1.09;
mu_r_pm = 1.05;

% Trapezoidal Flux density information

delta_1 = 0415*pi/180;
delta_2 = 4.271*pi/180;
Bm = 0.688;

% Geometry data

P = 14;                      % number of poles
Q = 18;                      % number of slots
g = 1.2 * 10^-3;              % airgap length
lst = 79 * 10^-3;             % Stack length
slot_opening = 1.2 * 10^-3;    % magnet length
lpm = 13.5 * 10^-3;           % magnet width
wpm = 2 *10^-3;               % cord length
C = 0.012666;                 % gap between the end of the PMs
Rr = 40 * 10^-3;               % Rotor radius
l2 = 0.796 * 10^-3;            % bridge width
l1 = 0.568 * 10^-3;            % length between two adjacent poles
l1 = l2;
R1 = l1 / 2;

beta = 2*asin((C-lg/2)/(2*lpm));          % angle between PMs

theta_1 = R1 / (Rr-l1);

```

```

pole_pitch=2*pi/P;

alpha = pi/2 + asin((lpm*sin(betha/2)+lg/2)/(Rr-l2))-(betha/2);
% internal angle of the PMs with the rotor circumference

x = l2 / sin(alpha);

gamma = 2*asin(C/(2*(Rr-l2)));

l_alpha = l2 * cos(alpha) / sin (alpha);

theta_2 = (pole_pitch - gamma) / 2 - (l_alpha / Rr);
% approximate angle of the point on the rotor
circumference where alpha is measured from

theta_resolution = 0.01;

MCL_g = g;

MCL_region_4_pre_run_data_generation; %generating data required by
                                         MCL_region_4 function

A0 = (theta_mu_r_100 * Rr) * lst ;

i = 0;

for theta_r = 0:theta_resolution:theta_1

    i = i+1;

    theta_data(i) = theta_r

    MCL(i) = MCL_g + MCL_region_1(theta) + MCL_region_2(theta_1) +
              MCL_region_3(theta_2) + MCL_region_4(theta) +
              II*(A1/(lpm*lst))*wpm/(mu_r_pm);

end

for theta_r = (theta_r + theta_resolution):theta_resolution:theta_2

    i = i+1;

    theta_data(i) = theta_r

    MCL(i) = MCL_g + MCL_region_2(theta) + MCL_region_3(theta_2) +
              MCL_region_4(theta) + II*(A1/(lpm*lst))*wpm/(mu_r_pm);

end

for theta_r = (theta_r + theta_resolution):theta_resolution:theta_3

    i = i+1;

    theta_data(i) = theta_r

```

```

MCL(i) = MCL_g + MCL_region_3(theta) + MCL_region_4(theta) +
          II*(A1/(lpm*lst))*wpm/(mu_r_pm);

end

k = 0;

for theta_r = (theta_r +
                 theta_resolution):theta_resolution:theta_mu_r_100

    i = i+1;

    theta_data(i) = theta_r

    MCL(i) = MCL_g + MCL_region_4(theta) +
              II*(A1/(lpm*lst))*wpm/(mu_r_pm);

end

for theta_r = (theta_r +
                 theta_resolution):theta_resolution:(pole_pitch/2)

    i = i+1;

    theta_data(i) = theta_r

    MCL(i) = MCL_g + II*(A1/(lpm*lst))*wpm/(mu_r_pm);

end

% The MCL function is complete for half a pitch now. In the follows
% the MCL function will be completed for one full pitch (over one pole).

k=0;

MCL_length = length(MCL);

for theta_r= (theta_r + theta_resolution):theta_resolution:pole_pitch

    i = i+1;

    theta_data(i) = theta_r

    MCL(i) = MCL(MCL_length - k);

    k = k+1;

end

%Now the MCL function will be regenerated for the whole circumference
%(over the P poles)

MCL_length = length(MCL);

for i=2:3*P

```

```
for j=1:MCL_length  
theta_data((i-1)*MCL_length+j) = theta_data((i-1)*MCL_length)  
+theta_data(j);  
  
MCL((i-1)*MCL_length+j)=MCL(j);  
  
end  
end  
  
MCL_f(:,1) = theta_data;  
  
MCL_f(:,2) = MCL;  
  
figure();plot(MCL_f(:,1),MCL_f(:,2))
```

# Appendix C

## Experimental Measurement of the FSCW IPM Machine Inductances

### C.1 Introduction

The  $d$ - and  $q$ -axis inductances of the prototype 14-pole 18-slot FSCW IPM machine are measured at different current and frequencies in this Appendix. This is performed through the standard AC standstill tests at rated and above-rated frequencies. A high accuracy measurement for the inductances is achieved by taking into account the effect of iron and magnet losses in the calculation. Variations of the measured inductances with respect to current amplitude and frequency are analyzed.

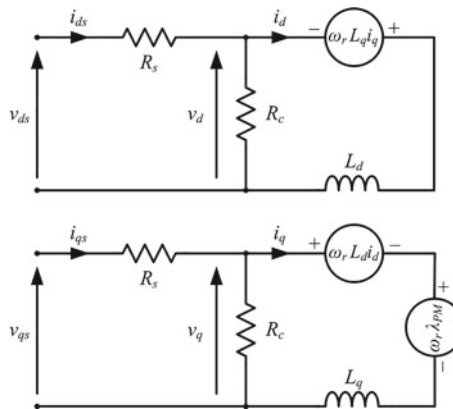


**Fig. C.1**  $dq$  equivalent circuit for PMSMs that considers core and magnet losses

## C.2 Two-Axis Equivalent Circuit

A  $dq$  equivalent circuit for PMSMs that considers core and magnet losses is shown in Fig. C.1. The parameters of the two-axis equivalent circuit is investigated in the following.

### C.2.1 Iron Core and Magnet Losses

In PMSMs, the main MMF harmonic is synchronous with the rotor and participates in average torque production. All other MMF harmonics are asynchronous with the rotor and contribute to iron core and magnet losses. In order to run the machine at high speeds, the frequency of the supply current has to be increased above the rated frequency. This increases the relative speed between the rotor and the asynchronous MMF harmonics, increasing the iron core and magnet losses. These losses are presented in form of a parallel resistant  $R_c$  in the  $dq$  equivalent circuit of Fig. C.1.

### C.2.2 Self- and Mutual Inductances

When a sinusoidal spatial distribution of MMF is assumed in a PMSM, the mean value for mutual inductance is analytically calculated equal to half of that for the self-inductance. Moreover, the second order harmonics in the self- and mutual inductances are calculated to have the same amplitudes [1]. For PMSMs with FSCW stators, the spatial MMF distribution contains a wide range of harmonics and is not sinusoidal. This alters inductances of the machine as explained in Chap. 7. Average torque is only the result of the mean values of the machine parameters; therefore, in machines with a non-sinusoidal spatial MMF distribution, the time-variant components of the  $dq$  parameters can be neglected. This results in the same  $dq$  equivalent circuit as shown in Fig. C.1. However, unlike PMSMs with sinusoidal spatial MMF harmonics, the  $d$ - and  $q$ -axis inductances for the FSCW PMSM should be calculated from Chap. 7 as follows:

$$L_d = (L_0 - M_0) - (L_2/2 + M_2) \quad (\text{C.1})$$

$$L_q = (L_0 - M_0) + (L_2/2 + M_2) \quad (\text{C.2})$$

In the above equations  $L_0$  and  $M_0$  are the mean values, and  $L_2$  and  $M_2$  represent the second spatial harmonic amplitude in the self- and mutual inductances, respectively.

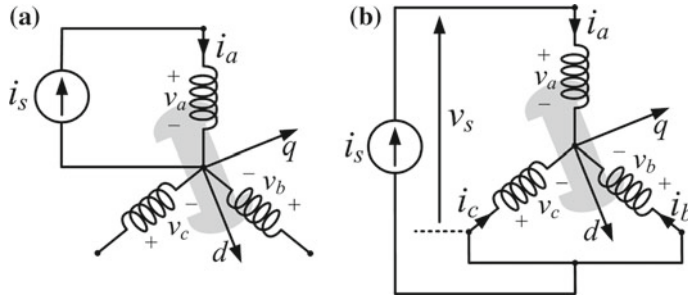


**Fig. C.2** Methods for measuring inductances in PMSMs. **a** Single-phase excitation AC standstill test. **b** Three-phase excitation AC standstill test

### C.3 Parameter Measurement

The parameters in the  $dq$  equivalent circuit of Fig. C.1 are the stator resistance,  $R_s$ , PM flux linkage,  $\lambda_{PM}$ , and the  $d$ - and  $q$ -axis inductances,  $L_d$  and  $L_q$ . Although these parameters are temperature dependent [2], their investigation is not of interest in this Appendix.

Among the parameters of the  $dq$  equivalent circuit as shown in Fig. C.1, the stator resistance can be simply and accurately measured using a four probe ohm-meter; the PM flux linkage can be calculated from the back-EMF using the method described in Chap. 7; and the  $dq$  inductances can be obtained using an AC standstill test that accounts for the iron core and magnet losses. To this end, a single-phase AC standstill test, and a three-phase AC standstill test as shown in Fig. C.2, will be analyzed and used in the following to measure the inductances for the prototype FSCW IPM machine.

#### C.3.1 Single-Phase AC Standstill Test

In this method is shown in Fig. C.2a and explained in Chap. 7, the self- and mutual inductances can be obtained as function of the rotor angular position  $\theta_{m,e}$  in electrical radians, as follows:

$$L_a(\theta_{m,e}) = \frac{\sqrt{(V_a/I_a)^2 - R_s^2}}{2\pi f} \quad (\text{C.3})$$

$$M_{ab}(\theta_{m,e}) = \frac{V_b}{2\pi f I_a} \quad (\text{C.4})$$

where  $V_a$  and  $V_b$  are the measured line-to-neutral voltages for phases  $a$  and  $b$ , respectively,  $I_a$  is the phase  $a$  current, and  $f$  is the current frequency.

The  $d$ - and  $q$ -axis inductances in this method are indirectly found by performing an FFT analysis on the measured self- and mutual inductances to obtain its harmonic content, after which they are used in (C.1) and (C.2) to give the  $dq$  inductances. This method has the drawback of neglecting the loss resistance,  $R_c$ .

### C.3.2 Three-Phase AC Standstill Test

In the three-phase AC stand still test, the  $d$ - and  $q$ -axis inductances are directly measured. This method benefits from considering the effect of the machine losses in the inductance measurement procedure. A schematic for this method is shown in Fig. C.2b where a single-phase AC current is injecting a certain current into the windings. In this method, the rotor is positioned in the  $d$ -axis and  $q$ -axis alignments, and the current,  $I_s$ , terminal voltage,  $V_s$ , and power factor,  $\cos(\varphi)$ , are measured. In this method, the machine instantaneous voltages in the  $abc$ -system are given by:

$$\begin{cases} v_a = (2\sqrt{2}/3)V_s \cos(\omega_e t) \\ v_b = (\sqrt{2}/3)V_s \cos(\omega_e t + \pi) \\ v_c = (\sqrt{2}/3)V_s \cos(\omega_e t + \pi) \end{cases} \quad (\text{C.5})$$

$$\begin{cases} i_a = \sqrt{2}I_s \cos(\omega_e t - \varphi) \\ i_b = (\sqrt{2}/2)I_s \cos(\omega_e t - \varphi + \pi) \\ i_c = (\sqrt{2}/2)I_s \cos(\omega_e t - \varphi + \pi) \end{cases} \quad (\text{C.6})$$

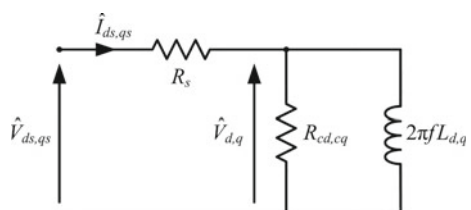
In the  $d$ -axis alignment,  $\theta_{m,e} = 0$ , transformation of (C.5) and (C.6) to the  $dq$  reference frame yields:

$$\begin{cases} v_d = (2\sqrt{2}/3)V_s \cos(\omega t) \\ v_q = 0 \end{cases} \quad (\text{C.7})$$

$$\begin{cases} i_d = \sqrt{2}I_s \cos(\omega t - \varphi) \\ i_q = 0 \end{cases} \quad (\text{C.8})$$

Similarly, in the  $q$ -axis alignment,  $\theta_{m,e} = -\pi/2$ , the  $dq$  voltages and currents are:

**Fig. C.3** Steady-state  $dq$  equivalent circuit for the machine under AC stand-still test



$$\begin{cases} v_d = 0 \\ v_q = (-2\sqrt{2}/3)V_s \cos(\omega t) \end{cases} \quad (\text{C.9})$$

$$\begin{cases} i_d = 0 \\ i_q = -\sqrt{2}I_s \cos(\omega t - \varphi) \end{cases} \quad (\text{C.10})$$

The equivalent circuit for the steady-state condition of the machine with a locked rotor is illustrated in Fig. C.3. By measuring the terminal voltage, current, and power factor, the  $dq$  voltage and current phasors for the equivalent circuit of Fig. C.3 can be found as follows:

$$\begin{cases} \hat{V}_{ds} = (2/3)V_s \angle 0 \\ \hat{I}_{ds} = I_s \angle -\varphi \end{cases} \quad \text{and} \quad \begin{cases} \hat{V}_{qs} = (-2/3)V_s \angle 0 \\ \hat{I}_{qs} = -I_s \angle -\varphi \end{cases} \quad (\text{C.11})$$

The voltage across the loss resistance is obtained by:

$$V_{d,q} = \sqrt{V_{ds,qs}^2 + R_s^2 I_{ds,qs}^2 + 2R_s P_{in}} \quad (\text{C.12})$$

where

$$P_{in} = V_{ds,qs} I_{ds,qs} \cos \varphi \quad (\text{C.13})$$

Equations (C.12) and (C.13) can now be used to find the parameters of the  $dq$  equivalent circuit (Fig. C.4):

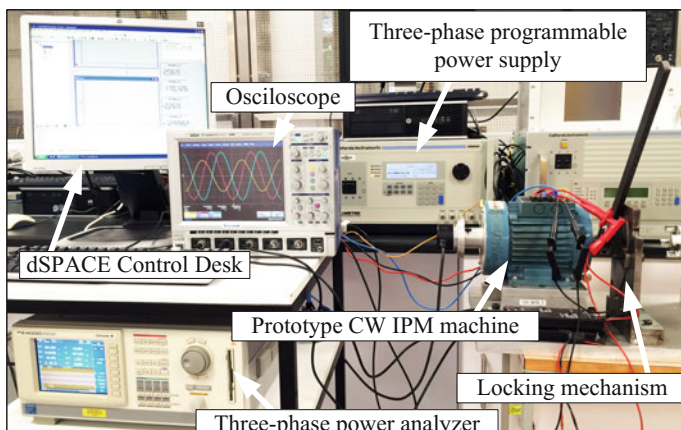


**Fig. C.4** Experimental setup for measurement of the inductances using AC standstill tests

$$R_{cd,cq} = \frac{V_{d,q}^2}{P_{in} - R_s I_{ds,qs}^2} \quad (C.14)$$

$$L_{d,q} = \frac{V_{d,q} R_{cd,cq}}{2\pi f} \frac{1}{\sqrt{R_{cd,cq}^2 I_{ds,qs}^2 - V_{d,q}^2}} \quad (C.15)$$

In (C.14), the input power,  $P_{in}$ , is affected by the machine losses and thus the frequency. Therefore, similar to the machine inductances, the loss resistances  $R_{cd}$  and  $R_{cq}$ , are dependent on the supply frequency and the supply current amplitude.

### C.3.3 Determination of the d- and q-axis Alignments

Determination of the  $d$ - and  $q$ -axis alignments are necessary to performing the three-phase AC standstill test.

In order to locate the  $d$ - and  $q$ -axis alignment, an AC voltage is applied to the test circuit of Fig. C.2b. The rotor is then slowly rotated for one electrical cycle and the currents in phase  $b$  and  $c$  are measured. In this process,  $I_b$  will become equal to  $I_c$  at two rotor positions. For these two rotor positions, the one at which the current is smaller represents the  $q$ -axis alignment of the rotor, while the other position at which the current is higher is the  $d$ -axis alignment. This is explained by  $L_q$  being greater than  $L_d$  in a standard PMSM.

## C.4 Experimental Results and Discussion

Figure C.5 shows the experimental setup for measuring the inductances of the 1 kW, 2.55 A 14-pole 18-slot prototype FSCW IPM machine at different current

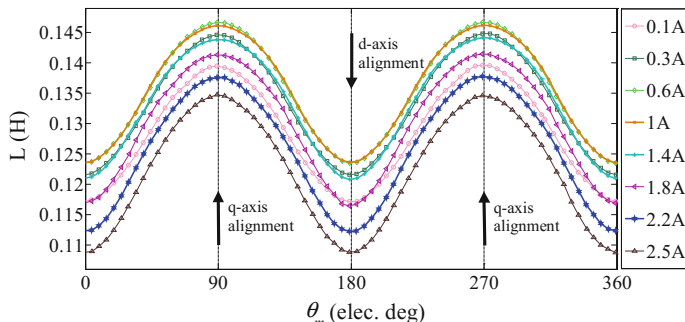


**Fig. C.5** Measured self-inductance using the single-phase AC standstill test for different currents at rated frequency 50 Hz

amplitudes and frequencies using the single-phase and three-phase AC standstill test. In the experimental setup a clamp is used for locking the rotor at different angular positions. A position sensor that is connected to a dSPACE control desk is used to obtain the rotor position. The AC current is generated by an AMETEK CSW5550 programmable power supply which allows easy adjusting of the supply current amplitude and frequency.

#### C.4 Machine Inductances at Rated Frequency

The measured self- and mutual inductances using the single-phase AC standstill test are shown in Figs. C.5 and C.6. It can be seen that at the peak value of the self-inductance occurs at the  $q$ -axis alignment of the rotor; while the minimum value of the self-inductance is at the  $d$ -axis alignment. For the mutual inductance,

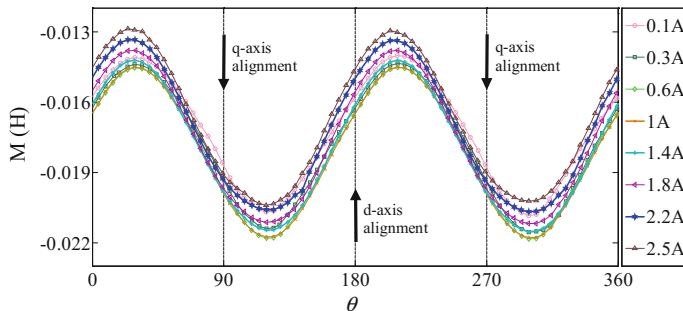


**Fig. C.6** Measured mutual inductance using the single-phase AC standstill test for different currents at rated frequency 50 Hz

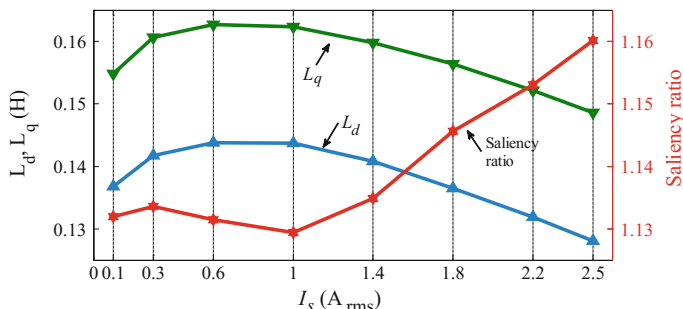


**Fig. C.7** Variations of the  $dq$  inductances and saliency ratio with respect to current amplitude obtained from the single-phase excitation AC standstill test at 50 Hz

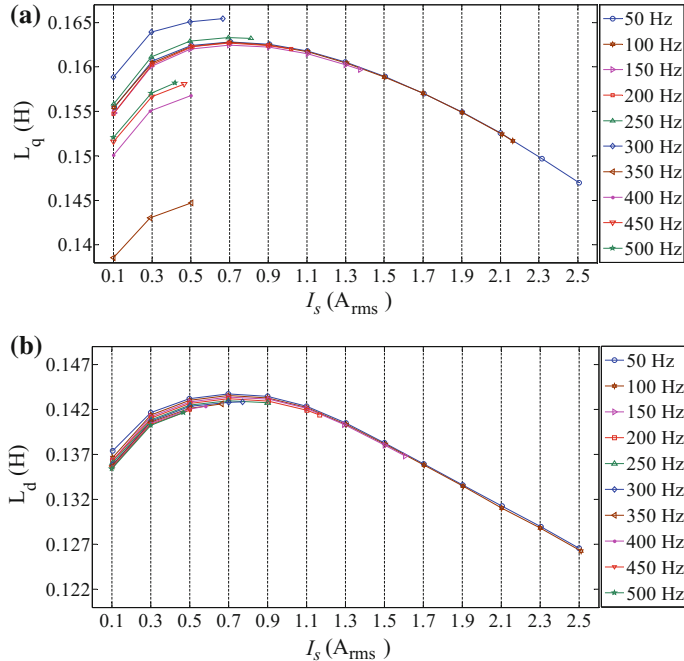


**Fig. C.8** Variations of the measured  $dq$  inductances using the three-phase AC standstill test with respect to current amplitude at different supply frequencies. **a** The  $q$ -axis inductance. **b** The  $d$ -axis inductance

its minimum and maximum values occur at a 60 electrical degrees displacement from the  $d$ -axis and  $q$ -axis alignments, respectively.

The harmonic content of the self-and mutual inductances of Figs. C.6 and C.7 are obtained using an FFT analysis and used in (C.1) and (C.2) to find the  $dq$  inductances as shown in Fig. C.8. It is observed that, unlike a DW PMSM, in the FSCW IPM machine,  $L_d$  and  $L_q$  are uniformly varying with respect to the current amplitude. Saliency ratio of the prototype machine is also shown in Fig. C.8, demonstrating an increase with the increasing current amplitude.

Figure C.9 shows variations of the  $dq$  inductances with respect to the current amplitude and frequency obtained using the three-phase AC standstill test. These results demonstrate the same behavior to that of the single-phase AC standstill test at 50 Hz.

#### C.4.2 Machine Inductances Above the Rated Frequency

The  $dq$  inductances for the machine at above the rated frequency and different current amplitudes are measured using the three-phase AC standstill test. The input

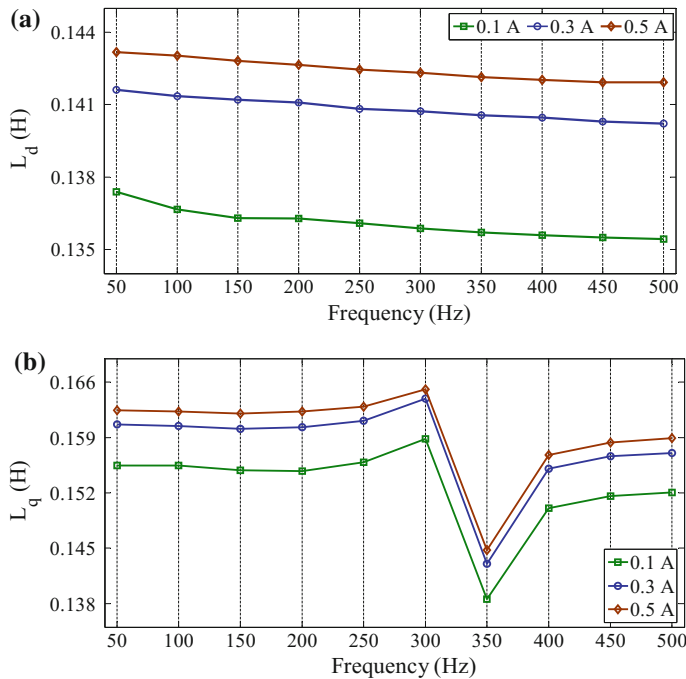


**Fig. C.9** Variations of the measured  $dq$  inductances with respect to frequency at different current amplitudes. **a** The  $d$ -axis inductance. **b** The  $q$ -axis inductance

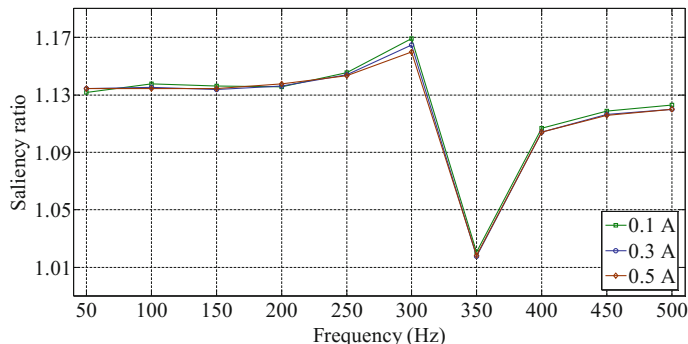


**Fig. C.10** Variations in the saliency ratio versus the supplied frequency, based on the measured  $L_d$  and  $L_q$  for the prototype machine

frequency is increased up to 500 Hz in 50 Hz increments. The inductances are obtained using (C.14) and (C.15) for each input current amplitude and frequency. It has to be noted that the utilized programmable power supply is limited to a voltage output of 312Vrms. This limits the measurements since the machine impedance increases with an increasing frequency, requiring a higher voltage to maintain a certain current amplitude. Therefore, at higher frequencies maintaining smaller current amplitudes are only feasible. This explains the fewer data points at high frequencies.

The measured  $dq$  inductances as a function of the current amplitude at different frequencies are shown in Fig. C.8. It is observed that variations of the inductance with the current amplitude follow the same trend at all frequencies.

Inductance variations with frequency at different currents are shown in Fig. C.9. Evidently,  $L_d$  is gradually decreasing with the increasing frequency. On the contrary, the measured  $q$ -axis inductance demonstrates anomalies as evident from Fig. C.9b. It is observed that  $L_q$  is almost constant with frequency up to 200 Hz. Above this frequency and up to 300 Hz, the  $q$ -axis inductance slightly increases. From Fig. C.9b, a sudden drop in the  $q$ -axis inductance can be observed at 350 Hz,

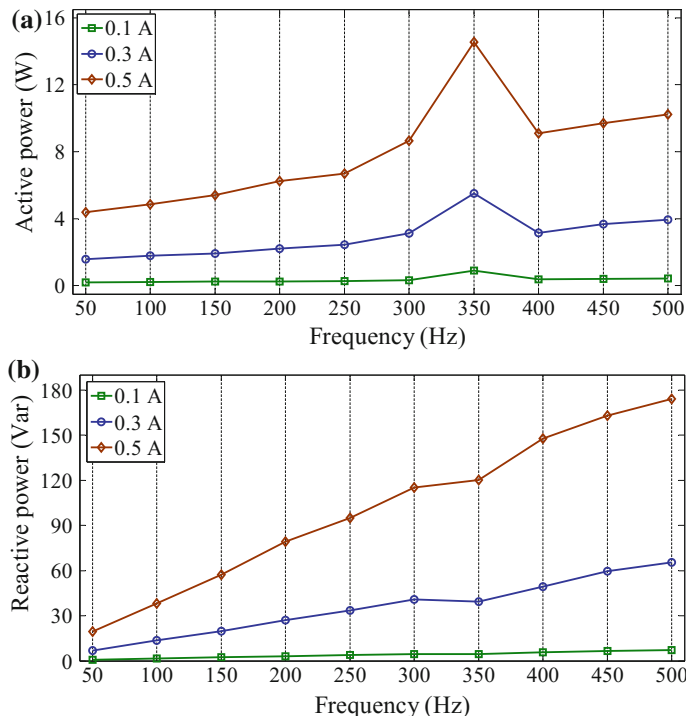


**Fig. C.11** Variations of the input powers to the machine with respect to the supply frequency.  
**a** Active power. **b** Reactive power

after which the inductance recovers to a lower value compared to its value prior to the drop.

Saliency ratio variations with respect to the supply frequency is obtained for the prototype FSCW IPM machine based on the measured  $dq$  inductances as shown in Fig. C.10. In this figure a significant drop is observed in the saliency ratio at 350 Hz. This is caused by the significant drop in  $L_q$  to a value close to  $L_d$  at this frequency. The observed phenomenon is explained in the following.

In salient-pole machines magnetic forces tend to rotate the rotor such that the equivalent air-gap length is always kept at its minimum value. The equivalent air-gap length of IPM machines in the  $q$ -axis alignment is larger than the  $d$ -axis alignment. Because of this, in the  $q$ -axis alignment the magnetic forces are acting to minimize the equivalent airgap length. Under the AC standstill test, this causes acoustic noise and vibrations. This becomes worse if the frequencies of the exciting forces in the machine are close to its natural frequency. Clearly, if the harmonic amplitudes of these magnetic forces are considerable and their frequencies are close to the machine resonant frequency, they could amplify the resonance and vibrations of the machine.

For the prototype FSCW IPM machine, when the rotor is locked at the  $q$ -axis alignment, high acoustic noise and vibrations were observed at 350 Hz. For the three-phase AC standstill test, the measured active and reactive powers with respect to the supplied current frequency are measured as shown in Fig. C.11a and b, respectively. Evidently, at all current amplitudes there is a steady rise in the reactive power as the frequency increases. Nevertheless, a significant and sudden increase is observed in the consumed active power at 350 Hz which corresponds to the stator resonance. This explains the sudden drop in the measured  $L_q$  at 350 Hz. In the AC standstill test, as the rotor is locked the mechanical output power is assumed to be zero. However, the mechanical vibrations at 350 Hz are drawing a significant amount of active power from the power source. Evidently, such phenomenon is introducing errors in the AC standstill test at 350 Hz.

## C.5 Conclusion

This appendix reported the measurement of the  $d$ - and  $q$ -axis inductances for a prototype FSCW IPM machine. The inductances were measured with respect to both the current amplitude and current frequency. It was observed that the  $dq$  inductances decrease with the increasing current amplitude as the machine is pushed into saturation. From the obtained results, increasing the sully frequency causes the  $d$ -axis inductance to decrease. However, for the  $q$ -axis inductance, anomalies were observed at a certain frequency close to the natural frequency of the machine. Causes of this behavior were investigated, leading to the conclusion that measurement of the inductances by the AC standstill test at high frequencies close to the resonance frequency of the machine negatively affects the accuracy of the AC standstill method.

## References

- [1] P.C. Krause, O. Wasynczuk, S.D. Sudhoff, S. Pekarek, *Analysis of electric machinery and drive systems*, vol. 75 (Wiley, 2013)
- [2] C. Chinchul, L. Wootaik, O.K. Soon, H. Jung-Pyo, Experimental estimation of inductance for interior permanent magnet synchronous machine considering temperature distribution. IEEE Trans. Magn. **49**, 2990–2996 (2013)

## About the Author



**Mohammad Farshadnia** received the Ph.D. degree in electrical engineering from the University of New South Wales, Sydney Australia in 2016, and the M.Sc. and B.Sc. degrees also in electrical engineering from the University of Kashan, Iran, in 2011 and 2008, respectively.

Mohammad is specialised in the design and electromagnetic analysis of multiphase electrical machines. He is currently a postdoctoral researcher with the Energy Systems Research Group at the University of New South Wales, Sydney, Australia. His main interests include multiphase PM machines, electromagnetics, fault tolerant drive systems, and renewable energy.